Magnetotelluric Instrument Development and Application

Darcy Nascimento

Doctor of Philosophy

The University of Edinburgh

1997

Declaration

This thesis has been composed by me and has not been submitted for any other degree. Except where acknowledgement is made, the work is original.

Darcy Nascimento

Acknowledgements

I wish to thank G.Dawes and Dr. B.Hobbs for their fundamental advice throughout the course of this work. I am particularly thankful to G.Dawes who gave me continuous supervision, suggestions and provided me with all facilities and material support needed for my investigation. His competence and expertise on a wide area of research and experience in all aspects of instrumentation and its applications were very important for the successfull outcome of this work. I also thank him for carefully and critically reading the manuscripts of this thesis and for many helpful suggestions he made.

I thank G.Dawes and Dr. O.Ritter for their help during field works, an experience from which I learnt a lot. I also thank Dr. A.Junge who gave me opportunity to participate on my first field work and suggested me applications for the equipment. In this particular, Dr. A.Junge has always new and original ideas which are very appreciated by people who develop instrumentation.

I am grateful to the former and present members of the EM group at the Department of Geology and Geophysics in Edinburgh; D.Bailey, G.Balasis, Dr. R.J. Banks, G.J.Dawes, Dr. B.A.Hobbs, Dr. R.V.S.Hutton, Dr. A.Jung, K.MacDonald, Dr. O.Ritter, Dr. P.Ritter, Dr. T.Volti, Prof. K.Whaler, A.Vickery, A.J.K.Wilson for the interesting and productive discussions during our regular meetings. The dedication of Dr. O.Ritter and more recently D.Bailey in setting up these meetings regularly must be acknowledged.

My participation in the Electrodes Workshop in Garchy, France was very important to introduce me into this area. I wish to thank Dr. R.Banks and G.Dawes for the financial support and Dr. G.Clerc, G.Petiau, F.Perrier and P.Marquis for the hospitality and facilities provided in Garchy.

The EMERALD software developed by Dr. O.Ritter was extensively used for SPAM Mk-III data analysis. I would like to thank him for allowing me to use the program and for giving me unlimited and prompt support whenever required. I also thank Dr. A.Junge who is the author of the robust processing ANAROB.

I would also like to thank some members of the departmental staff. Dr. I.Chisholm and S.Voss for maintaining the internal computer network and for their support

to my particular needs, G.Waugh and Dr. P.Simms for their help in administrative matters, and particularly to Mrs. Ann Menin for her fundamental advice in chemistry matters and material support to the electrodes design. A.Jackson should also be acknowledged among other things, for his expertise in mechanical matters.

I am grateful to CAPES, for funding my studies in Edinburgh, and CNPq-Observatório Nacional and Universidade Federal do Rio de Janeiro for supporting me during my studies in Edinburgh. Furthermore, I wish to thank my colleagues from ON and the Departamento de Eletrônica - UFRJ for giving me the opportunity to concentrate on my research, especially Prof. J.A.da Rocha for helping me in all matters related to the UFRJ.

I wish to thank Dr. S.L.Fontes from the Departamento de Geofísica for motivating me to apply for this project and for helping me with internal matters in the Observatório Nacional.

I would like to thank the people from NERC-GEP; M.Valiant, P.Kearney, A.Ball and J.Stevenson for their support to my needs. Also, theirs and G.Dawes's friendship were very important to keeping up a pleasant working atmosphere.

I want to thank Graham, Alicia and children for their hospitality and for making our stay in Edinburgh a very enjoyable period of our lives.

Finally, my very special thanks to my family. My wife Carmen Lúcia had a strong and fundamental commitment to my work and gave me tranquillity to concentrate exclusively on my research and above all, she gave me continuous emotional support and incentive to carry on my work. I also thank my daughters Paula and Natália for the daily happiness they bring me. Without the presence, motivation and emotional support of my family I would not have concluded this thesis.

Abstract

The magnetotelluric method (MT) has been used to study the conductivity structure of the earth. The method uses the time variations of the natural magnetic and the induced electric fields measured simultaneously at the earth's surface. The demand for new MT instrumentation has increased in the past few years. New applications require more complex sensor configurations. Characteristics like size, weight and real time data processing have become increasingly important to improve logistics and mobility, although it is becoming more and more difficult to measure electromagnetic fields without strong contamination from *man-made* sources. The ability to process MT results in the field is essential for a quick evaluation of the site conditions, enabling the time required to obtain a suitable amount of good quality data to be reduced.

SPAM Mk-III (Short-Period Automatic Magnetotelluric) developed at The Edinburgh University introduces new concepts in terms of geophysical instrumentation. The equipment is based on a family of Transputer devices widely used in parallel processing, incorporating the recent technologies and techniques. Its modular design allows flexible network configurations. A complete description of the equipment, design concepts, features and the precautions needed in designing low-noise instrumentation are presented in this thesis.

The distinctive SPAM Mk-III capabilities of multi-channel data acquisition were used in two field experiments. In the first experiment the effect of the electric dipole length on the impedance tensor was investigated. Results confirmed that the apparent resistivity and phase are quite consistent and that longer electric dipoles tend to be more susceptible to local interference. In the second experiment the rotation property of the impedance tensor was studied. The experiment reinforces the assumption that for a layered earth (1-D), the impedance tensor is independent of measuring coordinates.

New $Cu\text{-}CuSO_4$ electrodes were developed for the field work. These are to operate in the frequency range of the SPAM Mk-III (0.001Hz to 2kHz). Several electrodes were tested and the results indicate that noise and stability do not depend on the internal resistance. Also the frequency response of these electrodes shows they do not present any filter effects within the range of magnetotelluric application.

Contents

List of Tables

List of Figures

CHAPTER 1

Introduction

The magnetotelluric method (MT) is concerned with the determination of the conductivity structure of the earth's crust. The method, developed in the 1950's by Cagniard (1953) and Tikhonov (1950) is based on properties of electromagnetic wave propagation and establishes a frequency domain relationship between the orthogonal components of the earth's natural magnetic field and the induced electric field. The magnetic field is detected by magnetometers whose output is a voltage proportional to the field intensity. The electric field produces a potential difference between two points on the earth which can be detected by a pair of electrodes and produces a voltage proportional to the induced electric field strength. The resulting electric signals are pre-conditioned, converted to the digital domain and the discrete time-series stored for further robust processing based on statistical analysis. Chapter 2 presents the theoretical background required by the method and an overview of the basic concepts of magnetotelluric instrumentation.

Chemical electrodes are widely employed for measuring the electric field. These devices are the least studied of the geophysical sensors and the main source of uncertainty. From April 1995 to April 1996 a comprehensive experiment on electrodes was carried out at the Centre de Rechérches Geophysiques de Garchy-France whose objective was to compare different types of electrodes in terms of

long term stability, to identify the best designs and to propose installation methods. The first results of the research, presented in June 1996 by G.Clerc in the *13th Workshop on Electromagnetic Induction in the Earth* (Clerc et al. 1996a) are an important step forward to a better understanding of these devices. Chapter 3 describes test procedures of the experiment in France and make comments on test results of the electrodes gathered for the investigation. Chapter 3 also describes the design of an alternative Cu-$CuSO_4$ electrode to operate in the range 0.001Hz–2000Hz and an attempt to create an electric circuit model for the device. The noise characteristics and the frequency response of the new electrode are also presented.

Even though electronic instrumentation plays an essential role in the MT method there has been little published hitherto. The basic concepts and general approach set out by Cantwell and Madden (1960) on this early paper are still valid. However, not only has the technology been improved significantly but also the demand for new and more complex MT instrumentation has increased over the past few years. In 1990 Graham Dawes undertook the feasibility study for developing a new concept of equipment for the acquisition of time-varying geological data (Dawes 1990), the SPAM Mk - III, which aimed to provide, among other characteristics, modular framework, flexible configuration, upgradeable computational power, accurate time synchronization, continuous wide band recording and basic real-time MT analysis. The equipment is based on a family of Transputer devices and utilizes extensively digital data communication to apply the concept of distributed processing. SPAM Mk-III is based on three modules: Base, Remote and Sensor Box and each box contains specific hardware. Chapter 4 introduces all these concepts and explains the advantages of digital over analogue communication. In the same chapter some networked configurations are suggested and the first laboratory test with seismic sensors connected to the equipment is presented.

Chapter 5 explains in details the Base box which incorporates the main computational power, the network management software and the data analysis.

A GPS (Global Positioning System) receiver supported by dedicated hardware and software is an integral part of the system providing an accurate time reference for global synchronized data acquisition. System time-synchronization and an overview of digital cable communication are also explained in the same chapter. The Remote box, which provides a final analogue signal pre-conditioning, performs the synchronous analogue-to-digital conversion and fast Fourier transform (FFT) is explained in Chapter 6 which also comments on the importance of correcting the signals for the frequency response of sensors and analogue circuitry. The Sensor box provides analogue pre-conditioning for a set of local sensors (electric, magnetic or seismic). The Sensor box, sensor conditioning boards, the need for a low-noise electronics and important precautions required to achieve this objective are explained in Chapter 7.

Chapter 8 explains the Repeater box that is an accessory module designed to extend the distance of the digital data communication and to monitor the digital signal flow.

The multi-channel capabilities of the equipment are essential for the experiments described in Chapter 9. The first consists of simultaneous data acquisition of signals from three magnetic and eight orthogonal electric dipoles with line lengths between 10 and 80m aligned according to the traditional MT coordinate system (North-South,East-West). The aim is to study the influence of different electric line lengths on measuring the induced electric field. In the second experiment the magnetometers and four of the electric dipoles were kept in the same position. An additional set of sensors (two magnetometers and four electric dipoles) rotated 45 ° were included in the network and simultaneous data acquisition from thirteen channels performed. The objective is to investigate the rotation property of the magnetic and electric fields as represented by the impedance tensor.

SPAM Mk-III is a complex electronic instrument for geophysical application. I joined the project in February 1993 as a part of my PhD studies. My contri-

bution to the development consists of the design, construction and testing of the Cu-$CuSO_4$ electrodes (Chapter 3), the Sensor Box (Chapter 7) and the Repeater Box (Chapter 8) as well as in-depth studies of the operational parameters which led to final system modifications. Specifically these are:

- The study of long distance digital cable communication characteristics in section 5.8, and the tests relating digital data throughput and digital cable length in section 5.9.1. These were important to determine the digital line termination scheme for communication stages and to establish the maximum digital cable length for each digital communication speed.

- The study of the Operational Amplifier gain *versus* bandwidth characteristics in section 6.3.2.7, which enabled us to set limits for the Channel board output gain needed for the SPAM Mk-III High-Frequency operation mode.

- The study of the frequency limitations due to analogue communication in conjunction with the characteristics of the output amplifier in the Sensor board (section 7.3.2.5), which demonstrated the need for identical output stages for electric and magnetic boards, and which determined the maximum analogue cable length for the equipment Short-Period and High-Frequency operation modes.

The generation of the internal synchronisation pulse derived from 10MHz crystal as explained in section 5.5.2 is also my contribution.

Finally I used the instrument and the electrodes in complex configurations to perform the field experiments (Chapter 9).

CHAPTER 2

Magnetotelluric Method

2.1 Introduction

Magnetotelluric method (**MT**) is concerned with the determination of the structure of the earth's crust in terms of electrical conductivity. Those relationships were explained by Tikhonov (1950) and Cagniard (1953), who in particular appreciated the potential importance of magnetotellurics to exploration. The source signal for the method consists of naturally occurring fluctuations in the earth's electro-magnetic field which are present at any place on earth, practically any time and for a wide range of frequencies. The source of these fields is associated with micropulsations of the natural magnetic field caused by disturbances in the ionosphere and electric phenomena in the atmosphere, such as thunderstorms. The electromagnetic field propagates with little attenuation over large distances in the space between the ionosphere and earth surface, somewhat in the manner of a guided wave between parallel conducting planes. Due to the large resistivity contrast between the more conductive earth and the air, these plane electromagnetic waves penetrate vertically into the earth. According to the fundamental laws of electromagnetism, the time-varying magnetic field induces electric field in the geoelectrical structure. The transfer function in the frequency domain relating the natural electric field components to the natural magnetic field com-

ponents measured on the surface of the Earth contains information on the earth's conductivity distribution.

The frequency range commonly used for Magnetotelluric studies is from 0.0001 to several hundred hertz. Some applications utilize the higher part of the frequency range occupied by the natural electromagnetic spectrum, from 1Hz to 10000Hz. The latter is referred to in the literature as audiomagnetotellurics (AMT). The difference between MT and AMT is only in the depth ranges for which they are used and the equipment used for data acquisition. The same mathematical descriptions and physical principles apply to both.

In general, electromagnetic methods are widely used in geophysical exploration, including controlled-source techniques (both frequency and time-domain) and natural-source techniques such as AMT and MT (McCracken, Oristaglio, and Hohmann 1986). The depth of investigation and conductivity are important parameters on determining the exploration method (Spies 1989). All these methods are based on properties of electromagnetic wave propagation and require identical theoretical background.

2.1.1 Theoretical Background

An elementary development of electromagnetic theory can be used to describe magnetotelluric wave propagation. To understand the propagation and attenuation of such waves it is necessary to refer to Maxwell's equations:

$$\nabla \times \mathbf{E} = -\frac{\partial \mathbf{B}}{\partial t} \tag{2.1}$$

$$\nabla \times \mathbf{H} = \mathbf{J} + \frac{\partial \mathbf{D}}{\partial t} \tag{2.2}$$

The above equations represent vector fields in three-space ($F = (x, y, z)$) where $\mathbf{E}$ and $\mathbf{H}$ are the *electric* and *magnetic field strengths* respectively in volt

per meter ($V \cdot m^{-1}$) and ampere per meter ($A \cdot m^{-1}$), $\mathbf{B}$ is the *magnetic induction* in tesla (T), $\mathbf{J}$ is the *electric current density* in ampere per square meter ($A \cdot m^{-2}$) and $\mathbf{D}$ is the *displacement* in coulomb per square meter ($C \cdot m^{-2}$).

Equation 2.1 is a mathematical statement of Faraday's law that an electric field exists in the region of a time-varying magnetic field, such that the induced emf is proportional to the negative rate of change of magnetic flux. Equation 2.2 is a mathematical statement that a magnetic field is generated in space by current flow and that field is proportional to the total current (conduction plus displacement) in the region.

Using the vector identity $\nabla \cdot \nabla \times \mathbf{A} = 0$ the time-varying fields can be written as

$$\nabla \cdot \nabla \times \mathbf{E} = -\nabla \cdot \frac{\partial \mathbf{B}}{\partial t} \implies -\frac{\partial}{\partial t}(\nabla \cdot \mathbf{B}) = 0$$

hence

$$\nabla \cdot \mathbf{B} = 0 \tag{2.3}$$

Similarly,

$$\nabla \cdot \mathbf{J} + \nabla \cdot \frac{\partial \mathbf{D}}{\partial t} = \nabla \cdot \mathbf{J} + \frac{\partial}{\partial t}(\nabla \cdot \mathbf{D}) = 0 \tag{2.4}$$

The divergence of current density is equivalent to the rate of accumulation of charge density Q. From equation 2.4,

$$\nabla \cdot \mathbf{J} = -\frac{\partial Q}{\partial t} = \frac{\partial}{\partial t}(\nabla \cdot \mathbf{D})$$

hence

$$\nabla \cdot \mathbf{D} = 0$$

In regions of finite conductivity, charge does not accumulate to any extent during current flow, leading to Q=0. Then, a relationship between displacement and electric field can be written as

$$\nabla \cdot \mathbf{J} = 0 \qquad \nabla \cdot \mathbf{D} = \varepsilon\varepsilon_0 \nabla \cdot \mathbf{E} = 0 \tag{2.5}$$

where ε is the relative dielectric permittivity and ε_0 is the permittivity of free space in farad per meter ($\varepsilon_0 = 8.85 \times 10^{-12}$ F/m).

There is also a relationship between magnetic induction and magnetic field:

$$\mathbf{B} = \mu\mu_0 \mathbf{H}$$

where μ is the relative magnetic permeability of the medium and μ_0 is the permeability of free space ($\mu_0 = 4\pi \times 10^{-7}$ Tm/A).

In homogeneous isotropic media, these relationships and Ohm's law can be expressed as

$$\mathbf{B} = \mu\mathbf{H} \qquad \mathbf{D} = \varepsilon\mathbf{E} \qquad \mathbf{J} = \sigma\mathbf{E} \tag{2.6}$$

where σ is the conductivity. In the above equations $\mu = \mu_r\mu_0$ and $\varepsilon = \varepsilon_r\varepsilon_0$ where μ_r and ε_r are relative magnitudes of permeability and dielectric permittivity.

Therefore, Maxwell's equations 2.1 and 2.2 can be written as

$$\nabla \times \mathbf{E} = -\mu \frac{\partial \mathbf{H}}{\partial t} \tag{2.7}$$

$$\nabla \times \mathbf{H} = \sigma\mathbf{E} + \varepsilon \frac{\partial \mathbf{E}}{\partial t} \tag{2.8}$$

Equation 2.8 must incorporate additional current sources $\mathbf{J}_0$ not induced by the magnetic field, such as self-potential or power device and can be written as

$$\nabla \times \mathbf{H} = \mathbf{J}_0 + \sigma\mathbf{E} + \varepsilon \frac{\partial \mathbf{E}}{\partial t}$$

Taking the curl of equations 2.7 and 2.8, the statements of equations 2.3 and 2.5 and using the identity

$$\nabla \times (\nabla \times \mathbf{A}) = \nabla(\nabla \cdot \mathbf{A}) - \nabla^2\mathbf{A}$$

we obtain

$$\nabla^2 \mathbf{E} = \mu\sigma \frac{\partial \mathbf{E}}{\partial t} + \mu\varepsilon \frac{\partial^2 \mathbf{E}}{\partial t^2} \tag{2.9a}$$

$$\nabla^2 \mathbf{H} = \mu\sigma \frac{\partial \mathbf{H}}{\partial t} + \mu\varepsilon \frac{\partial^2 \mathbf{H}}{\partial t^2} \tag{2.9b}$$

Magnetotelluric works are concerned with sinusoidal time variations, thus the electric and magnetic field can be expressed as

$$\mathbf{E}(t) = \mathbf{E}_0\, e^{jwt} \qquad \text{and} \qquad \mathbf{H}(t) = \mathbf{H}_0\, e^{jwt}$$

hence

$$\frac{\partial \mathbf{E}}{\partial t} = jw\mathbf{E} \qquad \text{and} \qquad \frac{\partial \mathbf{H}}{\partial t} = jw\mathbf{H}$$

where $\omega = 2\pi f$ is the angular velocity of the field. Therefore, equations 2.9a and 2.9b can be simplified to

$$\nabla^2 \mathbf{E} = j\omega\mu\sigma\mathbf{E} - \omega^2\mu\varepsilon\mathbf{E} \tag{2.10a}$$

$$\nabla^2 \mathbf{H} = j\omega\mu\sigma\mathbf{H} - \omega^2\mu\varepsilon\mathbf{H} \tag{2.10b}$$

The above equations represent propagation of electric and magnetic field vectors in an isotropic homogeneous medium having conductivity σ, relative permeability μ and relative dielectric permittivity ε. The first and second terms on the right-hand side are related respectively to the conduction and displacement currents.

2.1.2 Attenuation of Electromagnetic Fields

The electromagnetic wave is attenuated in traveling through any media but not in free space. The significance of this attenuation depends on the frequency and the electrical characteristics of the material: ε, μ, ω and σ. The frequency range used in MT works is usually limited to a few thousands of Hertz. The dielectric permittivity of the water is $\varepsilon \approx 80$ and for most rocks and minerals $\varepsilon < 20$. The relative magnetic permeability of most of rocks and minerals are $\mu < 3$, normally

$\mu \approx 1$. Therefore, the displacement term of the propagation equation is negligible and equations 2.10a and 2.10b can be written as

$$\nabla^2 \mathbf{E} \approx \mu\sigma \frac{\partial \mathbf{E}}{\partial t} \approx j\omega\mu\sigma\mathbf{E} \tag{2.11a}$$

$$\nabla^2 \mathbf{H} \approx \mu\sigma \frac{\partial \mathbf{H}}{\partial t} \approx j\omega\mu\sigma\mathbf{H} \tag{2.11b}$$

This is the diffusion equation, which in the air and in rocks of low conductivity reduces to

$$\nabla^2 \mathbf{E} \approx 0 \qquad \nabla^2 \mathbf{H} \approx 0 \tag{2.12}$$

For a plane-polarized wave propagating along an axis perpendicular to the plane of polarization the above equations can be solved by assuming the form

$$H = H_y(z,t) = H_0 e^{jwt+mz}$$

where H is the magnitude of $\mathbf{H}$. Then,

$$\nabla^2 H = \frac{\partial^2 H_y}{\partial z^2} = m^2 H \qquad \text{and} \qquad \frac{\partial H_y}{\partial t} = j\omega H$$

Substituting these functions in equation 2.11b we have

$$m^2 = j\omega\mu\sigma \quad \text{or} \quad m = \pm(1+j)\sqrt{\frac{\omega\mu\sigma}{2}}$$

If we define:

$$k = \sqrt{\frac{\omega\mu\sigma}{2}} \qquad \text{then} \qquad m = \pm(1+j)k$$

Taking into account that H must be finite when $z = \infty$ we have

$$H_y = H_0 e^{j\omega t-(1+j)kz} = H_0 e^{-kz+j(\omega t-kz)} \tag{2.13}$$

The real part of the above equation is then

$$H_y = H_0 e^{-kz} \cos(\omega t - kz) \tag{2.14}$$

The right-hand term of the above equation represents an harmonic motion with a phase shift. The exponential represents an attenuation of the wave as a function of propagation distance z. By considering $\omega = 2\pi f$, $\mu = \mu_0 = 4\pi \times 10^{-7}$ and using resistivity (ρ) as the inverse of conductivity (σ), we can write equation 2.14 as

$$\left|\frac{H_y}{H_0}\right| \approx e^{-2\times 10^{-3} z \sqrt{f/\rho}} \tag{2.15}$$

An important concept in electromagnetic theory is the *skin depth*, that is the distance of penetration which the signal is attenuated by $1/e$, i.e. to 37% of its original value. Substituting $|H_y/H_0| = 1/e$ in equation 2.15 we have

$$z_s \approx 500\, z \sqrt{f/\rho} \quad \text{meters} \tag{2.16}$$

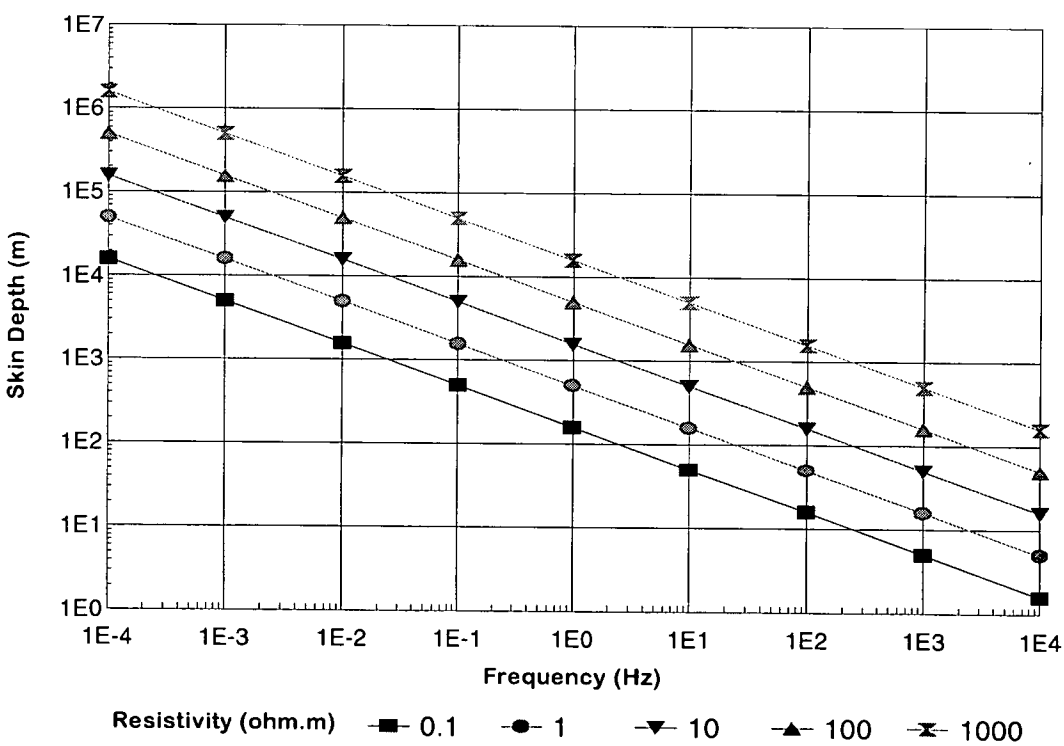

Figure 2.1: Skin Depth for a homogeneous media

Figure 2.1 shows *skin depths* for media with different resistivities and at different frequencies. If the resistivity is low, or the frequency high, or both, the

magnetic field will not penetrate deeply into the ground leading to small skin depths.

2.1.3 Magnetotelluric Fields

In order to adapt the electromagnetic theory to magnetotellurics it is necessary to make some assumptions.

- In general, the frequency of interest is low enough to ensure that the displacement currents, represented by the terms $\omega^2\mu\varepsilon\mathbf{E}$ and $\omega^2\mu\varepsilon\mathbf{H}$ respectively in equations 2.10a and 2.10b are negligible.
- For plane waves traveling at frequencies within the range of MT works, horizontal variations in $\mathbf{E}$ and $\mathbf{H}$ are small compared with vertical variations.
- Only periodic frequency field variations shall be considered in order to simplify the solution of the diffusion equation.

Considering the xy plane as horizontal and z positive downwards, these conditions can be expressed as

$$\frac{\partial D}{\partial t} = 0 \qquad \frac{\partial}{\partial x} = \frac{\partial}{\partial y} = 0 \qquad E \propto e^{-jwt} \qquad H \propto e^{-jwt} \qquad \frac{\partial}{\partial t} = -j\omega$$

Consider an electromagnetic wave polarized in the xy plane and traveling in the z direction. If the magnetic vector is H_0 at an angle θ to the x axis, the magnetic components of the wave in the polarization plane will be: $H_{x0} = H_0 \cos\theta$ and $H_{y0} = H_0 \sin\theta$ and the magnitude of H_0 (equation 2.14) can be written as

$$\begin{aligned} H_x &= (H_0 \cos\theta)\, e^{kz} \cos(\omega t - kz) \\ H_y &= (H_0 \sin\theta)\, e^{kz} \cos(\omega t - kz) \end{aligned} \tag{2.17}$$

Using equations 2.6 and 2.8 it is also possible to find the current for the same plane polarized wave in equation 2.14. The term $\partial\mathbf{E}/\partial t$ can be neglected because

$\omega\varepsilon \ll \sigma$. Then

$$\nabla \times \mathbf{H} = \sigma \mathbf{E} = \mathbf{J} \tag{2.18}$$

Therefore

$$J_y = J_z = 0 \qquad \text{and} \qquad J_x = -\frac{\partial H_y}{\partial z} \tag{2.19}$$

The x and y components of the electric vector can also be determined from equations 2.18 and 2.19

$$\begin{aligned} E_x &= \sqrt{2}\,\frac{k}{\sigma}\,(H_0 \sin\theta)\, e^{-kz} \cos\left(\omega t - kz + \frac{\pi}{4}\right) \\ E_y &= \sqrt{2}\,\frac{k}{\sigma}\,(H_0 \cos\theta)\, e^{-kz} \cos\left(\omega t - kz + \frac{\pi}{4}\right) \end{aligned} \tag{2.20}$$

The squares of the ratios of the orthogonal components of H (2.17) and E (2.20) can be expressed as

$$\left|\frac{E_y}{H_x}\right|^2 = \left|\frac{E_x}{H_y}\right|^2 = 2\left(\frac{k}{\sigma}\right)^2 = \omega\mu\rho \tag{2.21}$$

and

$$\rho = \frac{1}{\omega\mu}\left|\frac{E_y}{H_x}\right|^2 = \frac{1}{\omega\mu}\left|\frac{E_x}{H_y}\right|^2 \tag{2.22}$$

Because the x and y axis can be interchanged, it is possible to state the above expression in the more general form. Setting the magnetic permeability $\mu \approx \mu_0 = 4\pi \times 10^{-7}$ and changing the units of the electric and magnetic fields respectively to milivolts per kilometers and gammas (nT), equation 2.22 can be written as

$$\rho \approx 0.2\,T\left|\frac{\mathcal{E}}{\mathcal{H}}\right|^2 \quad \text{or} \quad \rho = \frac{1}{5f}\left|\frac{\mathcal{E}}{\mathcal{H}}\right|^2 \tag{2.23}$$

where $\mathcal{E}/\mathcal{H}$ is equal either to E_x/H_y or E_y/H_x and $T = 1/f$

The amplitudes of orthogonal components of the electric and magnetic fields measured at the earth's surface, for various frequencies, can determine the variation of resistivity with depth. This is the *apparent resistivity.*

2.1.4 The Impedance Tensor

The resistivity can also be estimated from the impedance Z, which is defined as the ratio of horizontal electric to horizontal magnetic fields.

$$Z = \frac{\mathcal{E}}{\mathcal{H}} = \frac{\mu\mathcal{E}}{\mathcal{B}} \qquad \text{for} \quad \mathcal{E} \perp \mathcal{H} \tag{2.24}$$

The frequency dependent impedance tensor $\mathbf{Z}$ is also called the *response function* of the earth and contains information related to the subsurface in terms of conductivity. The expression for the uniform half-space resistivity ρ_0 can be formulated for the scalar impedance Z as

$$\rho_0 = \frac{1}{\omega\mu_0}|Z|^2$$

However, the impedance Z can be expressed as a vector in the $xy - plane$ to represent general spatial structures of the conductivity.

$$\mathbf{Z} = \frac{\mathbf{E}}{\mathbf{H}} = \frac{\mu\mathbf{E}}{\mathbf{B}} \qquad \text{where} \qquad \mathbf{Z} = \begin{pmatrix} Z_{xx} & Z_{xy} \\ Z_{yx} & Z_{yy} \end{pmatrix} \tag{2.25}$$

The above expression can be written as

$$\begin{aligned} E_x &= Z_{xx}H_x + Z_{xy}H_y \\ E_y &= Z_{yx}H_x + Z_{yy}H_y \end{aligned} \tag{2.26}$$

For an uniform layered earth model, where the conductivity varies with the depth, the resistivity ρ_0 can be determine from the scalar impedance Z. For more general conductivity distribution a *vector apparent resistivity* ρ_a is related to the *impedance tensor* $\mathbf{Z}$ by the expressions

$$\rho_a = \frac{1}{\omega\mu}|\mathbf{Z}(\omega)|^2 \tag{2.27}$$

$$\phi(w) = \arctan\left[\frac{\mathcal{I}m\,\mathbf{Z}(\omega)}{\mathcal{R}e\,\mathbf{Z}(\omega)}\right] \tag{2.28}$$

There are two combinations for the orthogonal components of **E** and **H** leading to $\rho_{a_{xy}}(\omega)$, $\phi_{xy}(\omega)$, $\rho_{a_{yx}}(\omega)$ and $\phi_{yx}(\omega)$.

In discussing electrical structure it is common to refer them as *one-dimensional* (1-D), *two-dimensional* (2-D), or *three-dimensional* (3-D) structure. If conductivity depends only on depth the structure is one-dimensional [$\sigma = \sigma(z)$]. In two-dimensional structures conductivity varies along one horizontal coordinate and with depth [$\sigma = \sigma(x, z)$]. The perpendicular direction is called *strike*. When conductivity varies with both horizontal coordinates and with depth [$\sigma = \sigma(x, y, z)$] the structure is said to be three-dimensional and has no strike.

Over a homogeneous half-space (1-D model) the elements of the impedance tensor in equation 2.26 are

$$Z_{xx} = Z_{yy} = 0 \qquad \text{and} \qquad Z_{xy} = -Z_{yx} \tag{2.29}$$

The apparent resistivity and phase are connected by the relation (Weidelt 1972)

$$\phi(\omega) \approx \frac{\pi}{4}\left(1 - \frac{d\log\rho_a(w)}{d\log\left(\frac{2\pi}{\omega}\right)}\right) \tag{2.30}$$

Also for 1-D structure the impedance tensor does not depend on the directions used as long as E is measured perpendicular to H.

Two-dimensional structures are usually represented by a coordinate system rotated θ° clockwise from North in the $xy - plane$ based on properties of theoretical impedance tensors. In the rotated coordinate, the orthogonal axis x' and y' are respectively perpendicular and parallel to the electrical strike. One way of determining the rotation angle θ was proposed by Swift (1967) such that $|Z_{xx}^2 + Z_{yy}^2| \to 0$.

$$\theta = \frac{1}{4}\arctan\frac{2\,\mathcal{R}e\left[(Z_{xx} - Z_{yy})(Z_{xy} - Z_{yx})\right]}{|Z_{xx} - Z_{yy}|^2 - |Z_{xy} - Z_{yx}|^2} \pm \frac{\pi}{2} \tag{2.31}$$

The impedance tensor can be written in terms of the rotated coordinate system as

$$\mathbf{Z} = \begin{pmatrix} Z'_{xx} & Z'_{xy} \\ Z'_{yx} & Z'_{yy} \end{pmatrix} = \begin{pmatrix} 0 & Z_\perp \\ Z_\parallel & 0 \end{pmatrix}$$

Swift also defined the *skew* of the impedance tensor as a measure of complexity of the conductivity structure.

$$S = \frac{|Z'_{xx} + Z'_{yy}|}{|Z'_{xy} - Z'_{yx}|} \tag{2.32}$$

Small skew (<0.2) indicate 1-D or 2-D structures. Also symmetrical 3-D structures have skew within this range. The skew parameter as defined by Swift can lead to incorrect interpretations if the electric fields are distorted by local anomalies. (Bahr 1988) (Groom and Bailey 1989).

The rotation properties of impedance tensor applied to a layered earth upon any rotation leads to:

$$Z'_{xx} = Z'_{yy} = 0 \quad \text{and} \quad Z'_{xy} = -Z_{xy}, \quad Z'_{yx} = -Z_{yx}$$

This is a confirmation of the known result that for the isotropic earth the impedance is independent of the measurement coordinate system.

For three-dimensional conductivity structures the concept of impedance tensor components perpendicular and parallel to electrical strike is no longer valid. Such structures can be approached by integral equation solutions e.g. Hobbs (1971).

Horizontal components of electric and magnetic field are essential information for determining impedance tensor and apparent resistivity. However, magnetotelluric method also involves the measurement of the vertical magnetic field H_z which is generated by the interaction of the source field with those parts of geoelectrical subsurface structure which are not layered and laterally homogeneous. *Geomagnetic Deep Sounding* (GDS) refers to studies relating all magnetic field components. These fields are related by the equation

$$H_z(\omega) = Z_H(\omega)H_x(\omega) + Z_D(\omega)H_y(\omega) \tag{2.33}$$

where Z_H and Z_D are complex transfer functions in the frequency domain. Real and Imaginary parts of Z_H and Z_D can be combined to form two-dimensional

vectors called *Induction Arrows*[1] determined by the relations

$$\text{Real arrow :} \qquad \text{Ampl.} = \sqrt{A_R^2 + B_R^2} \quad \text{Angle} = \arctan \frac{-B_R}{-A_R} \tag{2.34}$$

$$\text{Imaginary arrow :} \quad \text{Ampl.} = \sqrt{A_I^2 + B_I^2} \quad \text{Angle} = \arctan \frac{B_I}{A_I} \tag{2.35}$$

where $A_R = \mathcal{R}e[Z_H]$, $A_I = \mathcal{I}m[Z_H]$, $B_R = \mathcal{R}e[Z_D]$ and $B_I = \mathcal{I}m[Z_D]$

The above equations were written according to the Parkinson convention (Parkinson 1959). The Wiese convention defines the same induction arrows except the angle of the real arrow which is written as $\arctan(B_R/A_R)$ (Wiese 1962).

The graphic representation of the induction arrows gives important information related to conductivity contrast of the geological structure. Induction arrows tend to point towards regions of higher conductivity according to Parkinson convention (away according to Wiese convention).

2.2 Instrumentation

The basic functions required from Magnetotelluric instruments are to measure the electric and magnetic fields, in different frequency ranges and to store the information for further signal processing and analysis. The limitations imposed by early instrumentation has been reduced thanks to new technologies. Modern equipment can process the data in real-time and present results in graphic format (printed or displayed on computer screen). Raw time-series and optionally magnetotelluric results are usually stored for further analysis by different techniques. Improved logistics such as smaller size and lighter weight yield a more complex sensor configuration and multi-site simultaneous data acquisition e.g. remote reference. The ability to perform real-time data acquisition, signal processing and MT analysis depends on the complexity of the network, the frequency range of interest and the computational power available in the equipment.

[1] also called *tipper* (Vozoff 1972)

2.2.1 Magnetic Field measurement

There is often confusion as to whether the quantity involved in MT studies is the *magnetic induction* **B** or the *magnetic field* **H**. Although we measure **B**, we are interested in the Earth's field **H**. However, because **B** and **H** are linearly related by the equation $\mathbf{B}=\mu\mu_0\,\mathbf{H}$ and usually $\mu \approx 1$, we can treat measurements of **B** as if they were measurements of **H**.

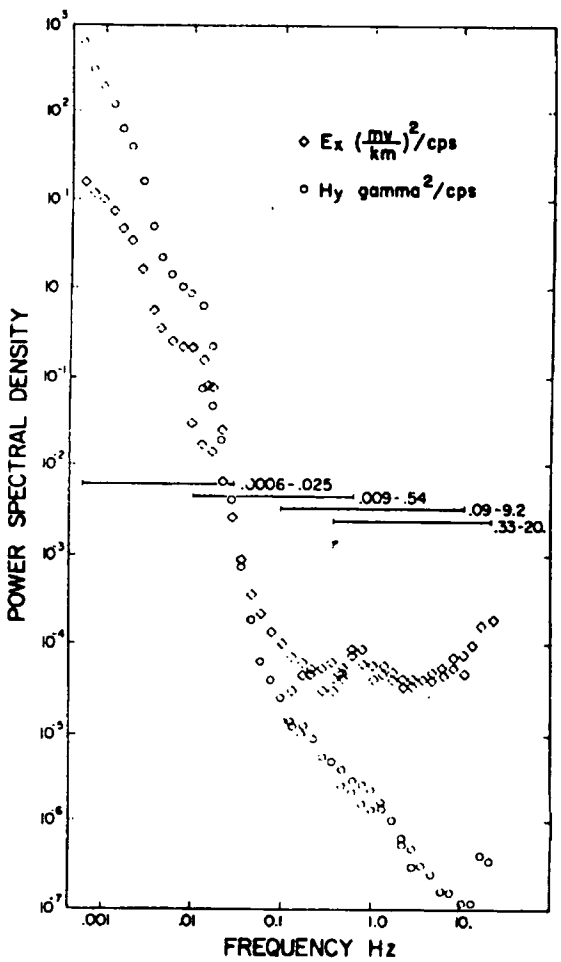

Figure 2.2: Power Spectra 0.001–10Hz

To determine the magnitude and direction of the magnetic field one has to measure the amplitude of the components of the field in a coordinate system, usually the axes are aligned to the North magnetic (x), East (y) and vertical (z). Thus, each component of the magnetic field is measured by one sensor aligned accordingly.

The signal levels produced by the natural magnetic field spectrum have been studied by some researches. Vozoff (1972) presents a graph for the power spectral densities recorded in the four overlaping frequency bands (0.0006–0.025, 0.009–0.54, 0.09–9.2 and .33–20Hz) at different times (Fig 2.2). The magnetic field decreases sharply from approximately $10\mathrm{nT}/\sqrt{Hz}$ at 0.001Hz to approximately $10^{-2}\mathrm{nT}/\sqrt{Hz}$ at 1Hz.

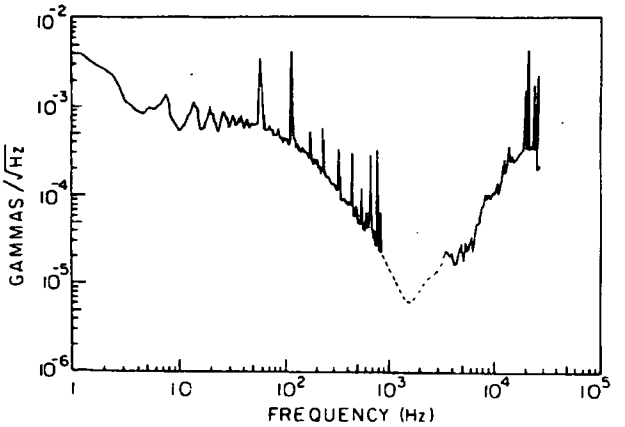

Figure 2.3: Magnetic Field Density 1–30kHz

A similar study was carried out by Labson et al. (1985) for frequency range 1 – 30kHz (Fig.2.3) and reveals not only the decay of the magnetic field beyound 1Hz but also common sources of noise that share the same frequency range. In his study, Labson points out the dominant features of a typical spectrum recorded in the early afternoon in the summer season at San Antonio Valley, California; Schumann resonances at 8, 14 and 20Hz; the 60Hz powerline and motor generator noise (used in his experiment) with its harmonics; and the VLF radio stations from 17 to 25kHz. The magnetic field spectrum shows a minimum between 1 and 2kHz. In the frequency range between 900Hz and 3kHz the spectral amplitudes are approximate because it was not possible to determine these field levels to the same degree of accuracy as the rest of the spectrum. Apart from small differences, Labson's study gives us a picture of cultural noises that are getting more and more frequent and have to be faced almost everywhere.

The purpose of these comments is to enphasize that the intrinsic noise level of the magnetometers shall be small enough to provide a good signal-to-noise relationship. This relationship can be jeopardized at frequencies where the magnetic signal is weak and the noise is strong. Fortunatelly, in most cases the noise has a fixed, known and reasonably stable fundamental frequency which can be removed by a suitable filtering scheme.

Among several types of magnetic sensors, induction coil magnetometers are the most used for the frequency range of MT works. These sensors are based on

different designs but are similar in principle: a core around which several tens of thousands of turns of copper wire are wound. Some of them are passive but most of them incorporate built-in amplification and filtering. Some magnetometers include three orthogonal coils in one package but usually present lower sensitivity related to single coil devices. Magnetometers have a fixed frequency bandwidth of operation and different sensors are often used to cover the frequency range of interest. Some magnetometers can operate alternatively in more than one complementary or overlapping bandwidth, being switched by an external signal. Even though induction coil magnetometers tend to be bulky and heavy they are relatively low-noise, trouble-free and service-free.

During the last decade a superconducting magnetometer (SQUID) has been used in some applications of MT data acquisition e.g. Clarke et al. (1983). SQUID magnetometers are generally quieter and more sensitive than coils, especially in the low-frequency range and are easy to install and carry because all three components are packaged in a single device. However, SQUID magnetometers need a good supply of helium to provide the near absolute-zero temperature at which superconductivity is present and this is a severe limitation in applications in remote areas.

2.2.2 Electric Field measurement

The electric field is measured by sensing a potential difference between a pair of electrodes. Induced electric signal are a function of the electric conductivity structure beneath the earth's surface. Electric signals are more prone to noise than magnetic signals. Electric sensors (electrodes) are preferably aligned to the same coordinate system as the horizontal magnetic sensors e.g. North, East. The distance between sensors is typically between 5 to 300m, where site topography and frequency range are determining factors. Longer electric field dipole separations yield higher signals but averaged over more near-surface effects. However, long lines are more prone to acquire ambient noise in the cables: at lower fre-

quencies due to cable movement and friction and at higher frequencies due to radio-frequency noise where the electric lines act as an aerial. Chapter 9 presents experiments using several dipole separation lengths to study the signal-to-noise relationship and the feasibility of using shorter dipole lengths in MT measurements.

Except for higher frequencies, electric signal sensors are usually chemical electrodes. These electrodes are built based on some properties of metal-salt, metal-ion combination such as copper-copper sulphate, lead-lead chloride, silver-silver chloride or cadmium-cadmium chloride and are classified as non-polarized electrodes, because they do not generate a contact potential with the ground.

Until 1996 chemical electrodes used to be the most poorly understood device in MT and AMT applications. In 1994 the *12^{th} Workshop on Electromagnetic Induction in the Earth, Brest-France* proposed a very comprehensive experiment to study several types of electrodes for long term monitoring the earth's electric field. The experiment was carried out at the *Centre de Recherches Géophysiques de Garchy-France (CNRS-INSU)* from April 1995 to April 1996, coordinated by Dr. Gérard Clerc. The first results of the experiment were presented in the *13^{th} Workshop, Onuma-Japan* in June 1996 (see Clerc et al. (1996a)) and further papers will be published by the end of 1996. Non-polarized electrodes are now better understood than before and parameters such as long and short term stability, variations due to temperature, rain and soil chemical composition among others, are better understood. The method of installation also plays an important role of keeping the soil surrounding the electrodes less prone to environmental changes such as temperature and humidity (see Chapter 3).

Metallic electrodes such as copper rod and lead plates can also be used for MT studies in the frequency range beyond approximately 10Hz because their noise at higher frequencies is the same order of magnitude of chemical electrodes.

2.2.3 Data acquisition and Storage

The level of signals to be measured by MT and AMT instruments can be very weak requiring high-quality, sensitive and low noise instrumentation. In general, the equipment must measure simultaneously at least three magnetic and two electric field signals (five channels), perform proper analogue signal conditioning, convert the signals to the digital domain, acquire data and store the digital data for further processing (see Cantwell and Madden (1960), Allsopp et al. (1973), Vozoff (1972) and Labson et al. (1985)). New instruments have become available for MT studies, developed by industry or developed universities and research centres. These follow the same sequence (from field measurents to data storage) but differ in implementation, components used, data storage device, computational power, input-output device for user interfacing, power consumption, frequency range of operation, etc. The specifications of these equipment reveal differences and similarities and are an important piece of information.

In order to process data in real time and to optimize the dynamic range some of the MT instruments split the frequency range of interest in more than one sub-bands. However, this technique implies the repetition of data acquisition for each sub-band, increasing the time required for covering the whole frequency range of interest at each location. Computational power has also increased and more and more results are expected in the field leading to a quick data quality checking. Data storage devices used by MT equipment have changed from bulky magnetic tape drives to floppy disks, cassette tapes, memory cards and hard-disk drives. The choice of the storage device depends on the amount of data to be stored, the writing speed and capacity of the storage media and the need to transfer data regularly.

2.2.4 Conclusions

Recent developments in electronics have helped designers to build better instrumentation. New equipment has been developed with lower power consumption,

lower intrinsic noise, wider operation frequency bandwidths, more computational power and increased capabilities of real-time operation. Unfortunately, scientific publications associated to the topic are rarely seen and commercial designers rarely discuss design processes.

An important factor to be considered is the cost involving MT surveys which require field and logistical support. People and equipment have to be transferred to remote areas, set up a station, test the equipment, simulate an acquisition, check the data quality acquire sufficient amount of good quality data and sometimes repeat the whole set up in another location. A small size, light weight and low power consumption equipment is easier to handle and consequently cheaper to transport. Logistics are simpler and can be carried out faster, increasing the productivity in the field. Another important item in increasing the productivity is the ability to record a continuous and wide frequency band of splitting the wide frequency band in sub-bands leading to a single instead of multiple data acquisitions (one per sub-band) per location. The use of multi-channel equipment allows additional information to be recorded. For instance, electrodes used to be the main source of uncertainty and may put the field work in jeopardy if just one fails during the operation. An alternative to improving the reliability of the field work would be to set-up more than one electric line in each direction and measure additional electric fields from different sets of electrodes. It is unlikely that more than one electrode in the same direction and the associated electronics fail at the same time.

However, the most important factor to increase productivity and reliability is the equipment's ability to deliver real-time MT analysis to allow a quick evaluation of the data quality before setting up the whole site and recording, to avoid waisting time in a difficult area. Reasonable conditions may be achieved if the sensors are moved just a few meters but sometimes the area is too noisy and should be abandoned. A quick decision upon the location is vital to improve the productivity and reduce costs.

CHAPTER 3

An Electrode Design for Magnetotelluric Soundings

3.1 Introduction

Electrodes are an integral part of geoelectrical surveys for measuring the electric field. Although they look simple, they are probably the least studied of the geophysical sensors and for that reason they are the main source of uncertainty. Electrodes are also electrochemical devices but only a few electrochemists are interested in then. Some topics related to electrodes can be found in electrochemistry books such as Greef (1990) and Hibbert (1993). These are useful references for the theory in self potential, dynamic activities, concentration and thermodynamics of cells but not focused on electrodes design. Traditional references related to electrodes for geophysical applications, construction and tests are Munaut (1973), Filloux (1973), Petiau (1976) and Petiau and Dupis (1980).

In general, electrodes are expected to operate under extreme weather conditions and environments, in temperatures from below 0 ° to 40 °, exposed to the sun, wind, rain and snow, buried in highly variable mineralogical and chemical soil compositions, including high organic or inorganic contaminations. Different ap-

plications require electrodes deployed from a few hours to several months or even years and they are expected to respond to time-varying signals from microseconds to months with the same performance and stability. Electrode construction is a mixture of science, craft and cookbook that not always lead to same results. There are several unanswered questions relating to different types of electrodes, the best design for specific applications, installation methods and stability (Vozoff 1995).

3.2 A Comprehensive Experiment on Electrodes

To improve the understanding of these geoelectrical sensors, a comprehensive experiment on electrodes was carried out at the Centre de Recherches Géophysiques de Garchy-France, started in August 95 and lasting for one year. The experiment was coordinated by Dr.Gérard Clerc and I am proud of being one of the participants. The aim of the project was to compare different types of electrodes in terms of long term stability, to identify best designs, to propose installation .methods and to detect problems and limitations. More than one hundred non-polarized[1] devices were gathered for the first part of the experiment, which included a workshop, tests in the laboratory and setting up for long term observation.

The electrodes were built in more than twenty assorted designs, metal-metal ion or metal-salt couples like lead-lead chloride ($Pb/PbCl_2$), silver-silver chloride ($Ag/AgCl$), copper-copper sulphate ($Cu/CuSO_4$) , cadmium-cadmium chloride ($Cd/CdCl_2$) in either liquid electrolyte or solid support with the solution fixed in agar-agar gel or in clay. The electrodes were classified as electrodes of the same

[1]Metallic electrodes in contact with ground generate a contact potential that polarizes the measurements. Chemical or Non-polarized electrodes consist of metallic conductors in contact with a saturated solution of one of their salts and produce a constant contact potential between metal-salt layers. The difference between two contact potentials from identical non-polarized electrodes in the absence of an external field is close to zero. Chemical electrodes are more common for geophysical applications.

type, based on the electrochemical combination (i.e $Cu/CuSO_4$, $Ag/AgCl$,..) and electrodes of the same *family* with same design, chemical composition and type of support (i.e $Pb/PbCl_2$ clay + KCl, $Pb/PbCl_2$ clay + $NaCl$,..). Electrodes from the same *family* are supposed to be identical and fabricated at the same time. It was proposed that the electrodes were tested in laboratory, in the field, deployed in different ways, surrounding by different soil composition and left measuring the electric field for one year, under local changes in temperature and humidity.

After one year the experiment answered some questions but also raised new ones that need a more comprehensive analysis to be sorted out. The following text will comment briefly on the test procedures held at Garchy, some results and personal conclusions. Additional information on results will be referred in subsection 3.2.4.

3.2.1 Laboratory and Field Tests

Before being deployed in the field, all electrodes were submitted to laboratory and soil tests with identical setup and procedures to ensure consistency in the results. All the measurements were taken involving pairs of electrodes from the same *family* and size. These preliminary tests are important because they show whether or not the electrodes have the necessary requirements for field use and reveal significant information for the instrumentation design.

3.2.1.1 Self-potential

The objective is to measure the DC potential between electrodes from the same family to determine how well matched they are. Matched electrodes are expected to produce very low self potential. As far as geophysical measurements are concerned, electrode self-potential is a kind of noise and should be as small as possible, ideally 0V.

All electrodes were placed on a foam soaked with solution of KCl, NaCl or $CuSO_4$ for individual DC potential measurements between one, chosen to be the *family reference* and the remainders (Fig.3.1). Potential difference between identical electrodes under the same test conditions should be as low as a few milivolts and higher values may indicate a contaminated metal surface or electrode dehydration. As an example, the maximum self potential measured between ten $Pb/PbCl_2$ family electrodes and the reference was 1.52mV. The same measurement for a particular pair of electrodes of the same type revealed -98.94mV and it was confirmed afterwards they were not working properly.

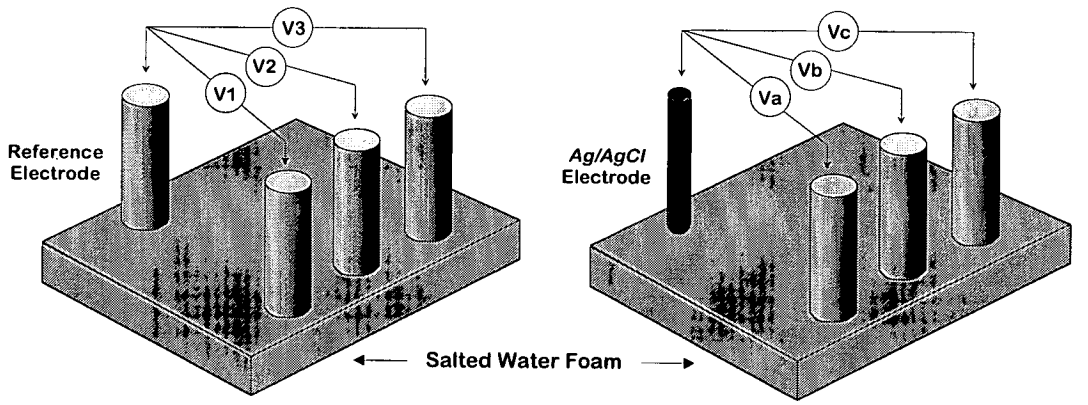

Figure 3.1: Electrode Self Potential Test Setup

It is important to emphasize that in general, any kind of measurement is influenced by the test setup and instrument parameters. As an example, a voltage measured by a voltmeter can be determined by starting at the positive lead input (+) and by going round the whole circuit adding up potential differences as they are encountered until the negative lead input (-) is reached. At this point the sum will be the measured potential. In electrochemical measurements there is a change in potential whenever a boundary between phases is crossed, these can be metal and solution, solution and solution or metal and metal. Among all these potentials, metal-electrolyte contact produces the most significant potential and can be assumed that it is approximately equal to the measured potential. The potential generated by boundary electrolyte-salted foam is negligible and should not

be considered, as with the voltage drop across the voltmeter test leads. In practice, electrodes are used in a similar setup to measure voltage differences between points and potentials intrinsic to the sensor should not interfere with the measurements. For instance, in magnetotelluric soundings two identical electrodes are used to measure the time-varying electric field but the electrode self-potentials are added to the natural signals. Electrode self potential is an additional source of noise and should be as small as possible. The composite DC components, natural plus instrumental, have to be blocked by a filter or compensated (backed-off) by electronic circuitry before the first amplification to avoid saturation and jeopardizing the measurements. Although DC components from natural sources can not be prevented, electrode DC noise might be minimized by selecting pairs with small self-potential differences.

The measurements described above always involve an electrode pair from the same family and the voltage obtained reflects the sum of two metal-salt contacts. Assuming the electrodes are identical, the potential due to a single electrode is half of the measured potential since they contribute equally to the total voltage. In electrochemistry, the usual method to determine the potential of a single electrode or half-cell is to compare its potential to the standard hydrogen electrode (or SHE) whose potential is zero ($E^{\ominus}$=0.0V). The second part of the self potential test is an attempt to determine the absolute potential of single electrodes by measuring the voltage between them and an Ingold Argenthal reference electrode whose potential related to the SHE is +207mV. By working out the self potential of single electrodes it is possible to validate the assumption that they give the same contribution to the total potential when measured in pairs. Also the self-potential created by a particular metal-salt combination can be compared to standards (reduction) potentials generated by electrochemical cells (Hibbert 1993). Tabulated values are absolute potentials, since they are measured against the hydrogen reference electrode (SHE).

3.2.1.2 Internal Resistance

The setup for measuring the internal resistance is almost identical to the setup for the self potential test (Fig.3.1). An alternate-current ohm-meter measures the impedance at 4kHz between one electrode chosen to be the *family reference* and each one of the remainders from the same family. The *family reference* electrode for both self potential and impedance measurements should be the same to ensure consistency in the tests. Also, the impedance between each electrode and the Ingold Argenthal reference electrode was measured to determine the internal impedance of a single electrode or half-cell as explained in subsection 3.2.1.1. However, Ingold Argenthal reference electrode is not essential for determining the electrode internal impedance. For instance, the relative impedances measured between three electrodes lead us to three independent equations and three unknowns (impedances) that can be easily calculated.

The test showed that internal impedances within the range 20Ω to 6200Ω are common. There is not an obvious correlation between electrode *type* and internal impedance and I believe the impedance is more related to the design of the surface in contact to the ground (or to the foam) than to the electrochemical combination. For instance, two electrode pairs from the same type (Ag/AgCl), with contact area to the ground of $18cm^2$ and $8cm^2$ had respectively 20Ω and 400Ω internal impedances. The higher the surface area is, the lower the internal impedance seems to be. However, electrodes with the same contact area may have different internal impedances and the reason may be related to different porosities of material. Also, the internal impedance measured between electrodes from the same family are not as matched as the self-potential and impedances variation within 10% range may be observed. The internal impedance of the electrodes also contributes to the instrument noise and will be explained in subsection 3.2.2.

3.2.1.3 Temperature Coefficient

The first step to determine the temperature coefficient of the electrodes is to measure their self potentials at different temperatures related to a reference electrode kept at room temperature. After the first measurement at room temperature the electrodes (except the reference electrode) are placed in an oven, the temperature raised and maintained at 40 ° C for twelve hours for the second self-potential measurement. The process is reversed, the environment in the oven is brought back to the room temperature and after twelve hours stabilization the third set of self potential measurements is carried out. The temperature coefficient can be worked out afterwards by a computer package. In order to have more accurate results the initial idea was to repeat the whole cycle three times but it was observed that some electrodes did not stabilize within twelve hours and more precise measurements with longer stabilization times were required. Temperature coefficient results can predict electrode variations when submitted to similar temperature changes in the field.

3.2.1.4 High Frequency Noise

The setup illustrated in figure 3.2 was used to analyse the noise density spectra of the electrodes. Two identical electrodes on a salted foam surface were connected to a low-noise differential amplifier and the electrodes signal amplified by a factor of 1000, 2000, 5000 or 10000 which is set accordingly to the internal self potential to achieve the maximum amplitude without signal saturation. The amplifier output is connected to a data acquisition system that performs the noise analysis in the frequency range between 5 Hz and 0.01 Hz. The resultant noise spectrum is displayed on a computer screen, saved on a file and printed out. Also, values of the electrodes spectral density at 5.0, 1.0, 0.1 and 0.01 Hz were tabulated. Table 3.1 shows these results for three different types of electrode.

It is important to consider that the total noise measured by the data acquisi-

	Total Noise ($mV_{rms}/\sqrt{Hz}$)			
	5.0Hz	*1.0Hz*	*0.1Hz*	*0.01Hz*
Amplifier (G=10000)	1.0	1.1	1.4	2.8
E_1 (Ag/AgCl)	1.1	1.2	1.7	17.0
E_2 ($Cu/CuSO_4$)	1.3	1.5	2.3	40.0
E_3 ($Pb/PbCl_2$)	1.1	1.2	1.7	9.2

Table 3.1: Spectral Noise Density Test Results

tion system (E_{n_T}) is a combination of noise generated by the electrode pair under test (E_{n_E}) multiplied by the amplification factor (G) and noise generated internally by the amplifier (E_{n_A}). The noise due to the amplifier had been evaluated at the beginning of the experiment by shorting its inputs to ground, performing the noise measurements in the same setup and tabulating the noise spectral density for the same frequencies. Amplifier noise at the device output is also dependent on the gain factor and these results for $G = 10000$ are also represented in table 3.1. To determine the noise of the electrodes, the contribution due to the amplifier must be removed from the total noise and the gain factor taken into account. Therefore, the electrode noise can be estimated by the expression

$$E_{n_E} = \frac{\sqrt{{E_{n_T}}^2 - {E_{n_A}}^2}}{G} \tag{3.1}$$

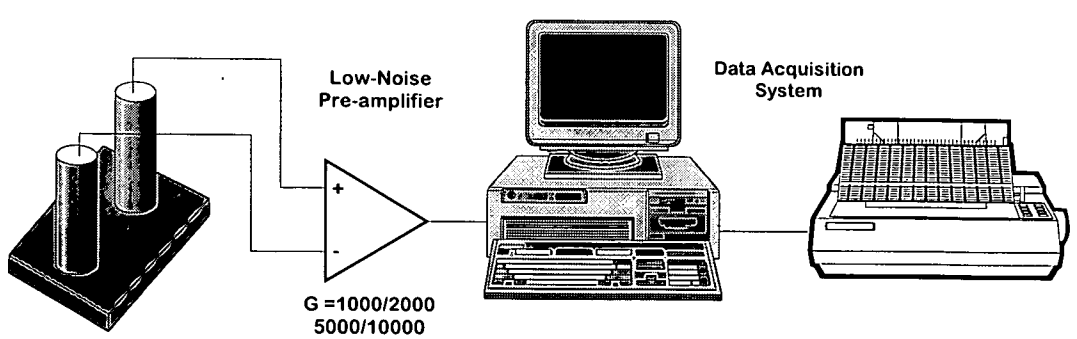

Figure 3.2: Electrode High Frequency Noise Test Setup

Table 3.2 shows the calculated electrodes spectral noise density for the same set mentioned in table 3.1.

	Electrode Noise ($mV_{rms}/\sqrt{Hz}$)			
	5.0Hz	*1.0Hz*	*0.1Hz*	*0.01Hz*
E_1 (Ag/AgCl)	0.05	0.05	0.10	1.67
E_2 ($Cu/CuSO_4$)	0.08	0.10	0.18	3.99
E_3 ($Pb/PbCl_2$)	0.05	0.05	0.10	0.87

Table 3.2: Electrode Spectral Noise Density

Complete noise test results from the experiment have not been released yet. Previous studies on electrodes noise spectra in the frequency range 100–0.001 Hz (Petiau and Dupis 1980) revealed that noise is maximum for copper-copper sulphate electrodes decreasing respectively for silver-silver chloride and lead-lead chloride electrodes. Even though a few electrodes such as those from the example above can not lead to general conclusions, they followed the same noise pattern. Also, experiments on copper-copper sulphate electrodes (Erkul and Muller 1995) revealed that those with solid support (plaster,clay or agar-agar gel) are noisier than electrodes with liquid electrolyte.

3.2.1.5 Soil Chemical Composition

The purpose of this test is to evaluate changes in electrode self potential buried in different soil compositions (figure 3.3). The first measurement is carried out with both electrodes in a hole filled with neutral salted clay. For the subsequent measurements one is moved into holes filled respectively with salted bentonite (basic medium) and clay with hydrochloric acid (acid medium). The results revealed that in general, there is no considerable change in the electrode self potential even when they are deployed in soils with a wide pH difference. All electrodes presented the same behaviour, regardless of electrochemical composition or design. However, this sort of test reveals only instantaneous changes in potential and conclusions related to the long term behavior should not be drawn.

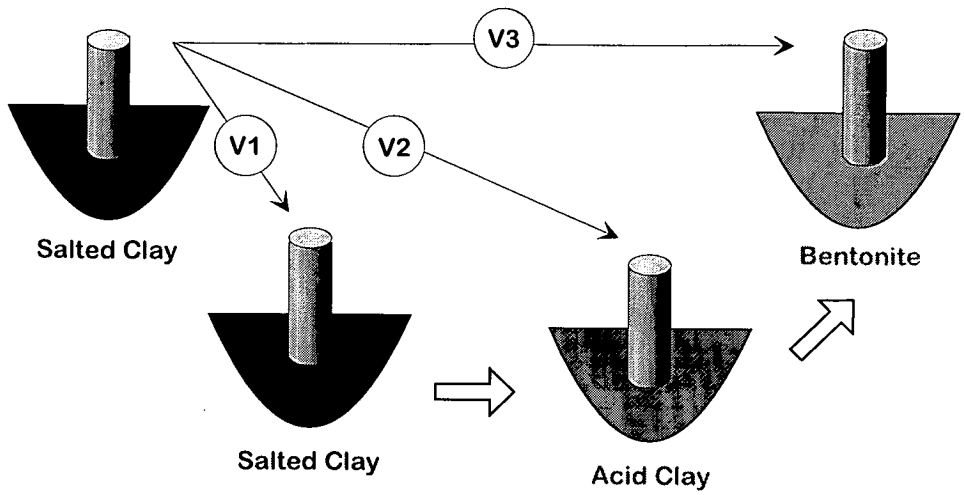

Figure 3.3: Soil Composition Test Setup

3.2.2 Considerations on Noise

The procedure described in 3.2.1.4 to determine the electrode noise actually measured a combination of electrode and amplifier noise. Electrode noise is mainly due to chemical reactions between layers and impurities. However, when connected to an amplifier, electrodes act as a source resistances to that amplifier and an additional noise is generated due to the interaction between electrode and active devices in the instrument. The circuit configuration for the amplifier may vary but usually the active device is an operational amplifier and for that reason I will concentrate on its noise characteristics. The same concepts apply to discrete or integrated active devices.

Figure 3.4 shows the block diagram of an electrode pair connected to an operational amplifier. Resistors and capacitors are also connected to the amplifier network in a real circuit, but they were omitted in the diagram to simplify calculations and to focus the analysis on the presence of the electrodes. The non-ideal operational amplifier is represented by its input-referred[2] noise model which consists in three noise generators, E_n, I_{n_1} and I_{n_2} connected to an *ideal*

[2]In the calculation of circuit noise it is customary to refer all noise sources to the amplifier input

noiseless amplifier (Analog Devices 1985). These noise generators combine all noises intrinsic to the device and include the white noise, which is characterized by a uniform spectral density and the $1/f$ noise (also called flicker or pink noise) because its power density varies with the frequency as $1/f$. The power of *white noise* is proportional to the bandwidth, regardless of the band's location within the frequency spectrum. For instance, the noise power in the 10Hz band between 20Hz and 30Hz is the same as that in the 10Hz band between 990Hz and 1000Hz. The power of $1/f$ noise is proportional to the logarithmic ratio of the frequency band extremes, regardless of the band's location within the frequency spectrum. Noise parameters for a particular device can be extracted from data sheet curves and specifications. The more important are voltage noise corner frequency (f_{ce}), current noise corner frequency (f_{ci}), voltage input noise (e_{nw}) and current input noise (i_{nw}). Voltage and current noise corner frequency parameters limit the regions between white noise towards higher frequencies and pink noise towards lower frequencies. Voltage and current input noise densities are specified for the white noise frequency region. Also, it is usual to determine noise characteristics over a bandwidth of interest ($BW = f_H - f_L$). Based on the parameters mentioned above, the *rms* voltage and current noise generators E_n, I_n over a specific bandwidth BW can be calculated by the expressions

$$E_n(f_H, f_L) = e_{nw} \sqrt{f_{ce} \cdot \ln\left(\frac{f_H}{f_L}\right) + (f_H - f_L)} \tag{3.2}$$

$$I_n(f_H, f_L) = i_{nw} \sqrt{f_{ci} \cdot \ln\left(\frac{f_H}{f_L}\right) + (f_H - f_L)} \tag{3.3}$$

The noise current generators I_n produce noise voltage drops across source resistors R_{s_1} and R_{s_2} which are a combination of electrode impedance and resistors of the circuit network. In addition to the noise generated by the active device, these resistors themselves generate thermal noise, also called *Johnson noise* which are present in all passive resistive element and is caused by random thermal motion of electrons. Thermal noise (E_t) can be modeled by a voltage noise source

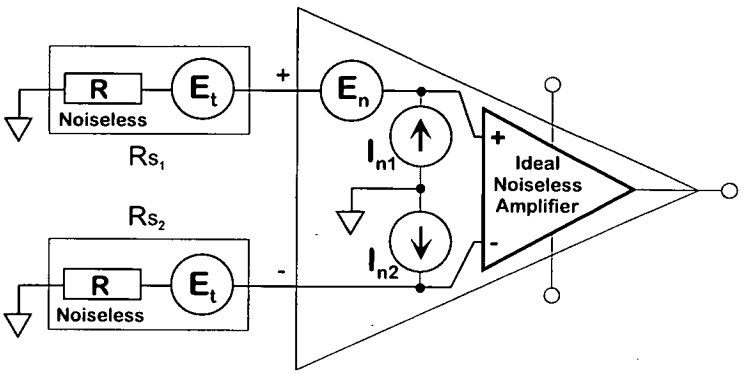

Figure 3.4: Operational Amplifier Internal Noise Model

E_t in series with a noiseless resistor R (see fig.3.4) and the expression of its power density over a specific bandwidth ($BW = f_H - f_L$) is

$$E_t = \sqrt{4kTR \cdot (f_H - f_L)} \tag{3.4}$$

where: k is Boltzmann's constant ($k = 1.38 \times 10^{-23}$ J/ ° K)
T is the absolute temperature in ° K

At room temperature, equation 3.4 simplifies to

$$E_t = 1.28 \times 10^{-10} \sqrt{R \cdot (f_H - f_L)} \tag{3.5}$$

The combined effect of several random noises is determined by root sum squared of the *rms* values of the separate noise sources. For the circuit of the figure 3.4, we can assume that the electrodes are almost identical with the same internal resistance ($R_{s_1} = R_{s_2} = R$) thus generating the same thermal noise ($E_{t1} = E_{t2} = E_t$). Also $I_{n_1} = I_{n_2} = I_n$ for symmetric circuit configurations. After these considerations, the total *rms* input-referred noise (E_{Tot}) over a defined bandwidth (f_H, f_L) can be expressed as

$$E_{Tot}(f_H, f_L) = \sqrt{{E_n}^2 + 2(I_n \cdot R)^2 + 2{E_t}^2} \tag{3.6}$$

It should be noted that the root sum of the squares has the effect of emphasizing the larger quantities; for example, if one quantity is three times greater

than the other the error incurred by ignoring the smaller quantity is only about 5%.

The way of minimizing the total noise E_{Tot} is to reduce the value of each individual source, preferably by improving the source that gives the greatest contribution. By examining equations 3.2, 3.3 and 3.4 it is possible to understand some rules to achieve low noise in circuits with operational amplifiers and electrodes.

- To reduce E_n, the noise characteristics of the operational amplifier should be as low as possible. It includes the four parameters; voltage and current spectral density e_{nw}, i_{nw} and the respective corner frequencies f_{ce}, f_{ci}.
- The source resistance R, related to electrode impedance and resistances associated to the circuit, should be kept as low as practical to reduce the thermal noise E_t and to minimize the effect of the operational amplifier current noise $(I_n \cdot R)$.
- The signal bandwidth $(BW = f_H - f_L)$ should be restricted to the bandwidth of interest.

To compare the contribution of each term of equation 3.6 to the total noise, some numerical values are presented based on noise characteristics of two different operational amplifiers. The frequency bandwidth limits for the exercise are the same as used in the electrode noise test mentioned in subsection 3.2.1.4, f_H=5Hz and f_L=0.01Hz. The source resistances were chosen at random in the range of electrode internal impedances as measured and described in subsection 3.2.1.2, 20Ω and 6200Ω being the highest and the lowest electrode internal impedances. The *rms* voltage noise figures for the first device (Amplifier-A) are in table 3.3 where the three last columns represent: the amplifier voltage noise (E_n), the voltage drop across the source resistances due to the amplifier current noise $(\sqrt{2(I_n R)^2})$ and the thermal noise due to the source resistances $(\sqrt{2E_t^2})$. This form of tabu-

lation allows an easier comparison between the total noise and each individual contribution.

R	E_{Tot}	E_n	$\sqrt{2(I_nR)^2}$	$\sqrt{2E_t^2}$
20	375.6	375.6	0.0	1.8
100	375.6	375.6	0.0	4.0
1000	375.8	375.6	0.3	12.7
6200	377.0	375.6	2.15	31.8

Table 3.3: Calculated Noise Sources in nanovolts (rms) for Amplifier-A. $e_{nw} = 90\text{nV}/\sqrt{Hz}$ and $i_{nw} = 2.2\text{fA}/\sqrt{Hz}$.

In this example, the total noise is dominated by the operational amplifier voltage noise (E_n) and the contribution due to the interaction between electrode and amplifier ($I_n \cdot R$) is negligible even for the highest electrode impedance. The thermal noise component is also much smaller than the operational amplifier voltage noise and can be ignored. This example points out that the noise generated by the interaction between electrodes and amplifier can be disregarded whenever a device with similar noise characteristics is used as the amplifier device.

If we consider that this device is identical to the device used in the amplifier of the electrode noise test mentioned in subsection 3.2.1.4, we will observe that the total noise measured by the data acquisition system was mainly due to the amplifier intrinsic noise and the noise due to chemical reactions and impurities in the electrodes. Therefore, equation 3.1 is a valid approximation to obtain the electrode intrinsic noise.

However, noise is only one parameter among others to select the device for amplifier stages and some of important ones go to opposite directions. For instance, components with very low noise characteristics have higher power consumption. If the amplifier had the active device changed the same experiment will lead us to different conclusions. As illustration let us repeat the exercise by using a different device (Amplifier-B). This device has a greater current noise compared to the

device in the first example and a higher noise component due to the interaction with electrodes is expected. Also, the voltage noise is smaller and no longer as predominant as it was in the first example. Table 3.4 shows the calculated noise values for the same noise contributions and in the same units as in the previous exercise.

R	E_{Tot}	E_n	$\sqrt{2(I_nR)^2}$	$\sqrt{2E_t^2}$
20	91.8	91.8	0.2	1.8
100	91.9	91.8	1.1	4.0
1000	93.3	91.8	11.0	12.7
6200	118.8	91.8	68.4	31.8

Table 3.4: Calculated Noise Sources in nanovolts (rms) for Amplifier-A. $e_{nw} = 20\text{nV}/\sqrt{Hz}$ and $i_{nw} = 70\text{fA}/\sqrt{Hz}$.

Again, the greater contribution to the total noise is due to the amplifier voltage noise. However, the current and thermal noises which are associated to the source resistance (R) increase proportionally. For the highest source resistance (6200Ω) these noises are significant compared to the amplifier voltage noise and cannot be neglected as they were in the first example.

To summarize, from the application point of view, the electrode noise is a combination of the noise generated by chemical reactions and the noise due to the interaction with the amplifier. Little can be done in reducing the former but the latter can be minimized by the right choice of the active device and circuit configuration.

3.2.3 Field Installation

For the second and most important part of the experiment, all electrodes were buried in a field at the same depth and data acquired over one year. Electrodes from the same electric line were placed 50 meters apart and each parallel line

2 meters distance from its neighbors. There are two different approaches for electrode installation. The first consists in digging the electrodes straight into the soil to keep the local environment equilibrium. The second consists in digging the electrodes into a artificially modified environment, by adding chemicals to the local soil or creating a new environment, the objective being to improve the electrical contact to the ground and to keep the soil moist. In order to study both approaches, electrodes from the same family were buried into holes prepared with different environments: local soil, clay, bentonite, clay with potassium chloride (KCl) and clay with sodium chloride (NaCl). This experiment also aims to reproduce the soil chemical composition test described in subsection 3.2.1.5 for much longer monitoring periods. Alternative ways of keeping the soil moist were also applied and are summarized below.

in vessel

electrodes are initially buried in plastic vessel and the whole assembly is buried afterwards.

in pipe

a bottomless plastic cylinder with approximately 20 cm. diameter is buried and the electrodes are buried inside it.

reservoir

electrodes are buried straight into the hole but are connected through a tube to a plastic bag which supplies electrolyte solution. An alternative to the buried plastic bag is to bring the tube to the surface to allow for electrode refilling from time to time.

The electric signal from each electrode pair were pre-conditioned by identical electronic channels and digitized at one sample per minute between May 1995 and April 1996. Additional signals recorded for the same period at the same sample rate were: three component magnetic field, temperature at 20cm and 60cm

depth, rain precipitation, soil moisture and amplifier noise. During the experiment any major problems were observed and every modification, maintenance, recalibration, power fault, etc. were logged for future reference.

3.2.4 Results and Recommendations

The first publication and poster related to the experiment was presented during the 13^{th} Workshop on Electromagnetic Induction in the Earth held at Onuma-Japan, in August 1996 (Clerc et al. 1996a), (Clerc et al. 1996b). It included results on long term stability and high frequency behavior of electrodes, short term instabilities, rain and diurnal effects, detection of transient signals, MT impedance and static shift. As a consequence of the interest drew in the conference, the authors have been asked to submit a Contributed Paper with the main results of the long term behaviour of the electrodes to be published together with the review papers in Onuma. The paper are due to be published in the Journal of Geomagnetism and Geoelectricity (JGG). A more complete technical report is being prepared by the participants and should be published by the end of 1996. The proposed outline includes:

- Experiment foreword
- Scientific issues
- Physical and chemistry of the electrodes and principles of electrodes design
- Practical realization of electrodes
- Description of the experiment
- Characterization of electrodes in the laboratory
- Data analysis and observations
- Additional experiments (Electroseismic and High Frequency data)
- Conclusions

3.3 An Alternative Electrode Design

In June 1995 the electrode issue in the Department had to be reconsidered. In that sense, my participation in the electrodes workshop and the first phase of the electrode experiment in Garchy-France, April 1995 gave me some ideas and confidence to build a new set of electric sensors. However, the main difference among the electrodes gathered for the experiment and my immediate necessity was the application. The aim of the campaign was to study the long term stability of the electrodes but my application required electrodes for shorter periods.

3.3.1 Design Goals

The idea was to build electrodes to operate in the range between 0.001Hz to 2kHz to meet the newly developed short period acquisition and processing system SPAM Mk-III. Magnetotelluric measurements in this range involve shorter period soundings at an average rate of one or two soundings per day. These electrodes should also be small, cheap, easy to build and assemble. Minimum maintenance requirements would also be desirable.

3.3.2 Brainstorm

Low noise and stability are the most important prerequisites to be addressed on designing electrodes. However, there are additional parameters that have to be taken into account and there will always be a balance among all these requirements before deciding the final design.

Noise

The natural induced electric signals measured by electrodes may be very weak and low noise electrodes are essential to carry out these measurements. Petiau

and Dupis (1980) compared the noise of different electrodes and the results were favourable to Pb-$PbCl_2$ metal-salt couples. The same study shows that beyond 10Hz the noise generated by the amplifier is predominant. This suggests that electrode noise should be considered relatively to the amplifier noise and in terms of the frequency bandwidth of operation. A good understanding of the noise mechanism as a function of frequency of electrode and instrument may relax the noise specifications for the former.

Stability

Electrodes for long-term monitoring of the electric field are required to present small variations within one year. The same stability is important but it is not essential for shorter observation periods because equipment and sensors are deployed from a few hours to a maximum one week in the same site. Electrode stability should be associated to the period they will be deployed in the field to acquire data.

Contact Surface to the Ground

Non-polarized electrodes require a porous surface to allow electric contact between metal-electrolyte and ground. These can be wood, calcium sulphate (Plaster of Paris) or clay among others. Electrodes with liquid support tends to dehydrate because the electrolyte leakage through the porous material. This is not a serious constraint if the electrodes can be refilled regularly. Again, the decision should take into account the period the electrode will be used continuously to acquire date and no maintenance or refilling is desirable.

Shape and Size

I believe there is a consensus among electrode makers that the cylindrical form is the most suitable. Diameter and height depends basically on the volume required

for electrolyte and metal core. In the field, the most time consuming task is to dig the hole. Electrode installation changes very little for the average size of the electrodes and it is not a considerable factor. My understanding is that electrodes with an usual cylindrical form, diameter between 3 to 5 centimeters and height within 30 centimeters are practical, easy to transport, to store and the weight may not be considerable.

Cost

The cost of the material depends mainly on the type of the electrode. Lead-lead chloride and copper-copper sulphate electrodes are usually cheaper. Silver-silver chloride electrodes are far more expensive. Service costs like machine shop and labor charges are sometimes higher than the material cost and have to be addressed carefully. An option to reduce service charges is to buy ready made parts from manufactures or stores whenever available. For instance, it is possible to buy off the shelf a machined silver core and a silver chloride disk to be used as electrode nucleus although they are still expensive. Also the electrode body can be designed to apply ready made components like plastic material and PVC (Polyvinyl Chloride) parts for plumbing which are widely available in shops in all sort of shapes and dimensions at affordable prices. However, some machine work will probably be necessary.

Parts and Material

I have observed that plastic materials have been used widely as a main electrodes body. That substance has strength enough to cope with the installation in all sorts of soils and is resistant to the usual careless handling during digging and recovering stages. Other options widely used are porous ceramic pots and glass that obviously do not have the same strength and have to be handled, carried and stored much more carefully. Porous cups have also a higher electrolyte leakage

rate unless the contact area to the ground is reduced or a solid support electrolyte applied.

Maintenance

Some people consider electrodes as disposable devices and prefer to build a new set of sensors for every field work. I believe the main reason is the lack of reliability of the electrodes after a long term storage and nobody knows what the electrode behaviour will be by the time next used. It is also a continuous and time consuming task to maintain the electrodes between field works. As an example, electrodes with solid support have to be kept wet all the time to avoid dehydration and irreversible damage, leading to constant supervision. In this issue, electrodes with liquid electrolyte are easier to manage and can last longer without care, except a cleaning after use.

Electrode assembly and electrolytes

I believe that electrodes should be reused for practical and economical reasons. Re-using parts of electrodes from previous field works is easier than to build a brand new batch for every mission and it is neither a considerable nor a time consuming task. The difficulties of preparing the electrolyte depends on the type and whether they use liquid or solid support electrolytes. Liquid electrolytes are easier to prepare. There is no difficulty in getting a saturated copper sulphate solution ready but a lead chloride solution is not as easy because the lead chloride powder does not dissolve readily. To achieve a homogeneous lead chloride solution is more difficult and time consuming. The process is even more complicated for solid electrolytes because an extra stage is required to mix the solution to agar-agar gel, calcium sulphate or other compounds before pouring the mixture into the electrodes body. Solid support electrodes have also to be kept on a wet salted foam or similar surface to avoid drying. A point to reflect on, not only when deciding upon electrodes but in general is that lead is harmful to the environment.

Conclusion

After the above considerations I decided to use transparent plastic tube (acrylic), PVC-U (Unplasticised Polyvinyl Chloride) sockets, plugs and bushes available from plumbing stores to build the electrode body to reduce as much as possible machine shop costs, copper rod in a liquid saturated solution of copper sulphate as the metal salt combination because the solution is easy to prepare and harmless to the environment. The bottom part of the electrode which performs contact to the ground is a PVC bush filled with porous calcium sulphate plaster.

3.3.3 Electrode Description and Fabrication

Figure 3.5 shows the proposed design with a brief description and some important dimensions.

The proposed electrode has three parts: body, core and base. The body is the easiest part to be built and does not require any particular skill. It is a piece of transparent acrylic tube with PVC sockets (plain/threaded) glued at the tips. The tube and the internal plain section of the sockets are fixed by epoxy resin or PVC cement. PVC tube can also be used instead of acrylic. The main advantage for the acrylic is that its transparency allows a visual inspection of the copper rod, electrolyte quality and general quantity inside the electrode. The tube is 150mm. long but can be bigger to accommodate larger volume of electrolyte. The nominal diameter for the tube and PVC parts is 1" but can be changed for the same reason.

The base is very simple to prepare as well. It is a 1" to 3/4" threaded reducing bush filled with porous material. The mixture, two parts of calcium sulphate, one part of water is poured into the bush and the internal thread helps to hold the plaster inside. The operation has to be done quickly since the plaster mixture starts hardening within a minute, then it will be to late to be poured. It is also important to produce a vibration while filling the base to avoid formation of

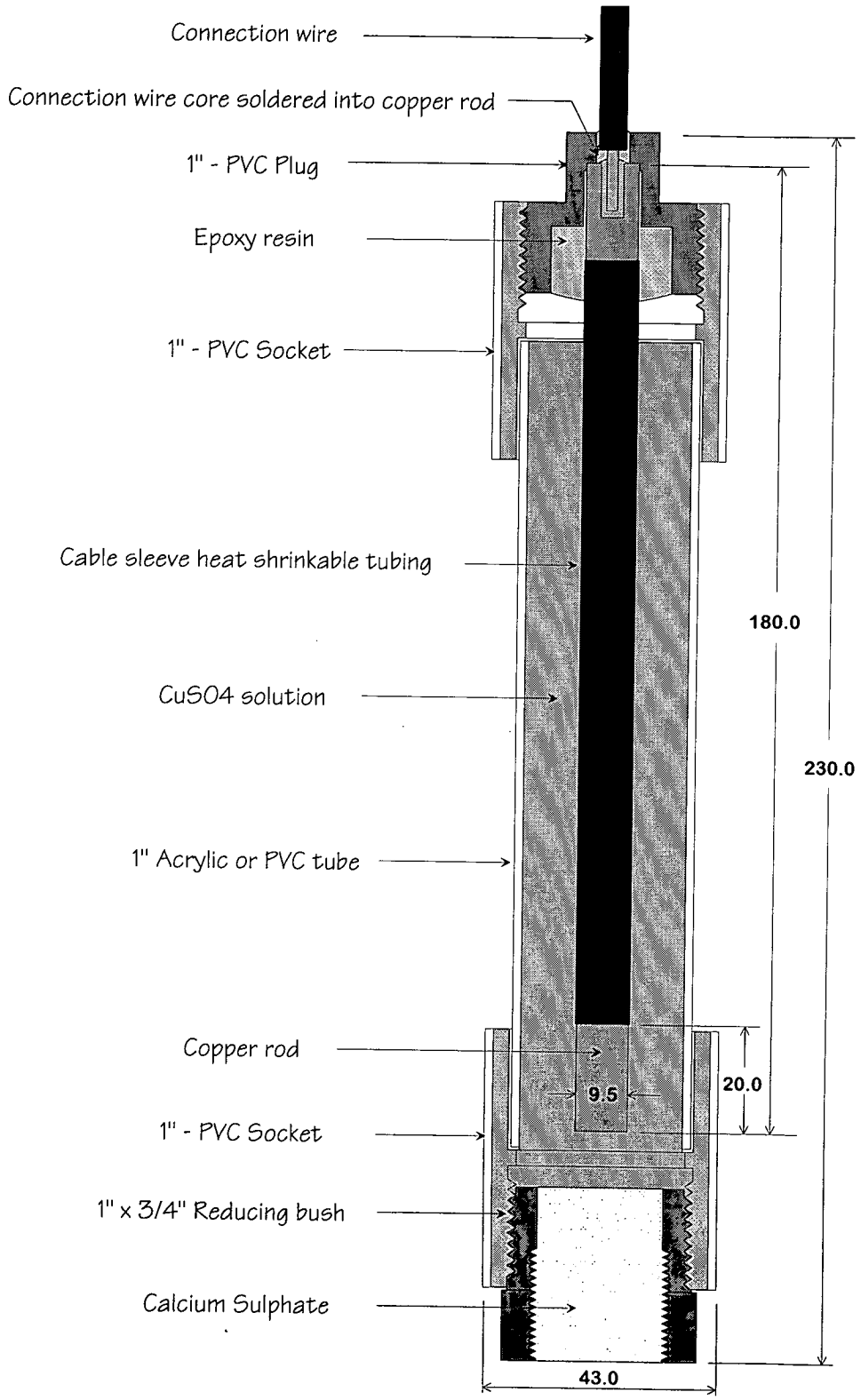

Figure 3.5: New Electrode Description and Dimensions

bubbles. The height of the PVC bush is approximately 30mm and can be filled up to the top with plaster. The thickness of the plaster in the base will determine the electrolyte leakage rate, the base strength and the electric contact to the ground. When complete, the base should be screwed gently into the electrode body socket. Teflon tape wrapped round the bush thread smoothes the operation and seals the parts. The assembly should be filled with water to check whether they are properly sealed, an abnormal leakage through the bottom might indicate the base has cracked. For example, the thinnest base (5mm) has to be screwed into the body socket very carefully to avoid cracking.

In order to study the influence of the plaster thickness on the electrode performance and characteristics I built some electrodes with different base thicknesses, from 5 to 30mm in steps of 5mm. Three out of the six base models are shown in figure 3.6.

The electrode core is subdivided in three parts. A connection wire, a PVC plug and a 9.5mm millimeter diameter copper rod with 99.95+% purity. The connection wire is a flexible tinned annealed stranded copper conductor, insulated with silicon rubber, suitable to operate in elevated temperatures and harsh environmental conditions. The wire overall diameter is 3.3mm. A hole with approximately 1mm depth has to be drilled into the copper rod and the connection wire soldered through the hole into the copper rod.

A typical problem related to electrodes with liquid electrolyte is the natural leakage of the solution through the contact surface to the ground. As a consequence, the metal core surface area in contact with the solution decreases proportionally to the electrolyte level yielding some self potential variation or instability due to the triple junction metal-salt-air. The problem is even worse for copper due to oxidation process. In an attempt to overcome that problem, I decided to leave only the bottom part of the copper rod in contact with the solution. This way, the contact area between metal and electrolyte is constant regardless of the solution level inside the electrode. Also, as the electrolyte level

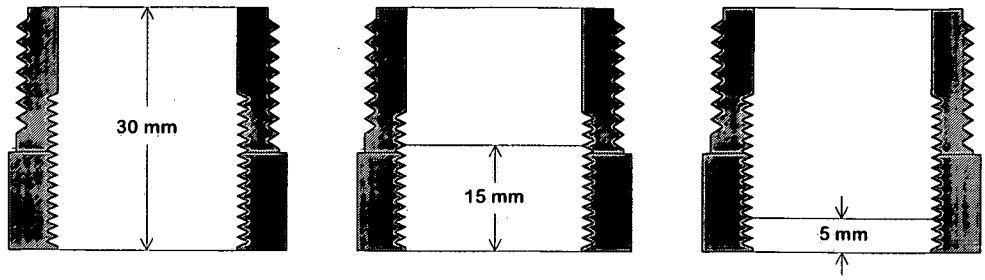

Figure 3.6: New Electrode Base and Plaster Thickness

decreases, copper is no longer exposed to the air preventing oxidation and triple junction instability inside the electrode. Semi-flexible heat shrinkable tubing with an integrally bonded adhesive, designed to provide a permanent encapsulation, was used to insulate the copper rod except for 20mm at the bottom.

The PVC plug has also to be drilled to allow the connection wire to go through and to retain the copper rod. Finally, epoxy resin must be poured into the plug to seal the piece to avoid external contamination through the connection wire hole, to avoid triple junction copper metal-copper solution-solder material at the wire/copper rod connection and to improve the part strength. The copper rod, the plug and the connection wire form a single and inseparable piece which is the electrode core. The final step is to fill the electrode with copper sulphate solution, clean the copper rod with diluted nitric acid and screw the core into the electrode body. The shrinkable tubing that covers the major part of the copper rod is resistant to the acid.

3.3.4 Electrolyte Preparation

Saturated copper sulphate solution is not difficult to prepare. However, in order to get the solution as pure as possible, I use copper sulphate anhydrous (AnalaR) crystals, minimum assay 99.0% and mill-Q water [3]. The saturated solution prepared at room temperature is boiled and more copper sulphate crystals added

[3]Ultrapure water free from metal traces

to it to super-saturate the solution. After cooling, the electrolyte is filtered before being poured into the electrodes. The natural pH of the $CuSO_4$ solution is slightly acid (pH between 5 and 6) which is a positive indication. Petiau (1995) studied Pb-PbCl electrode variations in self-potential, noise and temperature coefficient versus pH and concluded that the best working zone for internal pH is from 4 to 5.5. Within that range, self-potential is stable, noise is minimum and temperature coefficient is very small.

3.3.5 Laboratory Tests

Measurements in the laboratory were undertaken for 90 hours after the construction, following the same procedures applied at the Electrodes Campaign (Garchy-1995/96) described in section 3.2.1 whenever it was possible.

3.3.5.1 Self Potential

One electrode from the batch was chosen as a reference for self potential measurements (E_{13}). The table 3.5 shows the self-potential results for each electrode after the initial stabilization time (90 hours). There appears to be no relationship between base thickness and self-potential and all potentials were within a few milivolts, as expected for electrodes from the same type.

3.3.5.2 Internal Impedance

The most common way of measuring the electrode internal impedance is to use an alternate current resistance meter that gives the impedance amplitude at a particular frequency. However, it is not possible to work out the separate values for resistive and reactive components without the phase information. I took a different approach, measuring separately the resistive and the reactive components of the electrode internal impedance, for the following reasons:

Electrode Number	*Base Thickness (mm)*	*Self Potential (mV)*
E_1	5	0.284
E_2	5	0.283
E_3	10	0.248
E_4	10	0.252
E_5	15	0.246
E_6	15	0.246

Electrode Number	*Base Thickness (mm)*	*Self Potential (mV)*
E_7	20	0.260
E_8	20	0.260
E_9	25	0.258
E_{10}	25	0.257
E_{11}	30	0.263
E_{12}	30	0.264

Table 3.5: Self Potential Test Results

- An equivalent circuit for the electrodes can be established.
- The amplitude and phase of the equivalent impedance can be worked out from the resistive and reactive component readings.
- The individual contributions of resistive and reactive components to the composite impedance can be compared.
- The behaviour of the two components of the equivalent impedance as a function of the stabilization time can be traced.
- The relationship between the resistive and reactive components and the electrodes base thickness can be observed if it exists.
- The electrode Transfer Function can be calculated from its resistance and capacitance values and the *filter effect* studied.

A universal bridge [4] was used to perform the measurements and it displays direct readings for the *device under test* impedance in terms of the capacitance C and the parallel conductance G. It is more common to take the parallel resistance R, where $R = 1/G$. The equipment operating frequency for impedance measurements is 1591.5 Hz ($w^2 = 10^4$).

[4] Wayne Kerr model B642

It is important to emphasize that the *device under test* in this sort of measurement means two electrodes from the same type plus a salted wet foam contact in addition to the instrument in the circuit path. The capacitance and conductance readings (C, G) are related to the whole measurement setup as illustrated in figure 3.7a. There is no significant electrical resistance between the two electrodes due to the salted foam (see subsection 3.2.1.1) and the test setup can be represented by the equivalent circuit of figure 3.7b.

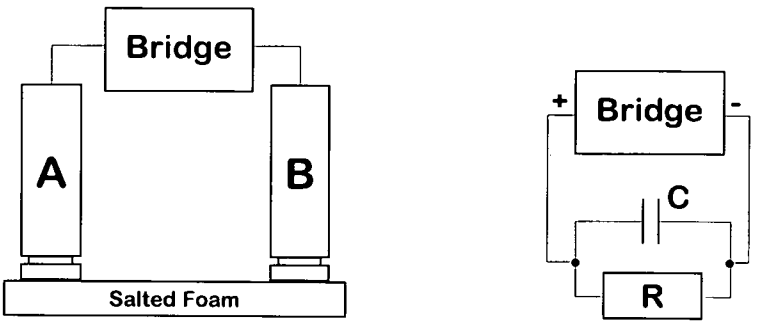

(a) Test Setup (b) Model

Figure 3.7: Internal Impedance Measurement Test Setup and Model

The equivalent impedance amplitude Z and phase ϕ for a resistance R and a capacitor C in parallel can be expressed as

$$Z = \frac{R}{\sqrt{1+\omega^2 R^2 C^2}} \quad (3.7) \qquad \text{and} \qquad \phi = \tan^{-1} \omega R C \quad (3.8)$$

In order to follow the stabilization process of the electrodes with different base thicknesses I measured the conductance and capacitance for 90 hours, starting just after the electrodes final assembly. The graphic of figure 3.8 indicates that the internal resistance is proportional to the base thickness . This result was expected since resistance is given by the expression $R = \rho l/S$, where ρ is the resistivity of the material, l is the base thickness and S is the sectional area. All electrode bases are filled with the same material (ρ), they have the same surface area to the ground (S) but different base thickness (l) and consequently the resistance

(R) should be proportional to the base thickness (l). There is also an assumption that the porosity of the $CaSO_4$ plaster at the base is the same for all electrodes, yielding an identical electrolyte flow. The relationship between internal resistance and base thickness is consistent for every measurement and electrodes with thicker bases have always higher resistance values. An approximate value for the resistance of a pair of electrodes as a function of base thickness can be written as $R \approx 120 + 16\,l$, where the constant term is due to the resistance between metal and electrolyte. The error between calculated and measured values are within 10%. Figure 3.8 also indicates that electrodes with thicker bases generally need longer times to stabilize compared to electrodes with thinner bases.

The capacitance cannot be determined with the same level of accuracy as the resistance due to the resolution given by the equipment (1nF). However, the readings for the same period (see figure 3.9) tends to indicate an inverse relationship between base thickness and internal capacitance. The highest value (5nF) is associated to the electrode with the thinner base (5 mm). However, the stabilization time for the capacitance follows the same tendency as the resistance and electrodes with thicker bases take longer to stabilize compared to electrodes with thinner bases.

The equivalent impedance amplitude Z and phase ρ for each electrode pair can be calculated by using the respective C and R readings, Equations 3.7 and 3.8. The results tabulated in 3.6 are based on the measurements after the stabilization period and shows that the internal impedance of the tested electrodes is essentially resistive, regardless the base thickness ($Z \approx R$). Also, the phase measured at the impedance bridge working frequency ($\omega^2 = 10^4$) is not significant even for the highest measured capacitance (5nF). The reactive component proper to the electrodes with the thinner plaster base is negligible compared to the resistive component and does not influence either amplitude or phase. These results indicate that no significant *filter effect* due to that type of electrode should be expected within the frequency range of interest for geophysical applications.

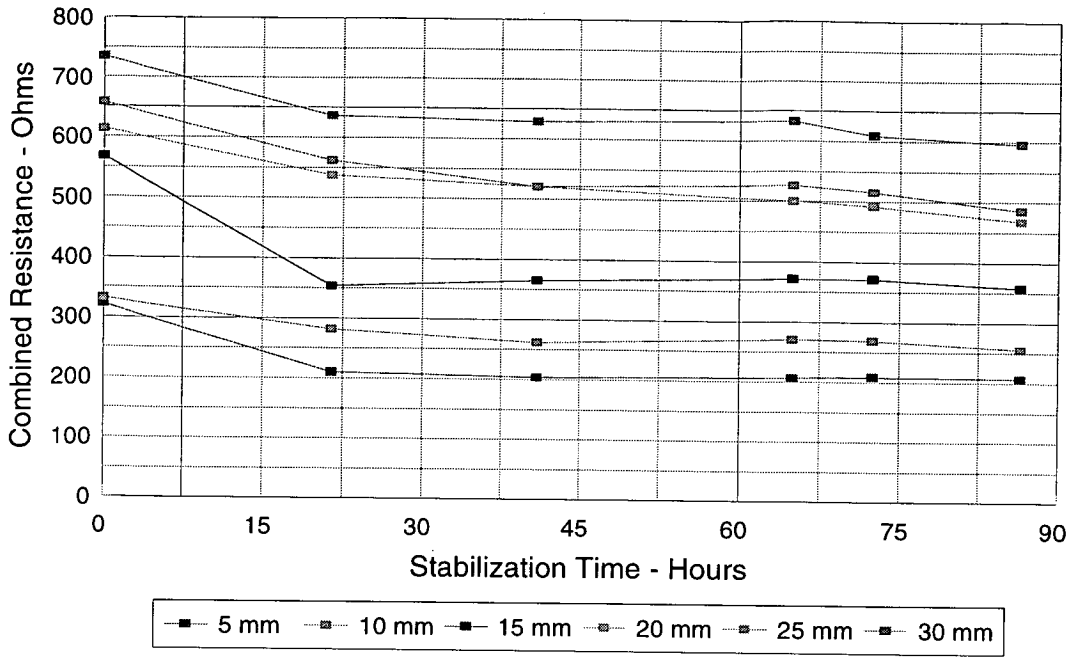

Figure 3.8: Combined electrode resistance as a function of stabilization time after the final assembly for different base thicknesses

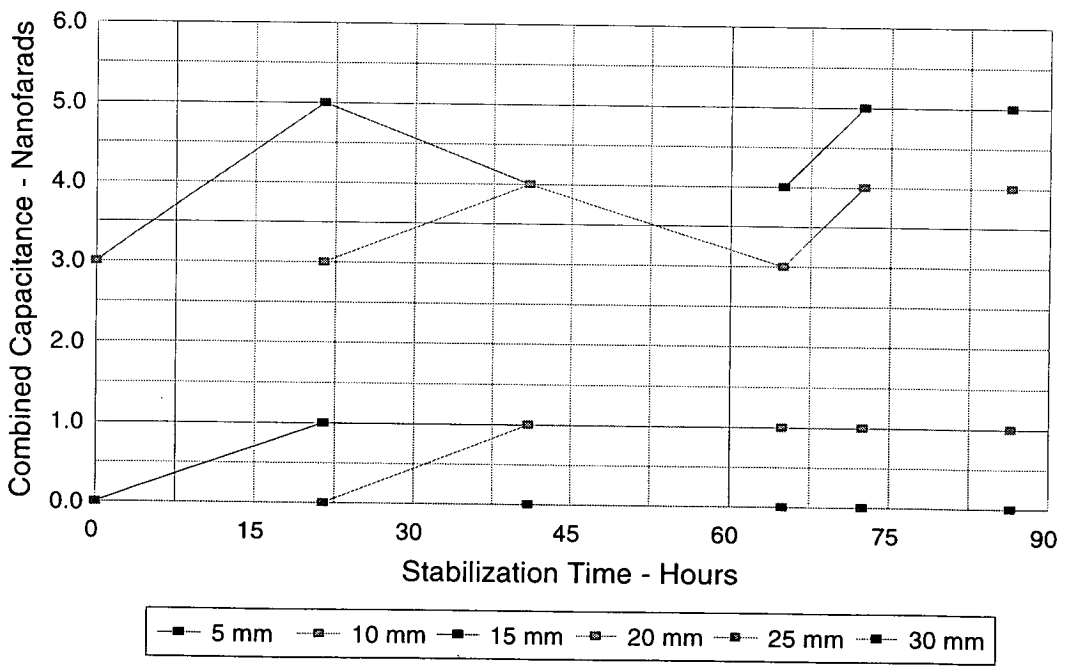

Figure 3.9: Combined electrode capacitance as a function of stabilization time after the final assembly for different base thicknesses

Electrode	*Base*	$R\,(\Omega)$	$C\,(\mu F)$	$Z\,(\Omega)$	$\phi\,(^\circ)$
E_{1-2}	5 mm	207.04	0.005	207.03	0.59
E_{3-4}	10 mm	255.10	0.004	255.09	0.58
E_{5-6}	15 mm	357.14	0.001	357.14	0.20
E_{7-8}	20 mm	467.29	0.001	467.28	0.27
E_{9-10}	25 mm	485.44	0.001	485.43	0.27
E_{11-12}	30 mm	595.24	-	595.00	-

Table 3.6: Internal Impedance Test Results

As mentioned before, electrodes are always tested in pairs and the results as in table 3.6 reflect combined value of their characteristics e.g. self-potential, impedance, etc. However, it may be interesting to visualize one electrode (hall-cell), determine its internal impedance, resistance and capacitance. Under this new approach, the equivalent circuit for the electrode pair shown in figure 3.7 can be modified to represent half-cells (A and B) connected in series, as shown in figure 3.10. Usually in these measurements the electrodes under test belong to the same family and are almost identical. Thus, $R_a \approx R_b$, $C_a \approx C_b$ and $Z_a \approx Z_b$. Each device contributes equally for the combined results and the impedance of a single electrode or half-cell is half of the total impedance ($Z_a = Z_b = Z/2$).

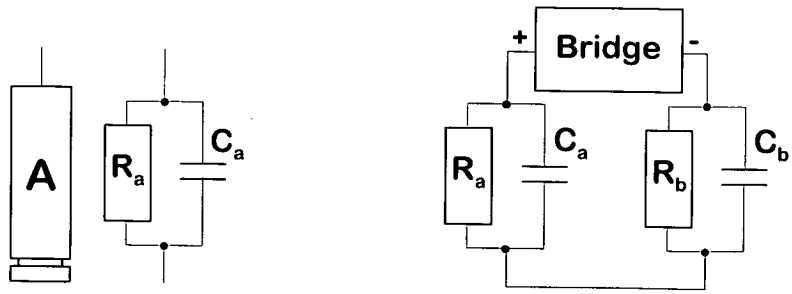

(a) Half-Cell (b) Test Circuit

Figure 3.10: Half-Cell Equivalent Circuit and Impedance Test Model

Simple circuit analysis shows that values for half-cell resistance (R_a, R_b) and capacitance (C_a, C_b) as represented in figure 3.10 can be determined from the parameters measured in pairs (R, C) since they are connected by the relationship: $R_a = R_b = R/2$ and $C_a = C_b = 2\,C$. Also, the approximate reasistance as a function of base thickness l can be written as $R \approx 60 + 8\,l$.

Single electrode parameters are not relevant for geophysical applications since electric fields measurements are always undertaken by using paired electrodes. However, the equivalent circuit of single electrode can be useful for simulations and circuit calculations.

3.3.5.3 Frequency Response

Electrode transfer function is becoming more of a concern, mainly for higher frequency applications. It has been assumed electrodes have a flat response in the range of interest and do not affect the natural signal spectra. Results from the new electrodes (see 3.3.5.2) revealed that there is a capacitance associated to the electrodes and its value is roughly inversely proportional to the base thickness. However, the contribution due to the capacitive component is negligible and the electrode internal impedance is basically resistive (see table 3.6). Therefore a filter effect at higher frequencies is expected.

In order to address the electrodes frequency response issue, a test for measuring electrode frequency characteristics was set up during the last phase of the Electrodes Campaign (Garchy-1995/96). The test set up consists of an electrode pair connected to a signal analyser placed on a salted wet foam connected to a signal generator (figure 3.11). The equipment[5] generates sine waveforms in the range 0.001Hz to 65kHz and displays the amplitude and phase of the signal measured across the electrodes related to the source signal.

[5]Schlumberger Model 1250 - Frequency Response Analyser

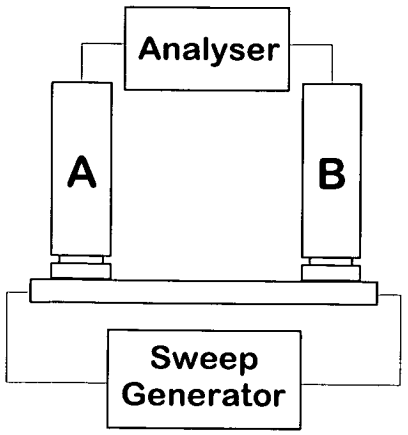

Figure 3.11: Frequency Response Test

All electrodes were tested and the results will be published soon. Two electrode pairs from the new design with the thinner and the thickest bases (5mm and 30mm) were also tested with the same set up. The amplitude and phase plots are illustrated in figures 3.12 and 3.13. The scale was chosen to emphasize the differences between the two electrode pairs. In general the electrodes are flat in the frequency range between 0.001Hz and 65kHz. The small difference noticed in the amplitude plot is due to the higher internal resistance of the electrode with the 30mm base (595Ω) that attenuates the signal in the whole frequency range. The effect due to the capacitive component of the electrode with the 5mm base (5nF) can be noticed in both amplitude and phase plots at the vicinity of 10kHz. The shape of the amplitude and phase plots related to the 30mm base electrode at higher frequencies are not consistent, since the change in the amplitude curve is not correlated to any change in the phase plot for the same region. It could be related to the test set up because that frequency range is more susceptible to external noise or signal distortions due to the generator, since 65kHz corresponds to the limit of its frequency range.

3.3.5.4 Noise

To observe the noise of the electrodes in the laboratory I took advantage of the SPAM Mk3 capabilities, including multi-channel data acquisition and real time processing. I buried six electrode pairs with different base thicknesses in a plastic bucket with local soil and connected the pairs to the equipment's differential inputs. The analogue pre-conditioning basically includes band-pass filtering

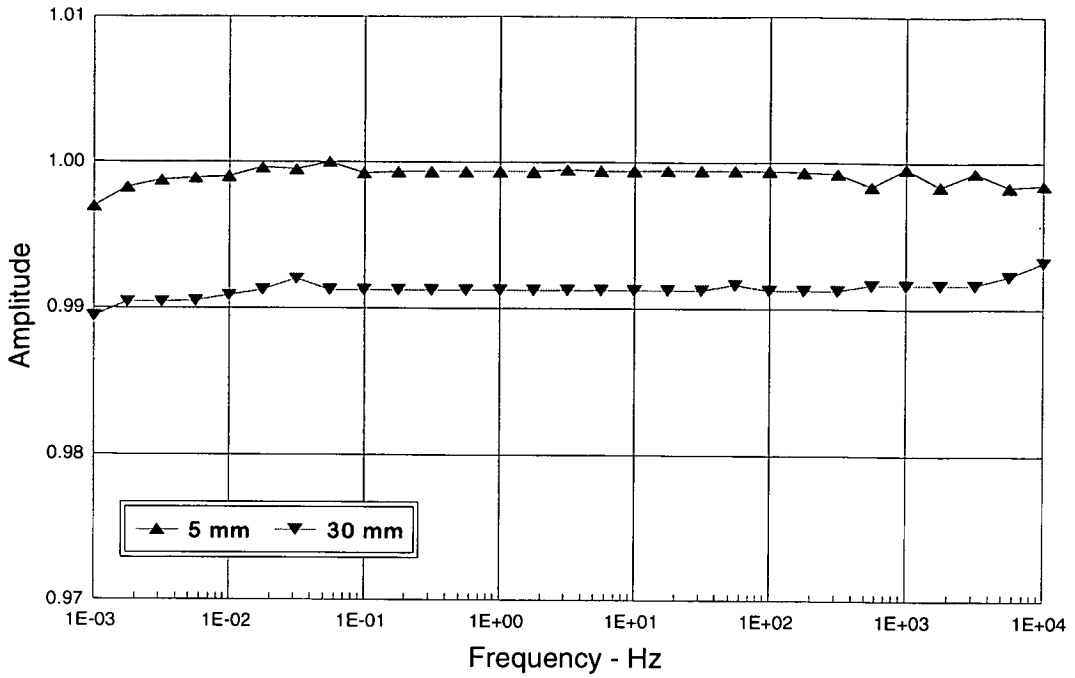

Figure 3.12: Electrode Frequency Response Gain. Generator Amplitude = 1

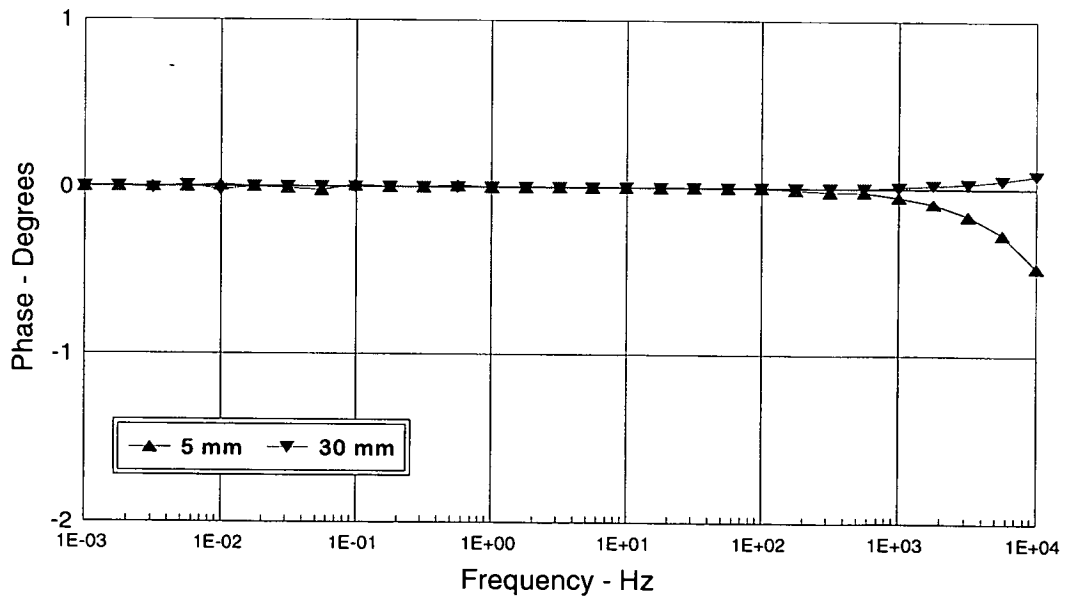

Figure 3.13: Electrode Frequency Response Phase. Generator Phase = 0 °

(fc_{HP} = 0.01Hz, fc_{LP} = 256Hz) and amplification (G=20) the channels being matched within 1% amplitude and 1 ° phase. After digital processing the time series and the frequency spectra are displayed on a computer screen. The equipment provides features like band and channel selection, scaling and signal storage which are very useful for laboratory tests.

Figures 3.14 and 3.15 are time series of the electrode noises for two different frequency windows. The pairs are identified by their base thicknesses (5mm...30mm) written above the respective channels. The scale on the left (0.1mV) indicates the signal amplitude between two adjacent channel traces. However, the scale factor has to be corrected because the signal is picked up after the first analogue amplification (G = 20). The corrected vertical scale is 5μV to reflect the signal at the input of the equipment (noise from the electrodes). Both figures indicate the noise is almost identical for all electrode pairs regardless the base thickness. The noise figures are smaller for higher frequencies than for longer periods. The maximum peak-to-peak noise for the higher frequency band is approximately 3μV and the average for all electrodes 1.0μV (see figure 3.14). The same parameters for the longer period band are 7μV and 2μV (3.15). As mentioned before, the measured noise referred to the equipment input is a combination of electrode noise and amplifier noise. The maximum measured noise related to the amplifier only is 0.15μV peak-to-peak at 128Hz, which is negligible compared to the results.

Figure 3.16 is a snap-shot of the noise frequency spectra between 128Hz and 0.004Hz (256s) for the same set of electrodes 24 hours after deployment. Also, the corrected vertical scale is 5μV. As observed before, the noise is almost the same for all electrodes up to 0.016Hz (64s). Beyond this point, there is an increase in the noise levels for some channels which is not consistent with the base thickness. For instance, the noise for 5mm and 30mm are practically the same. Also 10mm, 15mm and 20mm, 25mm have similar noise figures, this tends to indicate there is no correlation between the observed noise and the electrode base thickness. The

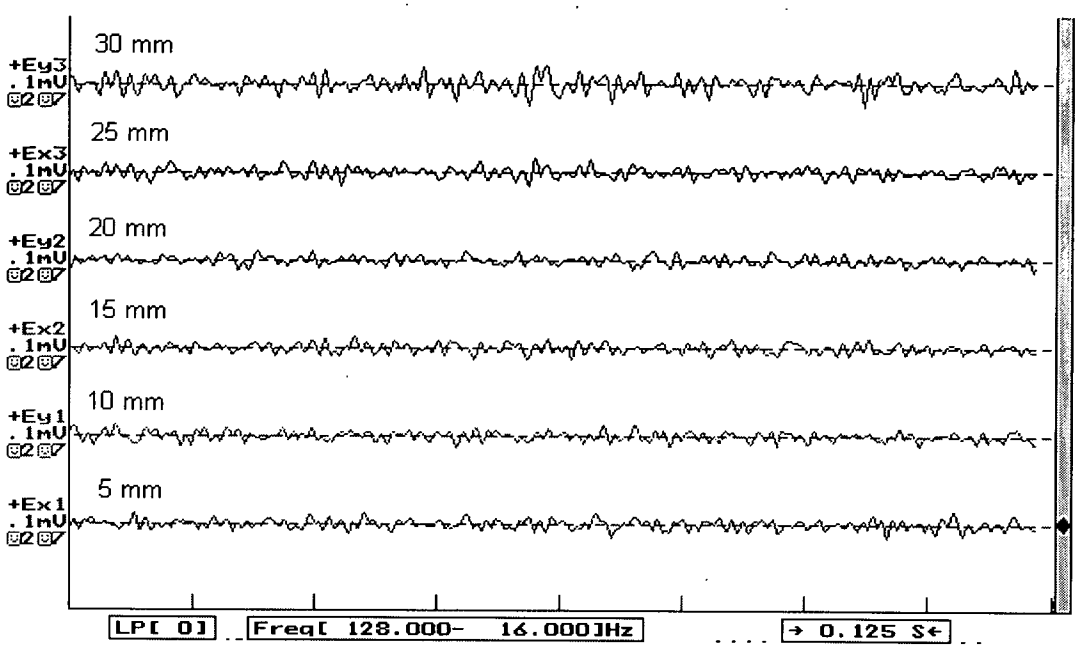

Figure 3.14: Electrode Noise 128 – 16Hz observed for 1 second.

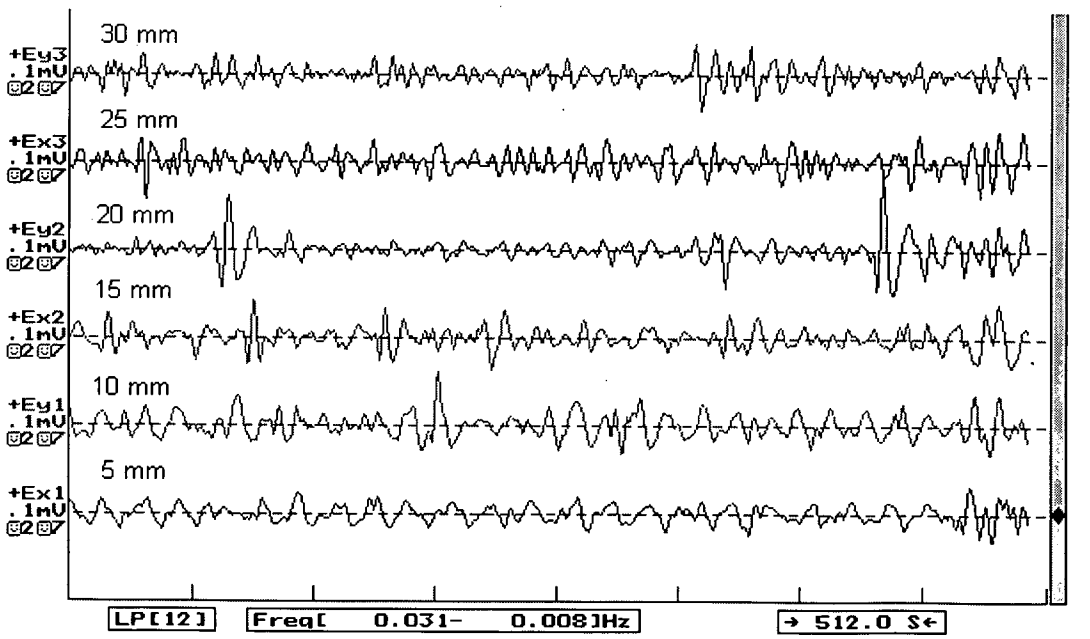

Figure 3.15: Electrode Noise 0.031 – 0.008Hz (32 – 128s) observed for 1 hour.

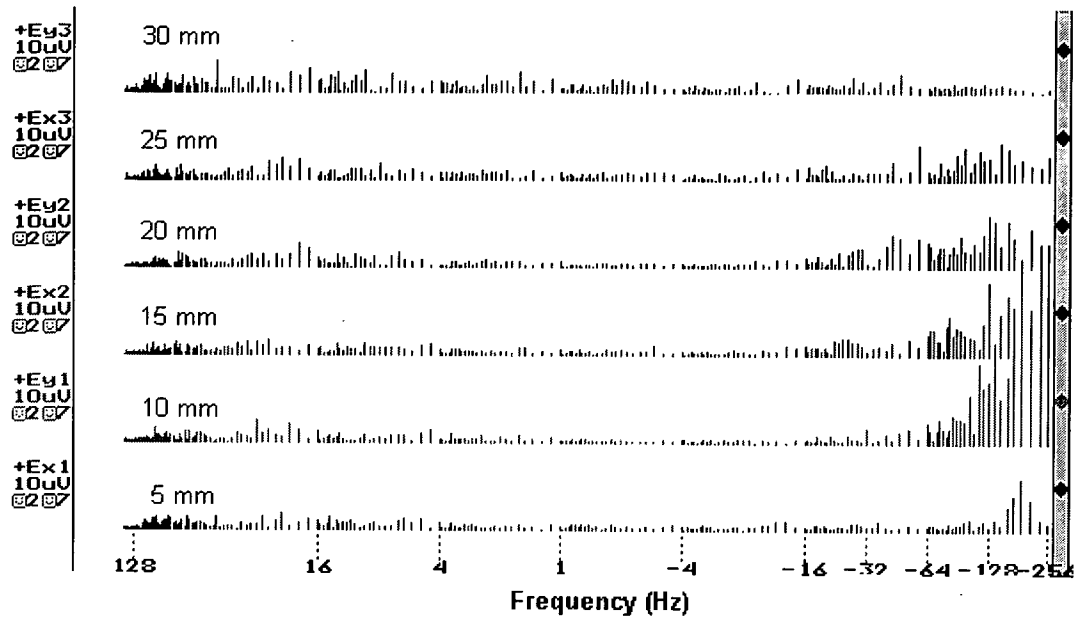

Figure 3.16: Electrode Noise Frequency Spectra 128Hz–256sec.

instantaneous noise values shown in figure 3.16 are not corrected for instrument frequency response (hardware and software) and FFT frequency distribution. If these parameters were corrected[6] noise levels would be smaller. In practice noise figures should be even smaller since the average process used in data acquisition tends to reduce non-periodical events like random noise.

3.3.6 Conclusions

Since April 1995 I have built and tested twenty electrodes following the design described in section 3.3.3, at unit price of approximately £ 25. Since then, there has been no need to modify the original design in any aspect. The construction and assembly of the parts are very simple. The total machine shop time for drilling the copper rods and the PVC bush did not exceed 3 hours and approximately sixteen working hours were spent for constructing the whole batch. The thinnest

[6]Hardware and Software frequency response and stacked FFT spectra were implemented in the latter version of SPAM-Mk III data acquisition software.

electrode base (5mm plaster height) is the most critical component to assemble and some of them cracked. Not only does the plaster have to be left drying for a few hours but also it has to be screwed into the electrode body with extreme care. Sometimes the crack is visible but in many cases only an abnormal leakage of the solution indicates a damaged plaster.

Despite strict care in preparing the solution with only pure metal and chemicals I experienced some copper rod oxidation just after the final assembly. I believe impurities left on the copper surface reacted with the $CuSO_4$ solution leading to an immediate metal oxidation and increase in the electrode self potential. In order to overcome this unexpected oxidation and contamination of the solution inside the electrodes I suggest the following procedure for the final fabrication step:

1. Clean the copper rod with diluted nitric acid.
2. Immerse the electrode core into a $CuSO_4$ solution and wait one hour for any first oxidation to take place.
3. Clean the copper with a piece of paper or cloth and screw the core into the electrode body containing the solution.

To verify the solution leakage rate for the different base thicknesses, all electrodes were left resting on an absorbent surface and monitored constantly for 48 hours. As expected, electrodes with thinner bases allowed a higher migration. However, no considerable change in the electrolyte level was observed and I found it would be possible to leave them in the field for at least two weeks without refilling.

Since 1995 the electrodes have been used regularly in conjunction with the acquisition system and have proved to be strong enough to deal with different soils and temperatures conditions. The electrodes were used in a field work over the last winter under temperatures below zero, the soil surrounding the sensors had

frozen but no physical damage was observed when they were dug up. The material seems to be very resistant to the soil compression-expansion due to temperature changes. The electrodes were also used in Kenya, in a very dry climate but they had to be refilled every few days. I have not experienced any cracked bases in the field proving that the most critical operation is screwing the 5mm plaster base into the electrode body.

The maintenance of the electrodes has been very simple and after a field work they have only to be emptied, cleaned and stored without any additional care. To prepare the electrodes for a new campaign the $CuSO_4$ solution has to be prepared and the final assembly performed, which can be done is a few hours. It is recommended to check the electrode bases. Since the first field work some of 5mm and 10mm bases had the plaster replaced due to excessive erosion.

The time series visualization and data analysis in the field have not shown any electrode instability within the frequency range 0.001 to 2000 Hz. Electric signals acquired through pair of sensors with several base thicknesses seemed to present the same characteristics. The higher internal impedance of the 30mm plaster base has neither jeopardized the contact to ground nor increased the noise. Based on observations in the field and tests in the laboratory I have decided to rebuild all electrodes with 30mm plaster thickness because they are more robust, resistant to damage, less likely to allow a fast electrolyte leakage and does not interfere on the electrical signal quality.

These copper-copper sulphate electrodes are to be used mainly for magnetotelluric measurements in the frequency range 0.001–2000Hz. At the moment, they are being tested for longer term signal observations and I believe I will have came to some conclusions by the middle of 1997. However, it has been known for some time (Petiau and Dupis 1980) and has been verified by this recent Electrode Experiment that lead-lead chloride and silver-silver chloride electrodes are better for long term signal monitoring because they seem to be more stable and less noisy compared to copper-copper sulphate electrodes. If the tests prove these

copper-copper sulphate electrodes are not stable enough for longer term monitoring I will suggest the development of a modified electrode for longer term applications. The same mechanical design could be used but a few modifications in the core to accommodate a lead-lead chloride metal salt couple.

Also, there is a new generation of electrodes by Petiau (1995) that uses a different approach to delay the electrolyte dehydration. The method consists on reducing the cross sectional area of the base producing a *channel effect.* This method can also be tried by including a few mechanical modifications on the original electrode base design.

CHAPTER 4

SPAM Mk–III Short–Period Automatic Magnetotelluric Data Acquisition and Processing System Version 3.0

4.1 Historic Background

SPAM systems are **S**hort– **P**eriod **A**utomatic **M**agnetotelluric instruments for geophysical field applications. They were designed, developed and constructed by Graham Dawes at the Department of Geology and Geophysics, Edinburgh University. The series started in 1980 and since then they have been updated as showed in Table 4.1.

The equipment has been used in many research projects not only at the University of Edinburgh but also by other research groups in the United Kingdom through loans from the Geophysical Equipment Pool – Natural Environment Re-

Revision	Year	Description
Mk I	1980/81	Prototype
Mk II	1983/84	Final design phase
Mk IIa	1986	CPU upgrade
Mk IIb	1988	Data storage and printer upgrade
Mk III	1990	Feasibility Study

Table 4.1: SPAM series and upgrades

search Council. Two systems were built and sold by the Department, one to the India Institute of Geomagnetism in Bombay and one to the University of Alberta in Canada. Since 1982 twelve PhD theses have been written in the Department using data acquired by the equipment. From 1982 to 1991 sixteen field work projects were carried out with the equipment in Scotland, England, Italy, Canada, Portugal, Greece, Sudan, Papua New Guinea, Kenya and during the same period a substantial number of abstracts or papers have been published by members of the Geophysics Group (Geophysics Group 1995a), (Geophysics Group 1995b). Further scientific publications based on SPAM–Mk II in Britain and abroad have not been traced.

Since the last hardware modification in 1988, technology has improved dramatically. New applications such as portable computers and mobile phones have pushed electronics to a new era where large scale integration, low power consumption and small size are mandatory. As a result, new components have been released and others greatly improved. New techniques like digital signal processing, low-noise analogue electronics and digital communications opened new horizons and possibilities in the instrumentation field.

In 1990 Graham Dawes undertook a feasibility study for developing new equipment. Not only will the system take advantage from new technologies available but will introduce new concepts in terms of equipment for the acquisition of time-varying geophysical data. This is the SPAM–Mk Version 3.

4.2 Magnetotelluric Instrumentation

The main aim of field equipment for magnetotelluric studies is to acquire data from a set of electric and magnetic sensors to determine the earth's structure in terms of certain physical proprieties, for instance the electrical resistivity. The geophysical method is the same, regardless the depth of penetration required by the application and consequently the period range of the signal to be measured. However, the equipment used to acquire the signals are historically divided into *Long Period Magnetotelluric* (LMT) and *Audio Magnetotelluric* (AMT) since they have different characteristics to cope with signals from distinct regions of the frequency spectra.

LMT equipment usually deals with signals in a period range approximately between 100 and 10000 seconds. Due to the long periods involved, the long term stability of the components are the main concern. In order to collect enough data, recording is undertaken for weeks or even months. LMT equipment usually do not perform real–time data processing. Initially the data were recorded on paper chart recorders. Later magnetic tape and floppy disks were used. Modern equipment does not record data continuously. Time series are sampled and stored digitally on memory cards.

AMT equipment usually deals with signals in a frequency range approximately between 1000Hz and 0.1Hz. Long term stability of the components is no longer a great concern since their electrical drift can be removed electronically without affecting the natural signals in the frequency range of interest. On the other hand the noise generated by electronic components inside the equipment (*intrinsic noise*) and the noise generated by external sources, like the main supply frequency, share the same bandwidth with the natural signals to be acquired and have to be eliminated or minimized (Schnegg and Fischer 1980). AMT equipment usually takes from a few hours to one day to collect enough data at each site and to enable a partial "in-field" data processing some systems record non–continuous time series (windows).

AMT and LMT equipment have some common features like low power consumption for extended battery life, low weight since they usually have to be carried to remote places, both take advantage from recent developed technologies and are becoming more portable. In most cases AMT and LMT equipment are used in the same geophysical application playing a complementary task to acquire data from different depths.

AMT systems are usually limited in the number of channels. New applications may require an increase in the number of channels to be gathered simultaneously or an increase in the frequency range for near surface studies.

4.3 SPAM–Mk III

One important characteristic related to electronic instrumentation for research application is flexibility. The equipment must support new and original ideas and should not be restricted to original concepts or standard applications. However, it is impossible to preview all the possibilities at the design phase. The alternative is to design modular equipment where each module itself can be reconfigured or upgraded easily. This concept, of course, must not jeopardize the high performance typical of equipment developed in research centres and universities. The SPAM–Mk III design aims were to provide:(Dawes 1990)

- **a modular framework.**
  allowing an unlimited number of hardware configurations to support real-time data acquisition and analysis simultaneously from any number of remote sites, each consisting of a wide range of possible sensors, as required for multi-site, multi disciplinary studies.

- **flexible and upgradeable computational power.**
  to perform any required computation, from basic analysis down to modeling.

- ▷ **a range of digital communication media.**
  to support efficiently a diverse range of inter-sensor distances at high speed data rates, thus accommodating most survey logistics.

- ▷ **battery operation, low power and small size.**
  for general ease of use, portable enough to work in remote areas and for quick site changes.

- ▷ **continuous wide band recording.**
  to cover as much as possible the whole frequency range with subsequent digital decimation and filtering into sub-bands.

- ▷ **calibration facilities.**
  to test the full functionality of the equipment and provide calibration facilities for sensors.

- ▷ **accurate time synchronization.**
  to enable applications like remote reference and seismic that need absolute or relative time synchronization.

- ▷ **support for mixed methodologies.**
  to enable common signal registration like magnetotelluric and seismic.

- ▷ **real time processing.**
  to provide a quick evaluation of data quality and noise conditions for the site.

- ▷ **stand alone operation and reconnection facilities.**
  to operate continuously without further user interaction and to allow periodic verification.

Modularity, distributed processing and high speed digital communication are typical characteristics of the Transputer. These features made it the ideal choice in forming the basic architecture of the new equipment.

4.3.1 The Transputer

A Transputer is a microcomputer with its own local memory and communication facilities for connecting one Transputer to another Transputer or device of the same family. A Transputer can be used in a single processor system or in networks to build a high performance concurrent system.

The Transputer architecture simplifies system design by using the point to point communication links at high speed rates which allows the construction of Transputer networks of arbitrary size and topology. Every member of the Transputer family has one or more standard links, each of which can be connected to a link of some other component of the same family. This innovative method of connection presents some advantages over the usual multi-processor bus:

There is no contention for the communication mechanism, regardless of the number of Transputers in the system.

There is no capacitive load penalty as Transputers are added to a system.

The communication bandwidth does not saturate as the size of the system increases. Rather, the larger the number of Transputers in the system, the higher the total communications bandwidth of the system.

The maximum speed for Transputer links is 20Mbits/s yielding data throughput rates of 1740kbytes/s and 2350kbytes/s respectively for unidirectional and bidirectional communications.

The Transputer family of VLSI[1] devices has several components with the same basic characteristics and the block diagram of one device is showed in figure 4.1. A complete reference guide for Transputer Family components can be found in reference (Inmos 1990).

The main features for T805 Transputer device are:

[1] Very Large Scale Integration

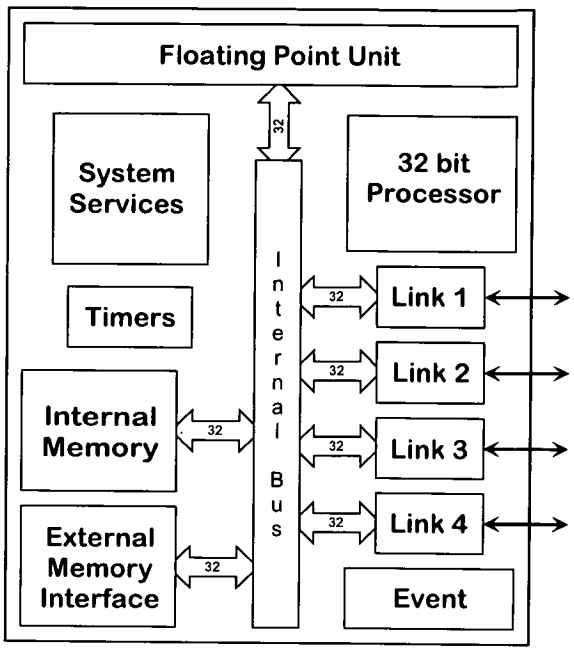

Figure 4.1: T805 Transputer Block Diagram

- A 32 bit or 16 bit reduced instruction set (RISC) central processor unit (CPU) operating at up to 30 million instructions per second (MIPS).

- Four high speed bidirectional direct memory access (DMA) links for inter-Transputer communications, providing full-duplex operations at up to 2.4Mbytes/s per link.

- High speed, 4kbytes static memory for data and program code storage.

- Optimal 64 bit floating point unit (FPU) operating up to 4.3 million floating point operations per second (Mflops).

- Interface for up to 4Gbytes external memory including all necessary control logic, operating at up to 40Mbytes/s. sustained data rate.

- System and link services such as reset, error I/O, analyse and boot.

- Two timers clocked at 1μs and 64μs.

All members of the Transputer family require a single +5V power supply and a single 5MHz external clock.

The power consumption and the performance depends on the Transputer category and the internal cycle time. However, it is very low if compared to similar devices with similar computational power. The Transputer chips available and their power consumption are presented in table 4.2.

Model	Type	mW
T805	32bit CPU internal bus + 64bit FPU	600
T425	32bit CPU internal bus	460
T225	16bit CPU internal bus	360

Table 4.2: Transputer Models and Power Consumption

A *process* is piece of program code running in a Transputer. Many processes may run in parallel (i.e. concurrently). This modularity consists of using *processes* as a standard building blocks for hardware and software. As far as the program is concerned, there is no distinction between a number of concurrent processes on one Transputer connected by *soft* channels (a path in the software program) and the same process distributed on more than one Transputer connected by *hard* channels (communication links). All *processes* communicate with each other by channels and only at the final program configuration they are defined as being *soft* or *hard* channels.

4.3.2 The Software

OCCAM is a high level language, designed to enable a system to be described as a collection of concurrent processes, which communicate with each other and with peripheral devices through channels. An entire system can be designed and programmed in OCCAM, from system configuration down to low level I/O and real time interrupts.

Transputers and OCCAM cannot be dissociated. Even though OCCAM can theoretically be compiled on any processor, it was designed to take full advantage of the Transputer instruction set.

High level languages like Fortran and C also have special libraries to support parallelism but the implementation is not as easy as it is in OCCAM. However an advantage of the high level languages is that they can express mathematical algorithms much more easily. OCCAM also interprets programs written in other language simply as another process. The equipment software uses the OCCAM language to implement overall network communication, synchronization, data processing, program imports and as a harness for other high level languages. The software that enables the equipment to communicate with the external computer is called ISERVER and a modified version called ISLPT was implemented by Oliver Ritter.

4.3.3 Operation Modes

The widest frequency range usually used for Magnetotelluric soundings is [10kHz - 0.0001Hz]. It is possible yet highly impractical to design a single signal conditioning and data acquisition piece of hardware to cover the whole range. An alternative to having a single high powered and expensive equipment being probably underused is to split the frequency band of interest in sub ranges. Each range must have signal conditioning and data acquisition hardware specific to its needs, leading to different equipment for different sub ranges, as mentioned in section 4.2. This principle is also used by magnetometer manufacturers that supply specific sensors for different operating frequencies.

SPAM–Mk III is designed to operate in the frequency range [2kHz - 0.0003Hz] too wide to be handled simultaneously. The solution used by the equipment is to provide exclusive *operation modes* for each of the frequency sub ranges. Each mode needs different software programs that set hardware and software parame-

ters required by the selected sub band. The hardware necessary for both operation modes is already available on the circuit boards and has only to be switched by the software. The operation modes presently available are showed in table 4.3 and cover the higher frequencies and the shorter periods allowing a generous overlap between ranges. It is important to emphasize that the mnemonics **HF** and **SP** when mentioned refer exclusively to the SPAM–MK III operation modes and not to the geophysical method which is obviously the same, regardless the frequency range.

Equipment	Operation Mode	Frequency Range
Others	LP (Long–Period)	DC – 0.05Hz
SPAM Mk-III	SP (Short–Period)	0.0003Hz – 128Hz
SPAM Mk-III	HF (High–Frequency)	4Hz – 2048Hz

Table 4.3: SPAM–Mk III Operation Modes

4.3.4 System Modules

The equipment is based on three modules. BASE, REMOTE and SENSOR. Each one includes sub-modules, which perform specific functions like computational, communication, pre-conditioning, storage, etc.

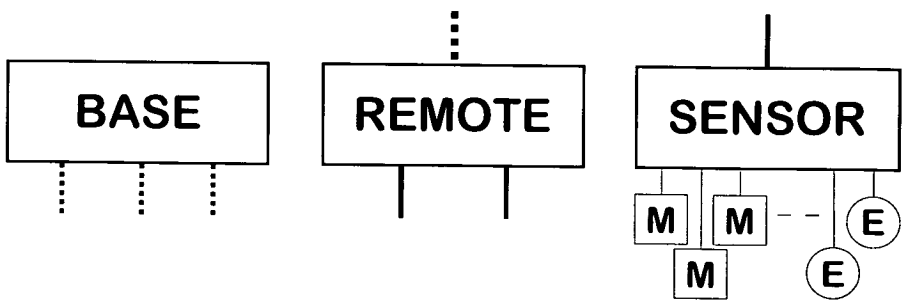

Figure 4.2: SPAM–Mk III Modules

The SENSOR module provides analogue pre-conditioning for a set of local sensors. The analogue signals related to each sensor are transmitted to the

REMOTE which performs an additional but common analogue conditioning, analogue to digital conversion and a digital processing of the signals. The digital information is then transmitted to the BASE which performs global data analysis, data storage and interface to an external computer. At least one module of each type must be present in every configuration. Modules also can be combined to build more complex networks. Some examples will be given in section 4.5.

The modules connected to the network generate a set of identification and configuration parameters such as Box and board serial number, number, type and orientation of sensors, filter setting and electric signal amplification factor, which are read by the system software and used for network management and calibration purposes. These identifiers are summarized in Table A.1.

4.4 Analogue *versus* Digital Communication

The modularity of the equipment and its ability to handle a large amount of information implies a massive data transfer between boxes at considerable distances. The data circulating into the media can be analogue or digital. Analog information is characterized by data whose value varies over a continuous range. Digital information is constructed from a set of symbols and more specifically a binary message consists in only two voltage levels. The task of the receiver is to extract information from a distorted and noisy signal at the media output and this extraction is often easier from digital signals than from analogue signals. The only decision at the receiver is the selection between two possible pulses received, not the details of the pulse shape, and the decision is readily made with reasonable certainty even if the pulses are distorted or noisy. In contrast, the waveform in analogue information is important, and even a slight distortion or interference in the waveform will cause an error in the received signal. Clearly, a digital communication system is more rugged than an analogue communication system in the sense that it can better withstand noise and distortion, as long as they are within a limit.

SPAM–Mk III relies heavily on digital communication to overcome logistics restrictions due to the noise and limited distances of analogue communications. Also, digital serial communication is a natural choice since it is used by the Transputer to exchange information through the communication links. Digital communication is used in SPAM–Mk III for connecting Transputers in the same box and Transputers in different boxes through two different types of link: **Internal Links** and **External Links**. These two links are both digital and serial but have some particular characteristics due to the distances involved. **Internal Links** are used for connecting devices inside the same box at shorter distances and higher speeds. These links are designed to transmit serial data between Transputer family devices at speeds up to 20Mbits/s up to 30 centimeters with no engineering except a simple wire connection. **External Links** are used for connecting devices in different boxes. These links are supposed to deliver information to greater distances and lower speeds. A hardware interface is required to prepare the signals accordingly. These communication links are mentioned in detail in section 5.9.

But the main reason for the superiority of digital systems over analogue is the viability of regenerative repeaters in the former. Repeater stations are placed along the communication path of a digital system at distances short enough to ensure that noise and distortion remain within a limit. This allows pulse detection with high accuracy. At each repeater station the incoming pulses are detected and new clean pulses are transmitted to the next repeater station. This process prevents accumulation of noise and distortion along the path by cleaning the pulses periodically at the repeater stations. We can thus transmit data over longer distances with greater accuracy.

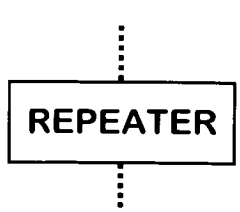

The REPEATER Box is an additional SPAM–Mk III module designed to regenerate the digital information and should be used whenever the distance between BASE and REMOTE is greater than 500 meters. Its function is to boost the digital signal after each cable section as described in the above paragraph. The module also provides facilities for monitoring the digital signal passing through.

Digital communication also permits a wide range of communication media and methods which are summarized below along with their advantages and disadvantages.

Multicore cables are very cheap, easy to install and repair in the field, do not require additional hardware, use low power consumption drivers/receivers and are very robust for field applications. However they are heavy compared to fiber optics and susceptible to external and internal interference (crosstalk).

Glass optical fibers can achieve long distances at high speed, are not susceptible to noise interference and have light weight compared to copper cables. Being totally electric isolated, there is no danger of grounding current loops and ground noise being coupled between modules. Optical fibers allow a wide signal propagation bandwidth and more than one signal could use the same fiber simultaneously in a frequency splitting system. However they are very fragile, break easily, are almost impossible to be repaired in the field and more expensive compared to copper cables.

Laser links can achieve distances up to 1000m at 2Mbits/s. However, they require additional and separated hardware for each direction of communication, the power consumption is high and a line of sight communication is essential which is not always possible in a field-word. Laser links are also very expensive.

Radio telemetry can achieve any distance depending on the radio frequency used. However they present limited bandwidth for the available spectral band, need additional and separated hardware for each direction of communication, the power consumption is considerably high compared to the SPAM–Mk III power consumption, the line of sight communication may be important depending on the radio frequency used and are very susceptible to external interference.

In order to choose the right option, not only are speed and distance important but also physical and practical parameters related to the operation in the field. Among them, robustness and low cost are decisive. Under these considerations, the use of cable communication was chosen for the first implementation.

Long distance cable communication is regulated by standards in order to allow connection between peripherals from different manufacturers and SPAM–Mk III adopts the RS–485 standard which is explained in section 5.8.1. Also, there is an important relationship between data speed and cable length, since the deformation of the pulse shape due to capacitive effects along the cable must be kept within acceptable limits. The electrical considerations related to cable communication are approached in section 5.8.2.

Analog communication is also used by the equipment to transfer data from the Sensor to Remote Boxes at distances up to 250m, since the information at that stage is purely analogue. However, the signals are transmitted in differential mode to reduce interference and distortion.

4.5 Network Configurations

The flexibility and modularity of the equipment can be exemplified by some suggested configurations. For each one of the following examples there are two schematics to associate the network and the sensor configuration.

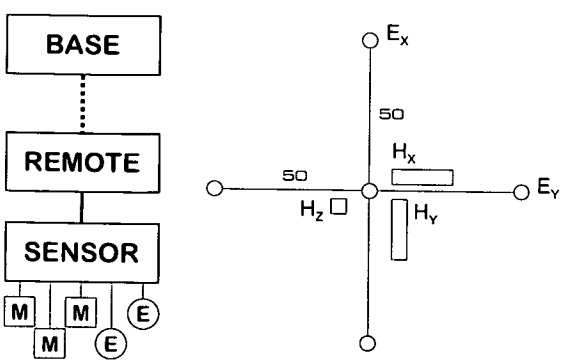

Figure 4.3: Five Components MT

Figure 4.3 shows the basic "five components" magnetotelluric configuration. This configuration has been employed in MT studies for decades. The intention is to show that the new design replaces the existing SPAM–Mk IIb with a much better computational power, frequency range and signal resolution. The power consumption is approximately one quarter, the size is half and the weight one quarter of the previous model.

Figure 4.4 is an extension of the previous example. Three more telluric pairs were added to the five component MT configuration. This can be achieved with only an additional SENSOR module. The aim is to provide instrumentation for applications that require a dense telluric array, for instance, to determine the resistivity map for a local area (High resolution AMT).

Another application for a multi-channel configuration is for testing electrodes. They can be buried side by side for short or long term stability comparison. Also in regular soundings two electric lines may be used to improve signal reliability. Electrodes are always of concern but simultaneous failures are most unlikely.

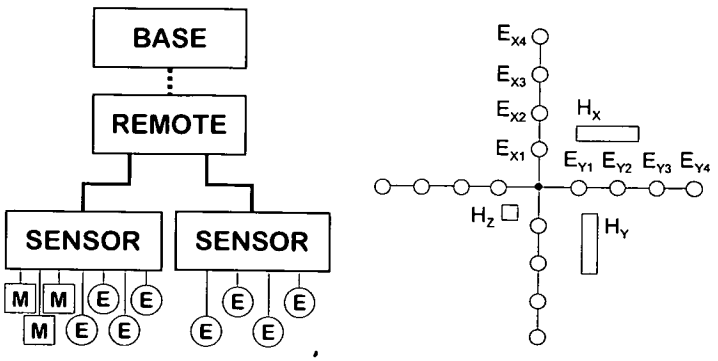

Figure 4.4: Additional Telluric Components

Figure 4.5 shows a more complex array with one five element MT station and four additional telluric stations. The distance between the station in the centre and the peripheral ones is 250 meters, which is the limit for the analogue connection from the SENSOR to the REMOTE modules.

It is also possible to operate in a remote reference mode with stations 2000 meters apart. This is possible because the communication between BASE and REMOTE is digital and much less subject to noise. However, a digital signal regeneration has to be performed as showed in figure 4.6.

There are many more possible configurations that can be achieved due to the modularity of the system. The main objective is to support a wider range of geophysical applications, which are, in essence, the reason why the equipment was developed.

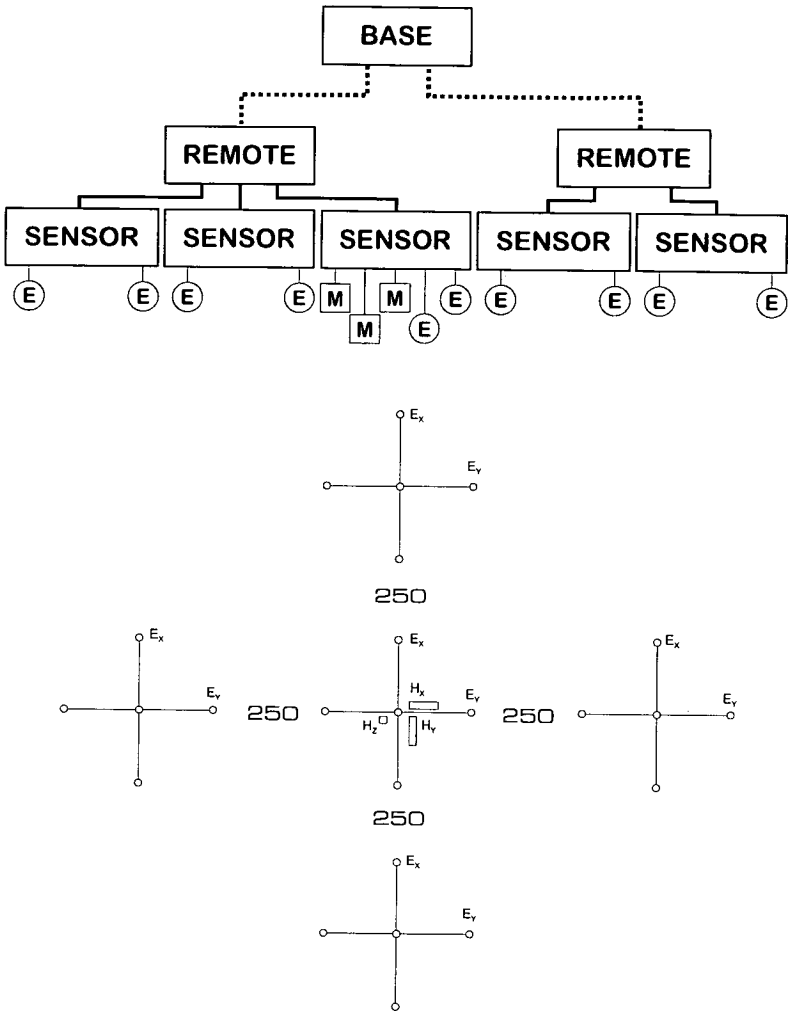

Figure 4.5: Five Component MT plus Four Telluric Stations

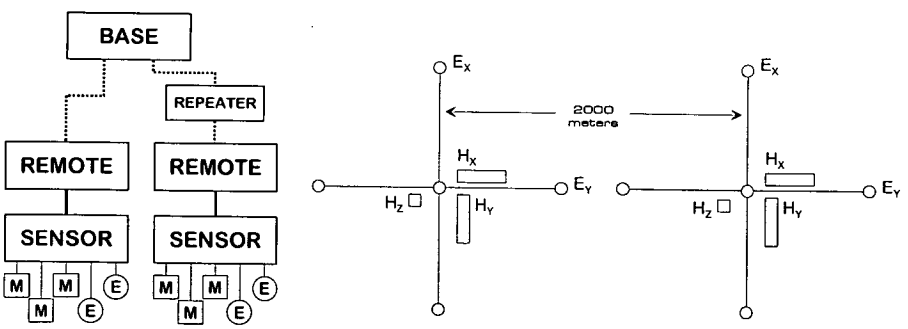

Figure 4.6: Two complete Five Component MT configuration

4.6 A Test for Seismic Applications

Although SPAM Mk-III has been tested widely in Magnetotelluric applications, it has not been used so far in Seismology. To find out the compatibility of the equipment hardware (mainly the sensor boards) with some seismic sensors, two experiments have been carried out in the laboratory.

The first experiment consists in connecting to the equipment four geophones approximately 1m apart, mounted in a wooden made base. The seismometers are connected to the Sensor Box by single wires and no additional hardware is required. Sensor, Remote, Base Box and a portable computer are connected in the same way as they are for magnetotelluric applications. The setup is shown in figure 4.7. An event is created by hitting the wooden base's edge with a hammer at 2m distance from the nearest seismometer (G1).

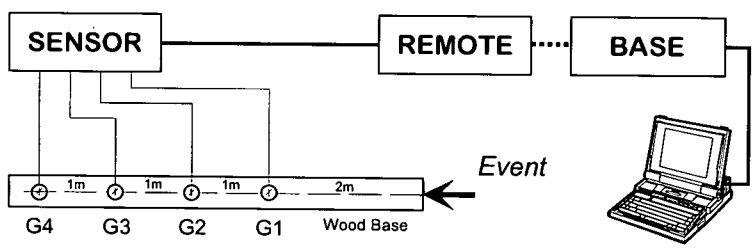

Figure 4.7: Experiment with SPAM Mk-III and Geophones

The mechanical wave propagates along the base and reaches sequentially geophones G1, G2, G3 and G4. The time-varying signals measured by the seismometers are conditioned (analogue and digital domain) and displayed on the Laptop's screen. There is a progressive attenuation in the original amplitude of the mechanic wave and measured respectively by the seismometer closest to the event (G1) and sequentially by G2, G3 and G4, as shown in figure 4.8.

The second experiment has a similar equipment setup. The geophones are replaced by three Willmore Mk IIIA seismometers deployed on the floor approximately 10cm apart (see figure 4.9). An event is created approximately 5m from

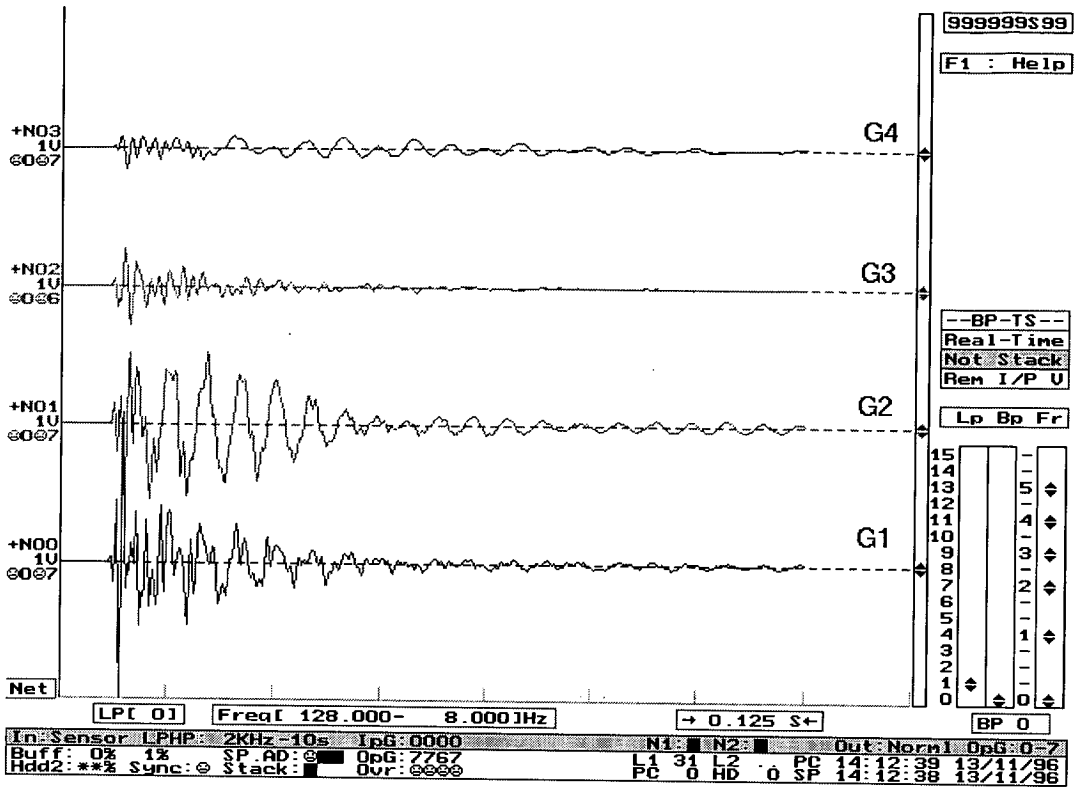

Figure 4.8: Time-series - Geophones

the seismometers and the time-varying signals measured by the sensors and processed by the equipment are shown in figure 4.10.

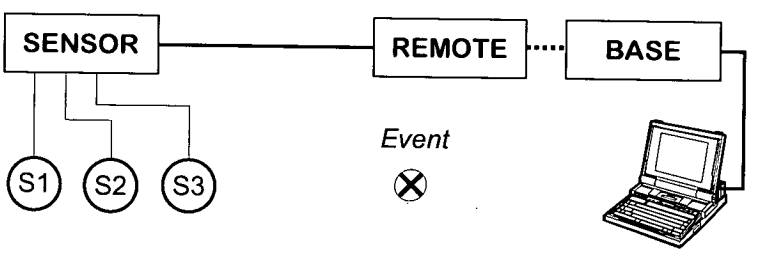

Figure 4.9: Experiment with SPAM Mk-III and Willmore MK IIIA Seismometers

The aim of these experiments was to verify whether the equipment is able to acquire data from two different types of seismometers without additional hardware. Tests suggested this is possible because the response to events of both types of seismometers were detected, processed, saved and displayed properly by the

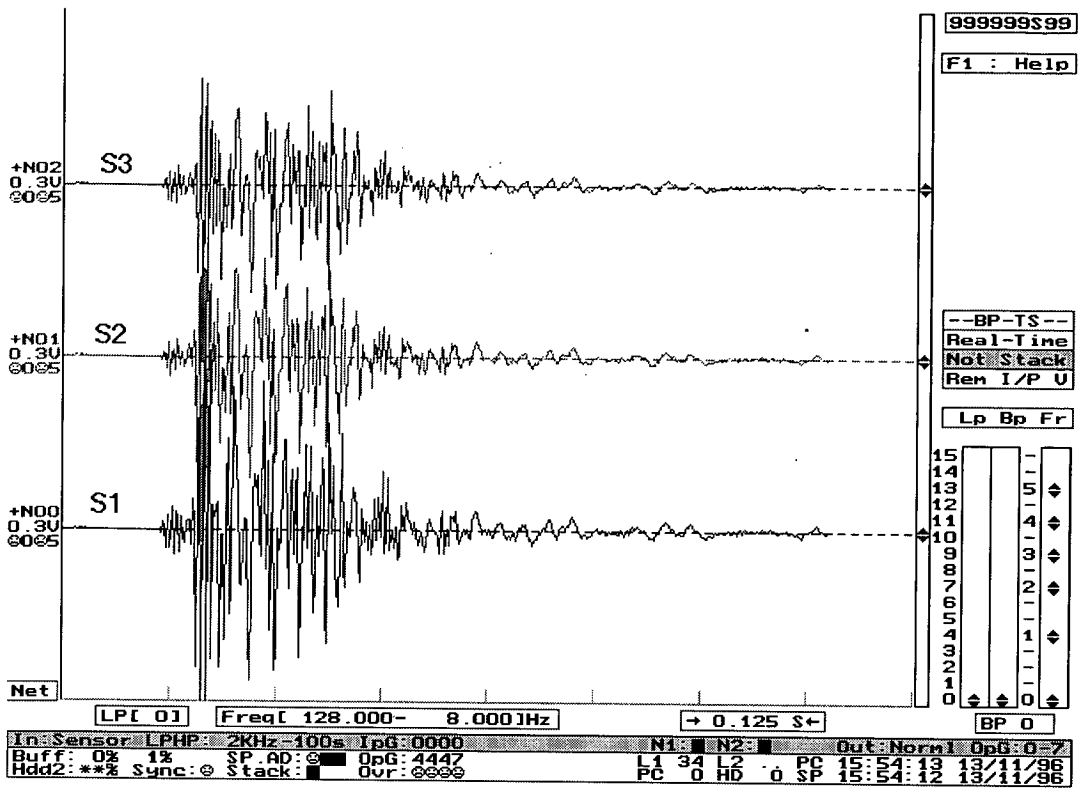

Figure 4.10: Time-series - Seismometers

equipment. However, a more comprehensive and detailed experiment in the field would be useful to evaluate more accurately these possibilities. This will answer questions like the amplification required by each type of seismometer, the type of filtering appropriate, the effect of signal saturation and probably others risen by seimologists. At the moment, there is no software for seismic analyses but the time-series can be recorded continuously for further processing..

4.7 Conclusions

The first field work with the new equipment was carried out in July 1994 in an audiomagnetotelluric investigation of the Southern Upland Fault - Scotland (Ritter 1995). The equipment proved very flexible and reliable. The set-up and operation was simple and the real-time analysis very useful in determining the site

quality in terms of noise. Since then SPAM–Mk III has been used by students in the University of Edinburgh and by scientific groups elsewhere. The Geophysical Equipment Pool of the Natural Environment Research Council owns two systems that can be used on a loan basis by the scientific community. There are three systems running in Germany at the GeoForschungsZentrum Potsdam, Technische Universität Berlin and the Johann Wolfgang Goethe-Universität Frankfurt am Main.

The modular concept on which the design was built allows the hardware to be upgraded as soon as new components or improved versions of the previous types become available. The present internal mass storage capacity is three times bigger than the first release and there is no doubt this is a continuing trend. The digital communication speed may also be improved. In terms of software improvement is always possible. As an example, data acquisition software is being improved frequently and new facilities for calibration and system management are incorporated. Multi-remote synchronized operation is now possible. However, there is much more to be done. For instance, external time synchronization by GPS (Global Positioning System) is essential for some applications. New analyses and modeling methods could be included. Surveys at shallower depths are becoming more and more common for archeology and environmental sciences and the equipment can be applied maybe without any implementation. Seismic applications is another field where the equipment can be used but so far it has not been implemented. SPAM–Mk III development cannot be considered finished. Actually, it is a continuous process.

The following chapters will explain more about the equipment. The three basic modules and the sub–modules will be described in detail. Being coherent with the modularity concept, modules and sub-modules will be treated like a block. The electronics will not be described in this thesis. However, some electronic theory and concepts will be mentioned whenever they are considered relevant to the topic. Operational procedures will be explained only when absolutely neces-

sary. My point of view is that it is important to explain the concerns related to the design of the equipment rather than its operation. The SPAM–Mk III User Manual (Ritter, Ritter, et al.) is a complete operation guide of the equipment and also includes the circuit diagrams of all available modules.

CHAPTER 5

The Base Box

5.1 Module Overview

The Base Box controls the whole network of Remote and Sensor Boxes and performs the highest-level data processing. A PC compatible portable computer must be connected to the Base for software loading and data visualization, acting as a computer terminal. The portable computer can be disconnected after the set-up stage leaving the system in "stand alone" operation and reconnected again without interrupting the automatic data-acquisition and analysis. The communication between the Base and the external computer is made through a bidirectional parallel port. Figure 5.1 shows the Base Box's block diagram and connections including the external portable computer.

The Base incorporates a high capacity and low-power hard disk drive where the acquired time-series are stored. An external SCSI[1] connector is available and may be used, for instance, to dump data in the field from the internal to an external mass storage device.

The data transfer between Base and Remote Boxes is accomplished through external communication links (see page 75). However, the system provides fa-

[1] Small Computer System Interface

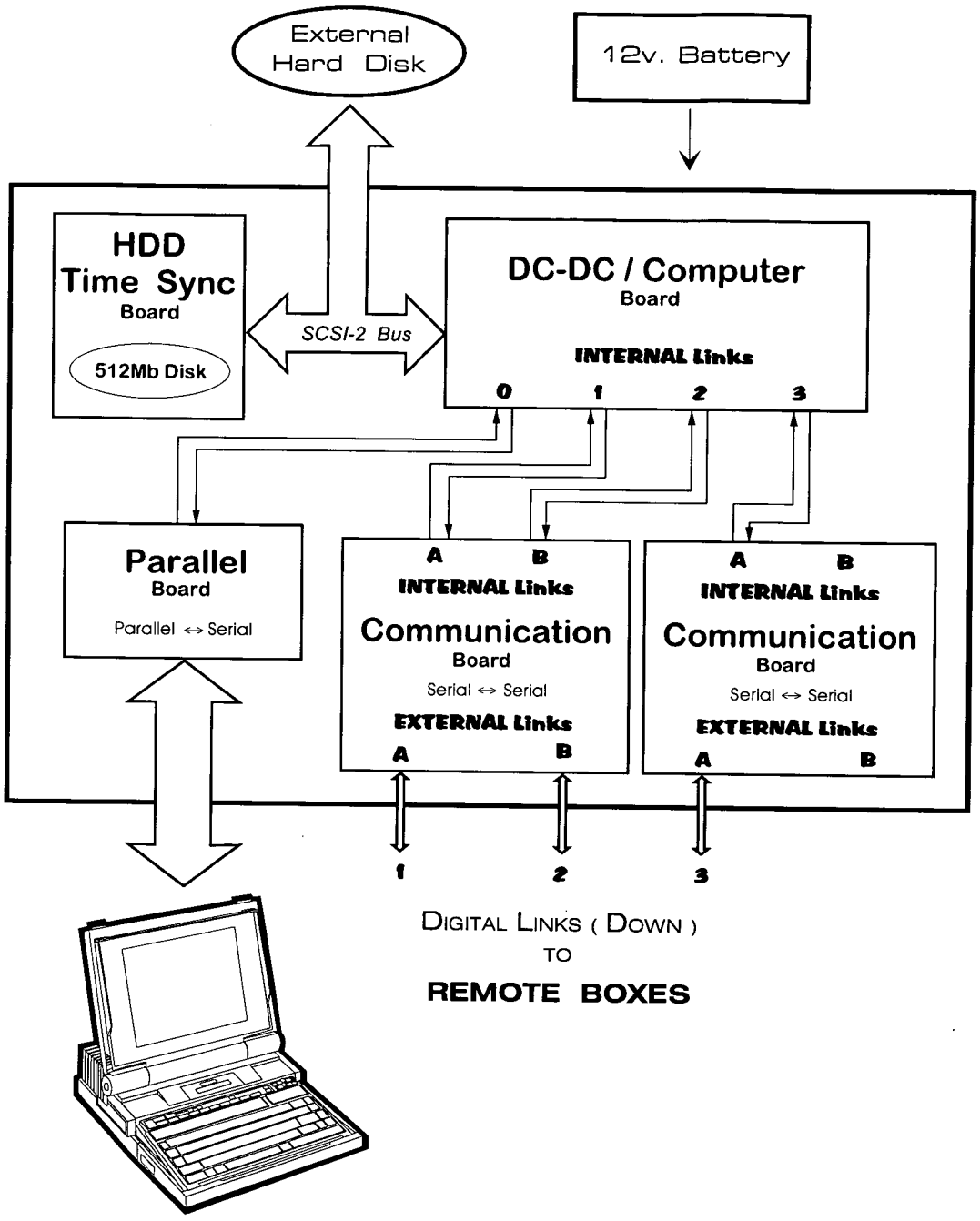

Figure 5.1: Base Box

cilities for direct connection between system control lines as explained in section 5.9. The communication media between the Base and the Remote modules is a twisted pair digital cable. Distances up to 500 meters can be covered without signal regeneration. A digital Repeater Box is needed between 500 meters segments

for longer distances. Field works have been carried out with 1500 meters distance between Base and Remote without any interruption or data integrity loss (Ritter 1995). Section 5.8 explains some digital signal transmission fundamentals and the reason why signal regeneration must be applied for long distance communication. Theoretically any number of Remotes can be connected to the Base. The practical limit is imposed by the processor's speed and the operation mode. At the moment, three Remote boxes operating in either Short-Period or High-Frequency mode can be connected, for instance, for remote-reference magnetotelluric data acquisition.

The Base Box is powered by an external 12V battery and the power consumption is less than 5 watts.

5.2 Software Implementation

The software implementations residing in the Base Box are:

- Network configuration determination
- Network bootstrapping
- Network monitoring and testing
- Network absolute or relative timing synchronization
- Terminal input and output
- Internal and external SCSI disk input and output
- Real-time time-series graphical display
- Real-time frequency spectra graphical display
- Global data analysis
  - Combining multi-sensor results

- Application of quality rejection criteria
- Full cross-spectral analysis
- Impedance tensor stacking
- 1-D transformation
- Comprehensive result plotting

5.3 Global Positioning Receiver

Geophysical applications like magnetotelluric remote reference and seismic require synchronous data acquisition based on an accurate time reference. SPAM Mk - III incorporates a compact, lightweight and low-power consumption (1.1 W) MOTOROLA ONCORE GPS receiver using a low-profile, active microstrip patch antenna, designed to bring GPS technology to special applications (see reference MOTOROLA-1995). The GPS receiver supplies autonomous position, velocity, heading, satellite tracking status and time information in three different, user selectable I/O protocols. SPAM Mk-III uses Motorola Binary Format which provides a more comprehensive set of commands.

The NAVigation Satellite Timing And Ranging (NAVSTAR) GPS is an all weather, radio based, satellite navigation system that enables users to accurately determine 3-dimensional position (within 25 meters), velocity and time. The overall system consists of three major segments: the space segment, the ground control segment and the user segment.

The space segment is a constellation of satellites operating in 12-hour orbits. When completed, this constellation will contain 21 satellites in six orbits. The ground control segment consists of a master control center and a number of widely separated monitoring stations. The ground control network tracks the satellites, precisely determines their orbits, and periodically uploads ephemeris correction and other system data to all satellites for retransmission to the user segment. The

user segment is the collection of all GPS receivers and their support equipment. The GPS receiver's position is determined by the geometric intersection of several simultaneously observed ranges (satellite to receiver distances) from satellites with known coordinates in space. The receiver measures the transmission time required for a satellite signal to reach the receiver. Transmit time is determined using code correlation techniques.

NAVSTAR satellites carry extremely accurate atomic clocks and broadcast coherent simultaneous time signals which are decoded by the GPS receivers. The decoded signal are compensated for cable delays and converted to a 1Hz pulse signal whose the raising edge can be used as the absolute time reference within 130 nanoseconds accuracy. This is the main feature for applications requiring accurate time synchronization.

In addition to time-synchronization, SPAM Mk-III software interprets and

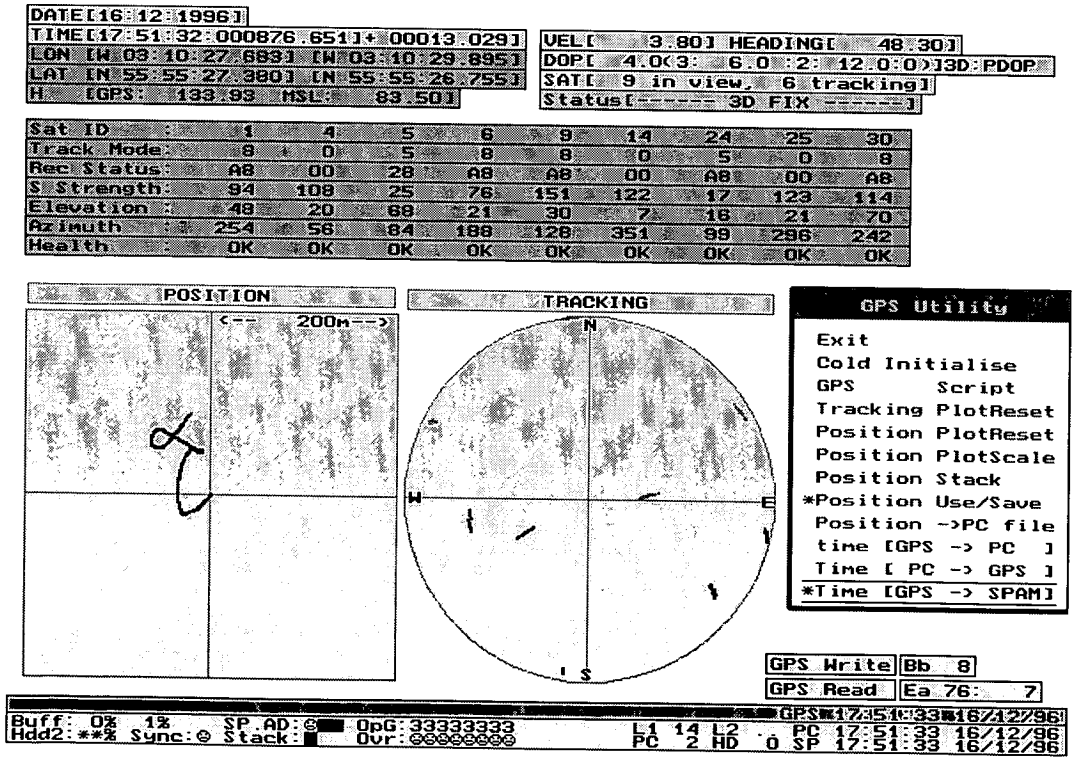

Figure 5.2: SPAM Mk-III GPS Screen and Time-Synchronization Menu

displays most of information delivered by the GPS receiver and provides a menu for the system synchronization based on GPS 1pps time-reference signal (see figure 5.2). The figure shows information about the satellites in view and being tracked (in this case 9 and 6 respectively), a graphic indication of the position on these satellites (TRACKING), the absolute time, longitude, latitude and altitude of the receiving station. Because the receiver is stationary, the line in the POSITION graphic window represents the error of the positioning system. On the right-bottom corner are displayed: the GPS time, the portable computer time and the data-acquisition time in the Remote Box (SP). These times are identical which means that the system has been synchronized already. The menu on the right guides the operation from the initialization to the system synchronization and also allows the POSITION and TRACKING windows to be controlled.

The GPS Serial board (see section 5.6 and figure 5.8) is the hardware interface which integrates the GPS receiver into the equipment as shown in figure 5.3. This board uses the third internal link on the DC/DC Computer board which can be used alternatively for connecting an additional Communication Board as shown in figure 5.1.

5.3.1 System Time Synchronization

SPAM Mk-III provides network time synchronization at two different levels of accuracy as shown in figure 5.4. The signal which performs this synchronization is the one second rate pulse transmitted from the Base to all Remotes connected to the network through a dedicated digital communication line. The reference signal (1pps) can be derived either internally from the 10MHz crystal system time base (see section 5.5.2) or provided externally by the GPS receiver. Thus yielding two different levels of synchronization: Internal (relative) and External (absolute). Internal mode provides network synchronized data acquisition, however the whole network drifts continuously related to the absolute time at a rate proportional to the stability of the system time base crystal (usually better than one part per

million). External mode provides globally synchronized data acquisition based on the absolute time received by the GPS. The use of the GPS system as an absolute time reference allows a global-networked, simultaneous, and accurately synchronized data acquisition.

Figure 5.5 shows the GPS based synchronization timing sequence performed in the system. During the system initialization the Base sends to all Remotes connected to the network a command to stop the data acquisition and request the time for the next incoming second from the GPS receiver. The time is received within 10 to 100ms after the one second pulse due to delays caused by hard-

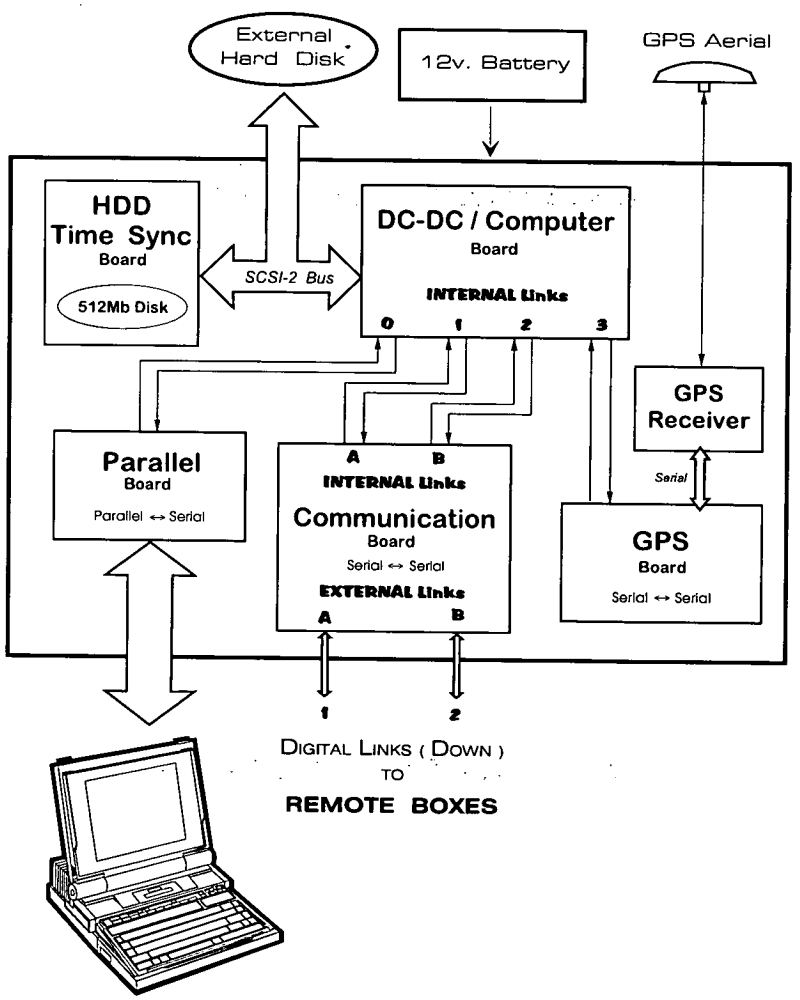

Figure 5.3: Base Box and integrated GPS facilities

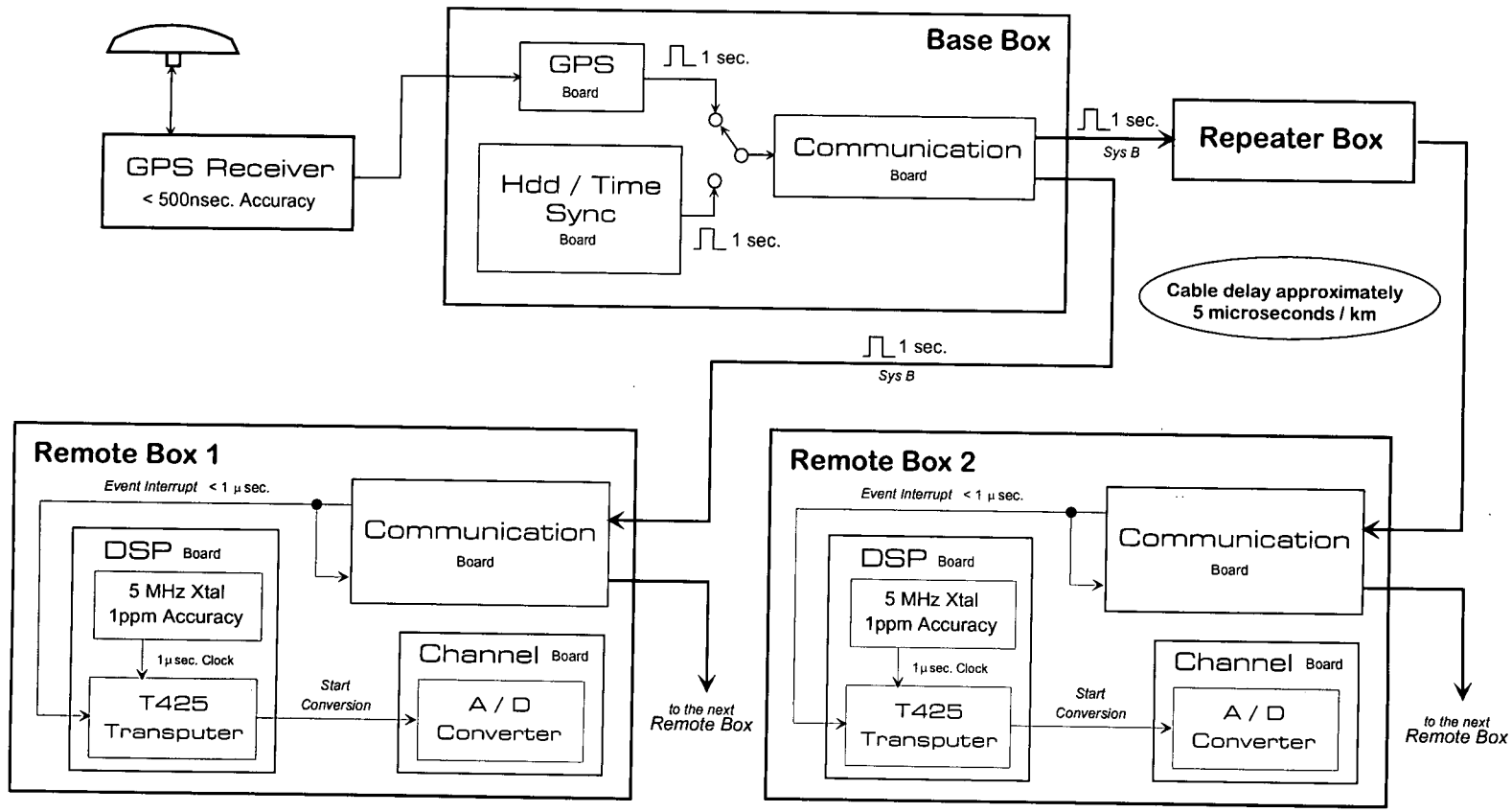

Figure 5.4: System Time Synchronitzation

ware (interface communication) and software (I/O operations). After receiving the correct time, a command is sent to the Remotes to wait for the next 1pps synchronization pulse to start the analog to digital conversion. When it occurs, the data acquisition re-starts synchronously with the 1pps leading edge and an acknowledge pulse is sent from the Remotes to the Base. The data acquisition is then re-synchronized continuously at a 1 second rate.

There are additional parameters that have to be taken into account if a precise time-synchronization is required. The first is the stability of the crystal in the Remote Boxes (usually 1ppm). The software uses the reference edge of the 1ppm pulse to adjust the *free-running* software clock derived from the crystal at every second. Between synchronization the data acquisition is controlled by this crystal which adds an instability of $1\,\mu s/s$ relative to the reference. The second is the digital cable which delays the sync pulse proportionally to its length. The latter is fixed and constant ($\approx 5\,\mu s/km$)

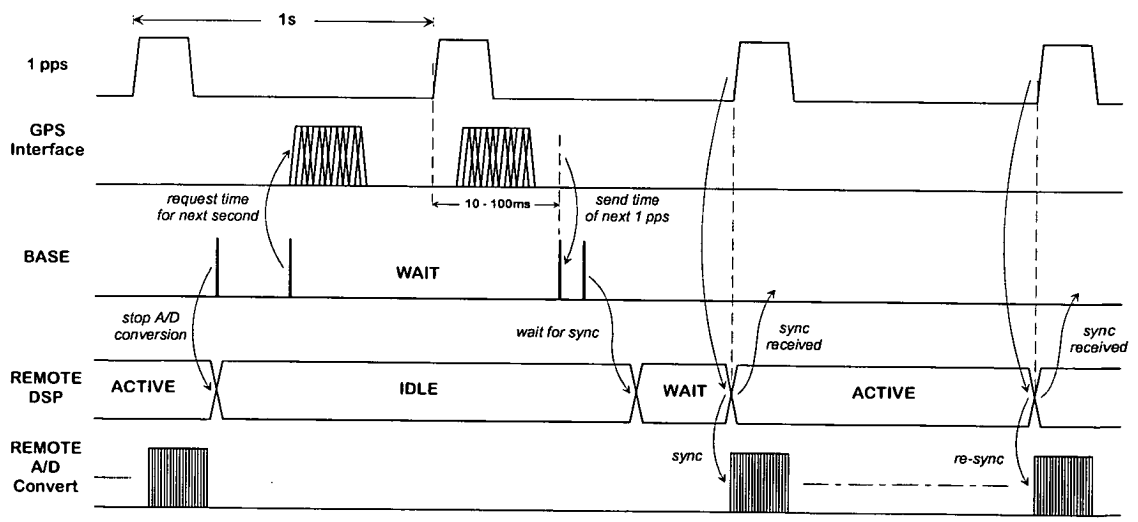

Figure 5.5: System Synchronization - Timing Diagram

5.4 DC-DC/Computer Board

The DC-DC/Computer board is the heart of the equipment. It contains the computational module, a crystal oscillator and related circuitry to provide the system synchronization time-base. The module also supplies the power requirements for all boards in the Base Box and logical circuitry to interface Transputer and backplane bus. The block diagram is shown in figure 5.6.

5.4.1 SCSI Transputer Module (SCSI-TRAM)

Transputer Modules (TRAM) are printed circuit boards based on Transputer devices that include additional features for specific applications, like graphics or interfacing. The SCSI TRAM, which is plugged onto the DC-DC/Computer board, includes facilities to interface the system and SCSI devices. The sub-module comprises a T805 32-bit Transputer running at 25MHz clock, 32-bit DMA SCSI processor, SCSI timing clock, 4Mbytes DRAM and four standard 20Mbits/s serial communication links. The interface facilities included are synchronous data transfer at 10Mbytes/s, single-ended connection, optional parity, socketed terminators, optional fused terminator power, active terminator option, configurable SCSI ID and 10kV ESD[2] protection. The module power consumption is 2.5W maximum.

At the start-up a boot file is transferred from the portable computer to the system memory. The Transputer runs the initialization software, loads all transputers connected to the system and takes control of the network operation. From that stage on the portable computer is no longer essential since the data acquisition and storage are fully controlled by the TRAM. The main features of this module are associated with the software implementations, which were described in section 5.2.

[2]Electrostatic Discharge

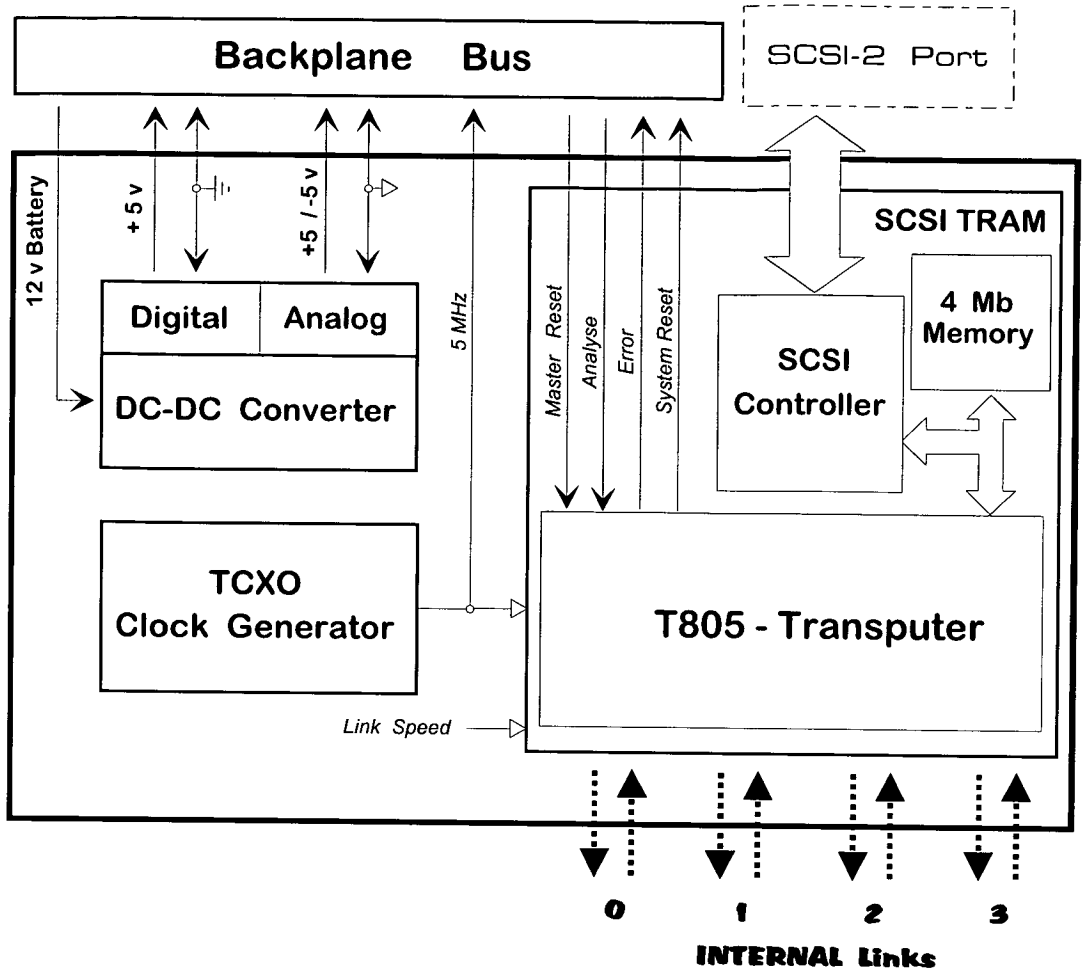

Figure 5.6: DC-DC/Computer Board

5.4.2 Power Supply

The board lay-out allows two independent power supply sections: analogue and digital. The digital section supplies only +5 V/0.9A maximum and consists of a 5V Step-Down, Current-Mode, DC-DC converter. The measured efficiency is 89% at 0.5A and 83% at 0.9A. The high current is due to the computer module which is the thirstiest power component of the system. The analogue section supplies ±5V/125mA and consists of a 5V CMOS, Step-Down, Switching Regulator for the positive supply and a subsequent -5V, Inverting, Current-Mode DC-DC converter. The efficiencies are 85% for the positive and 80% for the negative supply. Analogue and Digital power supply sections can be used independently.

For instance, all circuitry in the Base Box is digital and the analog power supply is not used. On the other hand, for the Remote Box circuitry both analog and digital power supplies are necessary. However, the printed circuit board is the same in both cases.

5.5 HDD/Time Synchronization Board

This board provides a physical environment required for connecting a SCSI compatible hard disk drive like: power, SCSI identification settings and signal connections. An additional function is to generate a pulse signal for synchronizing the data acquisition in all Remotes connected to the Base. Figure 5.7 shows the board's block diagram.

5.5.1 Hard Disk Drive

The hard-disk drive to be used on this board must be small, with low-power consumption, a SCSI interface and high storage capacity. The physical dimensions are important because the driver must fit within a standard equipment board's size and enclosure. The option is to use 2.5" drives which are widely used in portable computers. The low-power consumption is essential to match the equipment's characteristics and to extend the battery life during field-works. The typical power consumption during Read, Write and Seek operations is 1.4W and the maximum is 2.75W which is almost half of the total Base power consumption. The SCSI interface is very well known for its high speed data transfer rates and peripheral interconnection facilities. The disk drive is connected to the DC-DC/Computer board that incorporates a SCSI microcontroller. The peripheral identification (ID) is set by a switch at the board's edge.

The disk capacity has been improved since the first version without jeopardizing the power consumption characteristics. Such drivers are available in 127,

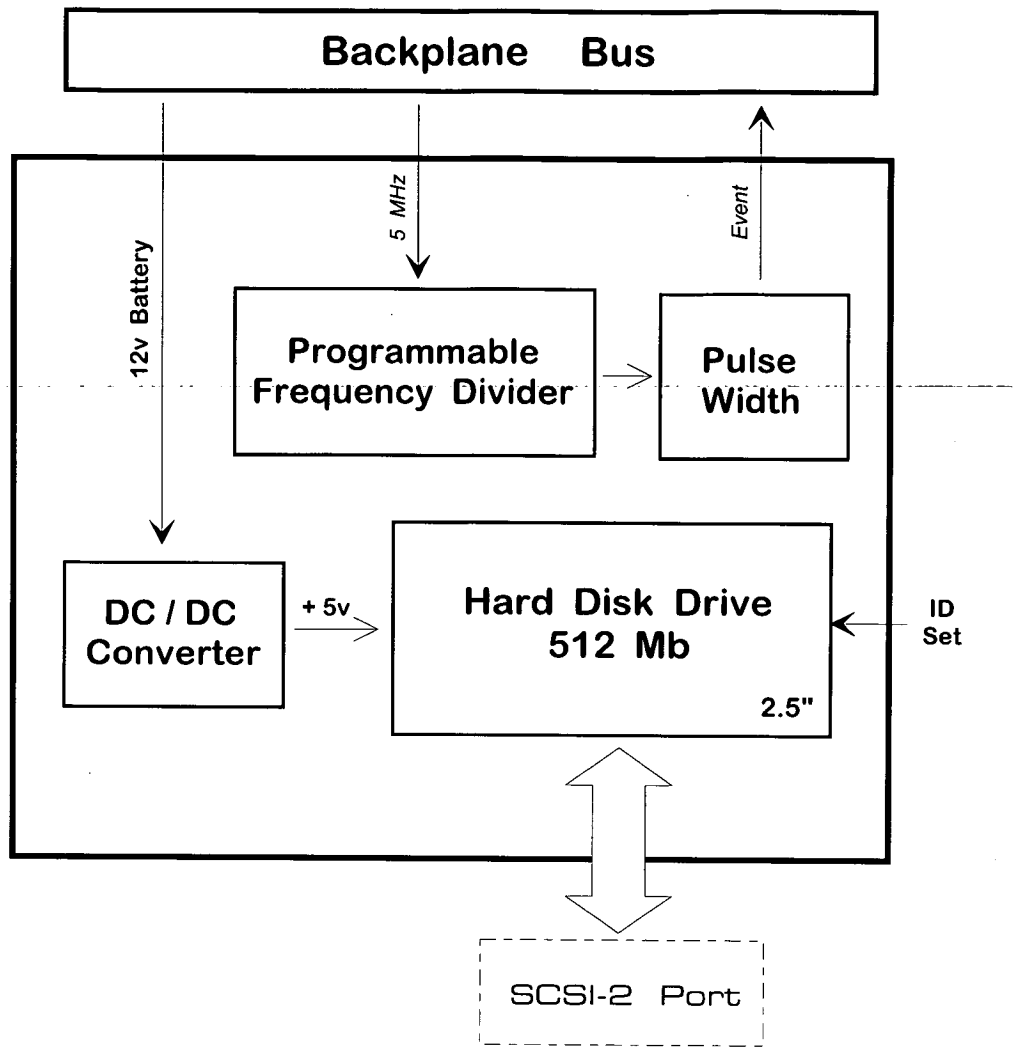

Figure 5.7: Hard-Disk Drive/Time Synchronization Board

170, 256, 341 and 514 Mbytes capacity. High capacity disks are important for multi-channel and higher frequencies data acquisition where a huge amount of data is stored for further processing. For shorter periods a lower capacity disk would be enough. A new 2.6Gbytes hard-drive with the same physical and electrical characteristics as the present ones has been announced recently and might be available shortly. The upgrade may be straightforward since hard disks with same characteristics but different capacities can be swapped without any additional hardware modification. The board also incorporates an independent +5 V power supply exclusively for the "on-board" disk drive. The circuit consists of

a step-down switching DC-DC converter that takes the power straight from the battery to avoid load regulation problems on the remaining boards and to allow a second hard drive in the Base Box.

If properly enclosed, the board can be used as an external stand-alone hard drive. This portable unit requires only a 12V battery input and can be connected through the SCSI port to the Base Box. The system provides the software necessary for managing both of internal and external units including standard hard disk and files operations like formatting, copying, erasing, etc. The main use for the external unit is to dump data from the internal drive, creating disk space for further data acquisitions.

5.5.2 Internal time synchronization pulse

The HDD/Time synchronization board generates an alternative timing reference derived from the system clock to synchronize the data acquisition in a local network. The 5MHz system clock signal available at the backplane bus is divided by a CMOS programmable Divide-by-"N" Counter device. Due to a component limitation ($N_{MAX} = 9999$), two stages are required to achieve 1Hz from the 5MHz system clock. The circuit also delivers 10 seconds and 2048Hz signals that can be used exclusively. The first can be used for synchronizing the internal clock of all modules connected to the network. The second was an attempt to get a periodic signal with the frequency as close as possible to the signal sampling rate (2048Hz) to attempt a direct synchronization of the A/D converter. However, the closest frequency that can be achieved with the available hardware is $5\text{MHz} \div 2041 = 2048.34\text{Hz}$ which is not accurate enough for some applications.

The output pulse shape from the counter has to be modified for compatibility reasons, regardless of the frequency. The final $1\mu s$ pulse width is given by a monostable circuit that also provides different pulse polarities, if required.

5.6 GPS Serial Board

The GPS serial board (figure 5.8) provides an interface between the GPS receiver module and the Transputer module on the DC/DC Computer board. The full-duplex serial data communication provided by the GPS has to be transformed into the high speed internal link protocol to be compatible with the Transputer communication standard. A programmable Universal Asynchronous Receiver Transmitter (UART) converts data from serial to parallel at the GPS side and a link adaptor re-converts the parallel data into internal link serial. There are two independent timing signals. The first is generated by a programmable clock which controls the communication speed between GPS receiver and the UART (9600 bits/s) and the second is the system time clock, from the back plane, which sets the internal link speed. Both chips are initialized simultaneously by a Master Reset pulse asserted from the backplane. Additional communication parameters like number of bits per character, parity and number of stop bits can also be changed. The board also provides suitable interface between the decoded 1pps signal generated by the GPS receiver and the system *Event* line to be used as the main time synchronization reference (as explained in section 5.3.1). An independent step-down DC/DC Converter supplies the power requirements to the GPS receiver (+5V/1.1W)

5.7 Parallel Interface Board

The communication between the equipment and the external computer is performed through a bidirectional parallel port. The parallel board provides the interface and the protocol required by the internal serial communication links and the parallel port. Figure 5.9 shows the board's block diagram

The hardware at the equipment side is quite simple. There is one link adaptor to convert information from serial to parallel, time and control logic circuitry. Presently, new computers have been released with parallel ports that can be configured in four types, as summarized in table 5.1. To communicate properly with

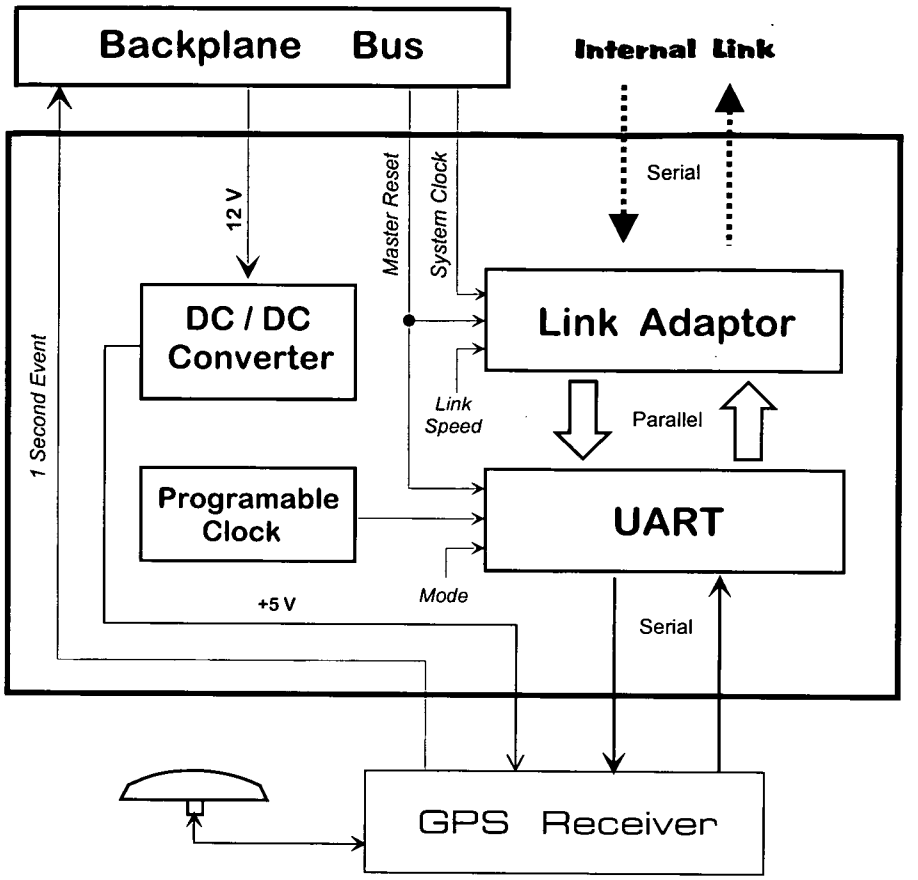

Figure 5.8: GPS Receiver Interface / Serial Board

the equipment, the computer's parallel port should be configured for bidirectional mode. The improved bidirectional port settings (EPP) should work since they are supposed to be compatible. This assumption is not always correct. We have tested computers from different manufacturers and the results were unpredictable. Only the bidirectional parallel port seems to be standard and compatible amid these machines. An additional difficulty on designing the parallel port is the lack of information related to the computer's hardware. This sort of information is not released by the suppliers, even upon request.

The parallel port speed is an important parameter to consider, since it will determine how fast the communication between the equipment and the external computer takes place. There are basically three different system operations that depend on the parallel port speed.

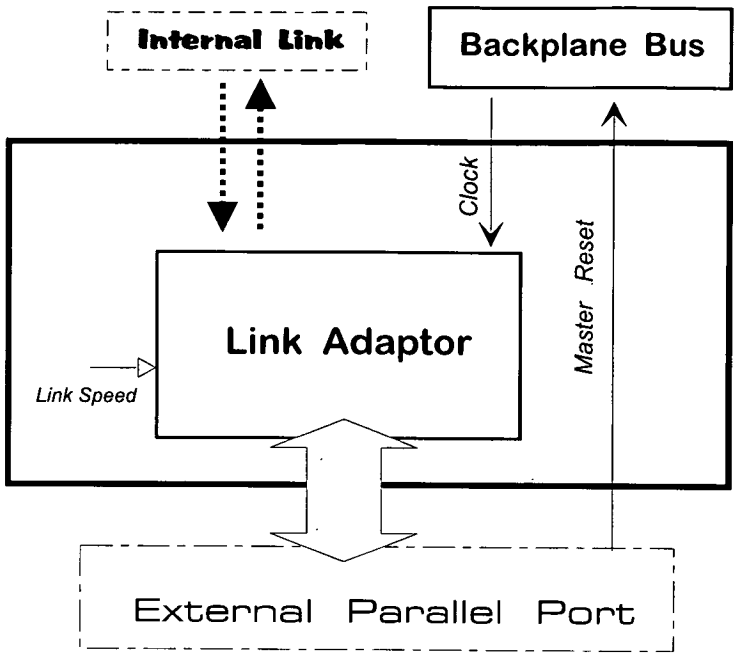

Figure 5.9: Parallel Interface Board

Type	Description
Normal/Compatible	Output mode. Data flow from the computer to the external peripheral only (unidirectional). It is used for most devices, such as parallel printer
Bidirectional	Full communication. Data flow in both directions to improve data transfer rate such as with network parallel adapter and SPAM-3
EPP Enhanced Parallel Port	Improved bidirectional communication. It takes advantage of the functionality of EPP devices, such external floppy, CD-ROM and hard disks
ECP Enhanced Capabilities Port	Improved bidirectional communication. It will take advantage of the ECP devices when they become available

Table 5.1: Computer Parallel Port Types

SPAM → PC memory

is the operation that dumps the data from the equipment into the computer memory and then to the screen. It happens every time the screen is updated.

SPAM → PC file

is the operation that dumps the data from the equipment into the computer's disk. This operation takes place when processed data is saved on a file.

PC file → SPAM

is the operation that transfers data from the computer into the equipment internal hardware. That is the "boot" speed, since at the start-up, a file stored on an external PC is loaded into the equipment memory.

These three speed values in Kbytes/s are displayed, among others, at the system "boot-up".

The parallel port speed cannot be changed because it is a function of the external computer processor's clock speed. Table 5.2 shows some parallel performances and makes clear that relationship.

	Processor type/Clock speed (MHz)			
	486/30.0	486/37.5	486/75.0	Pentium/100
PC file → SPAM	40.23	43.77	71.64	105.71

Table 5.2: Parallel Port Speed (kbytes/s)

However, these figures may change considerably if the computer has a built-in power manager facilities. In order to keep track of the power resources, they interrupt the processor while in operation, slowing down all other activities.

As the parallel port speed increases, the physical connection between the equipment and the computer becomes more critical. The cable quality and length affect the signal shape and attenuation and cables shorter than 1m. should be used. All concepts related to high speed digital interfacing must be applied to achieve reliable and stable communication.

5.8 Digital Cable Communication

The advantages of digital over analogue communication and the reason why a cable was chosen to be the digital communication media between SPAM-Mk III boxes were explained and justified in section 4.4. Before describing the module designed for the communication task, I believe it is useful to explain the inherent constrains in digital cable communications.

5.8.1 The RS-485 Digital Communication Standard

Communication standards provide an interface to facilitate communication between equipment from different suppliers. There are several standards available for different data rates and cable lengths. By considering the equipment's communication characteristics and the large noise immunity required, the RS-422/485 Balanced Voltage Digital Interface standard was the natural choice. RS-485 is an upgrade to RS-422. The signal levels are the same but it allows half-duplex multi-point communication.

There are three major controlling factors in a balanced voltage digital interface:

1. The data rate (or modulation rate)
2. The characteristics of the Driver and Receiver components
3. The cable length

The maximum modulation rate for data, timing or control signal specified by the RS-485 standard is 10Mbits/s. The maximum external data communication rate in the equipment is 5Mbits/s, within the standard.

The voltage digital interface devices meeting the electrical characteristics of this standard do not need to meet the entire specified data rate and may be

designed to operate over narrower ranges to satisfy specific applications. Characteristics such as internal propagation delay, response time, pulse rise and fall time and skew must be conformed to the maximum specified device speed. There are devices for operation beyond the 10Mbits/s standard limit but the price is a very high power consumption. Low-power devices do not operate at the highest speed and the usual maximum data rate for such components is 2.5Mbits/s.

There is no maximum cable length specified by the RS-485 standard. There are some guidelines with respect to operating distances as a function of modulation rate. These curves are based on empirical data for a well defined cable type and can be seen in figure 5.18 for a 24 AWG twisted-pair cable and a 2.5Mbits/s device. This will be explained in more detail latter.

Even though the maximum cable length between transmitter and receiver is a function of data rate, it is also influenced by the signal distortion tolerance, the amount of longitudinally coupled noise and the ground potential difference introduced between the generator and load circuit grounds.

5.8.2 Electrical considerations

Noise, signal distortion and attenuation are always present in data transmission systems and strictly limit performance. Digital communication by using a simple piece of wire can be accomplished at high speeds for short distances. Over greater distances, certain electrical parameters and limitations of the interconnection medium must be taken into account. It is important to understand the cable effect in order to overcome its limitations whenever it is possible or at least minimize its influence on the system performance.

5.8.2.1 Signal Attenuation

Any data transmission over wire experiences losses and distortion due to distributed parameters along the cable. At a given instant of time, high-frequency

current (i) and voltage (v) waveforms have different values at different points along a transmission line. This variation disallows the use of discrete parameters to represent the overall line. However, by regarding the line as a cascade of unit sections a distributed-parameter model can be created in which each section is represented with lumped parameters of resistance, inductance, capacitance and conductance. The model is represented in figure 5.10.

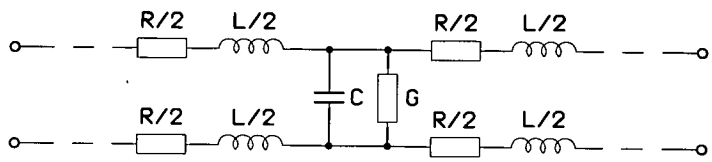

Figure 5.10: Transmission line model circuit

The resistance (R) represents the DC resistance of the cable and the skin effect, which is the tendency of electrons to travel along the surface of a conductor at higher frequencies. The skin effect leads to an increase in the resistance since the effective cross section area used by the electrons at higher frequencies is no longer the total cable section area but only a fraction of it. The series inductor (L) represents the opposition to change in current levels caused by the collapsing and expanding magnetic fields created due to fluctuating current levels. The shunt capacitance (C) is created by the two conductors in close proximity and separated by a dielectric. As the signal frequency increases the capacitive reactance decreases, reducing the opposition to current flow. The shunt transconductance (G) is a function of the dielectric loss of the insulator around each conductor which allows some leakage current passing between conductors. This parameter can be neglected for usual dielectrics. Solving for the ratio of instantaneous voltage and current gives the the impedance Z_0, defined as the *line's characteristic impedance.*

$$z_0 = \frac{v}{i} = \sqrt{\frac{R + jwL}{G + jwC}} \quad (5.1)$$

where

L in henries/unit length
R in ohms/unit length
C in farads/unit length
G in siemens/unit length

For short cables the DC resistance is negligible ($R \rightarrow 0$). The conductance can also be neglected as explained before ($G \rightarrow 0$). Also, for frequencies greater than 100 Kbits/s $R \ll jwL$ and $G \ll jwC$. Thus, equation 5.1 can be rewritten as:

$$z_0 = \frac{v}{i} = \sqrt{\frac{L}{C}} \tag{5.2}$$

The equation 5.2 is frequency independent.

Also, the waveform's propagation velocity $V = 1/\sqrt{LC}$ down the line does not depend on frequency. The propagation delay per unit length is $T = 1/V = \sqrt{LC}$. For the twisted-pair cable used by the equipment the delay is $T \approx 4.5\text{ns/meter}$.

For long cables or low frequencies the approximations are no longer valid, since the DC resistance R is no longer negligible, affecting the propagation delay. In that case, the signal velocity along the transmission media and the attenuation depends upon the propagation constant γ of the line, which is expressed as:

$$\gamma = \alpha + j\beta = \sqrt{(R + jwL)(G + jwC)} \tag{5.3}$$

The real term α is known as *attenuation constant* and represents the rate of the signal's attenuation. The imaginary term β is the *phase constant* and determines the phase velocity. That can be written as $V_p = w/\beta$. The variation of signal velocity with frequency is called *frequency dispersion.*

In practice the attenuation of a particular cable can be determined from a curve of frequency plotted against attenuation, usually quoted per 100ft or 30m.

5.8.2.2 Signal Distortion

As mentioned above, the cable attenuation at any frequency can be found easily by working out some plots. The problem arises when the signal has more than one frequency component. Fourier decomposition shows that a digital pulse-train is an infinite summation of harmonics. Lower-frequency harmonics contribute to the flat top and bottom portions of the pulse train and higher-frequency harmonics

mostly make up the leading and lagging edges. The high frequency components experience minimum delay and maximum attenuation. The low frequency components are subjected to increased delays and least attenuation. The result is that different components of the pulse train arrive at the receiving end at different times and with different levels. The received signal is distorted related to the original signal. That dispersion (Figure 5.11) increases with propagation distance, making the signal recovery and consequent reproduction of data increasingly difficult.

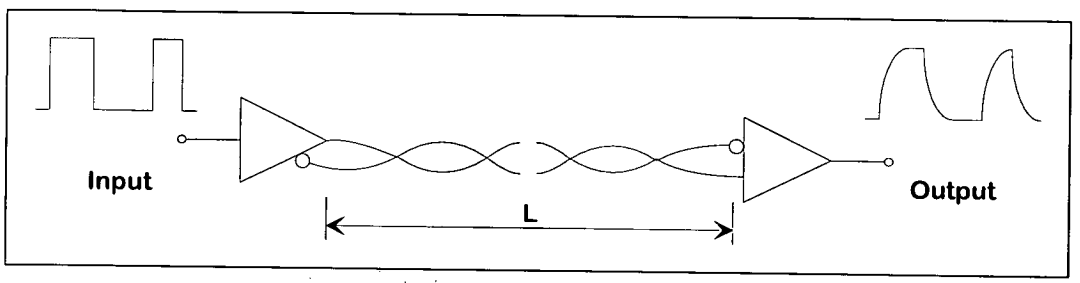

Figure 5.11: Velocity Dispersion Signal Distortion

5.8.2.3 Line Termination

A line termination resistor R_L equal to the characteristic impedance Z_0 absorbs all energy and makes the line look infinite to the preceding sections and no reflections occur. This type of termination is called *DC termination* (figure 5.12).

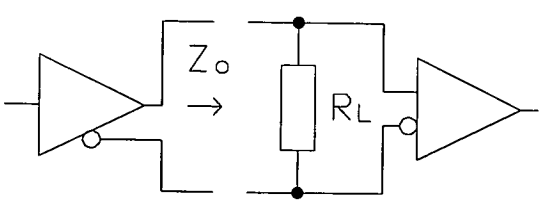

Figure 5.12: DC termination

A mismatch between R_L and Z_0 causes a portion of the incident wave to reflect back down the line, producing distortion in any approaching forward wave. *DC termination* also wastes power, since the load resistor draws current even with no data transmission.

To reduce the power dissipation, which is always important in battery-powered equipment, an *AC termination* can be used. It consists of adding a capacitor to the termination network (figure 5.13). The circuit is open when idle and no current is drained. The value of the capacitance C_L depends on the cable characteristics and the signal speed. However, the presence of a capacitor intensifies even more the signal distortion mentioned in 5.8.2.2.

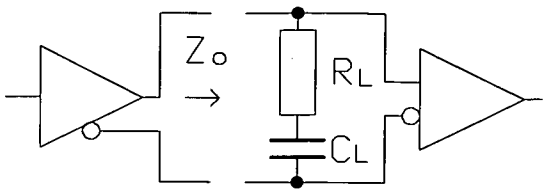

Figure 5.13: AC termination

5.8.2.4 Noise

Noise is generated from a variety of sources and can strongly limit the system performance. Any signals appearing at the receiving end of a transmission circuit that are not due to the input signal are considered as noise. The main source of noise that will affect data transmission systems is ground-loops. Usually receiver and transmitter have independent grounding references and ground-loops occur whenever there is a potential difference between these grounds. In practice, this always happens. Noise generated by ground-loops can be reduced by using differential line communication, involving the use of two signal carrying wires between transmitters and receivers. The receiver is only concerned with the *difference* in voltage between the two wires and the absolute value of the common-mode voltage of the two wires is not important. A change in the local ground potential at one end of the line will appear as an extra change in the common-voltage level of the signals, which the receiver is insensitive to. The same argument is applied to external noise sources and crosstalk interference. They will appear as another change in the common-mode voltage of the signals.

Twisted pair cables used in differential communication have an additional

advantage. They tend to cancel the magnetic fields generated by the current flowing through each wire, thus reducing the effective inductance of the pair.

5.9 Communication Board

The Communication board (figure 5.14) is the interface between SPAM-Mk III Boxes that carry out digital communication, usually Base and Remote. The distance between boxes may vary from a few meters to a few kilometers and the physical channel is a shielded, multi-core, four-pair twisted cable. There are two important tasks performed by the circuitry.

The first is to transform *Link IN* and *Link OUT* from **internal** into **external** links. These two data links perform a full-duplex communication between modules through the Transputers. The transformation consists basically in changing the speed of the data stream. The serial signals from the links are converted into parallel and converted again into serial by two Link Adaptor devices. The serial/parallel conversion enables independent speed settings for internal and external links without jeopardizing the compatibility. The internal link speed can be set to 20 or 10Mbits/s and the external speed set to 1/2, 1/4, 1/8 and 1/16 of the internal speed. At the moment, the equipment works with internal link speed set to 10Mbits/s leading respectively to external link speeds of 5.0, 2.5, 1.25 and 0.625Mbits/s. The available speeds will cope with most cable lengths required for any particular application and site configuration.

The second is to allow direct connection between the Base and the Remote backplane busses through the system links *Sys A* and *Sys B*. The control signals that use these links are Reset and Synchronization but there are facilities on board to select additional ones. The speed of the control signals does not have to be changed and remains the same along the path between backplanes. The typical direction for the system links is from Base to Remote (figure 5.15) but it can be changed if needed.

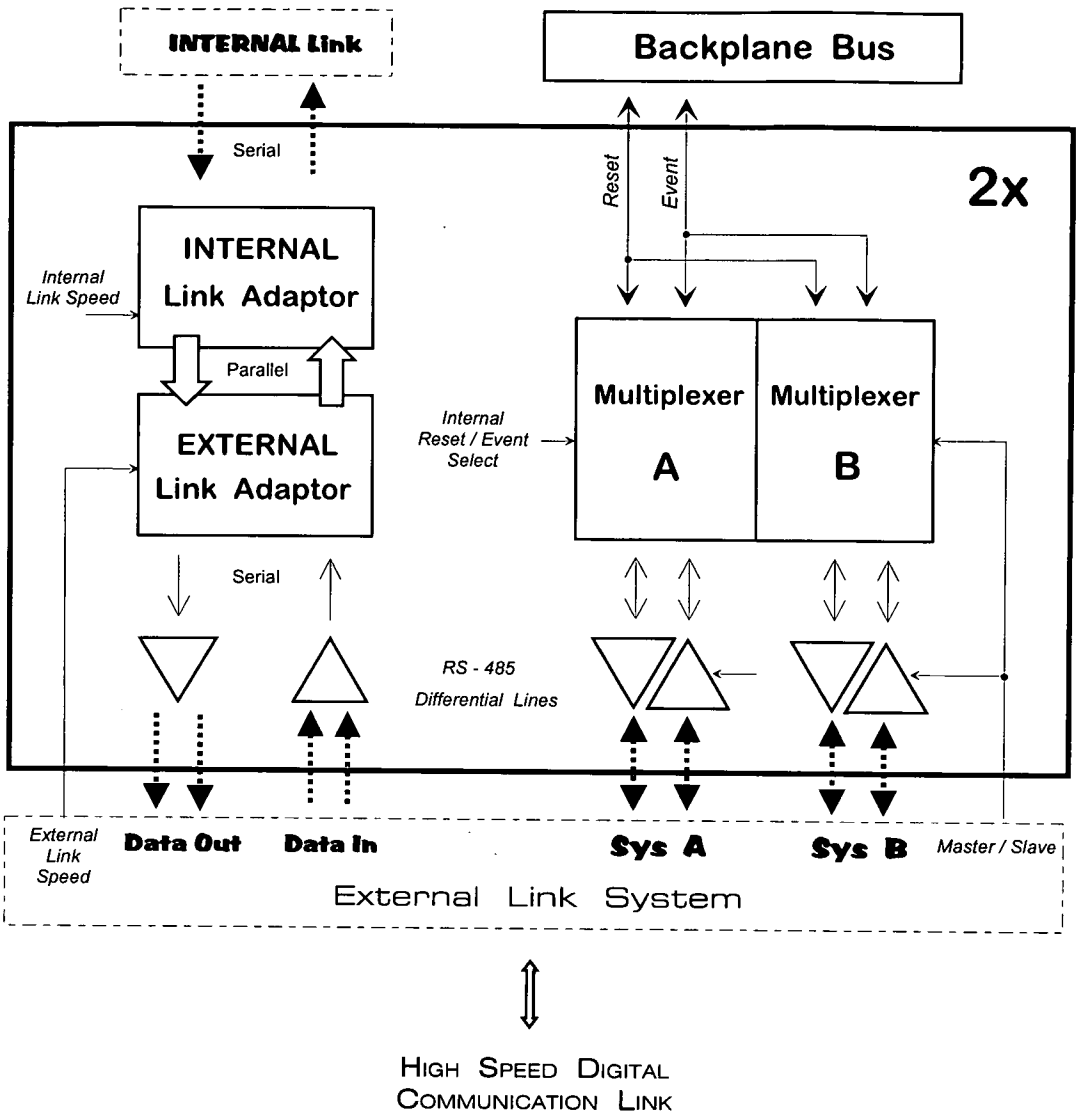

Figure 5.14: Communication Board

Therefore, a complete Link System includes two directional data links *Link In, Link Out* and two bidirectional system links *Sys A, Sys B*. Each communication board contains two identical and independent Link Systems. The communication board also transforms all external links into RS-485 standard for long distance data transmission (see section 5.8.1) and includes circuit protection from electrostatic discharge (ESD). The Schottky diodes used to protect the links from ESD up to 2kV also help to eliminate overshoot on received links.

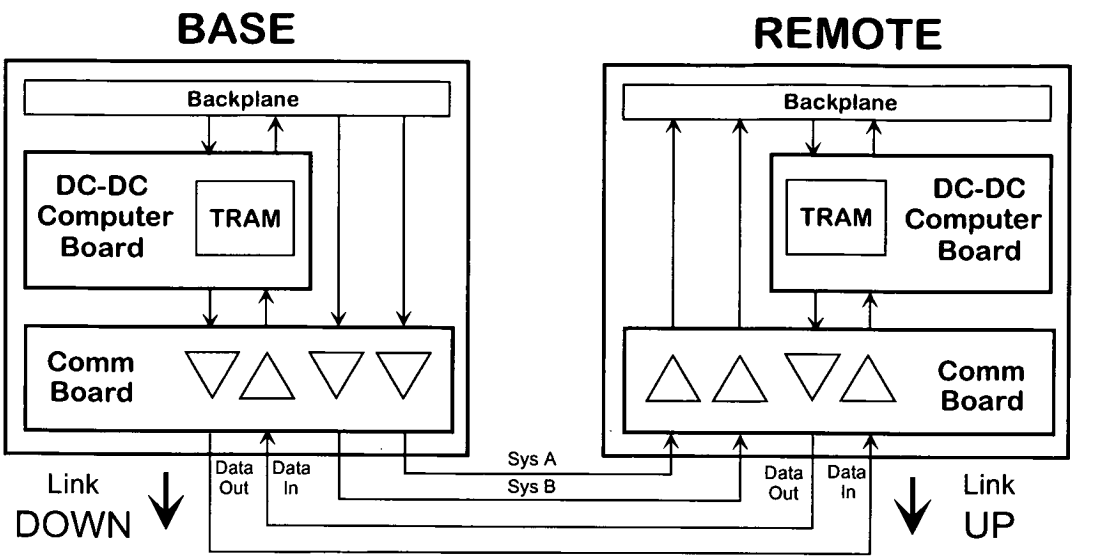

Figure 5.15: Remote and Base connection

The line termination schemes, explained in section 5.8.2.3, are different for system and data links. System links support AC termination since they are usually lower frequencies pulses and even when unterminated the wave reflections and signal distortion are not strong enough to cause instability during data transmission. Data links must use either AC termination for lower speeds or DC termination for higher speeds. In order to take advantage of the hardware and mainly the software the link speed should be pushed to the limit and the DC termination for the data links is essential being the price a higher power consumption.

5.9.1 Data Throughput *versus* Cable length

The data transmission principles and theory explained in section 5.8 allow the system data throughput rate calculation as a function of cable length and link speed. The additional information which is essential to this exercise is to understand briefly the Transputer link operation. Communication across links involves a simple protocol (Figure 5.16).

Each byte is transmitted as a start bit then a one bit, followed by the eight

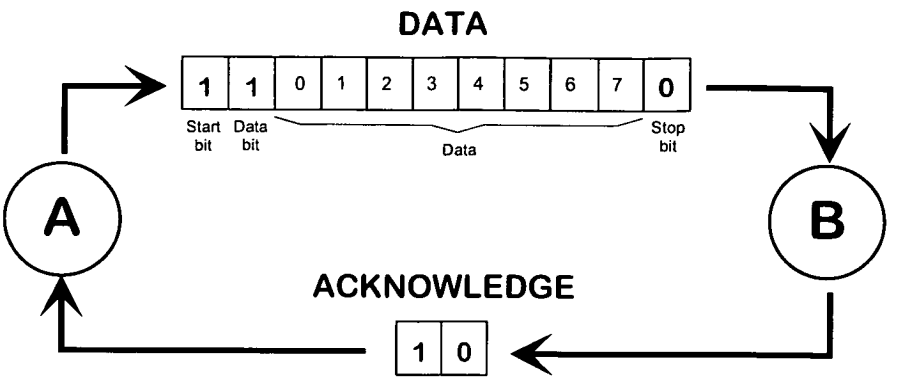

Figure 5.16: Transputer Link Protocol

data bits and a stop bit. After transmitting a data byte, the sender waits until an acknowledge is received. This consists of a start bit followed by a zero bit. The acknowledge signifies both that a process was able to receive the acknowledged byte, and that the receiving link is able to receive another byte.

In the equipment, two more variables must be included in the signal path (figure 5.17). The first is the communication board, which slows down the link speed from between half to one-sixteenth of the internal link speed. The second is the digital cable which delays the signal proportionally to its length . The times involved in the process are:

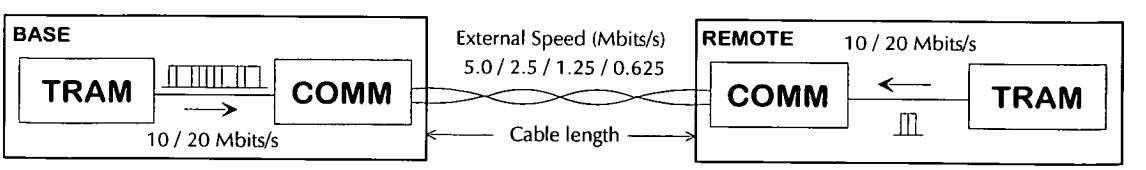

Figure 5.17: Digital Communication Test Set-up

t_{d_i} The internal link delay, which is the time spent by a data and acknowledge packet between Transputer and Communication board in each box and consists of 11+2 bits being transferred at the internal link speed $V_{L_{Int}}$

$$t_{d_i} = \frac{13}{V_{L_{Int}}} \quad \text{where} \quad V_{L_{Int}} = 10\,\text{Mbits/s}$$

t_{de} The external link delay, which is the time spent by a data and acknowledge packet between Base and Remote Communication boards only and consists of 11+2 bits being transferred at the external link speed $V_{L_{Ext}}$

$$t_{de} = \frac{13}{V_{L_{Ext}}} \quad \text{where} \quad V_{L_{Ext}} = 5.0,\ 2.5,\ 1.25 \text{ or } 0.625 \text{Mbits/s}$$

t_{dc} The cable delay, which is the time spent by a data and acknowledge packet to be transmitted across a cable of length l. The cable delay per unit length depends on the cable type. For the multicore twisted cable used by the equipment the delay per unit length approximately 4.9 ns/m.

$$t_{dc} = l \times 4.9 \text{ ns/m} \quad \text{where} \quad l = \text{cable length in meters}$$

The data throughput in Kbytes/s can be expressed as:

$$\text{Data throughput} = \frac{1}{2t_{d_i} + t_{de} + t_{dc}} \tag{5.4}$$

The signal delay due to the internal link connections and due to the driver/receiver signal propagation were not included in the above calculation since they are not significant.

Table 5.3 presents the results for the calculated data throughput for all possible external link speeds ($V_{L_{Ext}}$) and digital cables from 1 to 1000 meters.

The weakness of these calculations is that only hardware delays are included. Software delays (overhead) exist, depending on the task being performed. If a computer program is written to execute exclusively the task illustrated in figure 5.16 the system overhead (software and hardware) will be the minimum, consisting of sending the data packet and receiving the acknowledge. However, if a small sophistication is included in the program, such as to display the characters on the screen, the software overhead will increase. In addition to the time needed to handle the data transmission the software has also to output the characters onto the screen delaying the transmission of a new character. If more tasks

Cable length meters	Calculated Throughput				Measured Throughput			
	External Link Speed				External Link Speed			
	5.0	2.5	1.25	0.625	5.0	2.5	1.25	0.625
1	192	128	77	43	146	104	63	36
100	176	121	74	42	135	94	60	35
200	162	114	72	41	120	88	57	34
300	150	108	69	40	104	82	54	33
400	140	102	67	39	–	70	48	30
500	131	98	65	39	–	–	46	30
600	123	93	63	38	–	–	45	29
700	116	89	61	37	–	–	43	28
800	110	85	59	37	–	–	41	27
900	104	82	57	36	–	–	–	27
1000	99	79	56	35	–	–	–	26

Table 5.3: System Data Throughput in kbytes/s.

are included in the program the software overhead will increase proportionally becoming predominant when other more complex tasks are executed.

SPAM-Mk III data acquisition and processing software incorporates a routine that continuously measures and displays the link data throughput on the portable computer screen. This facility can be used to measure the data throughput for different combinations of external link speed and digital cable length. The results are also presented in table 5.3. It should be noticed that other concurrent and more complex tasks have to be managed by the system leading to system overheads which decrease the data throughput.

The constraints related to the signal distortion explained in subsection 5.8.2.2 are evident in that test. The signal integrity is jeopardized by the combination of high speed and long cables. The message cannot be recovered properly and the

handshake breaks down for some combinations (represented by – in the table).

By rearranging the latest results, it is possible to determine the maximum digital cable length for a particular external link speed that can be used in the field for connecting Base and Remote without regeneration (Table5.4).

External Link Speed – Mbits/s	5.0	2.5	1.25	0.625
Maximum digital cable length – m	300	400	800	1000

Table 5.4: External Link Speed *versus* Digital Cable Length

It is also possible to compare the actual figures to the cable length guideline since the cable type, devices and line termination are the same. Both are represented in figure 5.18. The RS-485 standard curve has three distinct regions. At low data rates (below 100Kbits/s) the main concern is the cable's DC resistance that causes signal attenuation along the cable and it is based on an arbitrary loss of 6dB (signal magnitude down by 50%). As the data rate increases, the cable's electrical characteristics limit the speed proportionally. That condition is represented by the sloping portion of the graph between 100 and 2500Kbits/s. The last region is where the speed is limited by the driver/receiver characteristics being the maximum quoted data rate for low-power devices 2.5Mbits/s. **SPAM-Mk III Communication Board** curve shows that these guidelines are conservatives. If the external link speed is set to 0.625Mbits/s up to 1200 meters distance can be achieved. At the maximum link speed of 5.0Mbits/s up to 300 meters and for 2.5 and 1.25Mbits/s the maximum distances are respectively 400 and 800 meters.

Even though both patterns in figure 5.18 set the communication rate limits as a function of signal speed, the methodology applied is different. The RS-485 curve is based on transmitted/received signals timing and the maximum tolerable signal distortion. The SPAM-3 curve is based on real communication between Base and Remote Boxes, thus including a software delay which makes the guidelines even more conservative.

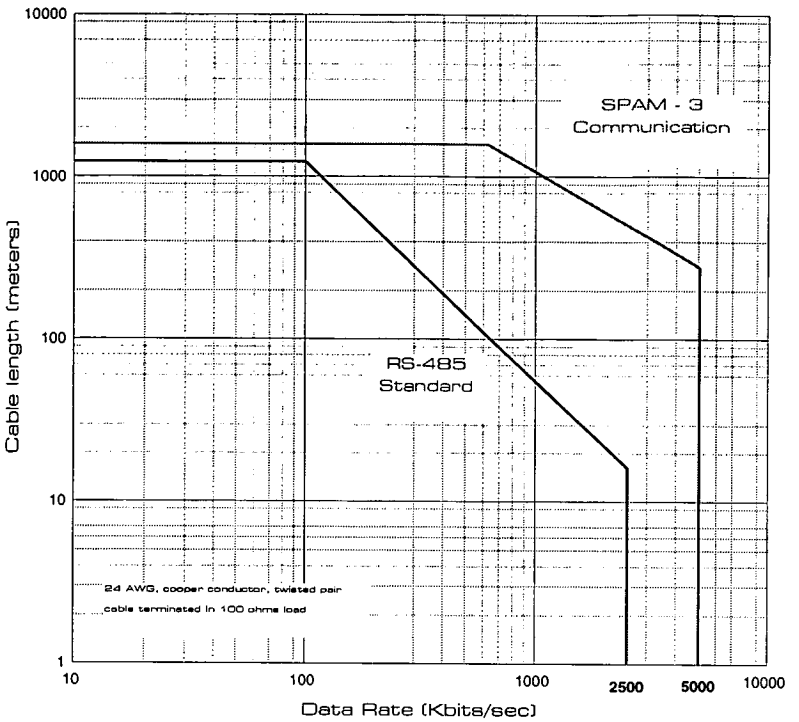

Figure 5.18: SPAM-Mk III and RS-485 Standard data rate limits

Figure 5.19 is a graphic representation of the data throughput from table 5.3. The difference between calculated and measured values is the system overhead. For instance the difference between calculated and measured data throughput for 5.0Mbits/s external link speed and 1m cable is 46Kbytes/s. That difference has the same order of magnitude for 100, 200 and 300m cable for the same link speed. Also, for the remainder link speeds the system overhead in Kbytes/s is practically constant regardless the cable lengths. Average values are 24, 14 and 7 Kbytes/s respectively for 2.5, 1.25 and 0.625Mbytes/s link speed. According to the Transputer link protocol (figure 5.16) one byte of information consists of (11+2) bits. The period of each byte is the reciprocal of the external link speed. As an example, the system overhead equivalent to the time required to transmit 46Kbytes of 13 bits/byte at 5.0Mbytes/s (200ns period) is:

$$46000 \times 13 \times 200\text{ns} = 0.120 \text{ seconds.}$$

The same calculations for 24, 14 and 7Kbytes/s at their respective link speeds

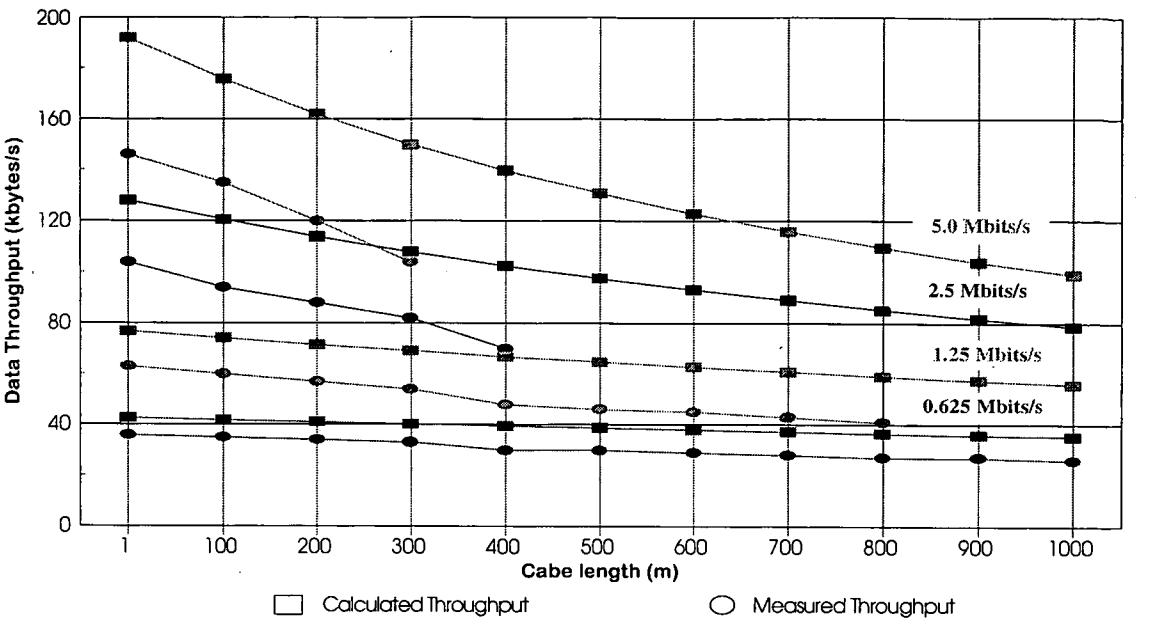

Figure 5.19: System Data Throughput

lead to 0.125, 0.146 and 0.146 seconds data throughput delays due to the system overhead. The delays have the same order of magnitude as they should be since the concurrent tasks to be managed by the system software are the same, have the same priority and do not depend on neither link speeds nor cable lengths.

CHAPTER 6

The Remote Box

6.1 Module Overview

The Remote Box receives analogue signal from up to three Sensor Boxes, performs analogue signal processing, data acquisition, digital signal processing, converts data into the frequency domain and send the digital data to the Base Box for further processing. The block diagram including internal connections is shown in figure 6.1

Each Remote Box connected to the network must have an unique identification number and can accommodate up to twelve channels. The communication between Sensor and Remote Boxes is made in differential-mode, to allow individual grounding of each remote subsystem and to reduce the noise. The board configuration of the Remote Box consists of one Channel board per sensor connected to the Sensor Boxes plus a DC-DC/Computer board (see 5.4), a Communication board (see 5.9) and a DSP board.

Software running on the DSP board Transputer controls the data acquisition and all Channel board functions like gain, filter settings and A/D converters output. These functions are controlled simultaneously and set identically in all Channel boards in the Remote Box except the input gain stage which can be

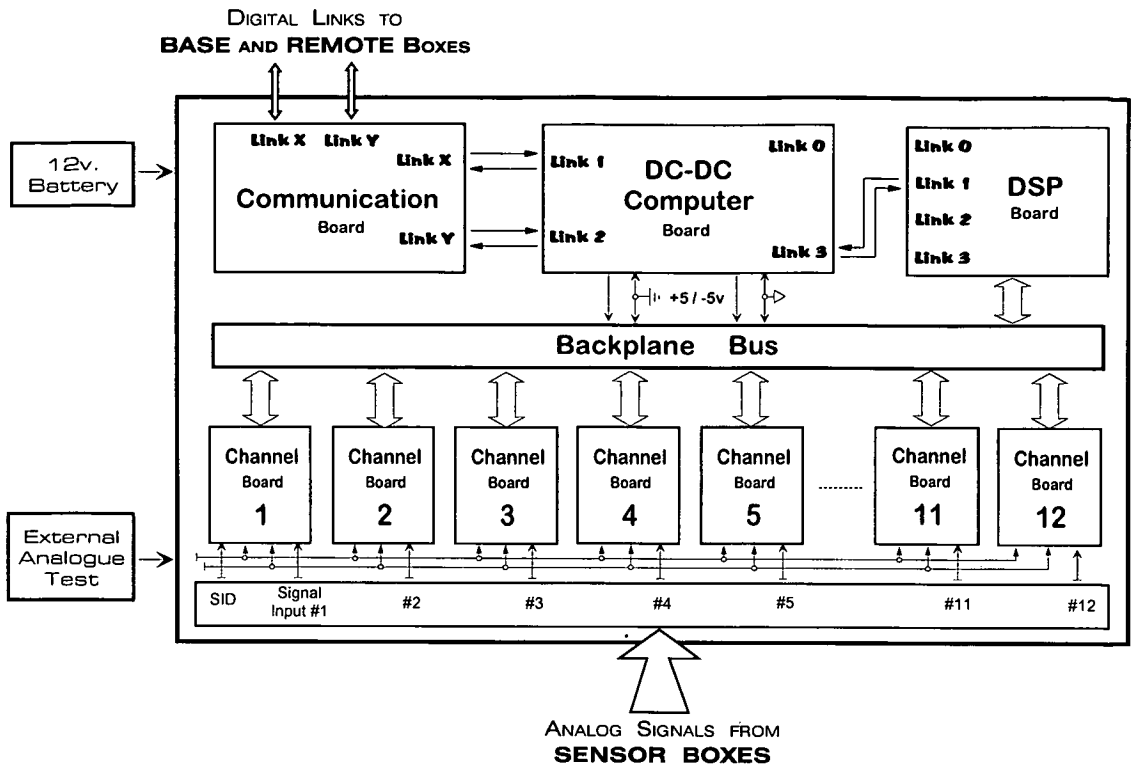

Figure 6.1: Remote Box

modified individually per Channel board, for instance, to compensate for larger fields in any particular direction. The analogue signal conditioning consists of filtering and amplification followed by analogue-to-digital conversion. SPAM Mk-III uses one A/D converter per channel the advantages being no skew between channels and more flexibility because each channel is self-contained in one board. Digital data is processed on the DSP board (oversampling decimation). Signals are then transferred to a Computer board through internal links for digital band-pass computation and transformation into the frequency-domain (FFT). Time series and frequency domain data are transferred via the Communication board to the Base Box for further processing and analysis.

An analogue test input is provided for calibration and maintenance purposes and a single 12V external battery supplies power to the module. The maximum power consumption for an 8-channel box is 5 watts.

6.2 Software in the Remote Box

The software residing in the Remote Box runs on two different Transputers. The first on the DSP board controls the analogue signal conditioning, the data acquisition and provides facilities for monitoring the signal through all analogue stages. The second on the DC-DC/Computer board performs the digital signal processing, converts the time series into the frequency domain (FFT) and apply signal correction to compensate for sensors and analogue filters frequency response.

6.2.1 Digital Filtering

With the availability of cheap data processing components and improved techniques it is more reliable and cost effective to transfer much of the analogue signal conditioning hardware to digital signal processing hardware and software. Analogue filtering accuracy for instance, relies heavily on component stability (temperature and time) and tolerance. Processing signals in a numerical form offers significant improvements. Digital signals may be reproduced and processed with guaranteed accuracy and the problems related to stability and tolerance are also substantially removed. However, some basic analogue filtering is always required to improve the dynamic range and prevent aliasing. These filters

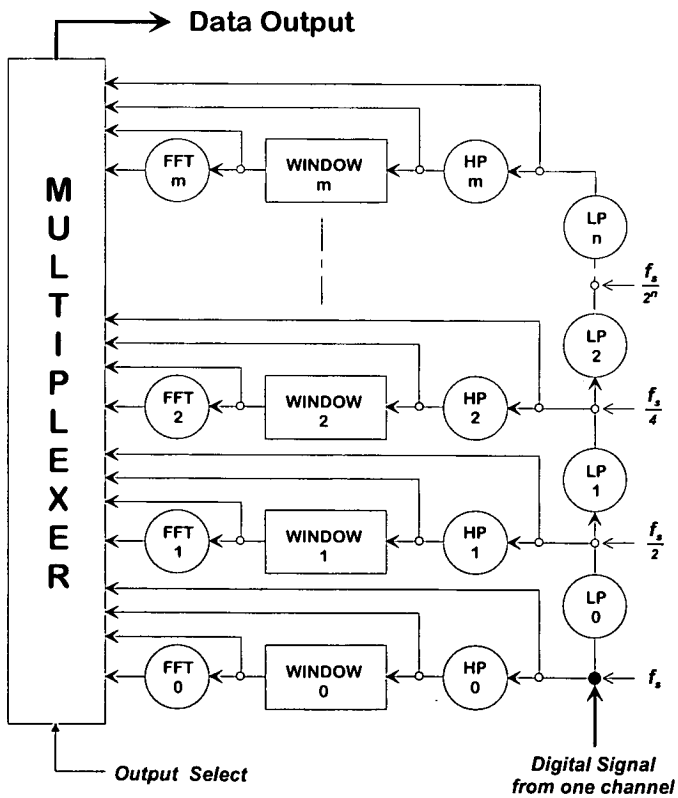

Figure 6.2: Remote Data Processing flow

have to be applied before the conversion to the digital domain. Another useful feature of digital processing is the ability to create or change filters by software, which is simpler than creating them by hardware. SPAM Mk-III uses this facility and allows the determination of a large number of bands by changing values of the low-pass and the high-pass frequency for each frequency band individually. These bands can overlaps or not. Figure 6.2 illustrates these features. The digitized time-series stream is successively low-pass filtered and decimated. This is achieved by sampling the signal at different sampling frequencies which must be done sequentially since the time-series sampled at $f_s/4$ is derived from the time-series previously sampled at $f_s/2$ which was derived from the original time-series sampled at f_s. Any low-pass filtered time-series can be high-pass filtered to generate band-pass filtered data. Transformation to the frequency domain is also applied. Figure 6.2 also shows that any combination of decimated and filtered time-series can be sent to the Base Box (data output) for further processing.

Up to eight frequency bands can be selected by the user. Low-pass corner frequencies and band width are selected in octaves and can be contiguous or overlapping. The table on the right is an example of band selection. Bands 0 to 5 are contiguous and Bands 5 to 7 are overlapping. Band 0 is 3 octaves width and the remainder are 2 octaves width.

As stated before, the filters' corner frequencies can be changed easily because they are software bands and are changed dynamically. No hardware change is required.

Band Number	Hertz	Octaves	
	LP – HP	LP	BW
0	128 – 16	7	3
1	16 – 4	4	2
2	4 – 1	2	2
3	1 – 1/4	0	2
4	1/4 – 1/16	-2	2
5	1/16 – 1/64	-4	2
6	1/32 – 1/128	-5	2
7	1/64 – 1/256	-6	2

Table 6.1: Frequency Bands

6.2.2 Response Function Calibration

Consider a continuous analogue signal $f(t)$ (or discrete signal $\{f(nt)\}$) applied to a linear time–invariant system. The response of the system to the excitation $f(t)$ (or $\{f(nt)\}$) is $g(t)$ (or $\{g(nt)\}$), which is a different signal. For all physically generated signals, such as magnetotelluric events, the function $f(t)$ is a real function of time. Consider the Fourier transforms of the signals:

$$f(t) \leftrightarrow F(w) \qquad \text{and} \qquad g(t) \leftrightarrow G(w)$$

The system function $H(w)$ is defined as the ratio of the response transform $G(w)$ to the excitation transform $F(w)$.

$$H(w) = \frac{G(w)}{F(w)} \tag{6.1}$$

If the excitation and response are defined at different points in the system, $H(w)$ is the *transfer function* as illustrated in figure 6.3 (Baher 1990).

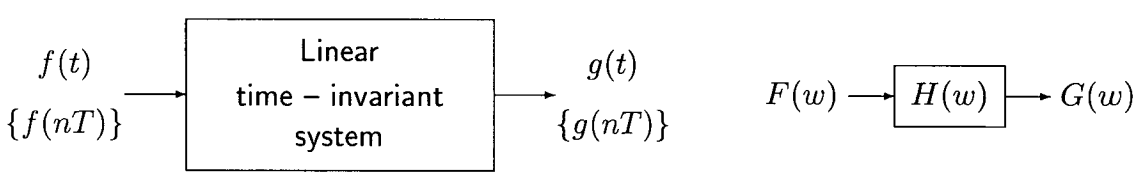

Figure 6.3: Transfer Function

If more than a single system is present in the signal path, then the response from the first stage will be the excitation to the second and so on. The overall system transfer function will be a combination of all individual transfer functions e.g $H_1(w) \cdot H_2(w) \cdots H_n(w)$. In order to recover the characteristics of the original excitation, one has to apply to the modified system response a *calibration* function $C(w)$ where:

$$C(w) = \frac{1}{\prod_{i=1}^{n} H_i(w)} \tag{6.2}$$

This is illustrated in figure 6.4.

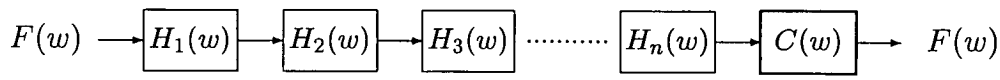

Figure 6.4: Multi-stage system Transfer Function

The natural time-varying signals measured by the sensors are submitted to sequential analogue filtering and amplification similarly to the figure 6.4. The signals from the electrodes are filtered and amplified in the Sensor Box. The frequency response due to this section depends on the filter's settings (low-pass and high-pass) and the amplification. There are two different settings for each hadware filter (Low-pass and High-pass) and two possible amplification levels, leading to eight possible frequency response characteristics for the electric signals. Induction coil magnetometers usually incorporate some similar analogue pre-conditioning and the output signals do not need to be pre-conditioned again in the Sensor Box. However, there is a frequency response due to the analogue signal pre-conditioning performed by the magnetometers and the characteristics are supplied by the manufacturers. All signals are processed again in the Remote Box. Initially, a second analogue pre-conditioning is performed by the Channel board followed by digital signal processing performed by the software. All analogue channels are matched with errors within 1.0% amplitude and 1.0 ° phase. The digital signal processing is similar for all channels. Therefore signals from the Sensor Box follow the same matched path and any frequency response due to the signal processing in the Remote Box is identical to all channels. Then software running on the DC-DC/Computer board Transputer can correct the signals to compensate for the frequency response of both hardware and software filters. However almost all MT analysis techniques use ratios of channels and only non-

common responses need to be corrected. This means that the calibration features applied to the signal due to the processing in the Remote Box is an improvement but is not essential. What is essential is the calibration due to the *non-common* frequency response of the magnetometers and electric pre-amplifier boards.

The frequency response calibration follows the sequence.

1. Identify the sensor board type connected to each logic channel, i.e. electric or magnetic boards.
2. Identify the serial number of the electric boards and magnetometers.
3. Identify the filter configuration used by the electric boards at the time of the data acquisition.
4. Read an auxiliary file which contains the transfer function table for the electric boards (calibration file).
5. Read a similar file which contains the transfer function table supplied by the manufacturer for the identified magnetometers.
6. Compare the required frequency layout to the frequency layout available in the calibration files.
7. Read the calibration data and interpolates available data for the required frequencies.
8. Calculate the calibration transfer function ($C(w)$ in figure 6.4).
9. Apply the calibration function to the signals in the frequency domain.

The calibration files consist of normalized amplitude and phase values as a function of frequency which are based on laboratory test results. All electric boards are matched within 0.1% amplitude and 1 ° phase error. Therefore, there are four calibration files for the electric boards, one per filter setting combination.

For the magnetometers, the calibration file has the same format but the data are based on the manufacturer's information. Usually, there is one calibration file per magnetometer.

Figure 6.5 presents the effect of the calibration.

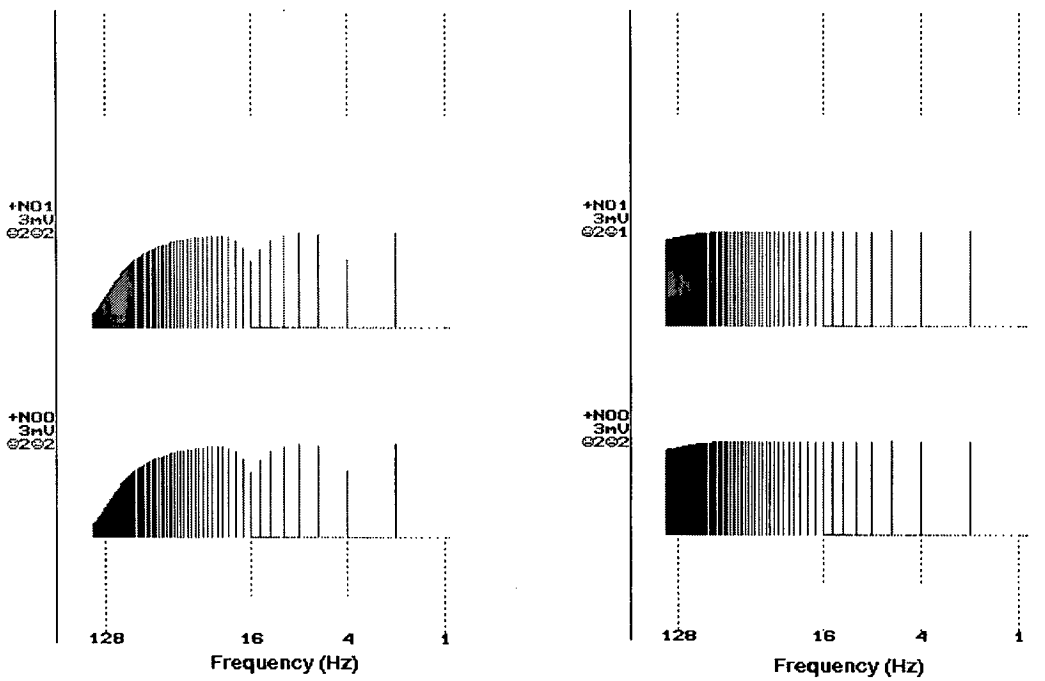

6.5.1: Non-calibrated

6.5.2: Calibrated

Figure 6.5: Analogue and Digital Transfer Function Calibration

The system was set up as for field measurements. An impulse test signal (2Hz) was connected to the Remote's test input. Figure 6.5.1 is the non-calibrated spectra of the input signal. The effect of the filter bands fall-off at the bandwidth edges is evident. Figure 6.5.2 is the calibrated spectra of the same signal. The flatness of the system's response was highly improved.

6.3 Channel Board

Analogue filtering, amplification and analogue to digital conversion for each channel are performed on this board. All functions are software controlled and interfaced by a set of registers. The block diagram is shown in figure 6.6. This board is the most densely populated in the whole system, combining digital and analogue circuits with separate grounds planes. Analogue and digital power supplies ± 5 V are also independent and drained from the DC-DC/Computer board.

6.3.1 Digital Section

In order to identify all channel boards in the system and associate them to the network configuration, the software reads the board's serial number and logical identification number at the start-up. They are the board *serial number* and the *logical channel number*. The *serial number* is hardwired on board. It is represented by an eight-digit number (0 - 255) which is unique among all channel boards. The *logical channel number* is set by a rotary hexadecimal switch on the board's edge and is unique and sequential per Remote Box. It also reflects the total number of sensor channels installed per box. If the logical number is set to 0 the channel will be disregarded by the software which is identical to disconnecting the channel without physically removing it. During normal operation, the software refers to the logical channel number to send commands for reading, writing or changing settings on that board.

Two synchronous serial-in parallel-out devices interface the 16-bit resolution serial signals from the analogue to digital converter to 8-bit parallel data bus. Two registers control the data flow operation when the specific channel board is selected. The *READ register* reads the converted data and board identification. The *WRITE register* writes all programmable analogue stage settings like output gain amplification factor, notches in-out, low-pass and high-pass corner frequencies and starts the analogue to digital conversion.

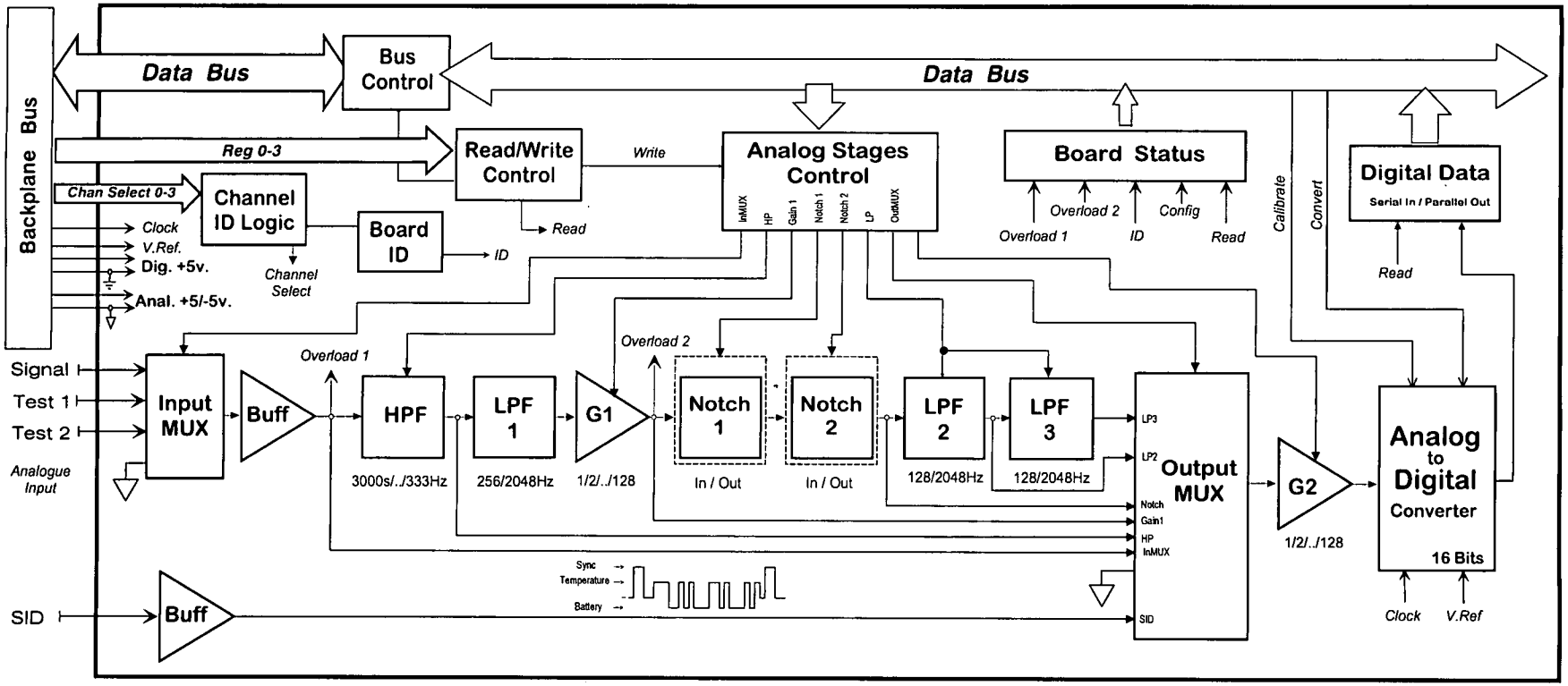

Figure 6.6: Channel Board

6.3.2 Analog Section

These boards have the last analogue section in the whole system and perform the final analogue pre-conditioning for the signals from the sensors.

6.3.2.1 Input Multiplexer

The circuit input is a 4-channel differential analogue multiplexer. Devices are internally full-protected up to ±75 volts. This internal protection solved a major problem related to electric/magnetic boards output protection and its effect on analogue cable length as explained in 7.3.2.5. One out of four inputs can be selected.

SPARE. Not yet implemented

TEST EXTERNAL. Selects a test signal connected to the external test input connector. This is very useful for set-up, maintenance and calibration purposes.

SENSORS. Selects signal from the sensors, being the normal operation mode, when real data are being acquired.

SHORTED. Selects an output for input(+) and input(-) shorted. These inputs can be either connected to ground or kept floating, depending on a jumper position. It is useful for calibration purposes like noise and common-mode rejection evaluation.

Selected output is fed to a high impedance true differential unit-gain buffer. Common-mode rejection tuning of 120dB is achieved at that stage.

6.3.2.2 High-Pass Filter

A single-pole high-pass filter is the next stage in the signal's path. It reduces high amplitude long period signals and blocks DC components from sensor boards'

stages in order to allow improved dynamic range by post-amplification. One out of thirteen corner frequencies between 0.00033 and 333Hz can be selected. High-pass filter **RESET** is also available in the HP Filter menu.

6.3.2.3 Low-Pass Filters

The low-pass filter section in the Remote Box Channel board consists of three Butterworth type filters. This type of filter was chosen due to its characteristics of flat gain response over the pass band.

The filter corner frequencies, selected by software, are determined according to SPAM-Mk III operation modes: 128Hz for **Short-Period** and 2048Hz for **High-Frequency**

The Low-pass filter is important in digital processing to limit the spectrum of the signal to be converted into the digital-domain and to avoid distortion of the recovered signals (aliasing).

Shannon's *Sampling Theorem* states an important relationship that must be preserved by every analog-to-digital conversion and also helps in understanding the relevance of the low-pass filter and its fall-off characteristics.

A time-domain continuous signal $f(t)$ whose spectrum is band-limited to below a frequency f_{Max}, can be completely recovered from its samples digitized at a rate

$$f_s \geq 2 \times f_{Max} \tag{6.3}$$

The frequency f_s is called *sampling frequency* or *sampling rate.* The maximum frequency component that can theoretically be recovered is widely referred to as the *Nyquist frequency* (f_n). Thus

$$f_n = \frac{f_s}{2} \tag{6.4}$$

To avoid unwanted frequency components being sampled, the signal $f(t)$ must be band-limited by an analogue low-pass filter whose cut-off frequency is f_c. If

the band of $f(t)$ is not completely limited at f_c, bands of the sampled signal will overlap producing *aliasing* in the output signal. For that reason these low-pass filters before the digitization process are also known as *anti-aliasing filters.*

Critical sampling with $f_s = 2f_{Max}$ requires an *ideal* low-pass filter to avoid aliasing. These filters are non-causal and hence are physically unrealizable. In practice, we make the sampling frequency one octave beyond the Nyquist frequency, this allows a more relaxed filter fall-off characteristic. Therefore, the practical sampling frequency f_s can be expressed as a function of the low-pass filter corner frequency f_c as

$$f_s = 2 \times f_n = 4 \times f_c \tag{6.5}$$

The requirements for the low-pass filter are still strict. The fall-off should be very sharp. In order to determine the sharpness of the filter and consequently the number of poles required, attenuation figures at the Nyquist frequency should be established.

The amplitude characteristics of a Butterworth filter can be expressed as

$$|H(w)| = \frac{1}{\sqrt{1 + \left(\frac{w}{w_c}\right)^{2N_P}}} \tag{6.6}$$

where: $w = 2\pi f$, $w_c = 2\pi f_c$ and N_P = Number of filter poles.

The main interest is to evaluate the effect of the filter at the Nyquist frequency, then $w = w_n \rightarrow f = f_n$.

In equation 6.6 if $w_n > w_c$ then $\left(\frac{w_n}{w_c}\right)^{2N_P} \gg 1$ and

$$|H(w)| \approx \frac{1}{\left(\frac{w_n}{w_c}\right)^{N_P}} \tag{6.7}$$

The denominator of equation 6.7 expresses the signal attenuation at frequency w_n due to a filter with N_P poles and corner frequency w_c. This attenuation can

be expressed in dB as

$$Attenuation\,(f_n) \approx 20\,\log_{10}\left(\frac{f_n}{f_c}\right)^{N_P} dB \tag{6.8}$$

The low-pass filter corner frequency f_c is determined at the design stage and takes into account the bandwidth required for the signal $f(t)$.

From equation 6.8 we see that there are two possibilities for increasing the attenuation at the Nyquist frequency.

1. To increase the number of poles (N_P) of the low-pass filter.
2. To increase the Nyquist frequency f_n relative to f_c.

The first approach is immediate. However to increase the order of the filter means more hardware, power consumption and frequency response mismatch between channels. The second solution increases the ratio f_n/f_c by increasing the sampling frequency f_s. This technique is called *oversampling*. This process is completed afterwards by additional low-pass filtering and sampling rate reduction in the digital domain (*decimation filter*). The heaviest task in this case is left to the software, leading to a relaxation on the anti-aliasing hardware filter requirements. Oversampling also has additional benefits: in the process of quantization, the resulting noise power is spread evenly over the complete spectrum and software filtering is much more accurate and introduces far less noise.

Consider an oversampling factor D such as $f_S = Df_s$. The actual Sampling Nyquist frequency is

$$f_N = Df_n \tag{6.9}$$

We can define D such as

$$D = 2^{O_s}\ (D = 1, 2, 4, 8, ..) \iff O_s = \log_2 D\ (O_s = 0, 1, 2, 3, ..)$$

where O_s is the number of octaves of oversampling.

From equation 6.5 we have: $f_n = 2 \times f_c$, then

$$f_N = 2^{O_s} \times f_n = 2^{O_s} \times 2f_c \quad \longrightarrow \quad f_N = 2^{(O_s+1)} \cdot f_c \tag{6.10}$$

and the expression of the attenuation (Eq.6.8) at the actual Nyquist frequency can be written as a function of the number of poles and the oversampling factor as

$$Attenuation\,(f_N) \approx 20\,\log_{10}\,2^{N_P\,(O_s+1)} \tag{6.11}$$

Table 6.2 represents attenuation in dB at the actual Nyquist frequency for different number of filter poles and oversampling factors, limited to 120 dB . An additional pole does not represent a significant increase in attenuation but it does in conjunction with oversampling. Usually a balanced combination of both is applied. For instance, 90 dB attenuation can be achieved by the combination $(N_P = 3) + (O_s = 4)$. The same attenuation would require N_P=15 poles if oversampling was not applied.

N_P	$f_S = 4f_c$ $O_s = 0$	$f_S = 8f_c$ $O_s = 1$	$f_S = 16f_c$ $O_s = 2$	$f_S = 32f_c$ $O_s = 3$	$f_S = 64f_c$ $O_s = 4$	... ...	$f_S = 4096f_c$ $O_s = 10$
1	6	12	18	24	30	...	60
2	12	24	36	48	60	...	120
3	18	36	54	72	90	...	-
4	24	48	72	96	120	...	-
5	30	60	90	120	-	...	-
6	36	72	108	-	-	...	-
⋮	⋮	⋮	⋮	⋮	⋮	...	⋮
10	60	120	-	-	-	...	-

Table 6.2: Low-Pass filter attenuation (dB)

Equation 6.11 can be simplified to

$$Attenuation\,(f_N) \approx 6\,N_P\,(O_s + 1)\;dB \tag{6.12}$$

An acceptable order of magnitude for the attenuation at f_N is the analogue-to-digital converter's resolution. This is a function of the number of bits N_{bits} and can be expressed as

$$Resolution_{A/D}\,(1\ bit) \approx 20 \log 2^{N_{bits}} \approx 6\,N_{bits}\ dB \tag{6.13}$$

Equations 6.12 and 6.13 can be compared to express a relationship between the A/D converter's number of bits, filter poles and oversampling factor.

$$N_{bits} \approx N_P\,(O_s + 1) \tag{6.14}$$

Another consideration on selecting the combination is that hardware poles are determined by the circuitry and oversampling factor is determined by software. The latter can be modified easier than the former to meet requirements. The total signal attenuation at the Nyquist frequency can be changed by software to optimize different frequency bandwidth data acquisition and processing e.g. SPAM Mk-III Short-Period and High-Frequency operation modes.

There are three low-pass filter stages on each channel board. One single-pole passive stage before the notches and two two-pole active stages after the notches ($N_P = 5$). Table 6.3 summarizes SPAM-3 low-pass filters and respective attenuations at the Nyquist frequency for both operation modes. The resolution of a 15 bits A/D converter is 90 dB (Equation 6.13).

Operation Mode	f_c Hz	Sampl Rate	N_P	O_s	Att dB	Comments
Short-Period	128	2048	5	2	90	
High-Frequency	2048	8192	5	0	30	Actual due to limitations of DSP
High-Frequency	2048	16384	5	1	60	Initially planned

Table 6.3: SPAM-3 Low-Pass filters and sampling characteristics

6.3.2.4 Input Gain

This stage provides the first signal amplification to the incoming signal. At that point, the DC level has been blocked by the high-pass filter but the noise from the mains supplies and other textitman-made disturbances is still present. The amplification factor is selected by software from 0 dB to 42 dB (x1 to x128) for each channel individually. The software sets the gain value and takes it into account for further calculations. There is a menu option to change these levels whilst monitoring the signals, as can be seen in figure 6.7. Saturation levels are also indicated. The input gain should be adjusted accordingly to just prevent saturation, then set down 1 or 2 further levels, for safety.

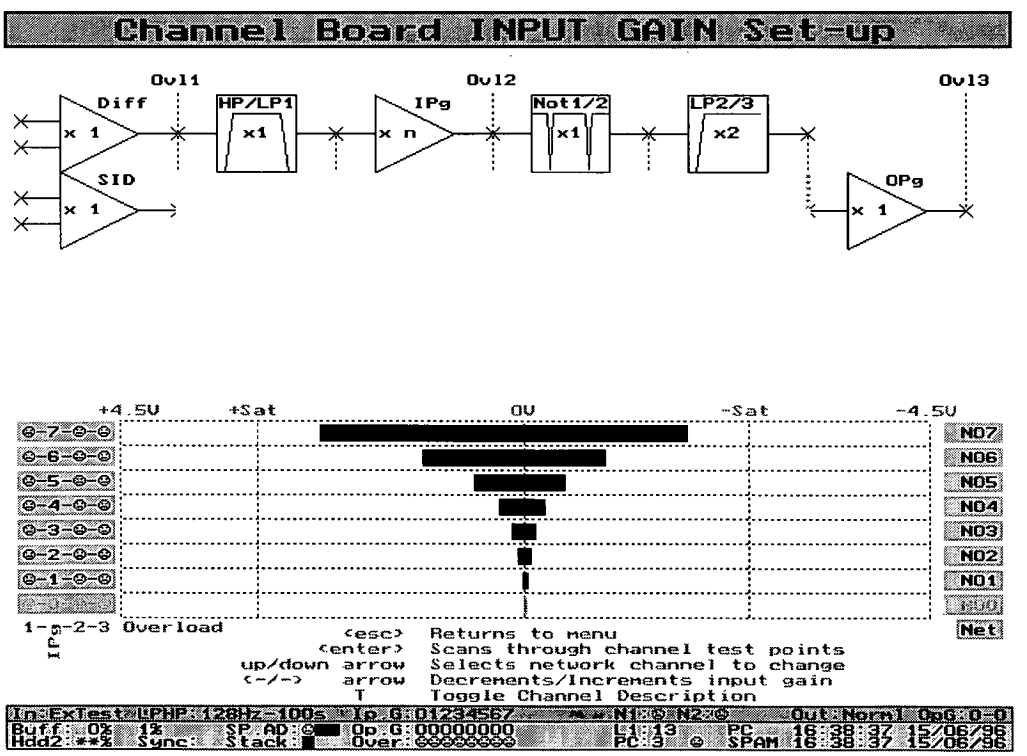

Figure 6.7: Input Gain screen

6.3.2.5 Notch Filters

Notch or band-reject filters are essential to attenuate some of the significant sources of *man-made* noise. The nature (and frequency) of these noises are usually well known like the mains supply, electric fences, electrified railroad system and redio-frequecy transmitters. The amplitude of the noise depends on the site distance from the source of noise and may be far higher than the natural signal. The frequency depends on the country and the source type, for instance 50/60Hz from mains supply, $16\frac{2}{3}$Hz from railways etc. Due to power line transmission and loading characteristics odd harmonics of the fundamental frequency are also present. Sometimes, due to main power rectification and poor grounding, the second harmonic may be the second highest noise source. These usually high amplitude noise signals should be attenuated before digitisation to improve the dynamic of the A/D conversion. The filter's selectivity is measured by the Q factor, which is expressed as

$$Q = \frac{f_0}{BW}$$

where $BW = f_H - f_L$ (the frequency bandwidth at -3dB attenuation points). Frequency f_0 is called the *notch frequency*.

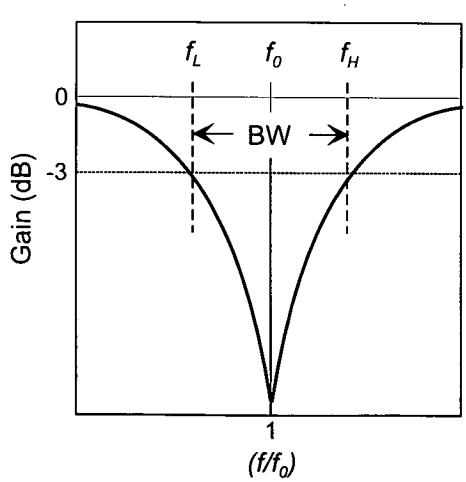

Figure 6.8: Second-order notch response

A typical magnitude response of a notch filter is shown in figure 6.8. It can be seen that the higher the value of Q the narrower the width of the notch and the attenuation in the vicinity of the notch frequency is poorer. If the noise were stable enough a high Q filter would be recommended. However, it is not the case in most situations. For mains derived sources it depends on local standards and specifications. Theoretically the notch depth is infinite but in practical realization, due to

component imperfections and mismatch, an attenuation of 60 dB can be expected.

SPAM-Mk III's notches are *Twin-T* type second-order active filters. Resistors are assembled in separate modules and plugged into the channel board, this is the easiest way of changing the center frequency. Two notch modules can be used at the same time in any combination. In order to accommodate a wide range of site conditions, the filter's selectivity can be chosen from $Q = 0.5$ and $Q = 1.75$ according to the local noise frequency stability. Figure 6.9 is an actual plot of the 50Hz notch filter amplitude response for the available selectivities. The shapes for different notch filters are identical. There are two potentiometers on these modules for fine-tuning the filters ($f_0 \pm 3\%$). Because they work interactively, they might unbalance the circuit branches leading to a slight change in the Q shape. This adjustment is very sensitive and requires as reference a very stable frequency generator.

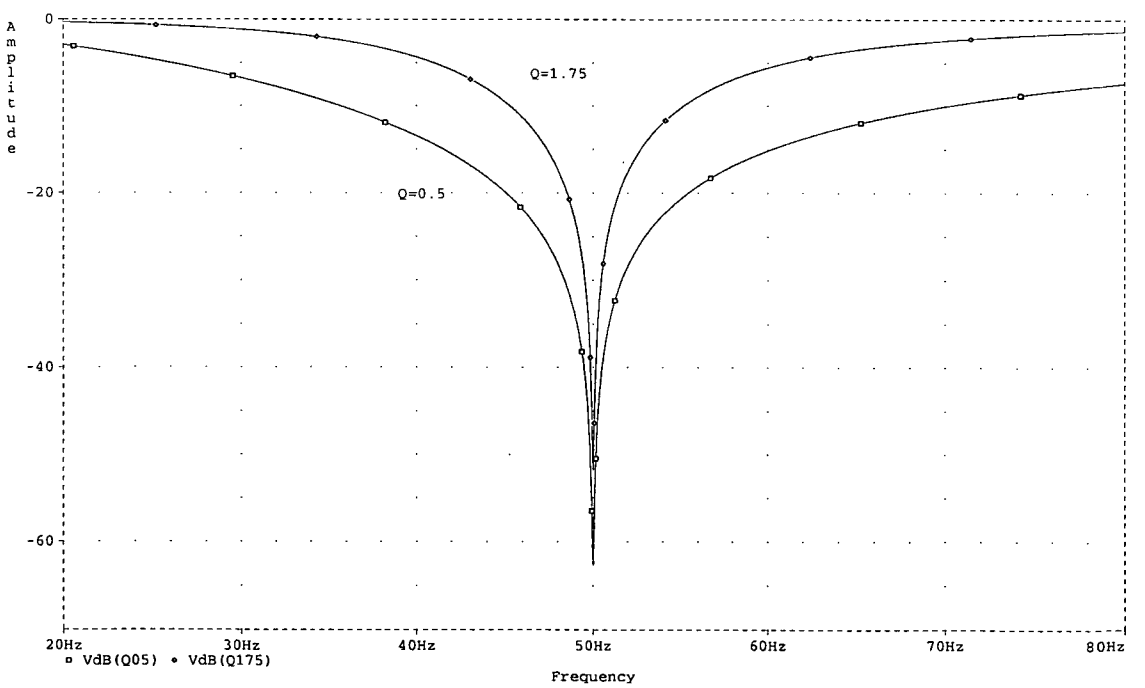

Figure 6.9: Notch Filters transfer function - Gain

6.3.2.6 Output Multiplexer

The output multiplexer selects the signal source to be digitized. There are eight possibilities to be choosen: six connected to the principal circuit stages in the analogue signal path (input multiplexer, high-pass filter, input gain, notch filters, low-pass$_1$ and low-pass$_2$), the serial system identification signal (SID) and ground for maintenance purposes and analogue to digital conversion noise evaluation. Figure 6.7 shows a graphic representation of this feature. It allows a quick check on the signal amplitudes to prevent overload at any stage. Also, it is a great help for *in-field* maintenance. By acting as *oscilloscope probe*, it samples the signal at any point, helping to detect and locate hardware faults.

6.3.2.7 Output Gain

The last amplification stage amplifies the signal from x1 to x128 in steps of 2 (1,2,4,8...128). The gain can be set by software to operate either in a *fixed gain* or *autoranging* mode.

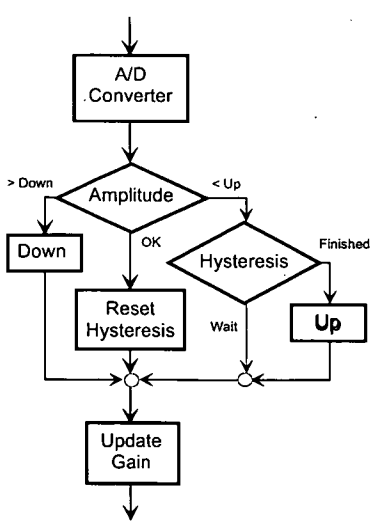

Figure 6.10: Autoranging signal flow

In *fixed gain* the amplification is constant, regardless the input signal amplitude. In *autoranging* mode, the gain changes between G_{min} and G_{MAX} in order to amplify the signal as much as possible before saturation. These limits can be set to any gain value the default being G_{min}=1 and G_{MAX}=128. The absolute maximum level for the signal is the analogue-to-digital converter's saturation level ($AD_{sat} = \pm 4.5\text{V}$). This level should never be reached. In order to perform this task, three levels relative to the absolute maximum (AD_{sat}) are defined: Sys-

tem Saturation (Sat), Gain Down (G_{down}) and Gain Up (G_{up}) approximately at $15/16^{th}$, $5/8^{th}$ and $3/8^{th}$ of AD_{sat} respectively. The digital sampled signal amplitude is compared to G_{down} and G_{up} levels in order to determine whether or not an action is required. If the output gain has to be reduced, the action will be immediate to avoid saturation. However, if the output gain has to be increased, an hysteresis takes place and the gain is actually increased only if that level is lower than G_{down} for 2000 samples. At the end, the output gain value is updated regardless of any change. For Short-period operation mode every sample from all channels is tested. For High-frequency mode it is not possible because of timing but a representative number of samples from all channels are tested. Figure 6.10 summarizes the operation.

Frequency response is a serious constraint on designing a 40 dB autoranging amplifier in one stage due to the *Gain-Bandwidth Product* characteristics of operational amplifiers which is constant value for any particular device. The higher the gain is, the narrower is the frequency bandwidth is and vice-versa. Figure 6.11 shows these characteristics (gain and phase shift) for a low-power consumption operational amplifier (Gain·Bandwidth= 2MHz). For gain=100 (40 dB) the frequency components of the signal beyond 20kHz will be attenuated at a rate of 20 dB per decade. The break-point frequencies for gain 10 (20 dB) and 1 (0 dB) are 200kHz and 2MHz respectively. As an example, if the gain of two channels are different the higher frequency components of the signal (beyond the break-points) will be affected by different attenuation leading to a relative amplitude and phase errors. The phase figures are less affected than the amplitude for most frequencies (< 200kHz for the device of figure 6.11) but significant relative phase errors should be expected at frequencies closer to the unity-gain break-point (2MHz). Unity-gain requires additional precautions to avoid oscillation due to signal feedback and the phase margin limits must be observed.

The above considerations are based on circuits where the frequency bandwith is limited only by the device characteristics. In most applications the frequency

bandwith is limited at an earlier stage and the importance is how close the corner frequency of these limits are and the attenuation (and phase shift) at these points.

For instance, for SPAM-Mk III Short-period operation mode these considerations do not apply because the signal bandwidth is limited to 128Hz and the maximum gain is 128 (42dB). The closest frequency affected by the gain dependent attenuation factor of the device is approximatelly 15kHz which is more than two decades beyond 128Hz. Any attenuation or phase shift imposed on the signals are due to the low-pass filtering (similar for all channels) and neither relative amplitude nor phase errors due to the device charcateristics are expected regardless the gain set by the autoranging mode.

For the High-frequency operation mode, the signal bandwidth is limited to 2kHz and the maximum gain is the same (128 or 42dB), the closest frequency affected by the gain dependent attenuation factor (15kHz) is less than one decade beyond. In this operation mode relative amplitude and phase errors at higher frequencies can be expected among channels with different gains. These errors are significant compared to the specifications (1% gain and 1 ° phase mismatch between channels). The solution for this problem is to choose a device with Gain-Bandwidth better than 25MHz (frequency break-point at least two decades beyond 2kHz at 42dB gain). However, such devices usually have much higher power consumption and are unstable

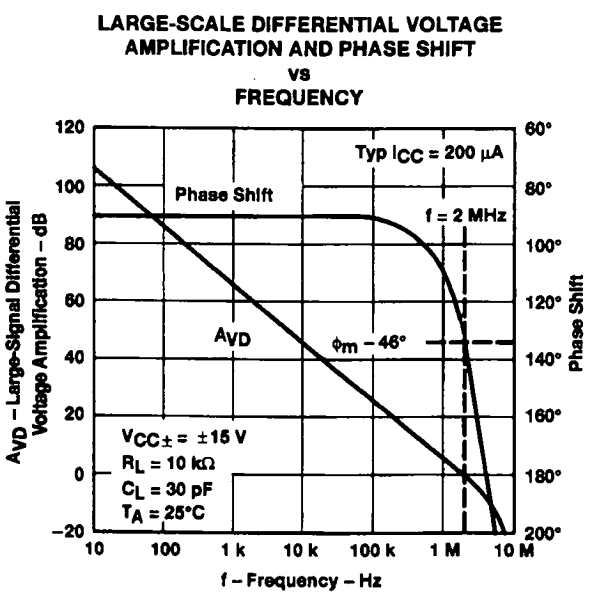

Figure 6.11: Op-Amp Gain-Bandwidth product

for low gains (usually less than 10) due to a lower phase margin.

To prevent amplitude and phase errors in the high-frequency mode the autorange limits need to be reduced. For instance, if G_{min}=2 and G_{MAX}=64, the maximum theoretical phase error expected is 0.6 °, though this reduces the dynamic range.

6.3.2.8 Analog to Digital Converter

The signal analogue to digital conversion is performed by a monolithic CMOS A/D converter incorporating a conversion and calibration microcontroller, clock generator, comparator, and serial communications port at 16-bit resolution (Crystal Semiconductor 1995). The converters' 16-bit data is output in serial form with either binary or 2's complement coding. The maximum output throughput is 20kHz for a single analogue input operation. An additional advantage for this particular device is its low power consumption (40mW).

The ability of any device to convert accurately to 16-bit depends on the accuracy of its internal comparator and DAC. Each device utilizes an *auto-zeroing* scheme to null errors introduced by the comparator. All offsets are stored on the capacitor array while in the track mode and are effectively subtracted from the input signal when a conversion is initiated. To achieve that accuracy, this particular device uses a self-calibration scheme. Several capacitors in parallel can be manipulated to adjust the overall bit weight. An internal microcontroller precisely adjusts each capacitor with a resolution of 18 bits. After a *power-on reset* a calibration cycle takes place. The device then stores its calibration coefficients in on-chip static memory (SRAM) and these do not need to be recalibrated during the data acquisition.

Among three different operation modes, *synchronous-self-clocking* timing mode was chosen. Each bit of the data is clocked-out synchronously to the clock input as it is being converted.

The clock frequency (hardware) for the A/D devices in all channels is a 2.5MHz signal generated in the DSP board. However, a second clock derived from the 5.0MHz Transputer system time clock and adjusted by software, actually triggers the conversion. Analog to digital conversions within a Remote Box (regardless the number of channels) are synchronized since the time-base is common. For multi-remote operation all Remote stations have to be synchronized by a common reference signal. In SPAM-3 this signal is generated by the Base and sent to all Remote Boxes via the digital cable. The major role is played by the software which has to synchronize the master timing line and the Remote's internal clock. Time synchronization modes including timing diagram is explained in section 5.3.1

A very careful power supply decoupling and grounding scheme should be used. Analogue and digital supplies are usually isolated in such devices and pinned out separately to minimize coupling between the analogue and the digital sections of the chip. Any noise riding on the device's ground input relative to the system's analogue ground will introduce conversion errors. This applies to the printed circuit board layout as well, where analogue and digital ground planes should be separated and connected at only one point as close as possible to the chip.

6.4 DSP Board

The DSP board controls all digital bus lines to channel boards and performs software data acquisition and decimation. The software implementation running on the DSP board is explained in section 6.2.

There are only digital circuits on board, including registers for *READ* and *WRITE* operations, control bus and multiplexers and are similar to the Channel board's digital section as described in 6.3.1. Two rotary switches set the Remote Box's 8-bit identification number which must be different and unique for each Remote Box connected to the network. The heart of the Digital Signal Processing

board is a 32–bit CMOS Transputer family microcomputer (Inmos 1989b) with 4 kbytes on-chip RAM for high speed processing, a configurable memory and four standard communication links. Digital ± 5V power supplies to the board are driven by the DC-DC/Computer board.

The DSP board supplies all channel boards with a voltage reference for the A/D converters. The device is a DC-DC stepdown precision regulator from +12V input to +4.5V ± 0.2mV output, with a temperature drift of less than ± 0.5ppm °C, equivalent to 1/60 LSB / °C at 16 bits. The precision voltage reference signal (VREF) is used by the analogue-to-digital converter chip to perform a self-calibration and consists of switching an internal set of calibration capacitors between VREF and Ground in a manner determined by the successive-approximation algorithm. The charging and discharging of the array results in a current load of VREF. Poor device's load current regulation leads to a conversion error. An internal crystal oscillator can provide an alternative clock frequency (*Internal clock*) for the system. The circuitry is identical to the DC-DC/Computer board's clock which provides the main system time-base. Either the external or internal clock frequency (10MHz) has to be properly divided to accomplish the A/D converter requirements before being delivered to all channel boards through the backplane.

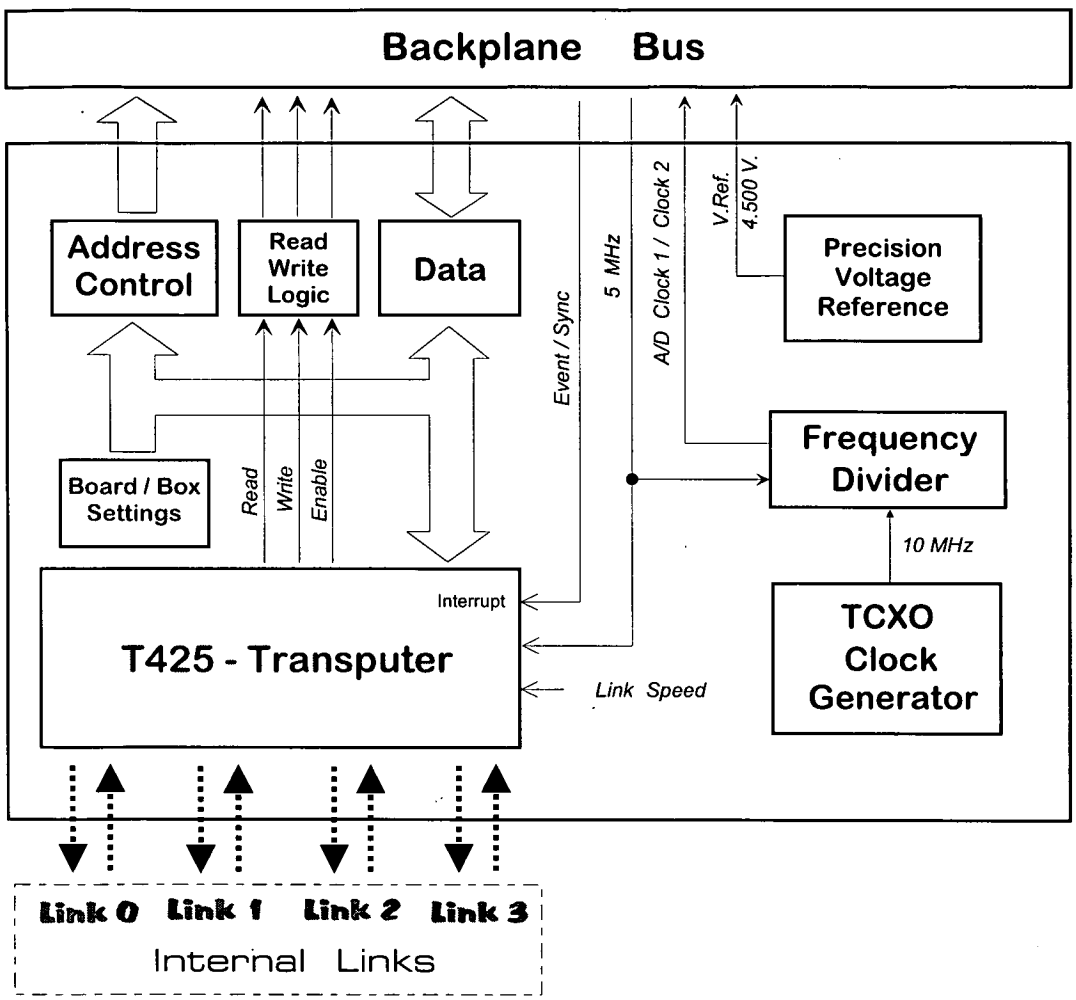

Figure 6.12: Digital Signal Processor Board

CHAPTER 7

The Sensor Box

7.1 Module Overview

The Sensor Box is the last node in SPAM-Mk III configuration tree and performs pre-conditioning for a set of local sensors. A typical configuration for the Sensor Box consists of one Control and up to 9 Sensor boards of any type and combination. There is one particular sensor board for each sensor type: Electric, which provides a more complete analogue signal pre-conditioning for a pair of electrodes and Magnetic, which provides power to the magnetometers and buffers the output signal. Magnetic boards can provide the same analogue signal pre-conditioning as the Electric boards but usually this pre-conditioning is performed inside the magnetometers. These two boards have in common a digital section that provides unique identification such as serial number, board type, configuration and signal overload detector which flashes a LED on respective panels. Electric and Magnetic boards are explained respectively in detail in sections 7.3 and 7.5.

The analogue pre-conditioning provided by the electric boards consists of filtering (high-pass and low-pass) and amplification. There are two corner frequencies for each type of filter which are set by hardware simultaneously in all boards according to the equipment operation mode (SP or HF). The common filter cor-

ner frequency controls (also high-pass filter Reset) are very important to ensure that all electric boards operate in the same frequency bandwidth. The gain is also set by hardware independently for each board to accommodate different electric fields strength.

An external analogue signal generator can be connected to the Sensor Box for quantitative calibration purposes. This signal performs different functions on electric and magnetic boards and will be explained in detail later on.

The Sensor Box provides suitable signal[1] for switching internally those magnetometers which support more than one frequency band operation mode like ECA CM216E or Metronix MFS05 (see Anvar-CNRS (1980) and Metronix (1991) for specifications). Again, to ensure the same operation conditions, this signal is common to all magnetometers.

An external 12 volt battery supplies power to the box and through the sensor boards to the magnetometers. Due to the very low-power consumption, low-dropout and high efficiency devices, the typical power consumption for a Five elements MT configuration box is 800 miliwatts (magnetometers not included).

As explained in section 4.5, the network configuration can be very diversified. The number of Remote and Sensor Boxes connected is virtually infinite. The sensor configuration used in MT works can be improved not only in number but also by using different directions instead of the usual North/South, East/West. In order to manage the data acquisition, the multi-sensors transfer functions calculation and to apply the correct frequency response calibration, the system must identify every module connected to the network. All required information is transmitted from the Sensor to the Remote Box in a single serial line and consists of:

- Sensor Box number, number of channels, temperature and battery level.
- Control board serial number

[1] Each magnetometer model require specific hardware to perform the switching

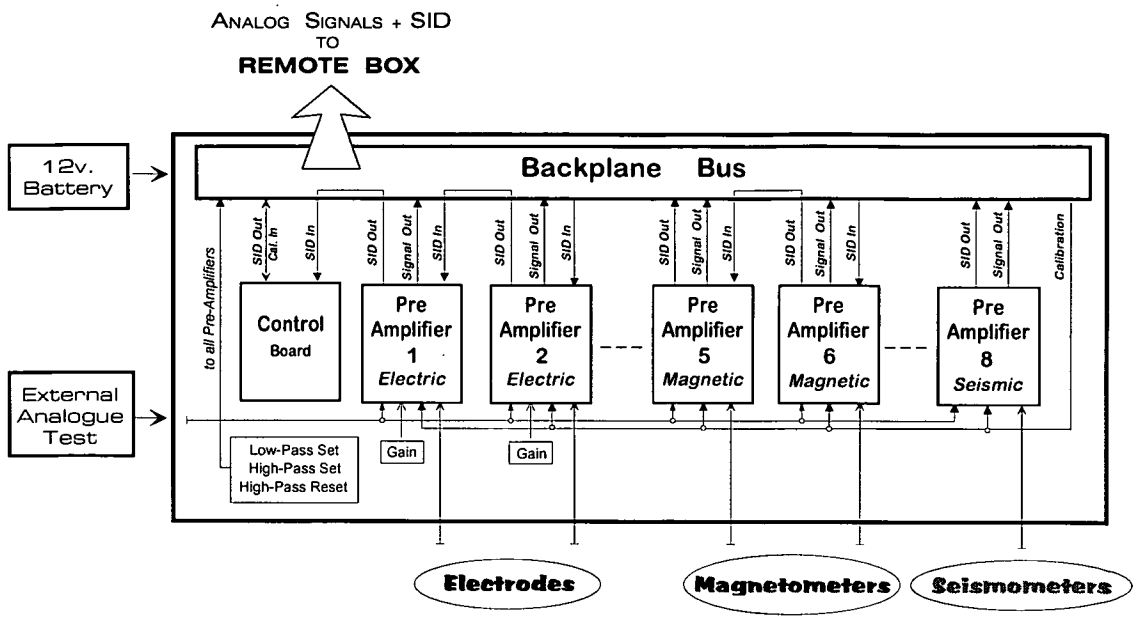

Figure 7.1: Sensor Box

- Sensor boards type, serial number, channel number, direction, low-pass and high-pass filter status, gain and signal overload
- Magnetometer operation mode (frequency band)

and will be explained in detail in the subsection 7.2.2.

The sensor identification signal (SID) mentioned above plus one output signal per sensor board are transmitted to the Remote Box through a multicore screened cable

7.1.1 Analogue Signal Transmission constraints

The analogue cable length depends on the network configuration and logistics. Field works have been carried out using 250 meters cable (Ritter 1995). However, if the application requires more than one Sensor Box in the high-frequency mode all analogue cables must have roughly the same length to avoid attenuation and phase mismatches. This is explained:

An analogue signal e_i driven by an amplifier with output impedance R_o ohms traveling into a cable with length l meters, resistance R_c ohms/meter and capacitance C_c picofarads/meter is attenuated to a value e_o by the frequency dependent expression

$$\frac{e_o}{e_i} = \frac{1}{1 - j\left(\frac{f}{f_c}\right)} \tag{7.1}$$

Equation 7.1 is a typical First order low pass filter response with corner frequency f_c. Real and complex part of this equation give us the amplitude attenuation (A) and phase shift (Θ) at a generic frequency f due to the filter characteristics (or due to a cable with similar filter effect) and can be expressed as

$$A = \frac{1}{\sqrt{1 + \left(\frac{f}{f_c}\right)^2}} \tag{7.2}$$

$$\Theta = \tan^{-1}\left(\frac{f}{f_c}\right) \tag{7.3}$$

An approximate expression for the corner frequency f_c can be written as

$$f_c = \frac{1}{2\pi(R_o + lR_c)(lC_c)} \tag{7.4}$$

Equation 7.4 can only be used if the load impedance *seen* by the output amplifier in the Sensor Box is much higher than its output impedance (R_o) and the cable DC resistance ($l \times R_c$). In this particular case, the load impedance is the Channel board input impedance (>10MΩ) which validates the approximation even for long cables. Equation 7.4 shows that the corner frequency f_c depends on the amplifier output resistance (R_o), the cable characteristics (R_c, C_c) and length (l). Thus, f_c is reduced by lower quality and longer cables (increase R_c, C_c and l) and higher amplifier's output impedance (increases R_o). The lower the f_c value is, the higher the attenuation for the signal's hi-frequency components will be. Similar effect is expected on the signal's phase. These distortions are nominated respectively *Group* and *Phase delay.*

The effect of the output impedance will be discussed later on. For the time

being we shall concentrate on the analogue cable's length and consider an output impedance R_o=100Ω matched within 1% (due to component tolerance) among all electric and magnetics boards. The analogue cable is the same and its characteristics are R_c=92Ω/km and C_c=220pF/m.

Therefore, the corner frequency due to different cable length and amplifier output impedance R_o=100Ω can be calculated by equation 7.4. The attenuation and the phase shift at different frequencies for different cables length (leading to different f_c) can also be calculated respectively by equations 7.2 and 7.3. Table 7.1 shows the results. The values in italic correspond to frequency limits of SPAM Mk-III Short-Period and High-Frequency operation modes, 128Hz and 2048Hz respectively. For a quantitative evaluation we shall consider the specifications for minimum amplitude and phase errors between the Channel boards, i.e. 1% and 1 °.

For Short-Period mode the amplitude and phase errors due to the cable are within the specifications. For this mode, two Sensor Boxes can be connected to the Remote Box respectively by analogue cables up to 300m without any significant amplitude or phase errors. The results are different for High-Frequency operation mode mainly because of the phase shift, if the same cables are used, phase shifts higher than 1 ° will be experienced at higher frequencies (> 500Hz). Analogue cables with the same length should be used if the application requires more than one Sensor Box and High-Frequency operation mode to avoid amplitude and phase mismatches at higher frequencies. The theoretical limit for the analogue cable length difference is approximately 60m (1 ° phase error at 2000Hz).

In addition to the filter effect mentioned above, longer cables are more prone to pick up hi-frequency noise and to crosstalk interference [2].

[2] A type of interference caused by signals from one circuit being coupled to adjacent circuits

Freq. (Hz)	Cable length – (meters)							
	10	**20**	**50**	**100**	**150**	**200**	**250**	**300**
Amplitude attenuation (%)								
1	0.00	0.00	0.00	0.00	0.00	0.00	0.00	0.00
10	0.00	0.00	0.00	0.00	0.00	0.00	0.00	0.00
100	0.00	0.00	0.00	0.00	0.00	0.00	0.00	0.00
128	*0.00*	*0.00*	*0.00*	*0.00*	*0.00*	*0.00*	*0.00*	*0.00*
1000	0.00	0.00	0.00	-0.01	-0.03	-0.05	-0.09	-0.14
2048	*0.00*	*0.00*	*-0.01*	*-0.05*	*-0.12*	*-0.22*	*-0.38*	*-0.58*
10000	-0.01	-0.04	-0.26	-1.12	-2.67	-4.96	-7.97	-11.61
Phase shift (degrees)								
1	0.00	0.00	0.00	0.00	0.00	0.00	0.00	0.00
10	0.00	0.00	0.00	-0.01	-0.01	-0.02	-0.02	-0.03
100	-0.01	-0.02	-0.04	-0.09	-0.14	-0.19	-0.24	-0.30
128	*-0.01*	*-0.02*	*-0.05*	*-0.11*	*-0.17*	*-0.24*	*-0.31*	*-0.39*
1000	-0.08	-0.16	-0.41	-0.86	-1.35	-1.87	-2.43	-3.03
2048	*-0.16*	*-0.33*	*-0.85*	*-1.77*	*-2.77*	*-3.84*	*-4.98*	*-6.18*
10000	-0.80	-1.61	-4.13	-8.58	-13.28	-18.12	-23.03	-27.89

Table 7.1: Amplitude and Phase distortion for different cable length and amplifier output impedance (R_o) 100 ohms

7.2 Control Board

There are basically two functions performed by the Control board: supply of regulated voltage to the sensor boards and transmission of information about this particular Sensor Box on a single serial identification line to the Remote. The Control Board block diagram is shown in figure 7.2

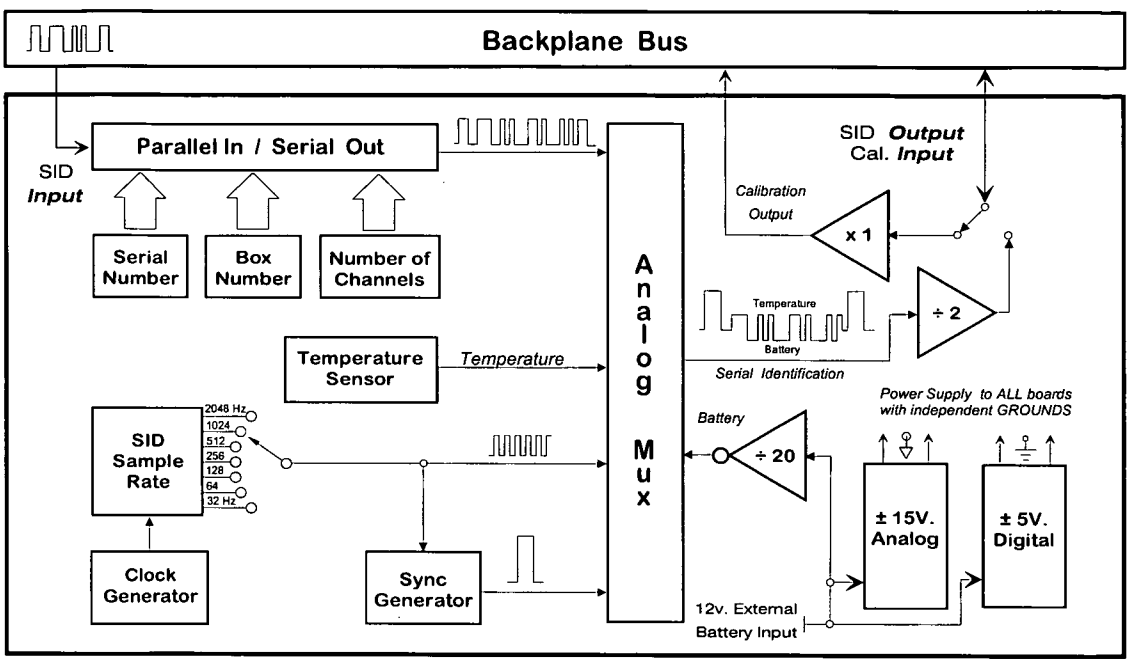

Figure 7.2: Control Board

7.2.1 Power Supply

Voltage from external 12 volts battery is converted into ± 15 volts and ± 5 volts power supplies for the analogue and the digital circuits respectively. They are isolated and provide separate ground path for analogue and digital circuitry. Switching regulators are used for DC-DC conversion and inversion. Their oscillation frequencies are higher than 45kHz, which is far beyond the instrument operation bandwidth.

7.2.2 Digital Sensor Identification line

The Control board generates clock and synchronization pulses to all boards connected to the back plane in order to provide the timing for each board to append to the serial line their particular identification set. After receiving the package from the nearest board, the Control board includes its serial number and Sensor Box's parameters (box number and number of channels) to this package, just after the synchronization pulse. An analogue multiplexer changes the shape of this package from a single digital into a three level pulse train. They are:

Synchronization level, a positive fixed 730 milivolts single pulse which starts the identification package. This level is given by a precision voltage reference with ± 1 % tolerance.

Temperature level, a positive voltage level proportional to the temperature inside the box. The reference is an integrated circuit sensor for $-40\,^{\circ}$C to $+110\,^{\circ}$C temperature range and $\pm$ 0.4 $^{\circ}$C typical accuracy at 25 $^{\circ}$C. The actual internal temperature T in degree Celsius and the positive voltage $+V$ in milivolts are related by the expression

$$T(^{\circ}C) = \frac{+V(mV) - 205}{5}$$

Battery level, a negative voltage level $(-V)$ proportional to the external battery voltage $V_{Bat}(V)$. Its actual value is expressed by $V_{Bat}(V) = 40 \times |-V(mV)|$.

After final buffering the signal is ready to be transmitted to the Remote Box and its final shape is shown in figure 7.3.

The Sensor Identification's peak-to-peak level was chosen carefully to avoid cross-talk interference on signal lines. This starts to affect analogue cables longer than 200m.

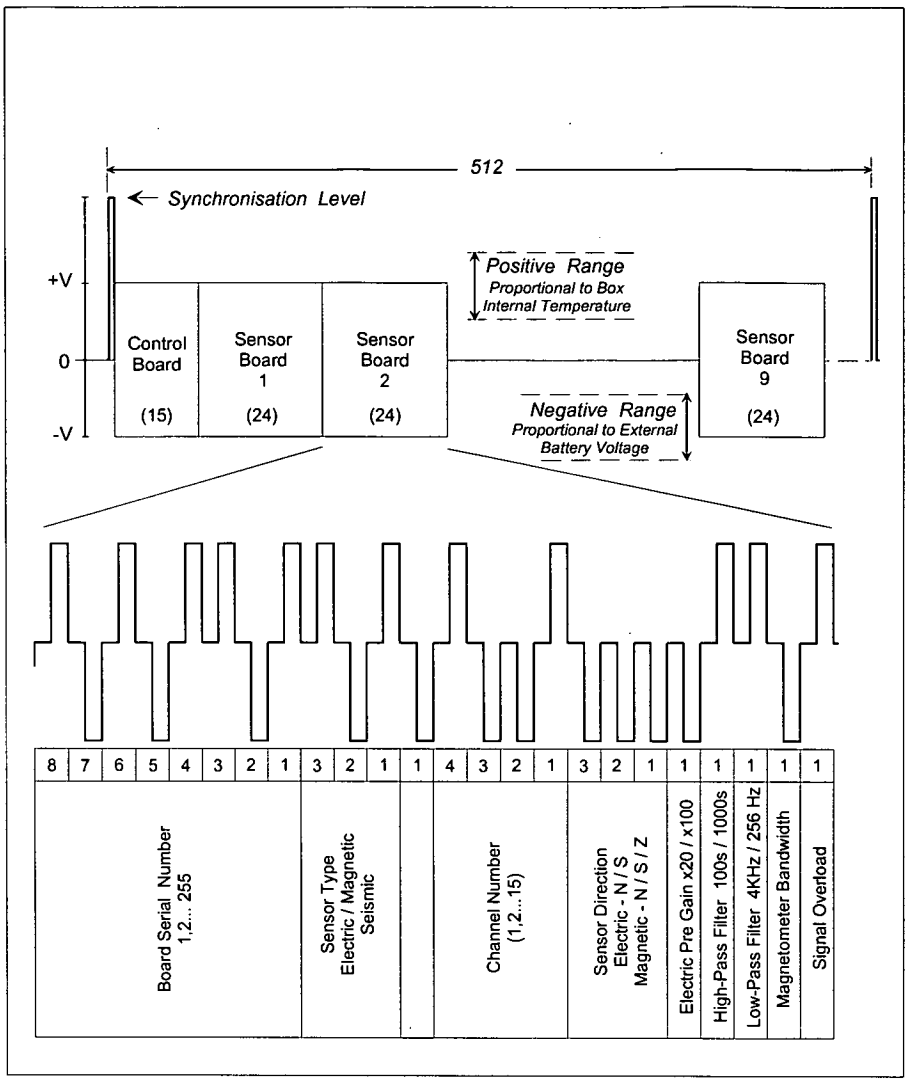

Figure 7.3: Sensor Identification Line

7.3 Electric Pre-Amplifier Board

The electric board performs the first analogue pre-conditioning (filtering and amplification) for the electric signals. The electric field is usually weak, the signal's amplitude is very small and highly affected by noise. Sometimes, there is a large DC level superimposed to the signals mainly due to generated by the electrodes and the circuitry must cope with these problems. Low power consumption and noise levels are essential. Electric boards have digital and analogue circuitry with separated ground planes and the block diagram is shown on figure 7.4.

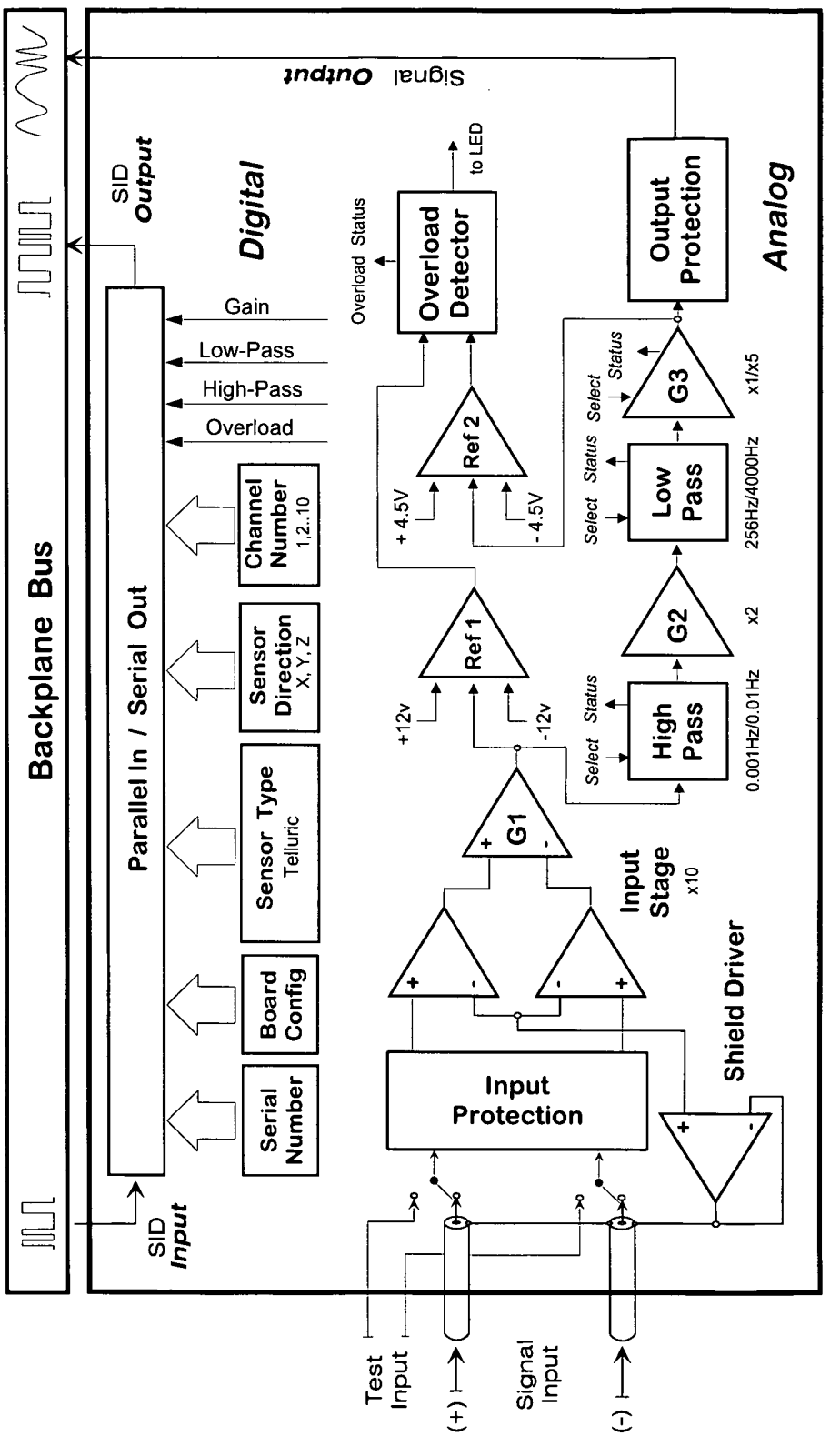

Figure 7.4: Electric Pre-Amplifier Board

7.3.1 Digital Section

As explained in section 7.2 each sensor board receives a digital serial information line from the adjacent board and adds its own identification. All this information is generated by switches on each board for serial number, board type, channel number, sensor direction and gain and by a common switch to all boards on the box's front panel for filter settings. Additional information for *overload* is also provided and will be explained in details in section 7.3.2.7.

The board's serial number is particularly important. Each board has its transfer function determined in the laboratory by a hi-precision frequency response analyser equipment. Normalized amplitude and phase responses are written into individual files whose names are associated to the board's serial number. These are used by the software to correct the frequency domain data from each sensor.

7.3.2 Analogue Section

The analog section consists of differential input amplifier, high-pass filter (0.001 and 0.01Hz), low-pass filter (256 and 4000Hz) and amplification (20 or 100). Filter corner frequencies and high-pass filter reset are asserted simultaneously in all boards by common switches. Gain is selected individually per channel by a switch on the Sensor Box panel. One signal overload indication per channel is also available on the front panel.

To design analogue preconditioning, not only is the choice of the components important but also the circuit configuration and printed circuit board layout. Before starting, some specific parameters related to the final application have to be taken into account.

Character of the application: The character of the application (inverter, follower, differential amplifier, etc.) will influence the choice of the amplifier. In electric amplifiers for MT measurements a differential amplifier is essential, since the electric fields are measured by a pair of electrodes. An instrumentation

amplifier might be considered but they usually do not allow enough control on gain, their intrinsic noise is higher than discrete operational amplifiers and fine tuning for common mode rejection is not usually possible.

Accurate description of the input signal: It is extremely important that the input signal be thoroughly characterized in terms of bandwidth and amplitude. The first step is to work out an *order of magnitude* for the signals that will be pre-conditioned, then what amplification and noise levels are required.

The sources of these electric signals are natural fluctuations in the earth's electro-magnetic field which exists over a wide range of frequencies. Figure 7.5 shows a typical graph of the magnetic field intensity. The induced telluric fields ($\mathcal{E}$) depend on the magnetic field strength ($\mathcal{H}$) and the electrical conductivity as explained by the apparent resistivity (ρ_a).

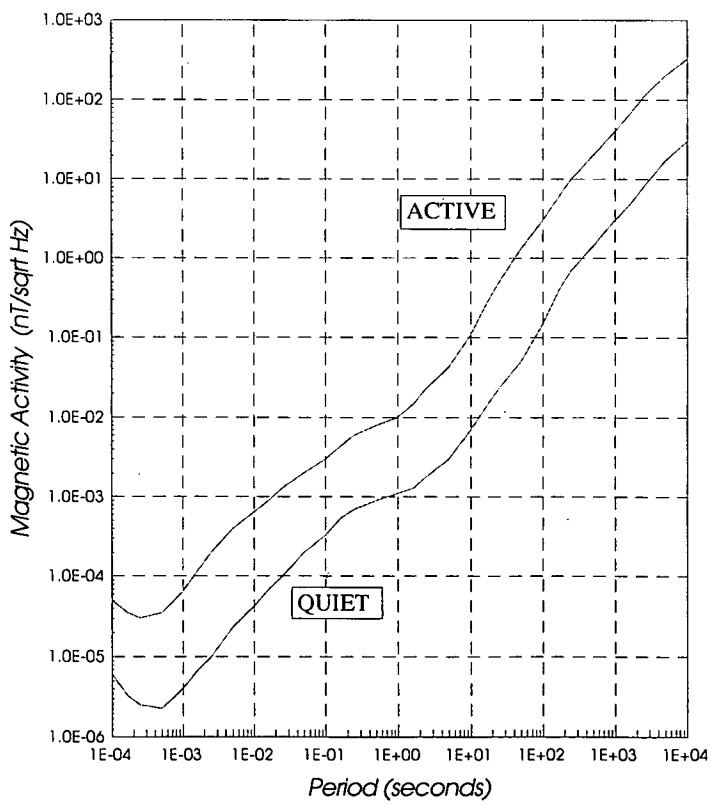

Figure 7.5: Typical Magnetic Activity Intensity

The relationship between magnetic and electric fields is given by equation 7.5. Equation 7.6 gives the factor to convert the graph of figure 7.5 into electric field densities for different values of apparent resistivity.

$$\rho_a = \frac{1}{5f}\left(\frac{\mathcal{E}}{\mathcal{H}}\right)^2 \qquad (7.5) \qquad \longrightarrow \qquad \mathcal{E} = \sqrt{5f\rho_a}\cdot\mathcal{H} \qquad (7.6)$$

Units are: ρ_a in Ω·m, f in Hz, $\mathcal{E}$ in mV/km and $\mathcal{H}$ in nano-Tesla.

The main idea of this exercise is to determine an *approximate range* for the electric signals and so the electric field density should be transformed into amplitudes. Therefore some adjustments have to be made. In a typical field configuration the distance between the electric sensors is in the order of 100m and the electric field units should be changed to mV/100m to reflect the *in-field* situation. A relative bandwidth Δf=100·f was chosen to represent a typical section of two decades in the frequency spectra. Relative bandwidth has much more physical significance at different frequencies than fixed bandwidth. Average voltage (rms) shall also be converted into peak-to-peak values. For periodic signals the relation is $V_{pp} = 2\sqrt{2}\cdot \mathrm{V}_{rms}$.

Therefore the factor to convert Electric field densities into millivolts peak-to-peak over a relative frequency bandwidth can be expressed as:

$$E(mV_{pp},\ \Delta f = 100f,\ l = 100m) \ = \ 2\sqrt{2}\times\sqrt{10f}\times\frac{\mathcal{E}}{10} = \sqrt{0.8f}\cdot\mathcal{E} \qquad (7.7)$$

Finally, equations 7.6 and 7.7 can be combined into equation 7.8 to give the conversion factor to transform $\mathcal{H}$ in nT$\sqrt{Hz}$ (fig. 7.5) into $\mathcal{E}$ in mV (fig. 7.6). Then

$$E(mV_{pp},\ \Delta f = 100f,\ l = 100m) \ = \ 2f\sqrt{\rho_a}\cdot\mathcal{H} \qquad (7.8)$$

The values of figure 7.6 derives from 'quiet' magnetic and highly conductivity ($\rho_a = 0.25\,\Omega$m) and 'active' magnetic and highly resistive ($\rho_a = 100.000\,\Omega$m) for the same relative bandwidth ($\Delta f = 100f$) and electric lines of 100m length.

The equipment frequency range is are 0.0003Hz and 2048Hz (Short-period and High-Frequency mode). The natural signal amplitudes to be accommodated for

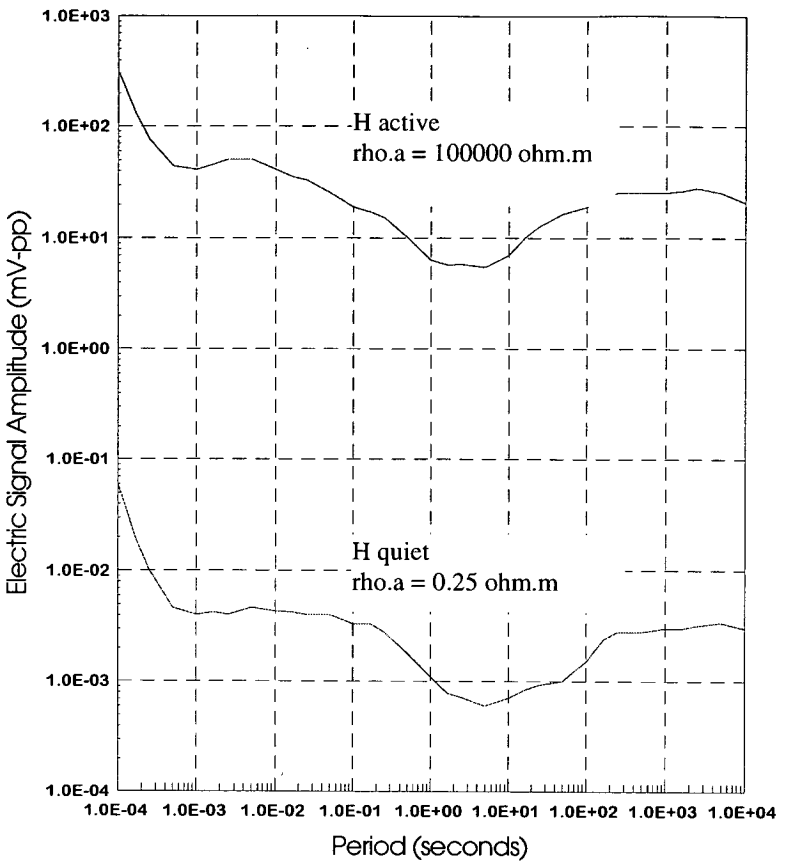

Figure 7.6: Typical Induced Electric Signals

by the pre-amplifiers within this range is between 0.6μV and 40mV. However, this range is usually extended by *man made* noise. These limits are important to the design of the amplifiers and to the calculation of the signal-to-noise relationship.

Environmental conditions: The maximum range of temperature, time and supply voltage over which the circuits must operate without readjustment should be known. MT measurements are made in extreme climates. Temperature ranges from below freezing to above 40 ° C are expected. Depending on the application, soundings are made from a few hours to several days. Supply voltage is a critical issue. Geophysics equipment is designed to operate in the field and the most suitable supply sources are batteries. The power consumption should be as low as possible to extend battery life and consequently to keep the equipment in operation as long as possible.

Accuracy desired: The accuracy should be defined in terms of the application with regards to bandwidth, DC off-set, power consumption,etc and will restrict the range of devices that can be used in the design. For instance, for battery powered equipment low power consumption is important and considering the signal levels to be measured low intrinsic noise is essential Low DC characteristics (input off-set and bias current, input off-set voltage), high common-mode and power-supplies rejection rates are also very important. Dynamic range should be as high as possible pointing to components with higher power supply limits because they cope with higher signal excursion limits (both input and output). However, the electronic industry seems to go on the opposite direction. It is far easier to find new and improved components for lower voltages, thanks to the portable applications like mobile phones and portable computers. Even though there are hundreds of operational amplifiers available, none entirely matched all the characteristics I was looking for. For instance, it is very difficult to find low noise and low power consumption characteristics for the same device. Usually, the lower the intrinsic noise is, the higher the power consumption will be and vice-versa. In the end, the choice was a compromise between these two parameters.

In addition, the design of very high impedance amplifiers introduces new sorts of problems related to the reduction of leakage paths and noise pickup. A primary consideration is to attempt to place the input device as near to the signal source as possible. Unfortunately this is impossible due the distance between electrodes and amplifiers. At printed circuit board level, the use of *guarding techniques* is essential to cope with ultra low input currents. It is achieved by applying a low impedance bootstrap potential to the outside of the insulation material surrounding the high impedance signal line. It also acts as a shield to reduce noise pickup and to reduce the effective capacitance to the input line.

7.3.2.1 Electric Inputs

Electric signals are connected direct to an input amplifier without any filtering. Source and amplifier are usually 10 to 100 meters apart and considerable care should be taken in designing the connecting lines carrying these high impedance signals. Shielded coaxial cables should be used mainly for radio-frequency noise reduction. However, use of coaxial cables for high impedance work can add problems related to cable leakage, capacitance and related noise. The best polyethylene or non-reconstituted Teflon should be used to obtain the highest possible insulation resistance. Cables should be made as rigid and vibration free as possible since cable movement can cause noise signals of three types, all significant in high impedance systems.

1. The movement of a conductor in a magnetic field generates a noise voltage.
2. Frictional movement of the shield over the insulation material generates a charge which is sensed by the signal line as a noise voltage.
3. Cable movements make small changes in the internal cable capacitance and capacitance to other objects. Since the total charge on these capacitances cannot be changed instantly, a noise voltage results as predicted from $\Delta V = Q/\Delta C$.

Noise due to cable movement is well known and its effect is practically impossible to be removed. However, the noise specific to coaxial cables (charge accumulation and discharge) can be reduced considerably by using the *Active–shield* technique which consists of connecting the cable shield to a guard potential instead of to the ground. The guard potential is usually a buffered common mode voltage at the same level as that of the high impedance lines. Therefore, there is no voltage drop across the insulator and hence no leakage or discharge. The guard will also act as a shield to radio-frequency signals. The electric boards

provide a jumper to connect telluric cables' shields either to ground or to a guard potential.

A field test showed that shielded telluric cables can attenuate radio-frequency noise better than non-shielded cables ($\approx 10\times$).

7.3.2.2 Input Protection

Equipment for field-operation usually have some input protection against over-voltage (lightning). The initial idea for the electric boards was to use transzorbs, which consists of two back-to-back, fast response avalanche diodes in the same pack. Alternatively zener diodes connected back-to-back to the ground.

Even though transzorbs are widely used for this kind of protection, they were discarded in favor of zener diodes because their specifications change among samples from the same lot yielding to a poorer common-mode rejection ratio. Two devices connected back-to-back represent to the differential input *sees* one forward plus one reverse resistance as a path to the ground. If they are mismatched, the circuit common-mode rejection which depends on component matching will be jeopardized. Zener diodes forward and reverse resistance characteristics' deviation among samples from the same lot are more consistent than transzorbs, as can be seen in table 7.2. Another problem arising from input protection devices is the noise generated by any electronic component.

Transzorbs			**Zener Diode**		
Sample	Rf (MΩ)	Rr (MΩ)	Sample	Rf (MΩ)	Rr (MΩ)
T1	1.74	8.37	Z1	4.32	>20
T2	1.83	12.56	Z2	4.35	>20
T3	1.71	9.40	Z3	4.39	>20
T4	1.47	4.52	Z4	4.39	>20
T5	1.54	7.70	Z5	4.30	>20

Table 7.2: Protection devices characteristics

However, taking into account all problems arising from input protection circuitry, it has been decided not to use them at all because it is better to take the risk of having the board destroyed than to have additional noise at all times. Electronics are getting cheaper and the circuit will be hardly protected by any device in case of serious hazard.

7.3.2.3 Input Stage

The input stage is a high input impedance true-differential configuration using precision operational amplifier devices. This stage is the most complex stage to be designed. The noise generated at this stage should be as low as possible because it will be amplified and propagated all the way through, this including the active device's intrinsic noise and the thermal noise generated by passive components. However, resistance values cannot be as low as desirable because it increases the power consumption. The gain should be as high as possible because all noise generated by subsequent stages will be divided by previous gain stages to reflect the *input-referred noise*. It wouldn't be a problem for accommodating induced electric signals'range (0.6μV to 40mV). However, these natural signals are usually superimposed to DC levels from the electrodes or noise from mains power (50Hz) and radio-frequency which will be amplified by the same gain leading to saturation. In practical terms, for an input-stage gain of 10, the limit for this *composite* signal is around $\pm$1V before overloading. Due to its very high input impedance, the current flowing into the active device is extremely low.

Input stage components are matched within 0.1% tolerance. Common-mode rejection potentiometer can be tuned to provide 120dB attenuation. To reduce the noise the signal bandwidth is limited at each amplifier and to allow a higher dynamic range, the circuitry is powered from regulated and low-pass filtered $\pm$12V power supplies.

7.3.2.4 High-Pass and Low-Pass Filters

They are both first-order filters. The main function for the High-pass filter is to block DC voltages from the electrode's self-potential and operational amplifier DC noise (voltage and current off-set). The main function for the Low-pass filter is to limit the high-frequency spectra and avoid unnecessary noise. Both filters' circuitry are highly modular and their corner frequencies can be changed if necessary. So far, the components have been chosen so that frequencies of 0.01 Hz and 0.001 Hz can be set for the High-pass filter and 256 Hz or 4000 Hz for the Low-pass filter. Electric boards should have as identical frequency response functions as possible and filters play an important role. Accurate low-pass corner frequencies are easier to achieve than hi-pass frequencies. The latter usually needs higher resistance values which are not available within 0.1% tolerance. To meet the specifications and avoid mismatches among boards filter components are selected individually leading to corner frequencies matched within 0.1% range. Figures 7.7 and 7.8 show a typical electric board transfer function.

7.3.2.5 Output Stage

This stage provides the final gain to the electric signals and drives them into the analogue cable. The gain is externally selected for 1 or 5, which in conjunction with two more fixed gain stages gives the total gain of 20 or 100 as labeled Lo/Hi on electric panel. The circuit configuration will determine the output impedance of the boards. The output impedance for the non-inverting closed-loop configuration is less than 1Ω. Even though lower output impedance is important for driving purposes it takes to much power and it is usual to increase the impedance by connecting an external resistor $Ro_{(Ext)}$ in the signal path between the amplifier and the signal output. This will firstly, limit the maximum current sunk/driven by the device protecting from overcurrent (the component might be irreversibly damaged). In most cases devices are protected internally so this precaution is not necessary. Secondly, and more importantly, is to isolate the device output and the

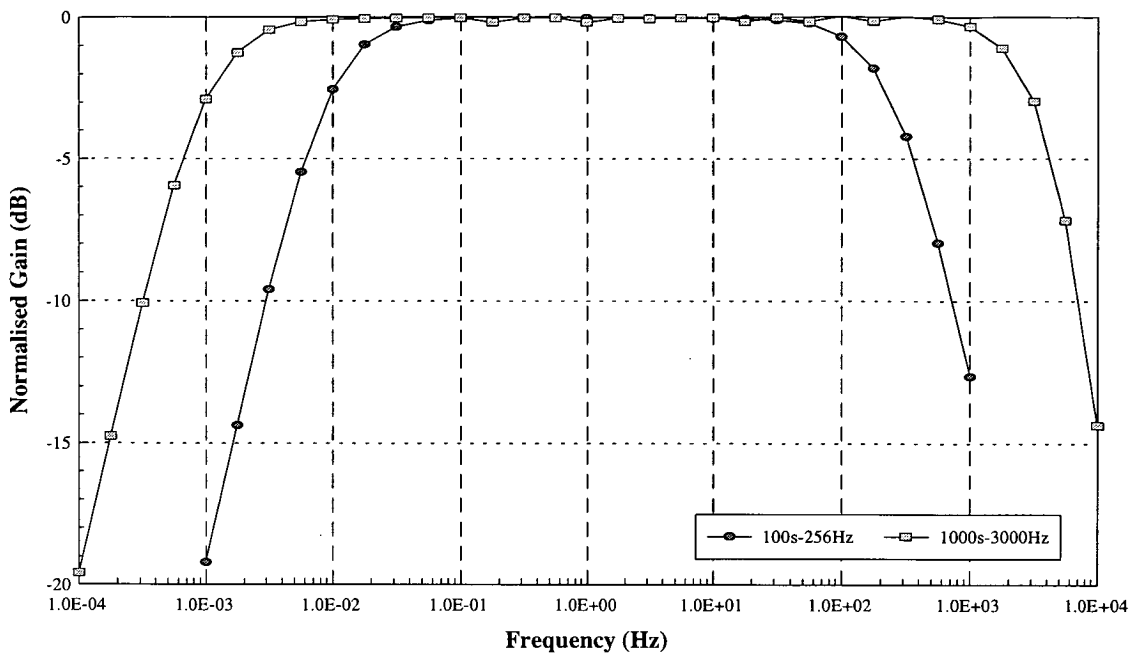

Figure 7.7: Electric Pre-Amplifier board Transfer function - Gain

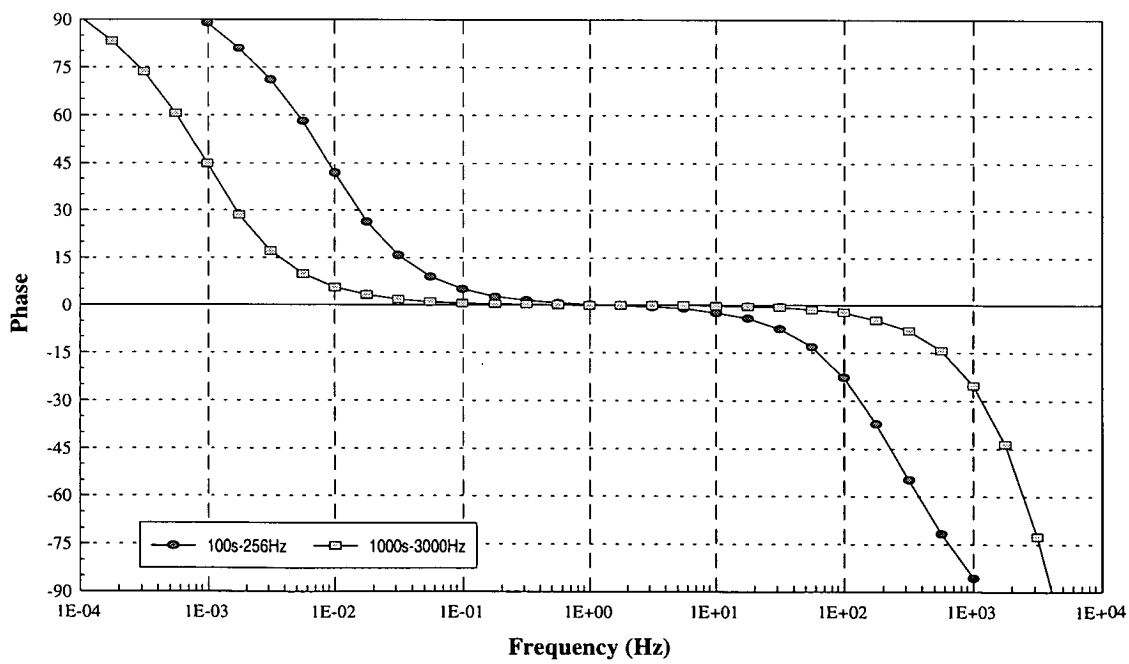

Figure 7.8: Electric Pre-Amplifier board Transfer function - Phase

capacitive load due to the analogue cable. Capacitive load changes the loop-gain characteristics leading to oscillation. This is more critical for low-gain operations (mainly unity-gain). Then, the board's output impedance can be expressed as:

$$R_o = Ro_{(Ampl)} + Ro_{(Ext)} \quad \longrightarrow \quad R_o \approx Ro_{(Ext)} \tag{7.9}$$

The output impedance $Ro_{(Ext)}$ and the cable characteristics are important to determine the cable's frequency response (equation 7.1). Usual values for multicore cable resistance are between 50–100 Ω/Km, which gives a maximum of 10 Ω for 100 meters cable. Practical values for $Ro_{(Ext)}$ are between 10 and 500Ω.

In section 7.1.1, the frequency dependent signal distortion as a function of the cable lengths was mentioned and the importance of using analogue cables with the same length for connecting Remote and multiple Sensor Boxes in high-frequency mode justified. All the considerations made at that stage were based on a fixed value for the amplifier's output impedance ($R_o = 100\Omega$) and the analysis focused on the cables length.

Now, let's analyse what happens in terms of response function for different combinations of analogue cable length and amplifier output impedance and then justify why all amplifiers in the same Sensor Box should have the same output characteristics.

The exercise consists in determining the signal attenuation and the phase shift at different frequencies as it is in table 7.1 and for different values of the output impedance R_o (1Ω, 10Ω, 50Ω and 100Ω). It is also important to consider the magnetic sensors, since they are connected to the Sensor Boxes and drive the magnetic signals through the same analogue cable. The output impedance of induction coil magnetometers *without additional pre-conditioning* can be $R_o = 500\Omega$ (also considered in graphs). The phase distortion, which is far more critical than the amplitude attenuation, is plotted on graphs 7.9 and 7.10 for short-period and hi-frequency limits of SPAM Mk-III operation modes (128Hz and 2048Hz respectively).

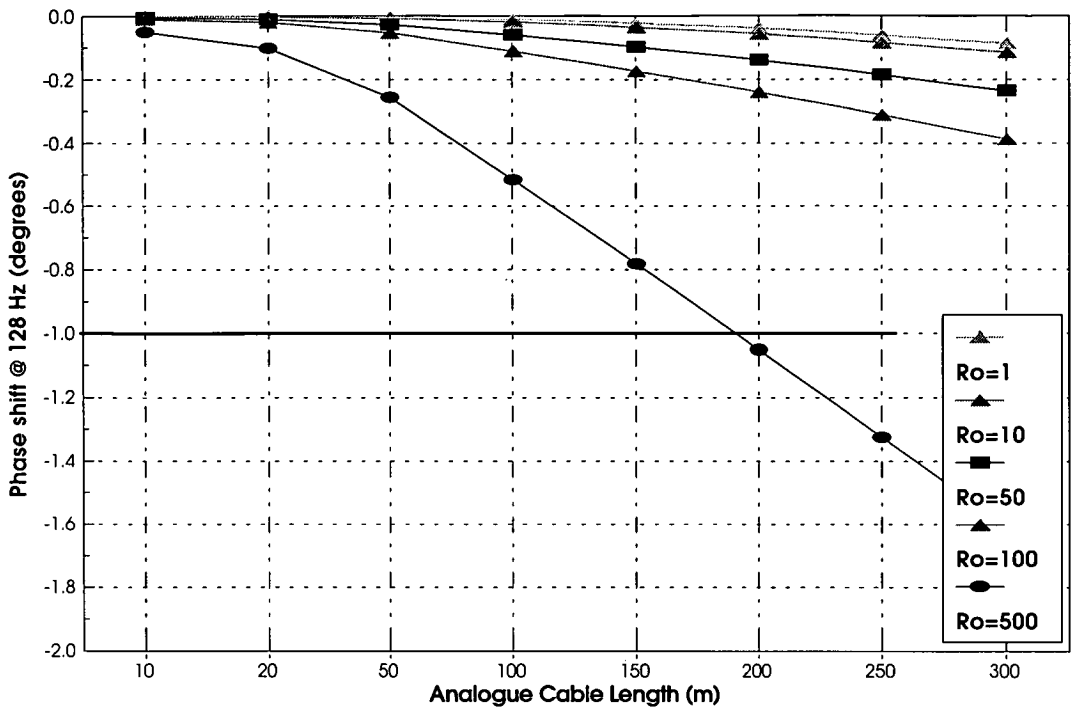

Figure 7.9: Phase Shift for Short-Period mode

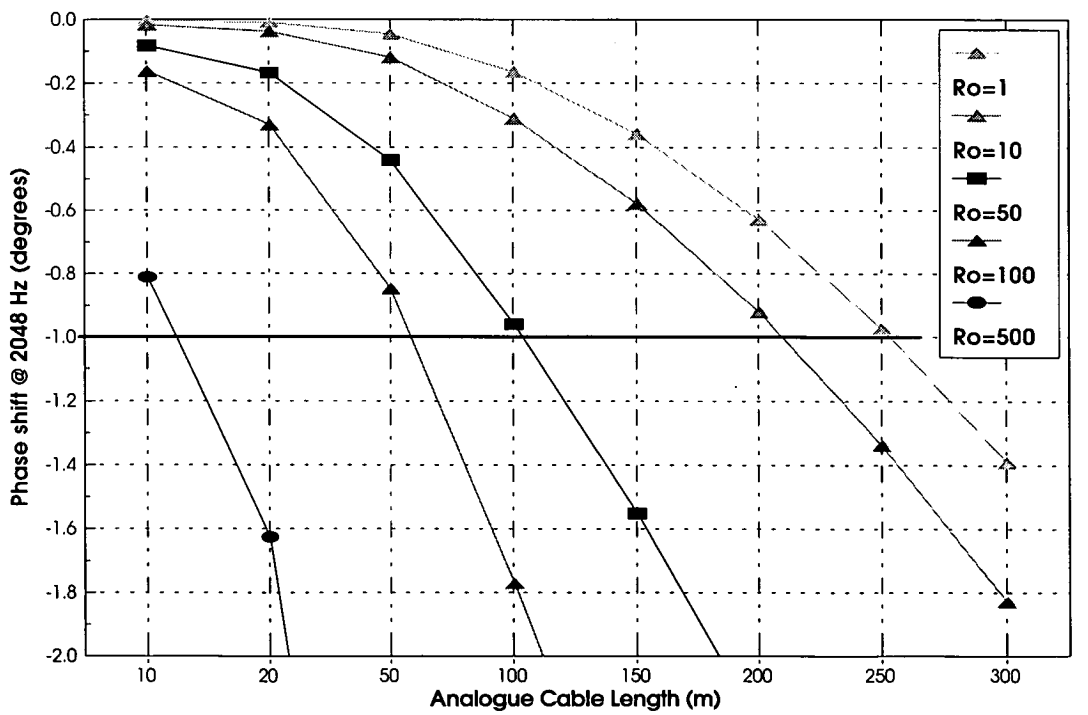

Figure 7.10: Phase Shift for Hi-Frequency mode

For the Short-Period mode, all phase shifts are within 1 ° for $R_o < 100\Omega$ and cable length up to 300m. For R_o=500Ω phase shifts in the order of 1 ° will be experienced for cables longer than approximately 100m. For the High-Frequency mode, the phase distortions are more noticeable and the phase shift limit (< 1 °) are preserved for analogue cable length mismatches within approximately 15m for all values of R_o.

The above exercice shows the importance of matched output amplifiers in all sensor boards to avoid relative phase errors due to different cable lengths and also that the value of the common output resistance sets the limit for analogue cable mismatches in multi-sensor operation.

The magnetic boards include identical output amplifier stage as the electric boards to buffer the output signals from the magnetometers and to match the output impedance of these boards no matter the output characteristics of the magnetometers.

The value of the output resistance common to all boards is $R_o = 50\Omega$ to provide reasonable power consumption and device protection and to keep phase errors within limits for practical analogue cable mismatches (100m for the high-frequency mode).

7.3.2.6 Output Protection

The output protection circuitry function is to limit the signal level to protect the input of the Channel board in the Remote Box. In the first version it was performed by two zener diodes back-to-back that clipped the signal at ±4.5V. In the present version the input device of the Channel boards include an internal protection against overvoltage and the output protection is no longer needed.

7.3.2.7 Overload Detector

There are two distinct overload sections: DC and AC. The first samples the signal after the first amplifier and indicates an overload when the voltage is higher than 10 volts. At that stage the signals have DC components superimposed because they have not been blocked yet by the high-pass filter. Overload in the first stage indicates DC potentials up to $\pm 1\,V$ at the inputs. The second stage samples the signal at the output and indicates an overload when the signal reaches ± 4.5 volts. At that stage all DC components have been blocked and an overload will reflect AC signals as high as 250 mV or 50 mV according to gain of 20 or 100 respectively. Gain too high and/or 50 Hz noise might be the reason. The overload output is common to both stages and it is impossible to identify which section set the overload indicator. However, for low-gain and short-period operation it is very unlikely that an AC overload occurs, except of course, on a noisy site, where interference from mains supply is strong. In most cases the overload is triggered by a high DC level at the electric inputs. Another common reason for overloading is an open-circuit at the electric input due to bad connection between amplifier and electrodes, which is very easy to trace.

7.4 Noise Characteristics

One important consideration on designing pre-amplifiers for low-level signals is noise. The choice of the active device (transistor, FET or operational amplifier), the circuit configuration and the resistor values are very important to achieve good results. In particular, the design of the input amplifier requires special attention because the noise generated at that stage is amplified through the circuit and usually contributes considerably to the total noise figures. However, the final choice does not depend only on noise requirements but also on other characteristics such as power consumption. Usually low-noise operational amplifier have higher power consumption and are not suitable to be used in battery

powered equipment. In addition, the noise figures of the pre-amplifier have to be considered in conjunction with other sources of noise particular to the type of application. The purpose of the pre-amplifier board is to provide amplification and filtering for electric signals measured by a pair of electrodes. The noise generated by the electrodes is usually higher than the noise generated by the circuitry (intrinsic noise) and should be used as a reference for the design. The circuit noise parameters may be relaxed in favor of power consumption if compared to the electrode noise because probably the later will be predominant. Electronic circuit noise figures (intrinsic noise) is difficult to be calculated and measured accurately due to the wide range of parameters involved. Noise calculation depends on the characteristics of the active device used (transistor, FET or operational amplifier), the circuit configuration and the frequency range of operation. However, it is possible to work out approximate figures for the design based on component parameters and knowledge of noise mechanisms. It is very important to have an idea of the noise generated by individual stages and their contribution to the total circuit noise because at the design stage it is always possible to modify the circuit configuration, component type and value to achieve better results.

The sensor board uses operational amplifiers for amplification stages, whereas the filters are passive. Part of the theory related to noise mechanism and characteristics in general, noise related to operational amplifiers and some equations to calculate noise figures are presented in section 3.2.2. In this section, the noise generated by the electrodes and the effect of electrodes as source resistance for the input amplifier are mentioned. Also, the order of magnitude of the noise generated by some electrodes are presented.

Figure 7.11 is a simplified block diagram of the sensor board and shows approximate noise density figures for individual stages and for all possible combinations of amplification and filters. The noise generated by one stage is combined with the noise generated by the next stage, the resultant noise amplified and combined with

additional sources of noise in subsequent stages. The final noise is then divided by the gain of the signal path to reflect the input referred noise (RTI), which is the usual way to represent the circuit noise. The noise characteristics of the amplifier used (LT 1013) are: Input noise voltage density ($f_0 = 1000\text{Hz}$) $= 22\text{nV}\sqrt{Hz}$ and Input noise current density ($f_0 = 10\text{Hz}$) $= 0.07\text{pA}\sqrt{Hz}$.

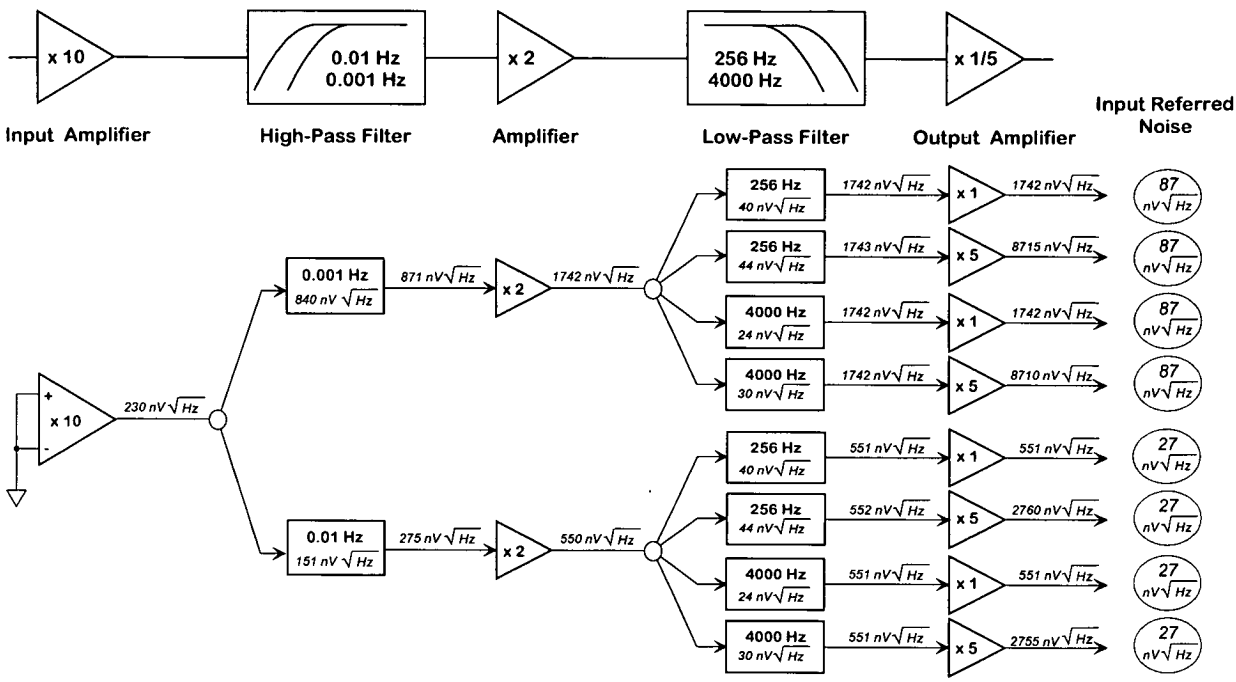

Figure 7.11: Electric Pre-Amplifier Board - Noise Calculation

The highest input-referred noise ($87\text{nV}\sqrt{Hz}$) is obtained when the 0.001Hz high-pass filter is used, regardless the low-pass filter and output gain settings. It can also be observed that practically all noise in the circuit is due to the high-pass filter stage which generates $871\text{nV}\sqrt{Hz}$ ($87.1\text{nV}\sqrt{Hz}$ RTI noise). The reason for the high noise at this stage is the value of the resistor needed to obtain the 0.001Hz corner frequency (10.4MΩ). The input noise current density of the next stage (x2) in conjunction with the resistor produces approximately $730\text{nV}\sqrt{Hz}$ of noise. The thermal noise generated by this resistor is $413\text{nV}\sqrt{Hz}$ (Equation 3.5). The noise due to this resistor (Equation 3.6) produces the total noise of the stage.

The lowest input-referred noise ($27\text{nV}\sqrt{Hz}$) is obtained when the 0.01Hz high-pass filter is used. The input amplifier ($230\text{nV}\sqrt{Hz}$) and the high-pass filter ($151\text{nV}\sqrt{Hz}$) are the noisier stages. Even though the noise of the high pass filter stage contributes to the total noise, it is no longer the main source. The resistor used for the 0.01Hz corner frequency (1.043MΩ) does not dominate the results. It can be seen that the input amplifier is the main source of noise and when referred to the input ($230\text{nV}\sqrt{Hz}/10=23.0\text{nV}\sqrt{Hz}$) it represents approximately 85% of the total noise. Furthermore, a comparison between the noise of the first stage (RTI) and the voltage noise characteristics of the device ($22\text{nV}\sqrt{Hz}$) leads to a conclusion that the device sets the total noise. There are devices with better noise characteristics few with lower power consumption for the same noise (0.31mA per amplifier for LT 1013).

Accurate noise measurement is even more difficult. In addition to the intrinsic noise of the circuitry there will always be noise picked up from radio frequency sources, noise due to grounding loops and poor connections. However, the peak-to-peak noise generated by an equipment can approximately be measured. The set-up consists of shorting the inputs and monitoring the output signal (which is mainly intrinsic noise). A similar setup was used in the laboratory to observe the noise of four electric boards. SPAM Mk III was used to process and display the time series as shown in figures 7.12 and 7.13 for two decades at higher frequencies and longer periods (Band 0 and Band 10 respectively).

The calculated noise (Fig.7.11) and the observed noise (Fig. 7.12 and 7.13) cannot be compared directly. The reasons are:

1. The calculations are based on device characteristics at higher frequencies (1000Hz for the voltage noise and 10Hz for the current noise densities). At these frequencies the noise is characterized by a uniform spectral density e.g. the noise in the range between 1Hz–101Hz is the same as in the range 200Hz–300Hz (Δf=100Hz). This noise is called *white noise*. A more accurate calculation would require that voltage and current density noises

were calculated taking into account the so called *pink noise* region, where the noise characteristic varies with the frequency as $1/f$ (see Section 3.2.2). The division between white and pink noise regions depends on the device but usualy is between 1Hz–10Hz.

2. The transformation from noise density into noise peak-to-peak takes into account the frequency bandwidth, not only the analogue filters but also the frequency bands determined by the softare have to be taken into account.

3. Noise should be interpreted on a statistical basis due to its random characteristics. This is used to establish the factor to convert V_{rms} into V_{pp} such as a reasonable percentage of converted events will probably fall within the peak-to-peak range. This is known as *crest factor*. Usually CF=6 is used to include approximately 99.99% of the rms values within the peak-to-peak limits ($V_{pp} = CF \times V_{rms}$).

Figure 7.12 shows that the maximun peak-to-peak noise is approximately 250nV for signals within the frequency range between 128Hz–32Hz ($\Delta f \approx$100Hz) when observed during 1 second. In this band the *white noise* is predominant.

Figure 7.13 shows peak-to-peak noise less than 150nV for signals within the frequency range between 0.125Hz–0.031Hz ($\Delta f \approx$0.1Hz) when observed during 17 minutes. The main contribution to the noise in this band is due to the *pink noise.*

Noise observed in Band 0 is higher and the bandwidth is the main factor. In addition, higher frequency bands are more prone to radio-frequency and 50Hz noise. Thus higher noise figures for Band 0 are expected.

In general, the noise figures are very encouraging mainly because they were achieved in conjunction with a power consumption of 6mA per board ($\leq$150mW).

Another important characteristic that can be observed from figures 7.12 and 7.13 is that the noise in all boards has the same order of magnitude (average

and peak). This is very important in applications where measurements are taken relatively as they are in the Magnetotelluric method.

Noise can be specified in terms of density over a bandwidth e.g. $nV\sqrt{Hz}$ or peak-to-peak (maximum) value for a specified frequency range in voltage units. In voltage comparator applications, such as A/D converters and precision multivibrators, accuracy and resolution are affected by *instantaneous* values of noise. In these situations the expected peak-to-peak value of noise is of more concearn than the rms value. Therefore, peak (or maximun) values of noise should be specified.

7.5 Magnetic Board

Magnetic boards utilize the same printed circuit board lay-out as the Electric boards. Signals from magnetometers are connected in *non-balanced* or *grounded* mode. There is no amplification nor filtering on board since these functions are usually performed by the magnetometers themselves. However, these stages can be populated if required. One important difference between electric and magnetic boards is that the latter has to supply power to the magnetometers. The same low-dropout linear regulators that provide power to the board's circuitry deliver power to the sensos. Some magnetometers require higher voltages and currents than others and cannot be powered through the magnetic board. These need an additional power supply board. In this case the power supply from the sensor boards is disabled.

7.5.1 Digital section

The magnetic and electric board have identical digital circuitry for board configuration and identification purposes as explained in 7.3.1.

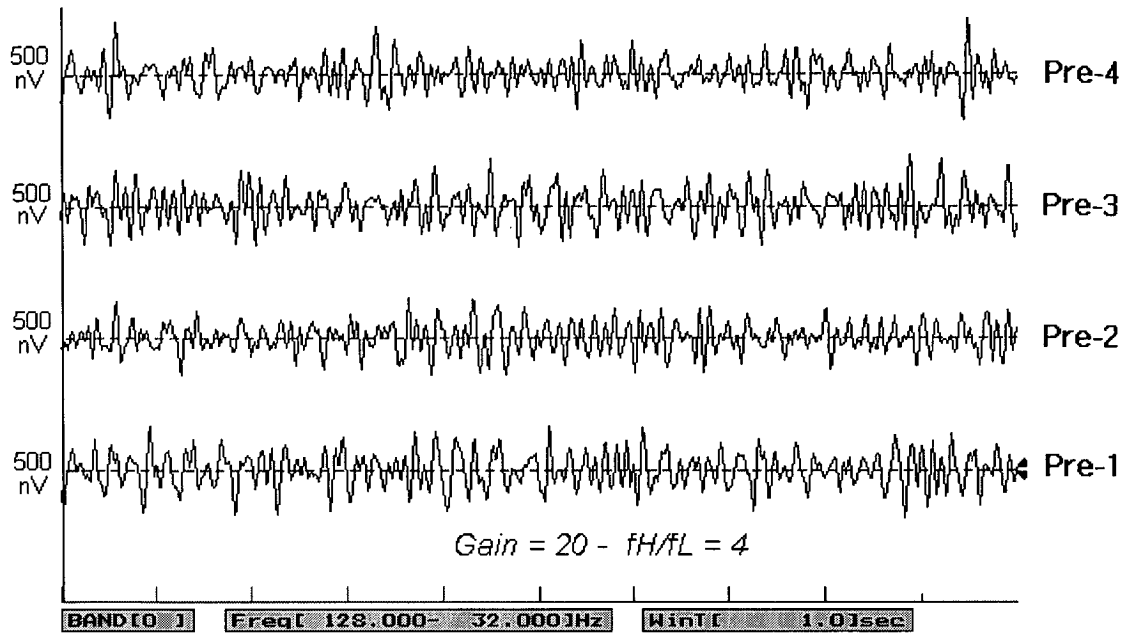

Figure 7.12: Electric board Input Referred Noise in nanovolts for Band 0 128Hz–32Hz ($\Delta f = 4$) observed during 1 second.

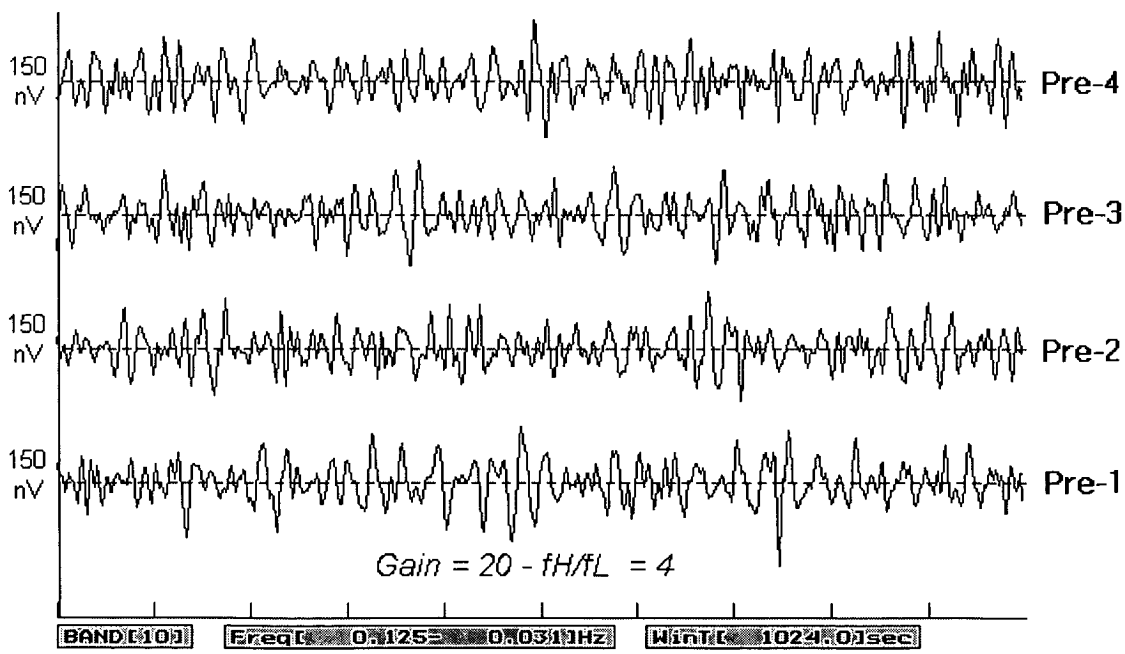

Figure 7.13: Electric board Input Referred Noise in nanovolts for Band 10 0.125Hz–0.031Hz ($\Delta f = 4$) observed during 1024 seconds.

7.5.2 Analogue section

The analog section of the magnetic boards consists of output amplifier, to buffer the magnetometer output and provide to the magnetic signals the same output characteristics as the electric signals and overload stage. There is neither signal filtering nor amplification because these functions are usually performed by the magnetometers. However these stages can be included if needed.

7.5.2.1 Output Stage

There is an unity-gain output amplifier for driving the signals into the analogue cable at the same output impedance (R_o) as the electric boards for reasons explained in 7.3.2.5. Some magnetometers have output impedance as high as 500Ω. If un-buffered, the phase shift between electric and magnetic signals at hi-frequencies would be beyond standards, as can be seen on figure 7.10. This procedure is essential to equalize magnetic and electric signals output characteristics.

7.5.2.2 Overload Stage

This stage is also identical to the electric boards and is explained in 7.3.2.7. The difference is that only the second AC section is used.

7.5.2.3 Calibration facilities

A calibration signal is also available. Some magnetometers have a second coil for calibration purposes which can be used in conjunction with this signal.

These can be useful to compare magnetometer frequency response characteristics in the field or laboratory. The operation consists of connecting a test signal to the coils and processing the output signals. This experiment has been carried

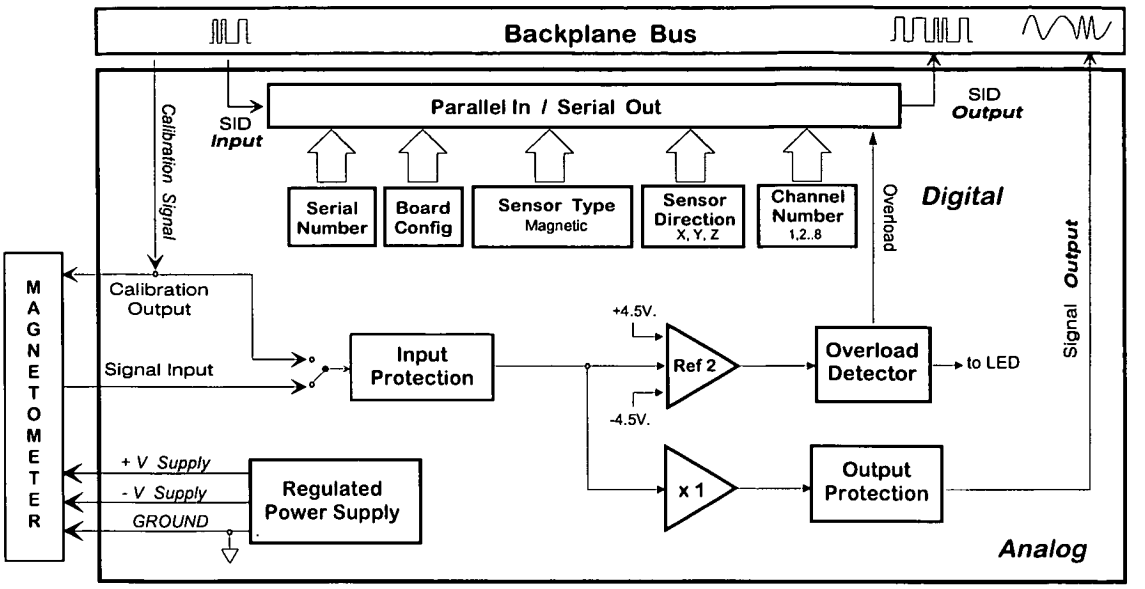

Figure 7.14: Magnetic Board

out in the field to compare three CM11-E induction coil magnetometers and results are shown in figure 7.15 which shows relative amplitude and phase errors for frequency bands 1 to 3 (128Hz to 1Hz). These results are reliable from 64Hz to 1Hz. At higher frequencies radio-frequency noise can influence the measurements leading to inaccurate results. For lower frequencies longer integration time would be necessary. The experiment was carried out with the coils buried. This means the calibration was performed with natural magnetic signals added to the test signal. However, reasonable results were achieved for both amplitude and phase errors.

CALIBRATION LISTING : [Esc = exit] [# = set DSP]

	Amplitude	%err	mean.uV	0	1	2
0	128.00	13.74	33.4	8.8	-3.8	-5.0
0	64.00	2.14	124.2	0.5	0.8	-1.3
0	32.00	2.35	196.2	-0.5	1.4	-0.9
0	16.00	2.30	169.7	-0.1	1.2	-1.1
1	8.00	2.45	244.3	-0.1	1.3	-1.2
1	4.00	2.47	175.4	0.1	1.2	-1.3
2	4.00	2.21	163.2	0.0	1.1	-1.1
2	2.00	2.18	251.4	0.0	1.1	-1.1
2	1.00	2.18	176.4	-0.0	1.1	-1.1
3	1.00	2.10	170.4	0.0	1.0	-1.1

	Phase	deg.err	mean	0	1	2
0	128.00	4.03	-136.7	-2.5	0.9	1.5
0	64.00	1.33	-162.7	-0.8	0.2	0.6
0	32.00	0.32	95.2	-0.2	0.1	0.1
0	16.00	0.29	-98.8	-0.1	0.0	0.1
1	8.00	0.17	123.1	0.0	0.1	-0.1
1	4.00	0.08	98.7	0.0	-0.0	-0.0
2	4.00	0.06	67.8	0.0	-0.0	-0.0
2	2.00	0.11	-25.2	0.0	-0.1	0.0
2	1.00	0.36	-156.5	0.2	-0.2	0.0
3	1.00	0.35	-6.2	0.2	-0.2	0.0

Figure 7.15: Results for three CM11 induction coils' *in field* calibration

7.5.3 Magnetometers used with SPAM Mk-III

Three models of magnetometers have been used regularly by the equipment in conjunction with the magnetic board. Table 7.3 shows some characteristics which are important for interfacing purposes. The Sensor Box includes an additional module (printed circuit board) to provide the signal to switch those magnetometers which operate in more than one frequency band. The power supply for these modules derives from the external battery due to the highly inductive load and consequently high current transients. For those magnetometers which requires an additional power supply module the same printed circuit boards contain power supply and switching circuitry. Figure B.1 shows typical Sensor Box internal wiring diagram including the magnetometer switching module.

Table 7.4 contains additional specifications for Model CM11E Induction coil Magnetometer because this sensor was used in the field experiments described in Chapter 9.

Manufacturer	ECA	ECA	Metronix
Model	CM11E	CM216E	MFS05
Type	Induction Coil	Induction Coil	Induction Coil
Operation			
Sensitivity (mV/γ)	50	100	800
Frequency Range (Hz)	0.0125–100	4–4000	0.00025–8000
Bands	1	2	2
Output Impedance (Ω)	475	475	$\approx$500
Calibration Coil	YES	YES	YES
Power Supply			
Voltage (V)	$\pm$ 10 to $\pm$ 15	$\pm$ 10 to $\pm$ 15	$\pm$ 15 $\pm$ 10%
Current (mA)	$<$ 30	$<$ 30	$<$ 50
Additional Power Module	NO	NO	YES

Table 7.3: Magnetometers used with SPAM Mk-III

Operation	
Sensitivity	50mV/γ
Range	0.0125Hz - 100Hz
Calibration Coil	1mV/mV
Background Noise Spectra	13.0 m$\gamma/\sqrt{Hz}$ @ 0.025Hz
	5.50 m$\gamma/\sqrt{Hz}$ @ 0.05Hz
	1.80 m$\gamma/\sqrt{Hz}$ @ 0.1Hz
	0.40 m$\gamma/\sqrt{Hz}$ @ 0.5Hz
	0.16 m$\gamma/\sqrt{Hz}$ @ 1.0Hz
	35.0 m$\gamma/\sqrt{Hz}$ @ 10Hz
	21.0 m$\gamma/\sqrt{Hz}$ @ 80Hz
Power Supply	
Voltage	$\pm$ 10V to $\pm$ 15V
Current	$<$ 30mA
Mechanic	
Length	1090mm
Diameter	98mm
Weight	13.4kg
Temperature	
Operation	-30 $^\circ$C to 60 $^\circ$C
Storage	-50 $^\circ$C to 60 $^\circ$C

Table 7.4: CM11E Induction Coil Magnetometer Specifications

CHAPTER 8

The Digital Repeater Box

8.1 Introduction

The Repeater Box is needed to improve the long distance digital communication between boxes (Base and Remote, Remote and Remote)

Some geophysical applications, such as Remote Reference, require long distances between sites. Sometimes Base and Remote Boxes must be several hundred meters apart for logistics reasons. In both situations the digital communication between these modules should cope with long distances and high speed without data integrity loss.

The digital cable used by the equipment (four twisted pair, shielded) is supplied either in 100 meters or 500 meters reel and two or more cable sections have to be joined where the application requires a digital communication length greater than the available cable sections.

The easiest way to connect two or more sections is to use a passive back-to-back connector and this method is regularly used in the laboratory to test the digital communication at distances greater than 500 meters e.g. to study the Communication board data throughput, as described in Chapter 5 Section 5.9.1. The results were explained in the same section.

An alternative and more sophisticated method to join two cable sections is to use active devices to *regenerate* the signal and give it enough power to overcome the next stage. This technique improves the communication and longer distances at higher speeds can be achieved. Theoretically there is no limit for the number of Repeater Boxes included in the digital path. Three of them were used in the past to cope with 1600 meters distance between two sites in a Remote Reference application (Ritter 1995).

8.2 Module Overview

The Repeater Box provides signal regeneration for an external link system *Sys A, Sys B, Data In* and *Data Out.* The lines labelled *Sys A* and *Sys B* usually carry the control signals Reset and Time Sync but can be reconfigured if needed. The module is highly portable due to its size and weight. The power consumption in normal operation is approximately 45 mA. An internal battery provides the power for the module but the power supply is activated only if the digital cable is connected to the box to prevent wasting energy. Solid state ultra-bright LEDs indicate the signal flow and this feature is very useful for maintenance purposes. The Repeater Box block diagram is show in figure 8.1. There is total compatibility between the Repeater Box and the Communication boards. The digital connector and internal cables are the same. In case of hardware failure the active electronics can be by-passed completely and the box acts like a passive junction between two cable sections. However there will be no signal regeneration and the constraints related to long distance digital communication explained in subsection 5.8.2 have to be considered.

8.2.1 Power Supply

The power source for the box is a 6V/4Ah, rechargeable internal battery. It lasts approximately 90 hours and can be recharged while in operation by a 12V

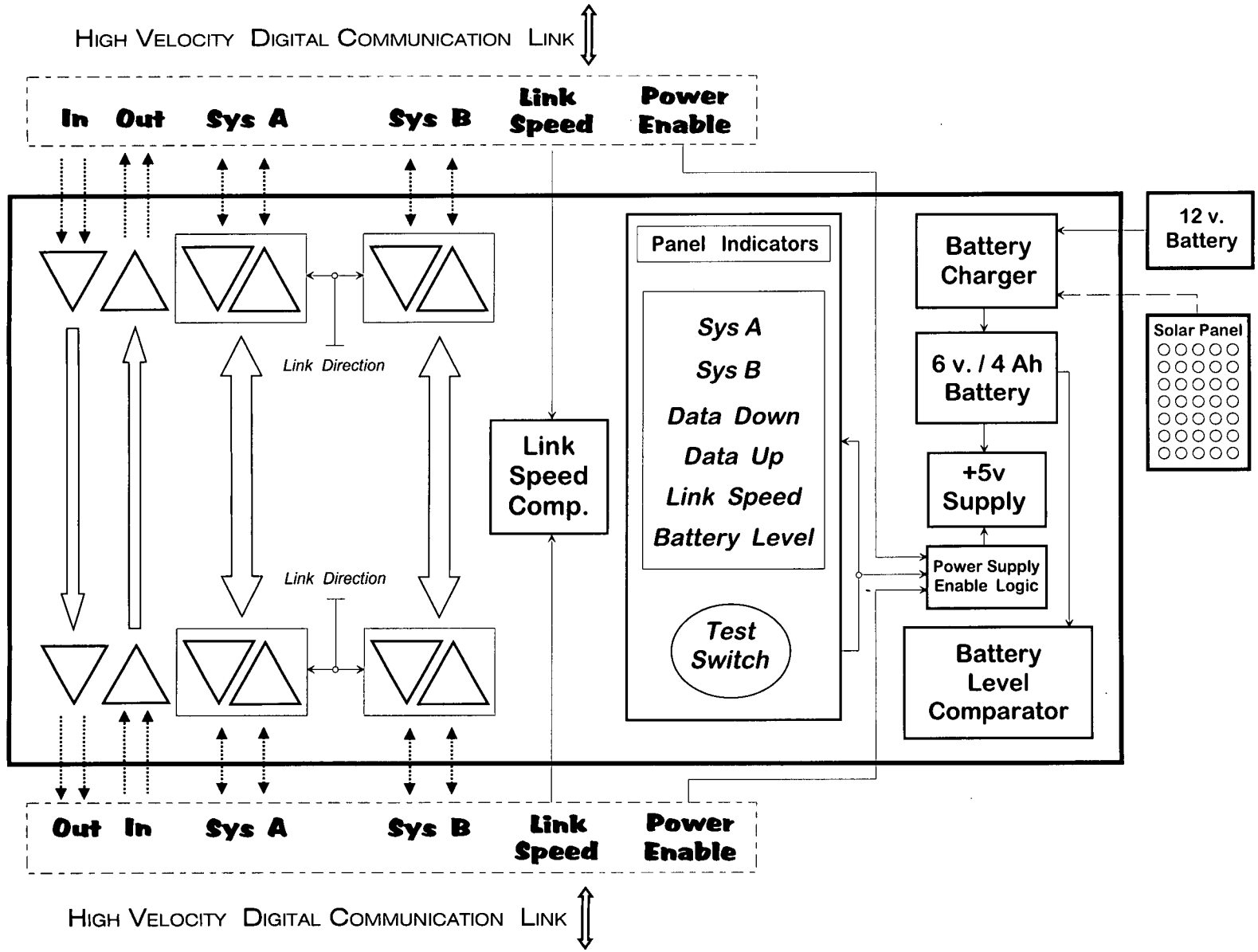

Figure 8.1: Digital Repeater Box - Ver.1

external battery. Alternatively , a small solar panel can be used e.g, a low-power polycrystaline silicon module 1W can supply up to 150mA with illumination of $1kW/m^2$. Not only does it supply charge for the running circuitry but also charges the internal battery. They are quite small and fit on the top of the box. Dimensions in millimeters are 161 (L) x 139 (W) x 10 (D). It can be a very good power option wherever possible.

There is a low dropout, low power consumption regulator between the external power source and the internal battery. It provides the voltage level and the current limit to charge the sealed lead-acid battery.

The +5V internal supply is generated by a micropower regulator with comparator and shutdown. The dropout voltage, which is the voltage difference between input and output, is quoted as 0.15V at 50mA. It means that the device is able to keep +5V regulated output as long as the input voltage is higher than 5.15V. In practice, it extends the operation without recharging the internal battery by at least 50% compared with other devices with higher dropout voltage (usually 0.5V). A very important facility is the possibility of logic shutdown of the output. In this mode, the power consumption is only 1.3mA. This is the default mode whenever the box is not in use to keep the internal battery charge as much as possible. The internal power is enabled automatically whenever at least one out of three conditions exists.

1. A digital cable is connected to the box. It corresponds to a normal operation where the Repeater Box is in between two digital cable sections.

2. The test momentary switch is pressed. It enables the LED indicators circuitry. It is useful for monitoring the battery level in any occasion.

3. The internal configuration jumper is changed. It disables the shutdown facility and should not be changed.

8.2.2 Signal Regeneration

The signal regeneration is performed by four independent RS-485 standard, low power transceivers. Each signal is received in differential mode, converted into a single-ended signal and reconverted again into differential mode. The signal's amplitude, which has been attenuated through the cable, has its amplitude recovered to the original level but not the pulse width. The regeneration process takes place in approximately 100 nanoseconds, which is the delay equivalent to a 20m digital cable. The pulse width cannot be regenerated by the Repeater Box and it is reduced by approximately 5ns due to the regeneration. Pulse width reduction is an important constraint to digital communication because it changes the signal shape and usually limits the transfer speed. The receiving lines are protected from overvoltage by special devices (transzorbs) which clip all line voltage levels above the power supply and below ground.

The lines can be terminated by either AC or DC termination at the receiving end. The termination must match the configuration used for similar lines in the Communication boards.

8.2.3 Signal and Battery Indicators

The data flow can be monitored by watching the respective indicators on the front panel. They blink whenever *Sys A, Sys B, Data In* and *Data Out* are passing through. They are sampled after the receiver stage. The data links signal pulse width are not enough for a good visualization and are extended to a 0.5 milliseconds pulse.

The absence of any signal might indicate a cable or communication fault. This is not conclusive, since there is still one active device between the monitored and the output signal. However, it is unlikely to be the fault.

There is also an indication for the Link Speed which is "on" whenever the link speeds are set to the same value at Base and Remote Box (or Remote and

Remote). This is the a common configuration mistake that can be detected easily.

The battery level is monitored and compared to a reference voltage. The comparator outputs drive a bicolour LED that gives three combinations according to that level as shown in table 8.1.

GREEN	$V_{Battery} > 5.85\text{V}$
ORANGE	$5.30\text{V} > V_{Battery} > 5.85\text{V}$
RED	$V_{Battery} < 5.30\text{V}$

Table 8.1: Battery Level Indicator

Even though these LEDs are low-power devices, they double the box power consumption. That is why they are disabled and only operate in conjunction with a momentary switch.

8.3 Grounding Considerations

The grounding scheme for balanced digital communication is less critical than the ones applied to single ended method. Changes in ground potentials are common-mode voltages which are rejected by the receivers. However, these can not be disregarded. Long cables act as antennas that pick up high-frequency interference and couple it through the interface device to the electronics. Ground potentials that exceed the device's maximum common-mode voltage can corrupt data or even destroy the receiver. In order to minimize these effects, the cable shield should be grounded at one end only to avoid ground loops, normally the *receiver* end. The choice is easy for point to point full duplex communication but it is not as clear where half duplex communication is applied. The ground scheme used in the equipment is shown in figure 8.2.

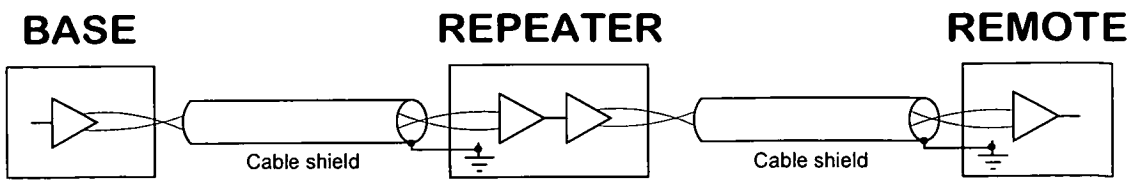

Figure 8.2: Digital Link Ground Connection

8.4 Test and Performance

The Repeater Box is most effective for regenerating the signal amplitude at the expense of speed. The signal distortion (pulse width reduction) due to the cable electric characteristics explained in section 5.8.2 are cumulative and can not be avoided. The only way to regenerate the original pulse width after each cable section would be to connect two complete communication boards which is not the purpose of the Repeater Box. Table 5.3 shows that a digital communication at 5.0Mbits/s is feasible up to 300 meters but it is not for 300 + 300 meters with a Repeater in the middle. The external link speed must be reduced due to cumulative pulse width reductions through 600m cable plus one regeneration in the Repeater Box.

8.5 The Repeater Box version 2

In August 1996 a new version was released. It has the same principles and characteristics as the first version. The modifications are:

- The line protection devices were removed. Even though it is not critical in digital applications, the transzorbs are an additional source of noise.
- The transceivers devices were changed. The new type incorporates a protection against ±15kV electrostatic discharge.

- The link speed comparator and indicator no longer exist. This is due to the change in the way that the link speed are set. Previously, both link direction and speed were set by jumpers at the connectors. By comparing the settings at both sides it was possible to determine whether or not they matched. Presently they are set by a switch on the digital connector board and the comparison is no longer available.

- There is only one LED for signal. The source can be selected among Sys A/B, Data In and Data Out. Sys A/B is a logical combination of *Sys A* + *Sys B*. This combination can be changed internally is order to display individually *Sys A* or *Sys B*.

- The pushbutton for enabling the internal power supply no longer exists. The same signal select switch enables the power supply at any position but OFF.

- When the switch has its position changed to Sys A/B, Data In or Data Out it triggers an internal timing which enables the power to the LED for approximately 10 seconds. It prevents waste of energy whenever someone does not return the switch to OFF, thus disabling the internal power supply.

The Repeater Box Version 2 block diagram is shown in figure 8.3.

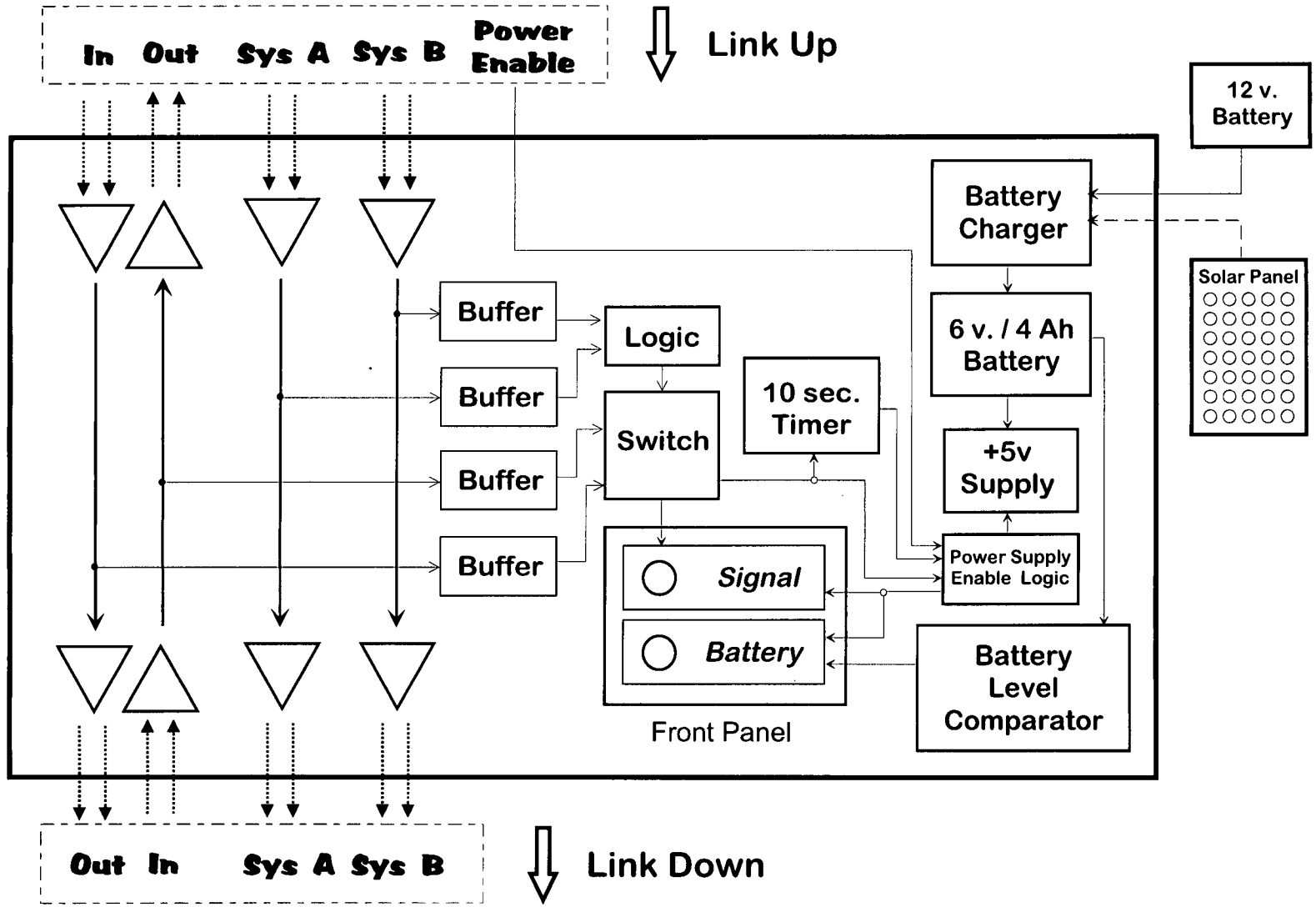

Figure 8.3: Digital Repeater Box - Ver.2

CHAPTER 9

A Magnetotelluric Field Investigation

9.1 Introduction

Magnetotelluric method deals with natural magnetic and electric fields measured at the earth's surface. The method, characteristics of these fields, sensors and basic instrumentation are explained in chapter 2. The newly developed short-period data acquisition and processing system (SPAM Mk-III), explained in Chapters 1 to 8 has opened new possibilities of field configuration and multi-channel synchronized data acquisition. This chapter describes two experiments that have been carried out taking advantage of these capabilities.

The first involves simultaneous data acquisition of the magnetic field and the induced electric field measured by dipoles with four different separations. The aim of this experiment is to investigate the signal-to-noise relationship of the measured electric fields and its effect on the impedance tensor determination.

The second experiment consists in measuring simultaneously the magnetic and electric fields in the usual coordinate system (e.g. North, East), plus a complete sensor configuration (magnetic and electric) with the coordinate system rotated

45 ° positive from North to East. The aim is to investigate the assumption that for a layered earth (1-D), the impedance tensor does not depend on the measuring coordinates. Both rotated and non-rotated configurations include two electric lines with different lengths as an attempt to investigate the signal-to-noise relationship as well.

These experiments are described in detail and the result presented respectively in sections 9.5 and 9.6. The site, equipment set-up, data acquisition and processing are common to both experiments and are described in the following text.

9.2 Site Location and Geological Background

The aim of these experiments is to investigate some assumptions related to the magnetotelluric method independent of the earth's structure. Both experiments investigate the signal-to-noise relationship among electric dipoles with different line lengths, so in the near-field the electric noise due to electric fences, gas pipes[1] and power lines should be avoided. Additional requirements are easy access and not too far from Edinburgh. These conditions are virtually impossible to be fulfilled. After an extensive survey, I chose **Upper-Bolton** near to Gifford and Pencaitland. The exact location of the site is shown in table 9.1

Latitude	Longitude	North	Easting
55 ° 54 ′ 39.9 ″ N	2 ° 48 ′ 28.9 ″ W	668900	349500

Table 9.1: Upper Bolton site details

The geological map indicates that the area is composed of Carboniferous sedimentary rocks. The Calciferous Sandstone Measures of the Carboniferous Limestone Series (Dinatian) indicates about 780m of strata, composed of an upper, predominantly sandy subdivision, and a lower sandstone, shale and cementstone

[1]The electric discharge applied to avoid corosion on pipes' wall

subdivision. (BGS 1983). The map does not show any two-dimensional conductivity contrast in the region. Figure 9.1 is a section of a geographic map af the area (OS 1988). Noise is expected due to some farms and a secondary road (B6355) within 1Km.

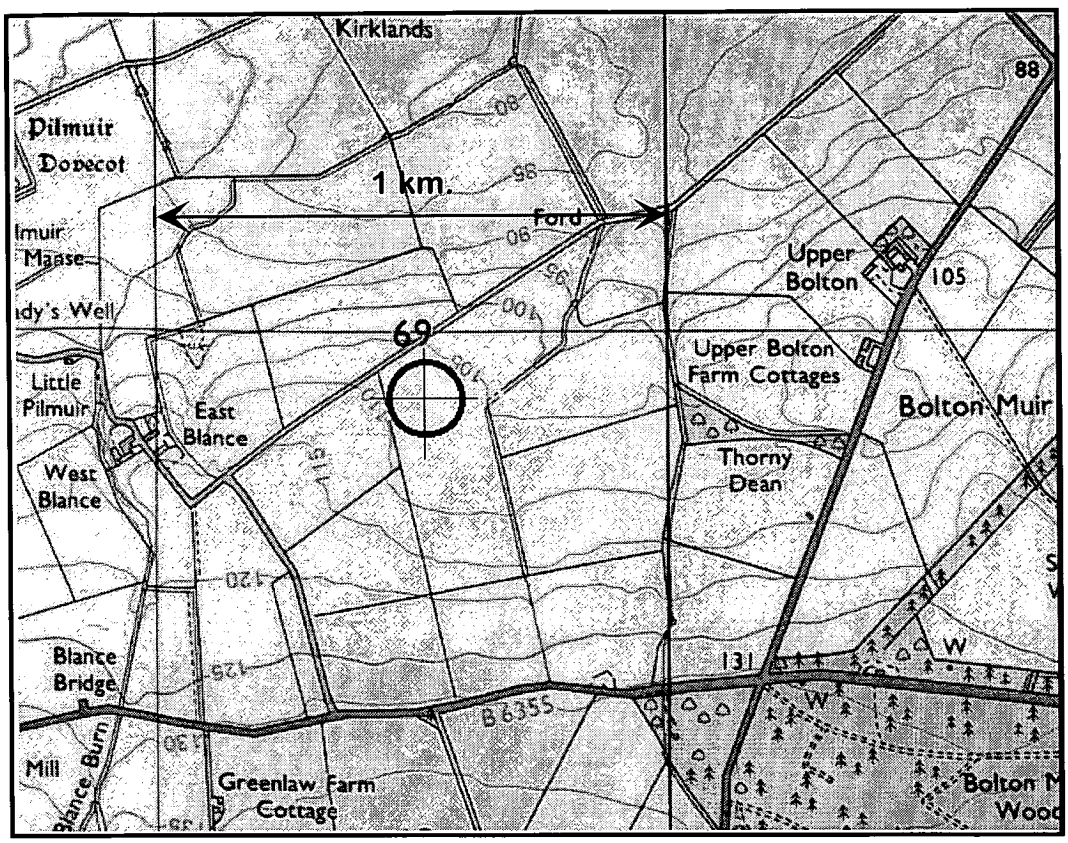

Figure 9.1: Upper Bolton site map

9.3 Equipment set-up and Data acquisition

The instrumentation and sensors used in both experiments are the same. The difference is the number and physical layout of the sensors. The electric sensors are copper-copper sulphate electrodes and details related to design, construction, laboratory tests field are described in Chapter 3. The magnetic sensors are Model CM11E (ANVAR-CNRS License) induction coil magnetometers pro-

duced by ECA France and its characteristics are shown in table 7.4 and reference Anvar-CNRS (1984).

The short-period data acquisition and processing system (SPAM Mk-III) is as described in detail in previous chapters. The configuration required for both experiments includes two Sensor Boxes, one Remote Box and one Base Box. Shielded cables and multi-core twisted pairs were used to connect respectively electrodes and magnetometers to the Sensor Boxes. The first Sensor Box was configured with three magnetic and four electric boards to provide the first analogue pre-conditioning for magnetic and electric signals (Hx_1, Hy_1, Hz_1, Ex_1, Ey_1, Ex_2 and Ey_2). The second Sensor Box provides identical pre-conditioning for electric signals (Ex_3, Ey_3, Ex_4 and Ey_4). For the second experiment two magnetic boards were included in the second Sensor Box for two more magnetic sensor (Hx_2 and Hy_2). In both experiments the Sensor Boxes were connected to the Remote Box through 150m analogue cable. The Remote Box was populated with 11 channel boards (13 for the second experiment) and connected to the Base Box through a one meter digital cable at the system's maximum digital data transfer rate (5.0Mbps). The Sensor Boxes and respective batteries were placed close to the centre of the sensor layout. Remote, Base and a common hi-capacity battery were deployed approximately 50m distance from the Sensor Boxes.

After proper installation placement of the sensors and basic electrodes test (resistance and self-potential) the equipment was initialized. It consists of connecting a laptop computer to the Base Box and running a start-up program which bootstraps a file to the system memory. The Transputer in the Base Box (DC-DC/Computer board) runs the initialization software, identifies the network and asks for some parameters such as project name, site and run numbers, electric line lengths, magnetometer serial numbers and comments. The correct identification of the magnetometers and the electric boards[2] are essential, these are used to apply their frequency response corrections.

[2]Electric boards' serial numbers are read automatically during the system boot-up

SPAM Mk-III provides two operation modes: Short-period and Hi-frequency. However the frequency range for the experiments were limited by the induction coil magnetometers to the band between 100Hz and 0.01Hz. Therefore, only the short-period operation mode (0.001Hz–128Hz) was used. In this mode, a wide band signal is measured and digitized with an effective sampling rate of 512Hz. The continuous stream of wide-band data is digitally decimated into narrower bands previously selected during the equipment set up and data recorded for "off-field" processing. For both experiments the frequency bands selected are shown in table 9.2

SPAM Mk-III also performs basic MT data analysis in real-time and displays results such as apparent resistivity and phase on the laptop screen. A typical screen dumped during the field work is shown in figure 9.2. In this example, parameters like Apparent Resistivity, Phase, Predicted Coherence and number of estimates stacked for each frequency are plotted. The number of accepted events (windows) in each bandwidth is displayed as well in the right botton corner.

The system creates and saves on its internal hard-disk one binary file of time-series data for each specified band per run. These files are DOS compatible and contain all the information needed for data analysis and network identification. The facility provided by the equipment to dump data from the internal disk allows gathering a large amount of data for further processing. For instance, 2.16Gbytes of data were collected in the field for the two main experiments and for tests of the electrodes and instrumentation (whose results may be used for further publications). The distribution of recorded data and time per frequency band and experiment is shown in table 9.3.

9.4 Data Processing Software

Each file created by the system in the field contains the time-series data and information about the whole network configuration at the time of the data ac-

Band Number	Low-pass (Hz)	High-pass (Hz)	Sampling Rate (Hz)
0	128	16	512
1	16	4	256
2	4	1	64
3	1	0.25	4
4	0.25	0.0625	1
5	0.0625	0.0156	0.25
6	0.0312	0.0078	0.125
7	0.0156	0.0039	0.062

Table 9.2: Frequency Bands for the experiment

quisition. The format of these files is unique due to the characteristics of parallel multi-channel data acquisition. Thus, special software is required to handle these files properly.

EMERALD - **E**lectro-**M**agnetic **E**quipment, **R**aw-data **A**nd **L**ocations **D**atabase is a set of programs written in FORTRAN and C which generates Magnetotelluric results from low-level time series date. The package was developed by Oliver Ritter as part of his PhD studies at Edinburgh University (Ritter 1995). EMERALD includes programs which are able to handle the unique data file format generated by SPAM Mk-III and convert them to other formats.

The software allows the interaction of the user at every stage of the process. The default parameters supplied by the package can be changed in order to tune the analysis performance.

The main program in the EMERALD package is called EMshell which is an interface between the user and the structure of the software. This looks for files, ask for inputs and calls sequentially the required programs for each processing phase.

At the first step EMshell looks for SPAM Mk-III time-series data files and convert them into EMERALD raw-data files and database extract files. The latter contains complete information about the network configuration such as:

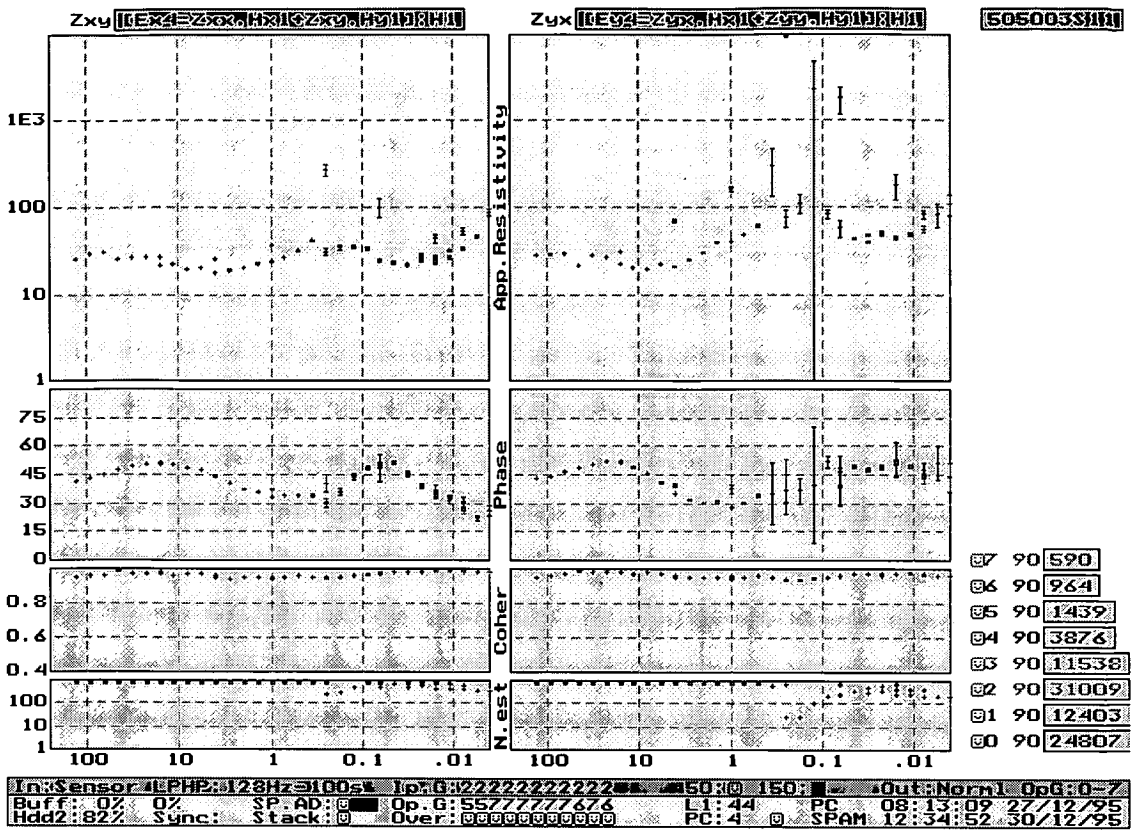

Figure 9.2: SPAM Mk-III Magnetotelluric Results Screen

number of sites, number of channels per site, type of sensors, sensor direction, electric line lengths, magnetometers and electric boards serial number. Extract files are the reference files for the data processing programs. Even though all information related to the network can be observed by browsing the extract files, the easiest way to verify the site configuration and identify the hardware used is to view the text file SPANCHAN.TBL, also generated by EMshell, that gives all this information in tabular format.

At this stage, EMshell also has created frequency response calibration files for each magnetometer and electric board detected.

The second step consists on transforming the time domain into the frequency domain data. The user can modify the default parameters for the length of the time segments for each frequency band. The frequency distribution layout must

	Electric Line Length Separation		Sensor Rotation Experiment		Equipment/Electrode Setup and Test	
Band	Mbytes	HH:MM	Mbytes	HH:MM	Mbytes	HH:MM
BP0	112	1:22	119	1:14	49	0:30
BP1	112	2:46	146	3:02	47	0:59
BP2	450	44:22	333	27:46	121	10:07
BP3	256	404:22	195	260:59	42	55:53
BP4	64	404:25	49	261:00	10	55:55
BP5	16	404:32	12	260:59	2.6	56:11
BP6	8	404:44	6	261:08	1.3	56:38
BP7	4	408:23	3	263:16	0.7	58:10
Total	1022		863		274	

Table 9.3: Amount of data recorded from 13 Dec 95 to 23 Jan 96

be chosen (binary or logarithmic). EMshell creates suitable input files such as frequency layout and calibration which are needed for generating the single event auto-spectra and cross-spectra files.

The third step consists of a robust stacking of all single event frequency domain data files. This part of the program is based on A.Junge's ANAROB software (Junge 1992). In this step the user must specify the sites to be processed and the method to be applied. There are many options e.g. single-site or remote-reference, include or not the vertical magnetic field, impedance or admittance, magnetotelluric or GDS, etc. Data can be stacked individually for each data file, frequency band or combined (all data files and frequency bands together).

The final step is to view the results in graphic format. An utility program takes input files created by EMshell and provides facilities for choosing between several types of graphics, axis re-scaling, printing and plotting the graphics to printer, plotter or file.

Parts of EMshell can be re-run to improve the data processing. This involves running individual steps with different parameters.

The package written by Oliver Ritter also incorporates utility programs. As an example, READSP3 converts SPAM Mk-III time-series data into ASCII tabular format that can be imported into other packages. This utility also extracts the header from original SPAM files, these contain all information necessary to define the site configuration, sensors, bands and recording times.

SP3EDIT is a very useful utility program which enables modification of important parameters in SPAM Mk-III binary time-series data files. In a very complex field configuration is very easy to make mistakes like to install one particular sensor in a wrong direction, to provide wrong information about the electric line lengths, project or site number, etc. Some of these are not important and do not affect the data processing. However, some of them are crucial and must be provided correctly otherwise data cannot be processed properly. These mistakes can be corrected by SP3EDIT which reads, edits and re-writes the modified files in the original binary format.

All data related to the experiments were processed by these programs written by O.Ritter and A.Junge. More information about the package and its utilisation can be found in Ritter (1996a).

9.5 Electric Dipole Separation Experiment

The natural electro-magnetic field, which is the source for Magnetotelluric measurements, can be very weak at some frequencies hence so are the induced electric fields (see Section 7.3.2). The voltage measured across the electrode pair is proportional to the induced electric field strength and the distance between sensors. In practice, electric dipoles from 10 to 300m are used in X or L shape layout. Longer electric field dipoles yield higher signals but also average more near-surface effects. However, long lines are more prone to pick up ambient noise

and are restricted by the site topography. In order to investigate the effect of determining the impedance tensor by relating the magnetic field to the electric field measured by dipoles with different lengths an experiment was carried out with the sensors configured as shown in figure 9.3.

The basic equipment set-up, band selection and data acquisition were described in section 9.3. In this experiment, two Sensor Boxes were used. The first, with seven channels, connected to the magnetic sensors (Hx_1, Hy_1, Hz_1) and to the 10 and 20m line length electric dipoles: Ex_1, Ey_1, Ex_2 and Ey_2. The second connected to the 40 and 80m line length electric dipoles: Ex_3, Ey_3, Ex_4 and Ey_4 (see figure 9.4).

9.5.1 Time series

EMERALD software can display time-series recorded in the field for data quality evaluation. This is a useful feature because time-series may give information about hardware and sensor failures, signal saturation, the strength of electric and magnetic fields and sources of noise which may bias the apparent resistivity and phase results. Typical time series from the experiment can be seen in figures 9.5 to 9.12 for Band 0 to Band 7 respectively (see table 9.2 for frequency band layout). The title, axis and legends of these graphs are similar and display information read from the header of the original SPAM raw data file . The reference for the following examples is figure 9.5 but the parameters are similar for all time-series graphs. The graph title consists of the displayed time segment interval and the name of the EMERALD raw data file, e.g.

Fri 29 Dec 1995 18:00:34.000000 - Fri 29 Dec 1995 18:00:35.000000 / (27H74X11.RAW)

Time-series graphs display all recorded channels identified in the left-Y-axis. From the bottom to the top the sequence is; The elements of the magnetic field B_x, B_y and B_z[3]; the elements of the electric field E_x and E_y. Scales are nano-

[3]The magnetic fields are labeled B instead of H in accordance with the plots

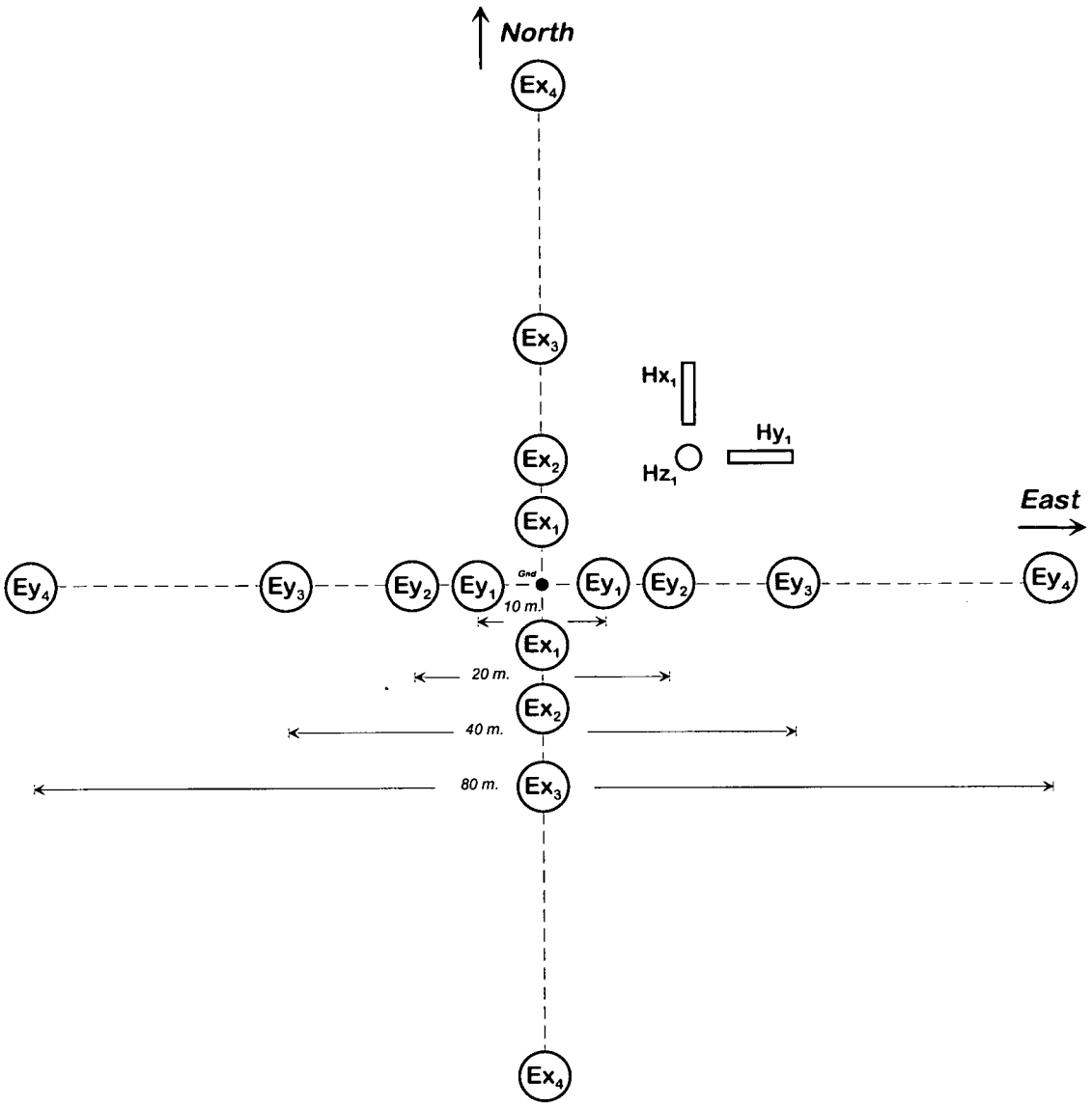

Figure 9.3: Sensor layout for measuring the electric field simultaneously with four different electric line's length

Tesla (nT) and millivolts per kilometer (mV/km) respectively for the magnetic and the electric fields and are corrected for the magnetometer sensitivity and the electric line lengths. Magnetic and electric channels are associated to SITES whose names are identified in the right-Y-axis. The sensor configuration per site is shown in table 9.4.

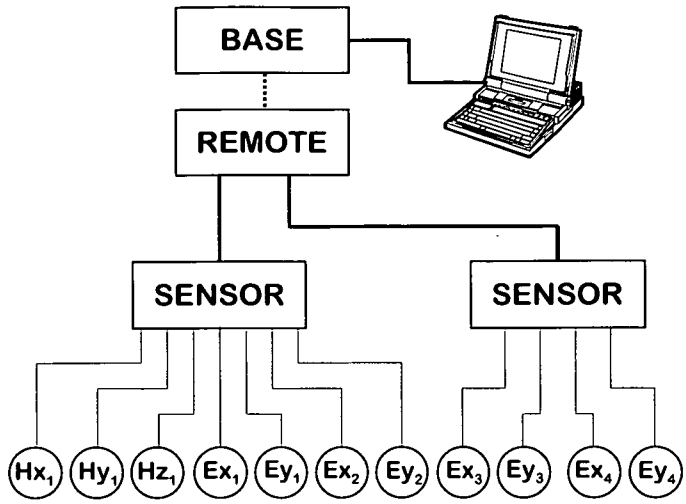

Figure 9.4: Equipment configuration for the sensor layout of figure 9.3

Site	Magnetic	Electric
0031	B_x, B_y, B_z	E_x, E_y - 10m
0032	-	E_x, E_y - 20m
0033	-	E_x, E_y - 40m
0034	-	E_x, E_y - 80m

Table 9.4: Sensor configuration per Site

Frequency band 0 is the most contaminated by the 50Hz noise and this was observed in various time segments recorded at different days and times. It is important to consider that the notch filter attenuates the 50Hz noise approximately 40dB. The actual noise is two or three orders of magnitude higher than the signals. Figure 9.5 shows a small 50Hz noise contamination (not as strong as in time segments recorded from 6:00 AM to 6:00 PM in working days) because this particular time segment was recorded in December 29^{th} at 18:00 and not much activity in the surrounding farms is expected in this time of the year and at that time. Although a clear 50Hz periodic signal can be seen superimposed on the magnetic field, the expected correlations between magnetic and electric channels can be observed in the presence of natural activity (e.g. 0.6s–0.8s).

One E_y component of the electric field (0033) is noisier at higher frequencies than the others and it was observed in several time segments of frequency band 0. However this is due neither to the electric line length nor to the direction because this is observed at this particular channel. Probably this may be due to a noisier hardware channel or an electrode fault. As an example, Figure 9.5 shows that the 50Hz noise is more prominent at this channel. The main reason for this particular noise may be the notch filter for this particular channel not properly tuned.

The chosen time-series segments for all frequency bands (Fig.9.5 to 9.12) show important facts.

The amplitude of the electric fields corrected for the respective line lengths are very similar, as expected for this experiment.

The expected correlation between orthogonal components of the magnetic and electric fields B_x, E_y and B_y, E_x can be observed mostly for all electric channels (0031 to 0034). The expected correlation mentioned above can be observed between the magnetics and at least one of the electrics and there will probably be useful set of events to determine the apparent resistivity and phase if a hardware or sensor failure occurs during the field work. This emphasizes the importance of recording additional data.

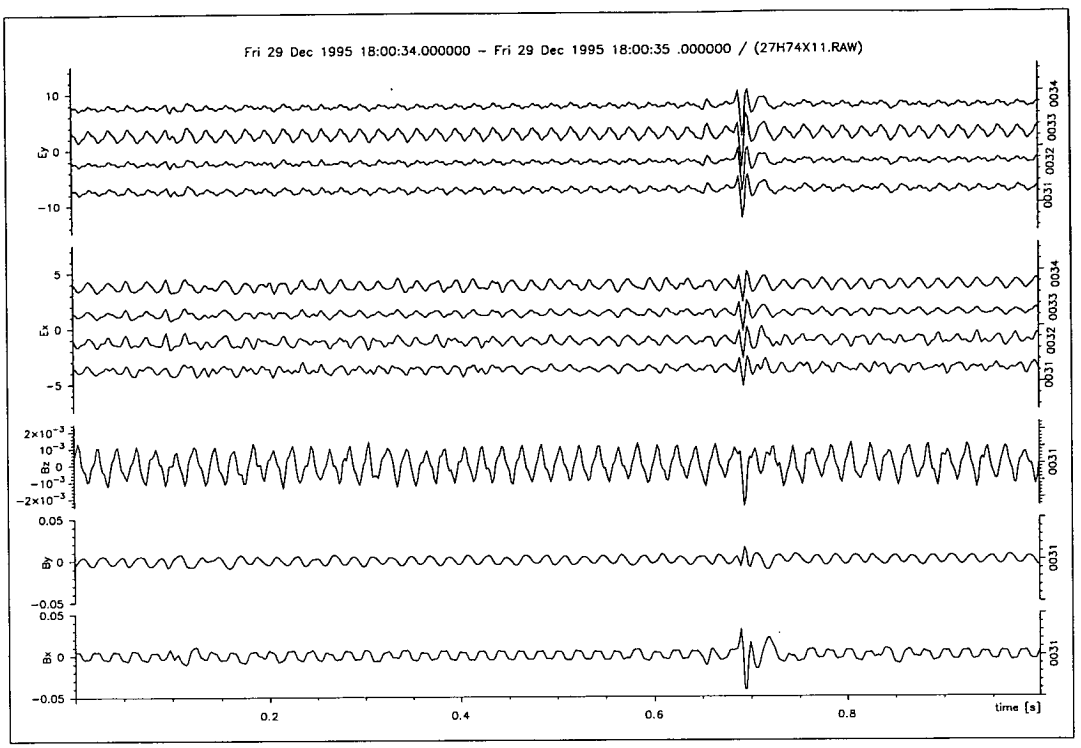

Figure 9.5: Time series of Band 0: 128Hz–16Hz (B(nT), E(mV/km))

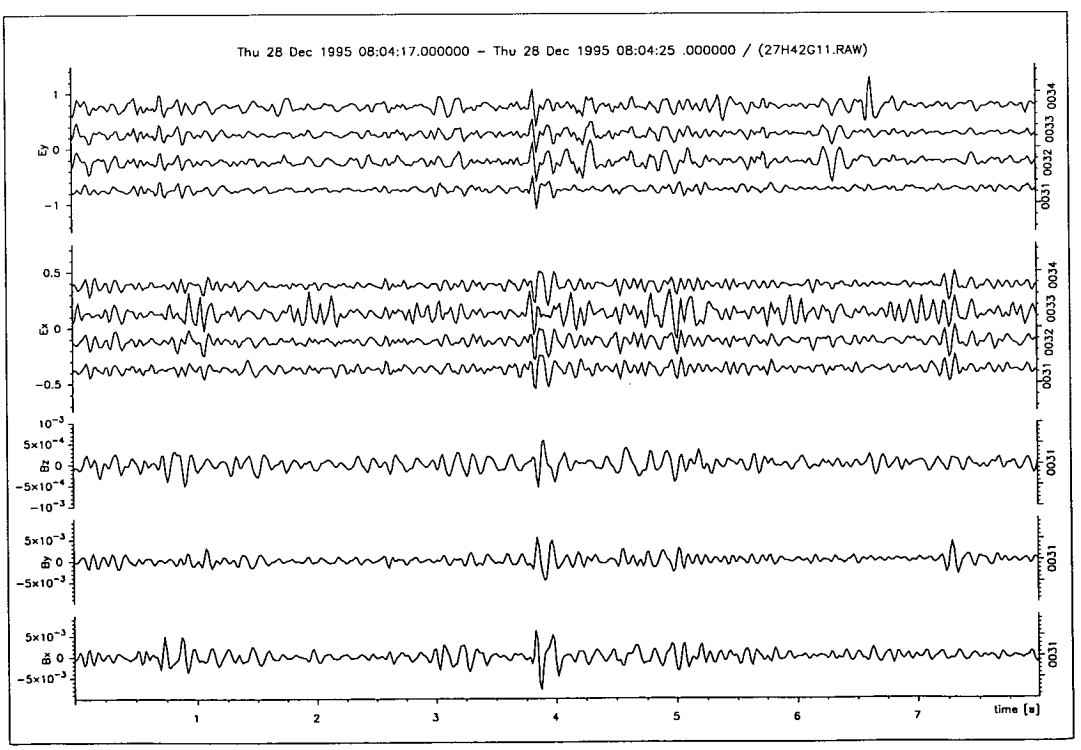

Figure 9.6: Time series of Band 1: 16Hz–4Hz (B(nT), E(mV/km))

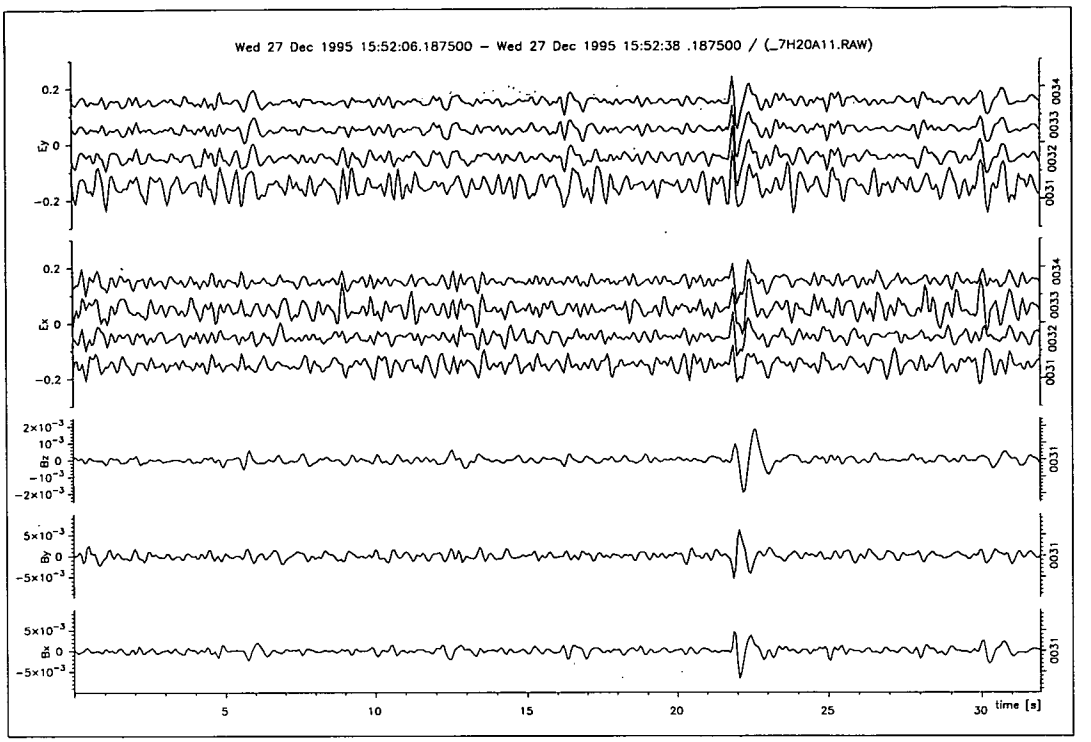

Figure 9.7: Time series of Band 2: 4Hz–1Hz (B(nT), E(mV/km))

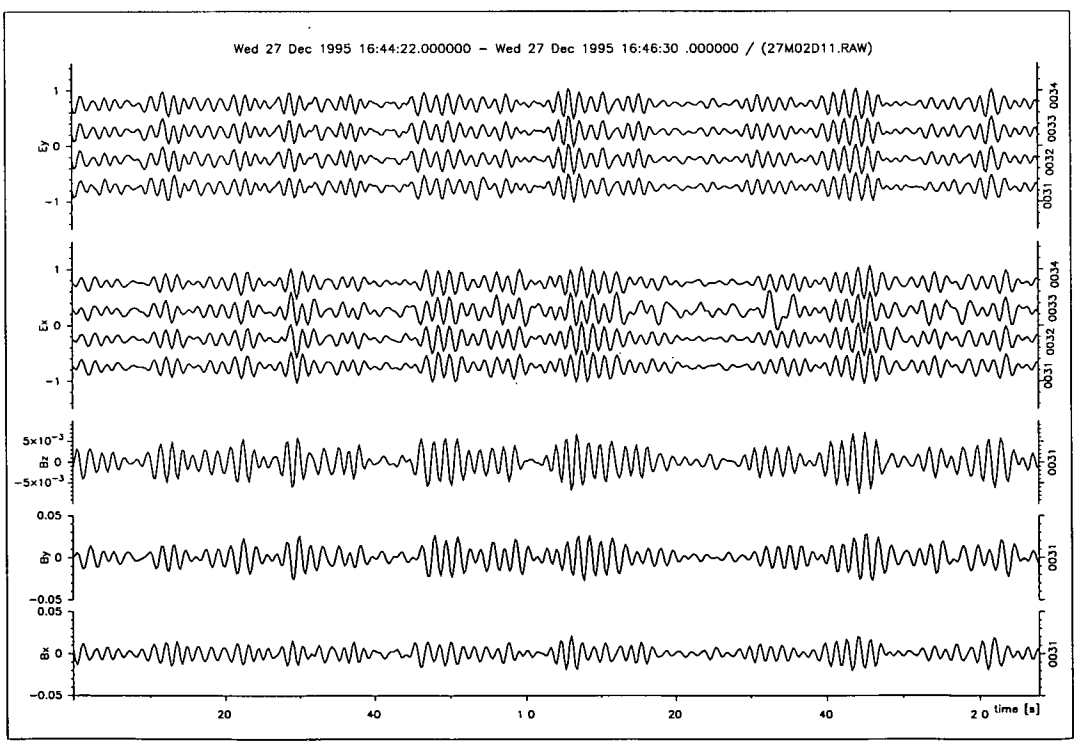

Figure 9.8: Time series Band 3: 1Hz–0.25Hz (1s–4s) (B(nT), E(mV/km))

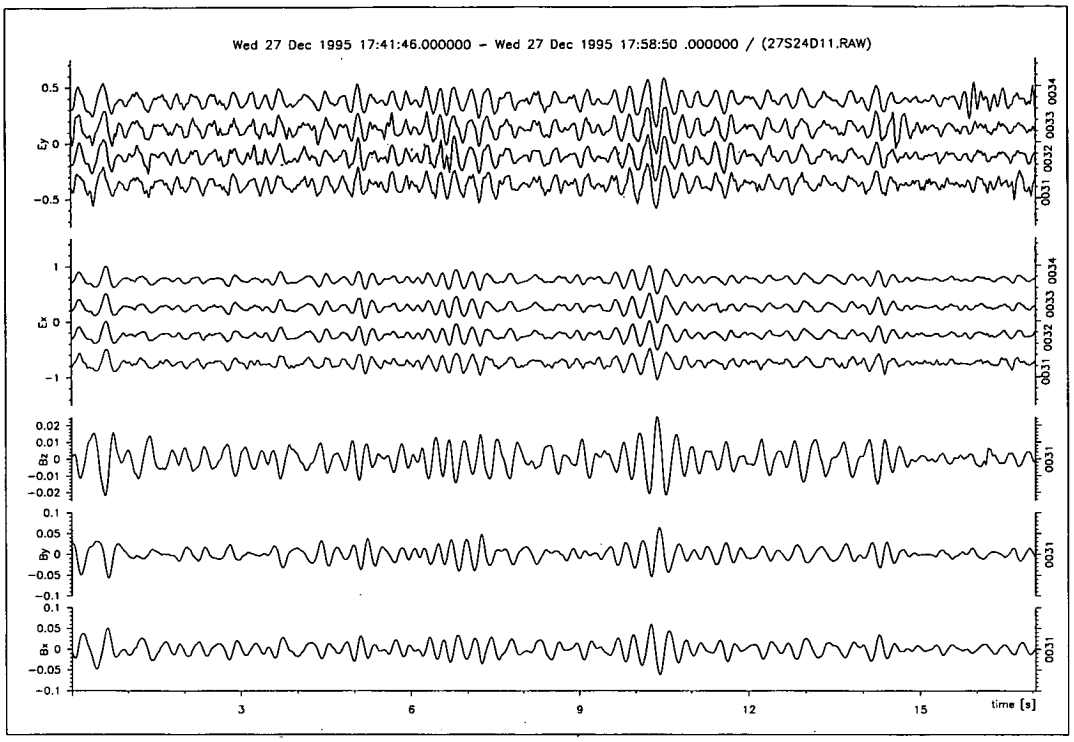

Figure 9.9: Time series Band 4: 0.25 Hz–0.0625 Hz (4s–16s) (B(nT), E(mV/km))

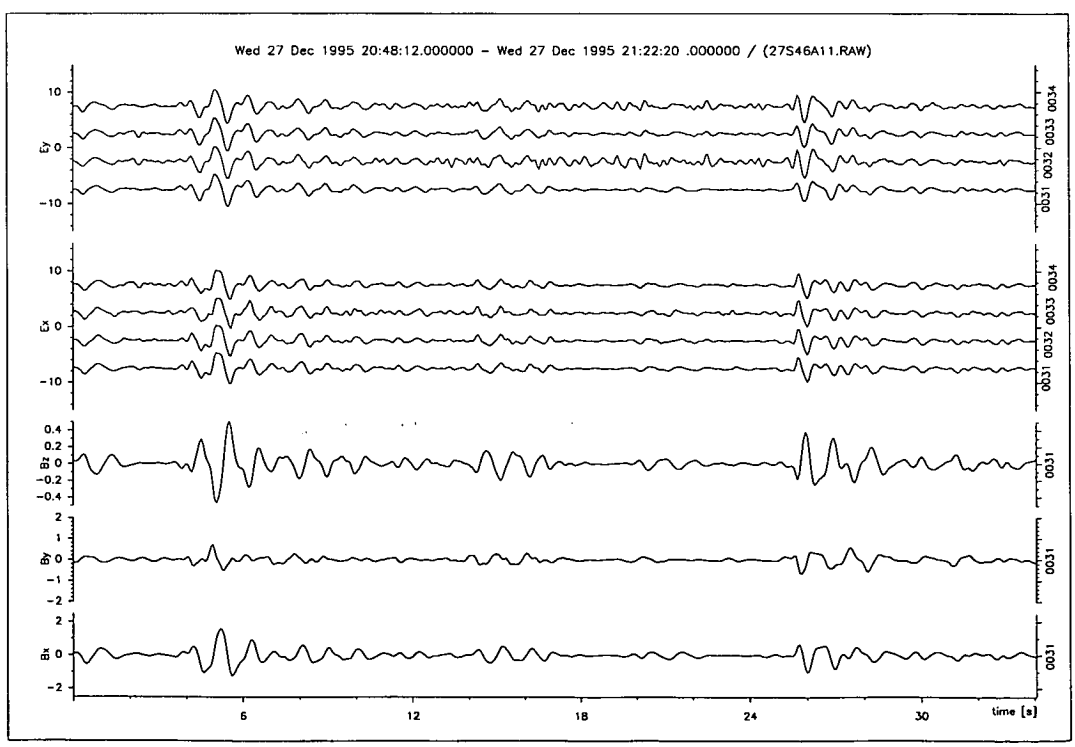

Figure 9.10: Time series of Band 5: 0.0625 Hz–0.0156 Hz (16s–64s) (B(nT), E(mV/km))

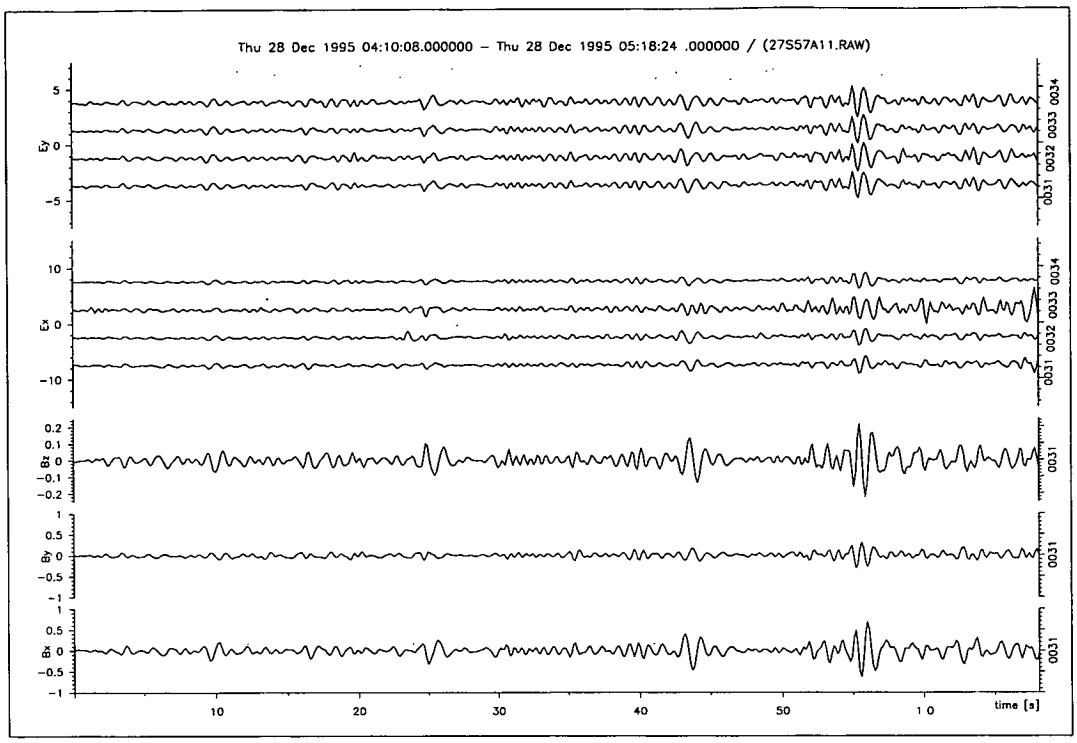

Figure 9.11: Time series of Band 6: 0.0312Hz–0.0078Hz (32s–128s) (B(nT), E(mV/km))

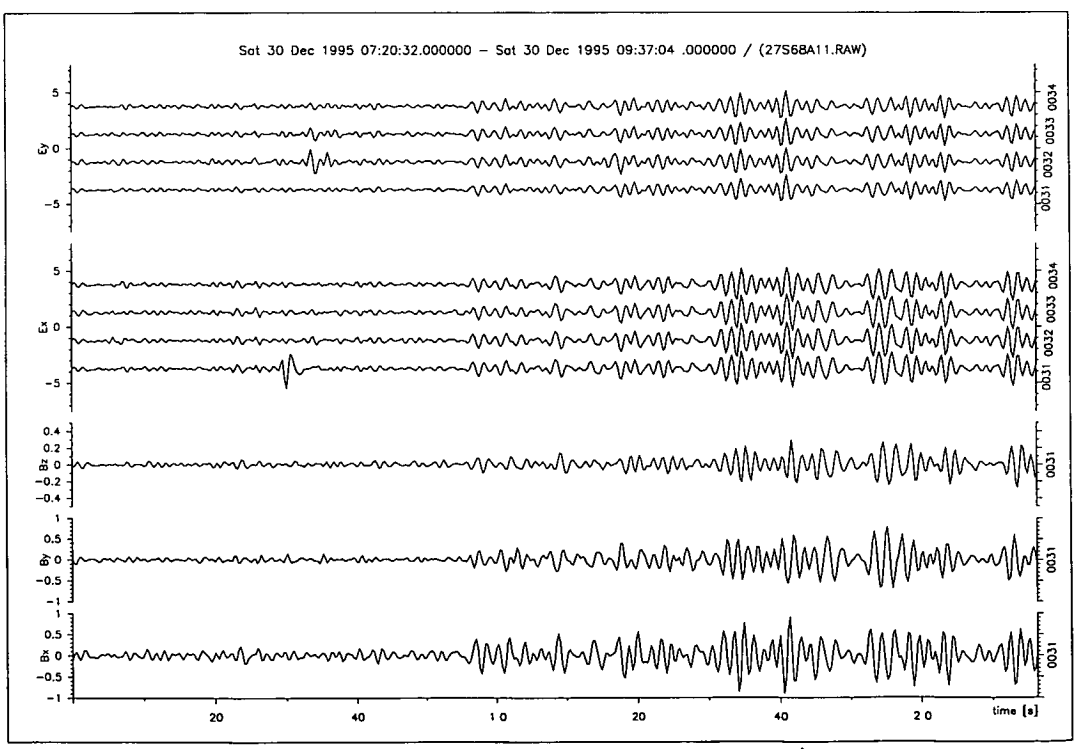

Figure 9.12: Time series of Band 7: 0.0156Hz–0.0039Hz (64s–256s) (B(nT), E(mV/km))

9.5.2 Apparent Resistivity and Phase

The apparent resistivity and phase presented in Figures 9.13 to 9.16 were calculated by the EMERALD package (the robust processing is based on A.Junge's ANAROB program). Each graph shows the unrotated Apparent Resistivity and Phase derived from the impedance tensor off-diagonals (XY and YX). Legends and axis titles are common for all graphs and are self explanatory, except the graph title which is show below.

MTSI 0031 null null Unrot. (0031mtsi.000)

These contain the site number according to the Table 9.4, the method used MagnetoTelluric, Singe site, Impedance, there is no rotation applied to the results (Unrot) followed by the the file name which contains the information required to plot the graph (0031mtsi.000). The difference observed in the title of the remainder graph in that there is a second site identification in the title e.g. MTSI 0031 0032 null Unrot which indicates that in this case the electric field of the site 0032 was combined with the magnetic field of the site 0031. This is an artifice to combine different electric fields and one magnetic field set of measurements (as in Remote-Reference MT) although they are in the same site.

The figures shown in the following four graphs respectively for 10m, 20m, 40m and 80m indicate a slight improvement for longer electric lines. Apparent resistivity and phase curves for 80m electric lines (Fig.9.16) are smoother and present less discontinuity compared to the shorter electric lines. The discontinuity observed in the range 1s–10s in the Apparent resistivity [XY] curve in figure 9.13 decreases gradually for longer electric lines and is not observed in figure 9.16 for the 80m electric lines. This may be an indication of improvement in the signal-to-noise relationship since this frequency range coincides with the so called *dead-band*, where the magnetic field strength is weaker. The order of magnitude of the apparent resistivity and phase are similar regardless of the electric line lengths and the shape of the respective curves can also be predicted within a

reasonable degree of accuracy.

It is interesting to note the comparison of fig.9.16 with fig.9.2. The latter shows results for the same sensor set only calculated by the simpler in-field real-time analysis (using different data sets).

The results for the higher frequencies of the Phase [YX] plot of figure 9.15 (40m electric line) is different to the corresponding graphs of other electric line lengths. These may happen if the high-pass analogue filter for this particular electric channel did not work properly. In this case the frequency response calibration performed by the software[4] applies amplitude and phase correction values which are not compatible to the filter's frequency response, leading to an under or overcorrection (in this case) in both amplitude and phase. A more detailed observation in the correspondent apparent resistivity graph for the same frequency range reveals that the values are slightly higher for 40m electric line than the for 10, 20 and 80m lines.

A more accurate way to compare these results is to plot them together as in figure 9.17 to 9.20 respectively for the apparent resistivity and phase [XY] and apparent resistivity and phase [YX]. The scale for the apparent resistivity is limited between 10 and 100 Ω·m and the error bars can also be observed more accurately. These plots emphasize what has been noticed so far. The improvement in the signal-to-noise relationship for the longer electric lines can be better observed in the figures 9.17 and 9.18 in the period range between 2–10s (and even better at 4s). The discontinuity in the curves due to a poor signal to noise relationship is more expressive for the 10m, improves respectively for 20m and 40m and almost disappears for the 80m lines. Figures 9.19 and 9.20 emphasize the difference of the apparent resistivity and phase for the 40m electric line length at higher frequencies, possibly due to a hardware failure in a low-pass filter stage and further frequency response calibration. Apart from that difference,

[4]The frequency response calibration performed by EMERALD and SPAM Mk-III software running on the DSP board Transputer explained is section 6.2.2 are similar

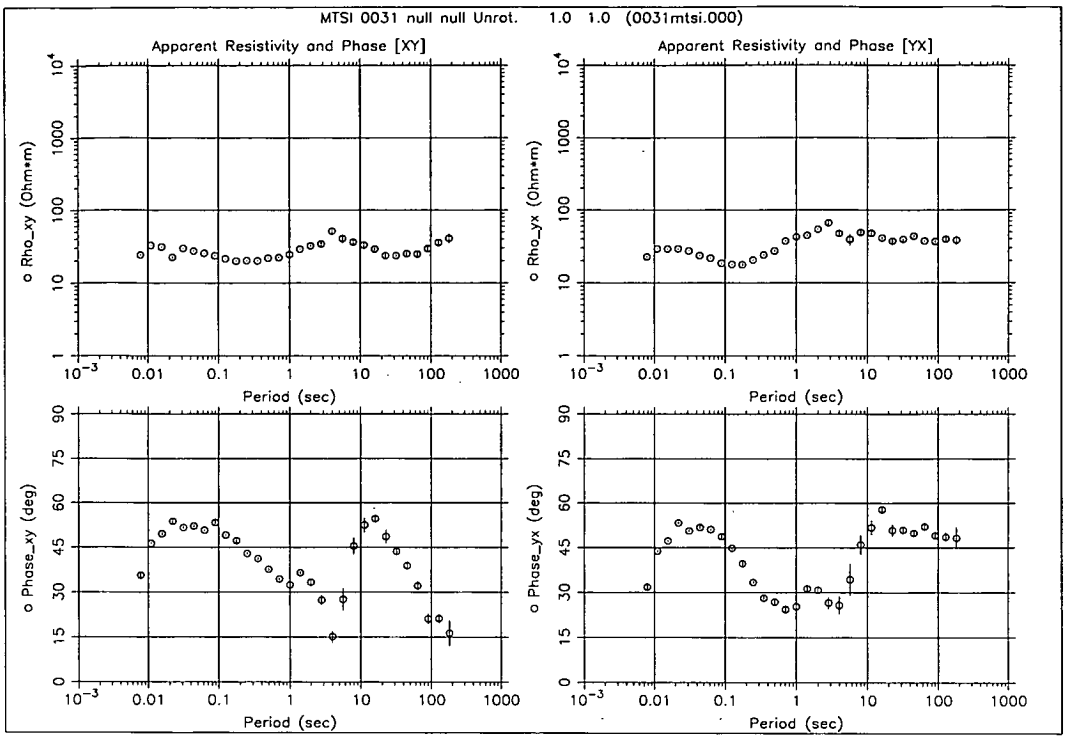

Figure 9.13: Apparent Resistivity and Phase - 10m Electric lines

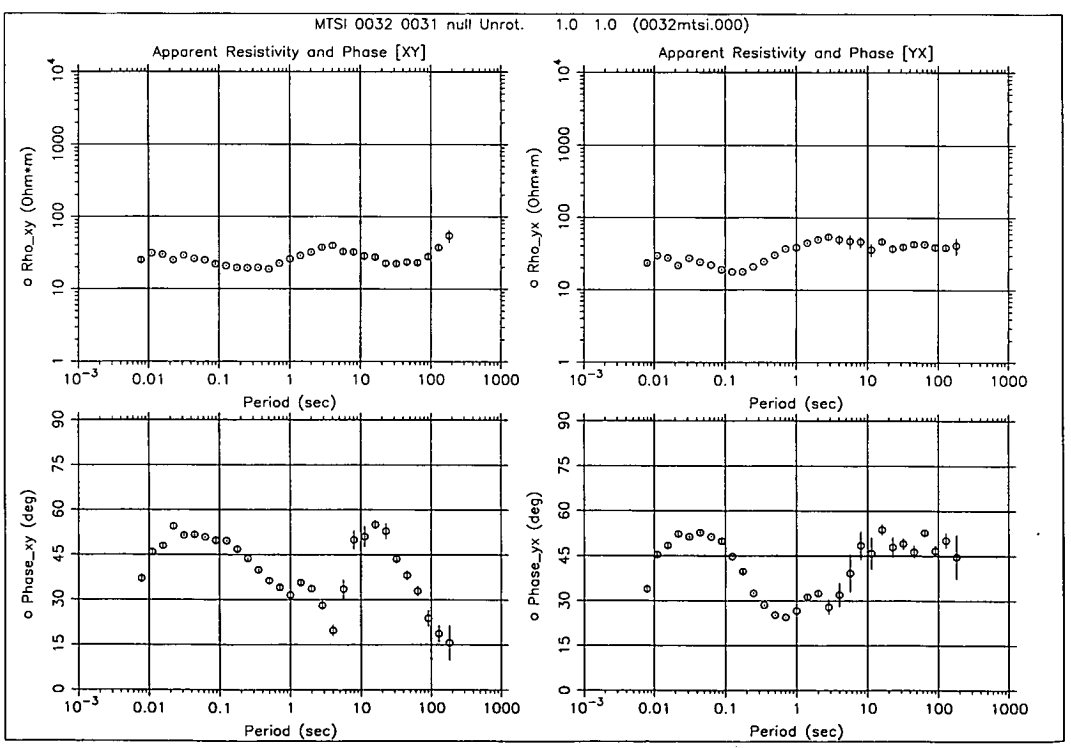

Figure 9.14: Apparent Resistivity and Phase - 20m Electric lines

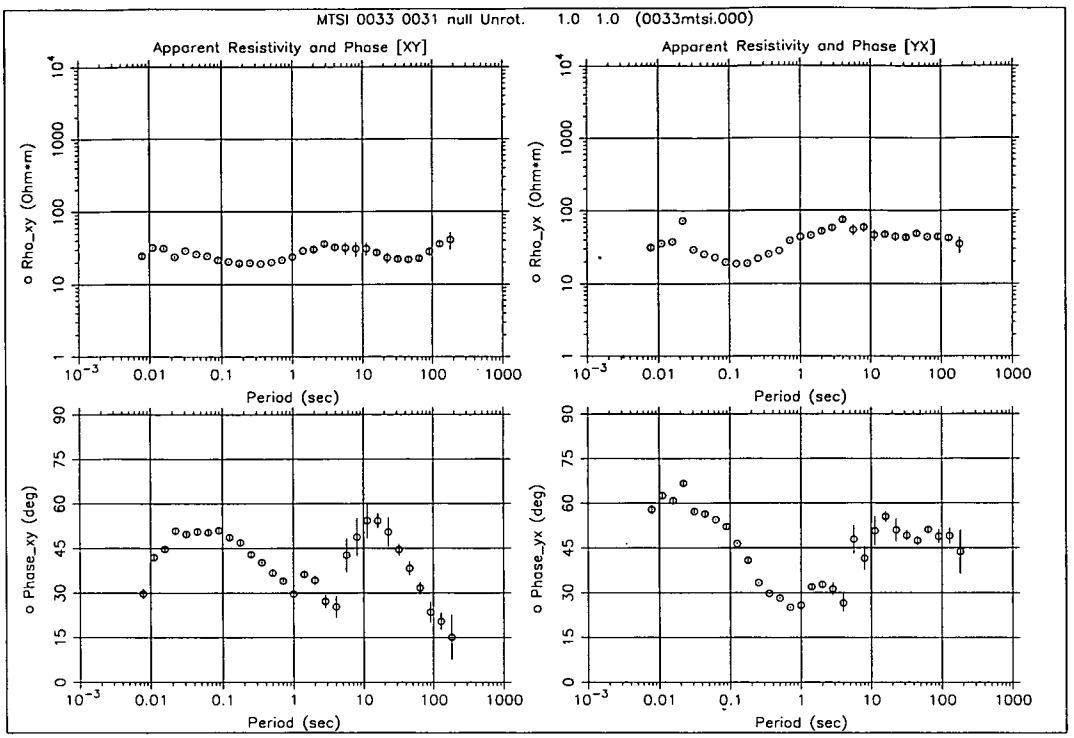

Figure 9.15: Apparent Resistivity and Phase - 40m Electric lines

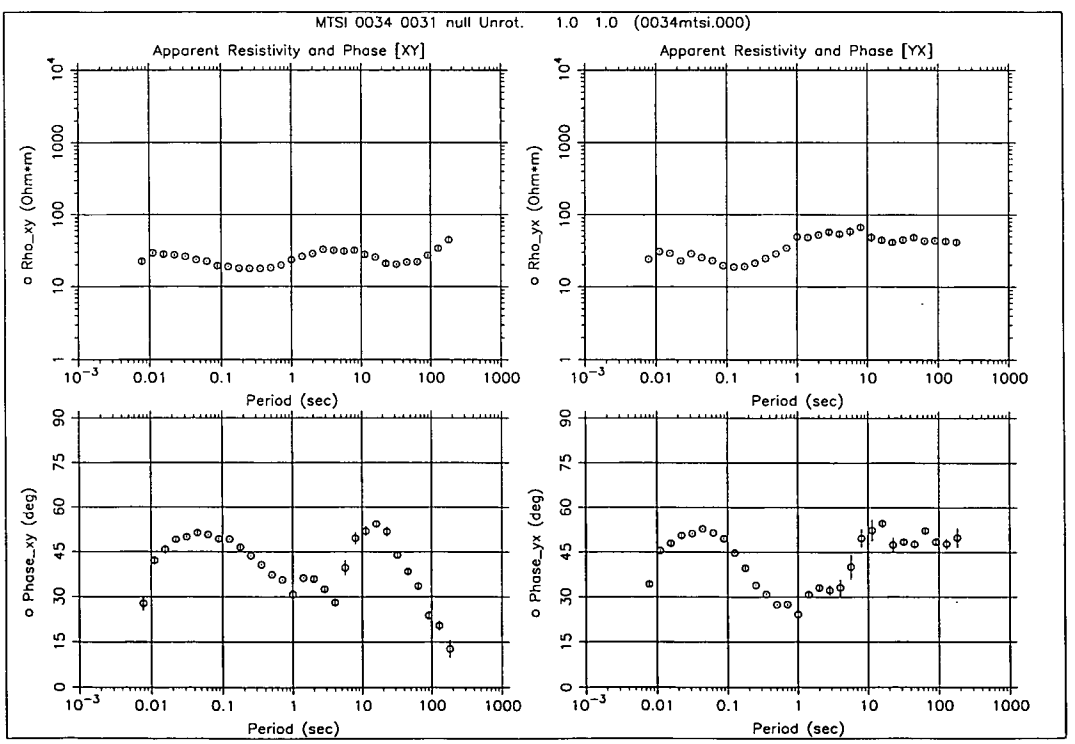

Figure 9.16: Apparent Resistivity and Phase - 80m Electric lines

all electric line lengths present similar apparent resistivity and phase (XY and YX) for the measured frequency range.

Figure 9.17 shows a shift in the apparent resistivity curve for the 80m electric line in the entire frequency range which may be explained either by an error in the electric line length during the field set up or by a gain mismatch at this particular channel or a near surface inhomogeneity in the last 40m of the line.

Figures 9.21 to 9.24 are plots of apparent resistivity and phase errors related to the average for all different electric lines. Figure 9.21 shows that the shift in the apparent resistivity curve for the 80m electric line is approximately 10%.

In general the error among the apparent resistivities for all electric lines fall within 10% in the frequency range between 0.01Hz and 100Hz (see figures 9.21 and 9.23). In the range between 2s and 10s the errors are higher and the highest error due to the 10m electric line biased above the average. The figures for the phase show that the error falls within 5 ° except for the period range between 2s and 10s (see figures 9.22 and 9.24). The phase errors would probably be better (within 2%) if the phase error due to the 40m electric line were not included.

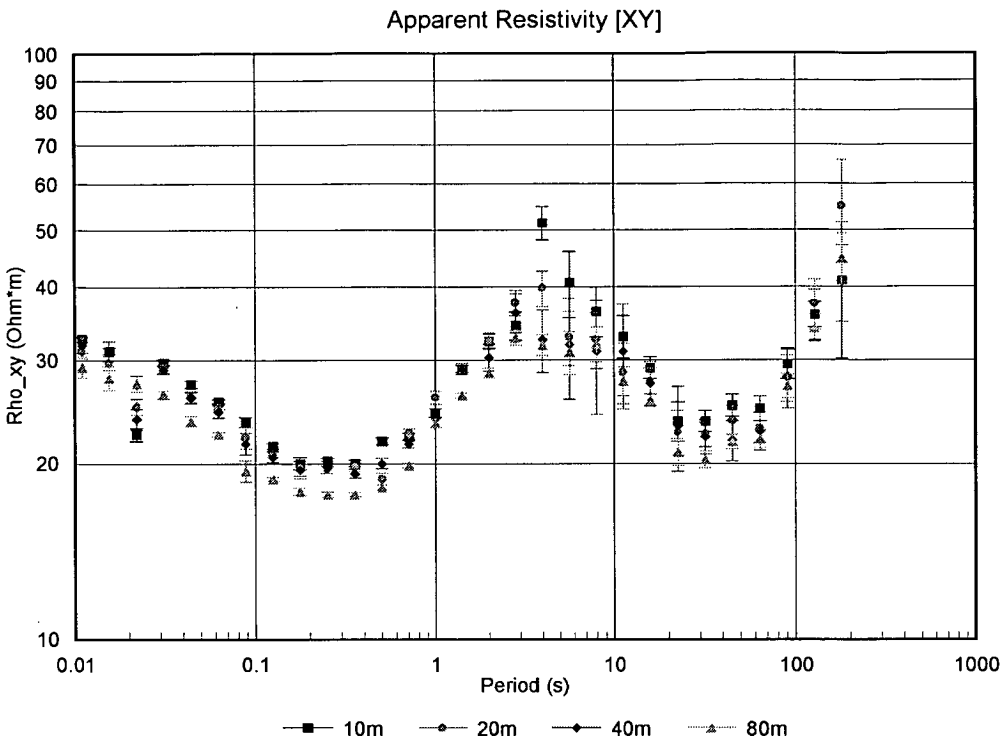

Figure 9.17: Apparent Resistivity [XY] - All lines

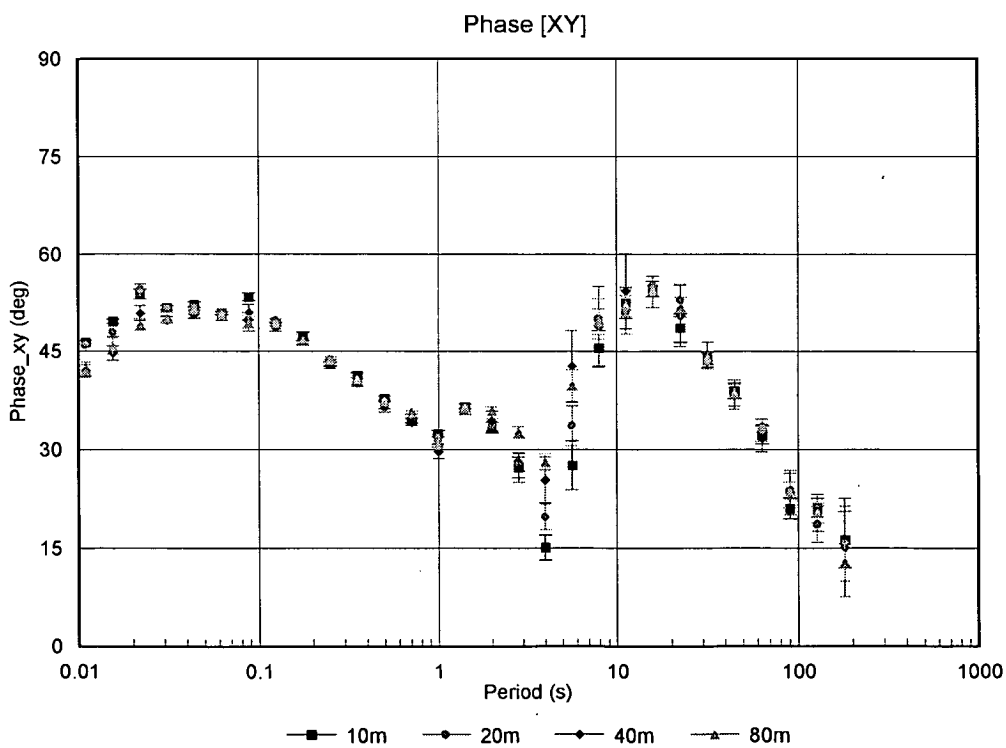

Figure 9.18: Phase [XY] - All lines

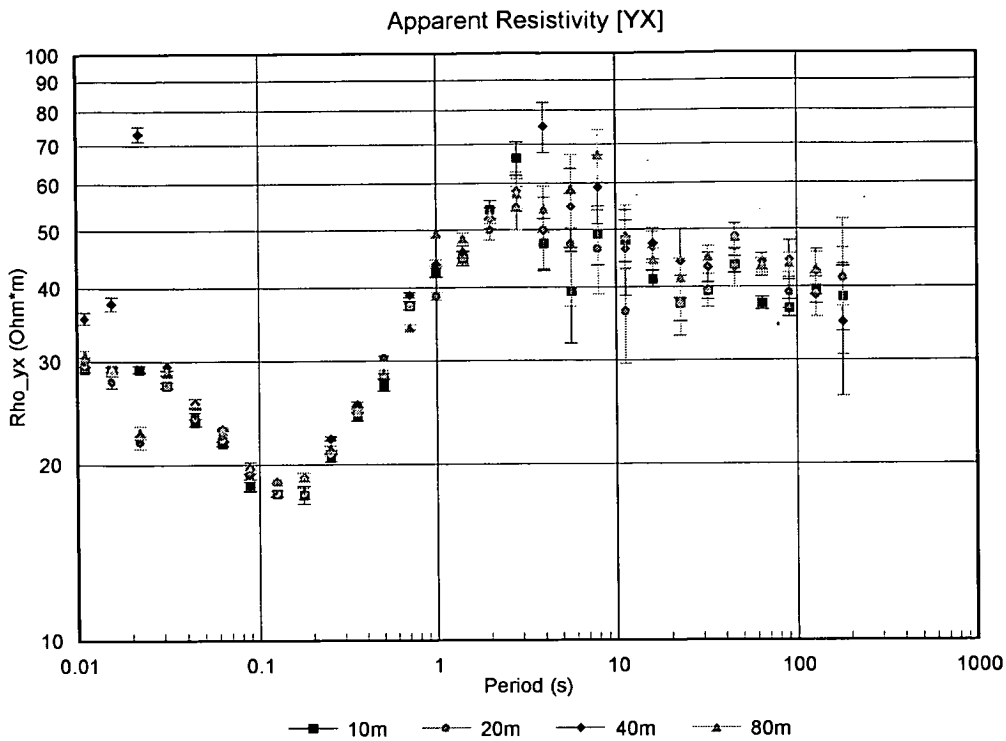

Figure 9.19: Apparent Resistivity [YX] - All lines

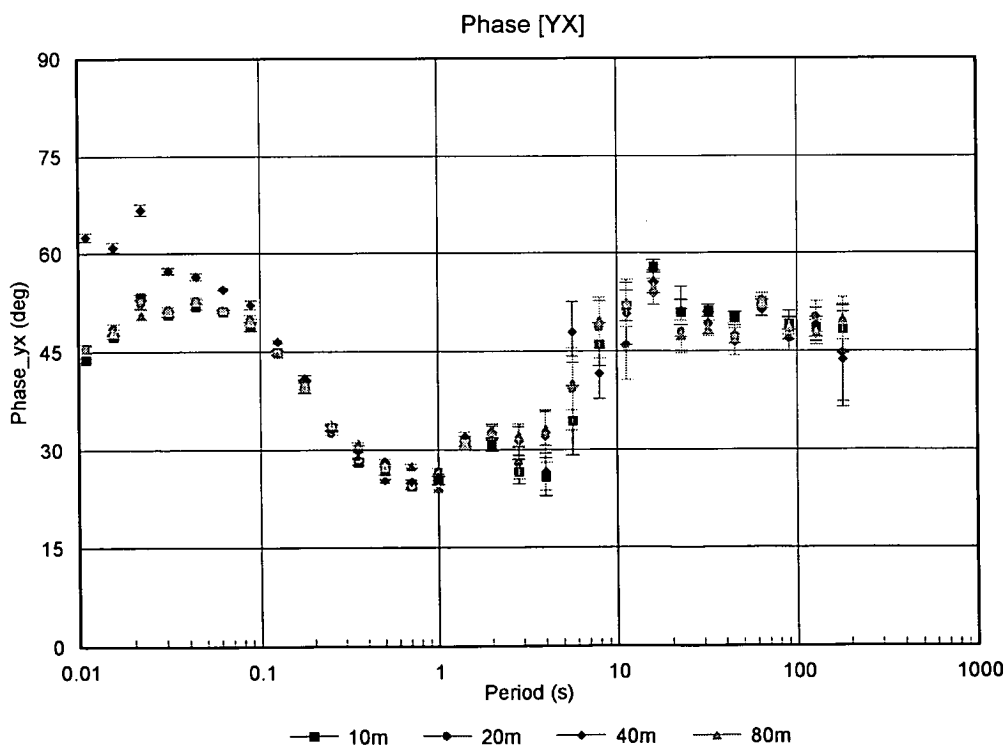

Figure 9.20: Phase [YX] All lines

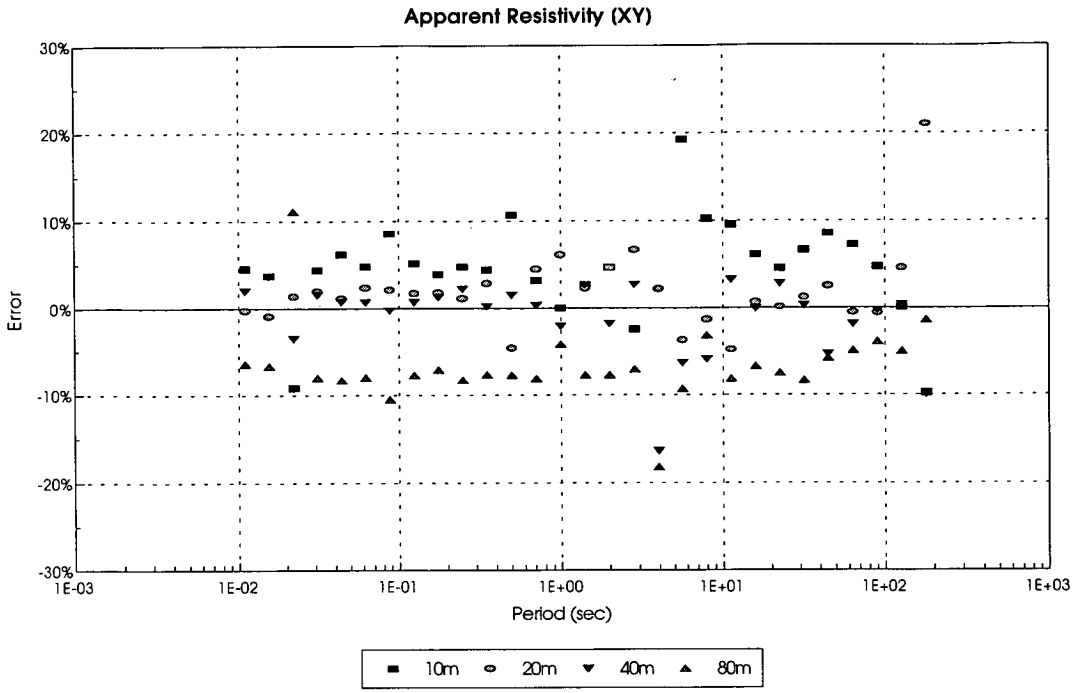

Figure 9.21: Apparent Resistivity Error [XY] - All lines

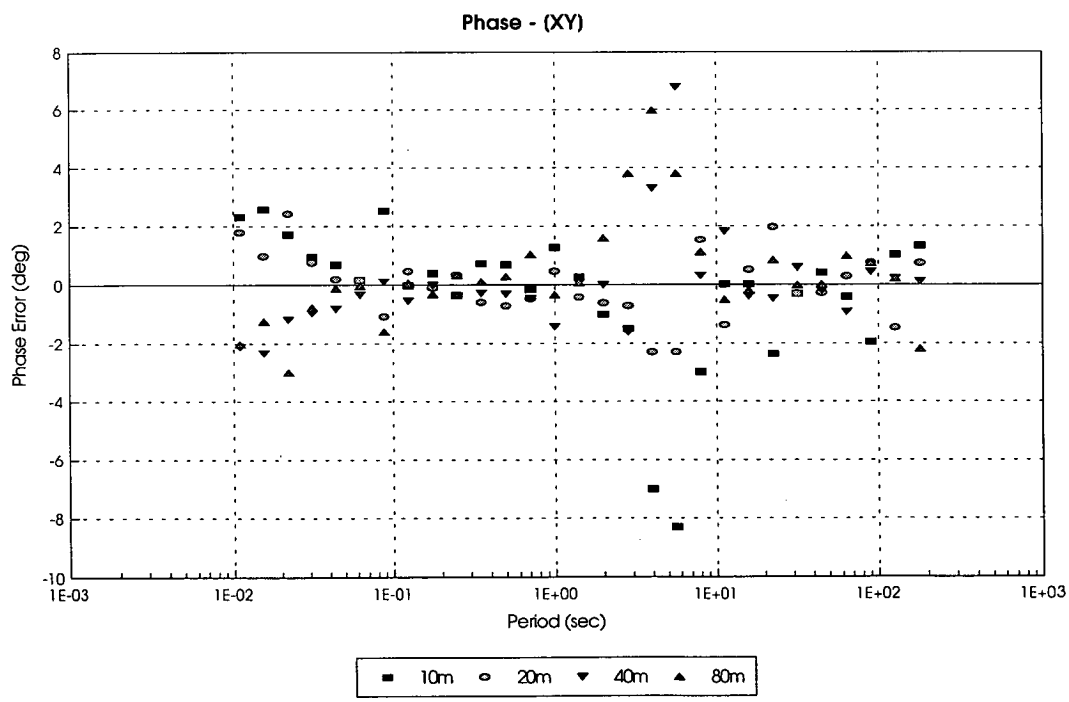

Figure 9.22: Phase Error [XY] - All lines

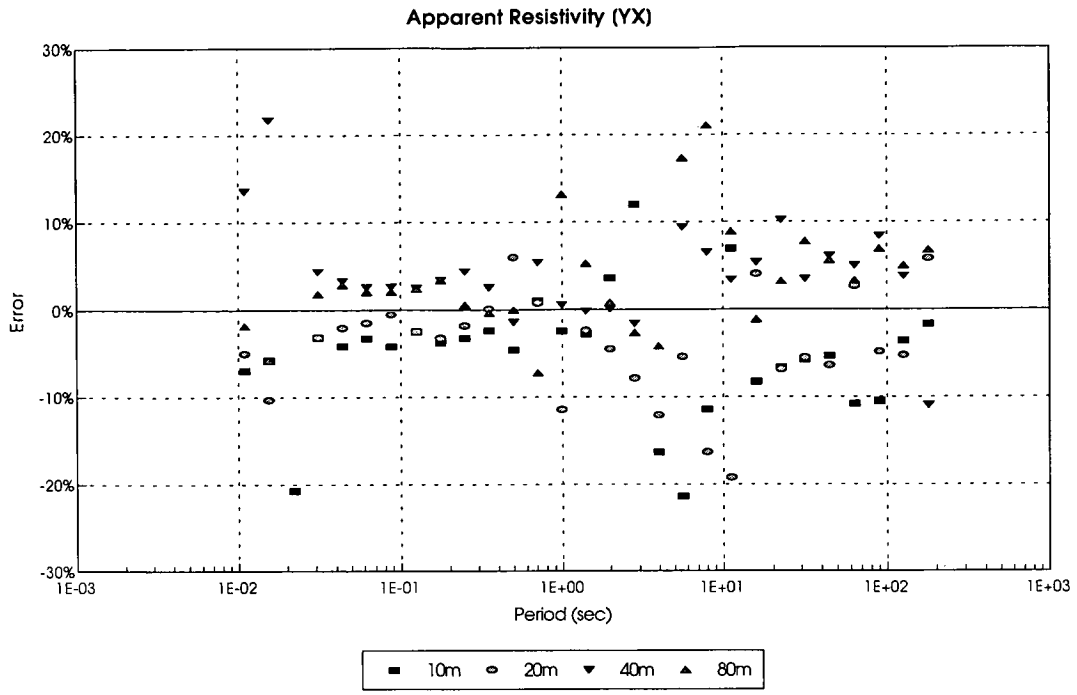

Figure 9.23: Apparent Resistivity Error [YX] - All lines

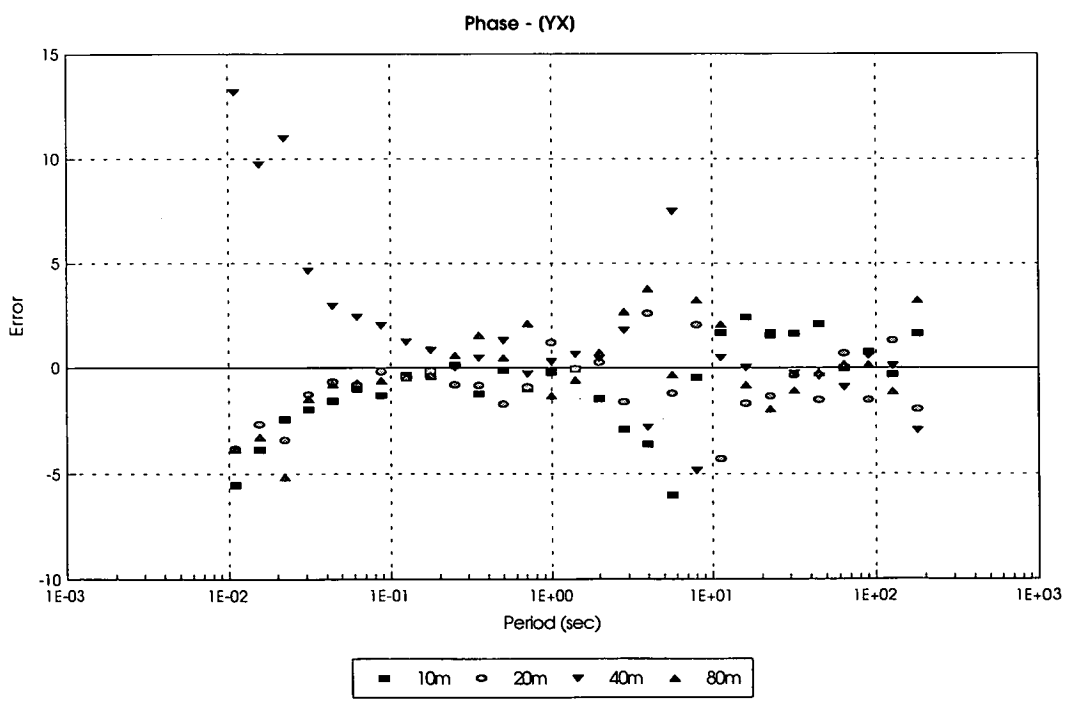

Figure 9.24: Phase Error [YX] - All lines

9.6 Sensor Rotation Experiment

The objective of the second experiment is to investigate the rotational properties of the magnetic and electric fields as represented by the impedance tensor.

The field work setup consists of simultaneous measurements of the electric and magnetic field with a set of sensors ($\mathcal{S}_0$) aligned to the traditional coordinate system (x axis North, y East, and z down) and a set of sensors ($\mathcal{S}_{45}$) aligned to a coordinate system rotated through a positive angle $\theta = 45^\circ$ from North to East. Then, the apparent resistivity and phase of the sensors $\mathcal{S}_{45}$ is rotated mathematically by -45 ° and apparent resistivity and phase of the sensors $\mathcal{S}_0$ are compared. In addition, to observe the signal to noise relationship, two dipoles with line length separations of 20m and 80m were used in both configurations (rotated and non-rotated). The complete sensor configuration is shown if figure 9.25.

In addition to two more induction coil magnetometers needed for the rotated configuration, the Sensor and Remote boxes had to be reconfigured to accommodate the new network (see figure 9.26). This consists of the addition of two magnetic boards (Sensor Box) and two channel boards (Remote Box). The first Sensor box is connected to the sensors of the non-rotated configuration ($\mathcal{S}_0$), i.e: Hx_1, Hy_1, Hz_1, Ex_1, Ey_1 (20m), Ex_2 and Ey_2 (80m). The second Sensor box is connected to the sensors of the rotated configuration ($\mathcal{S}_{45}$) i.e: Ex_3, Ey_3 (20m), Ex_4, Ey_4 (80m), Hx_2 and Hy_2. The remaining equipment configuration is identical to the first experiment.

9.6.1 Time series

In the following set of time series plots, the title, axis, legends and scale are identical to the time series plots of the first experiment, as explained in section 9.5.1. However, there are two differences; two new magnetic sensors are included (from the rotated configuration); magnetic and electric sensors are associated with SITE numbers according to the table 9.5.

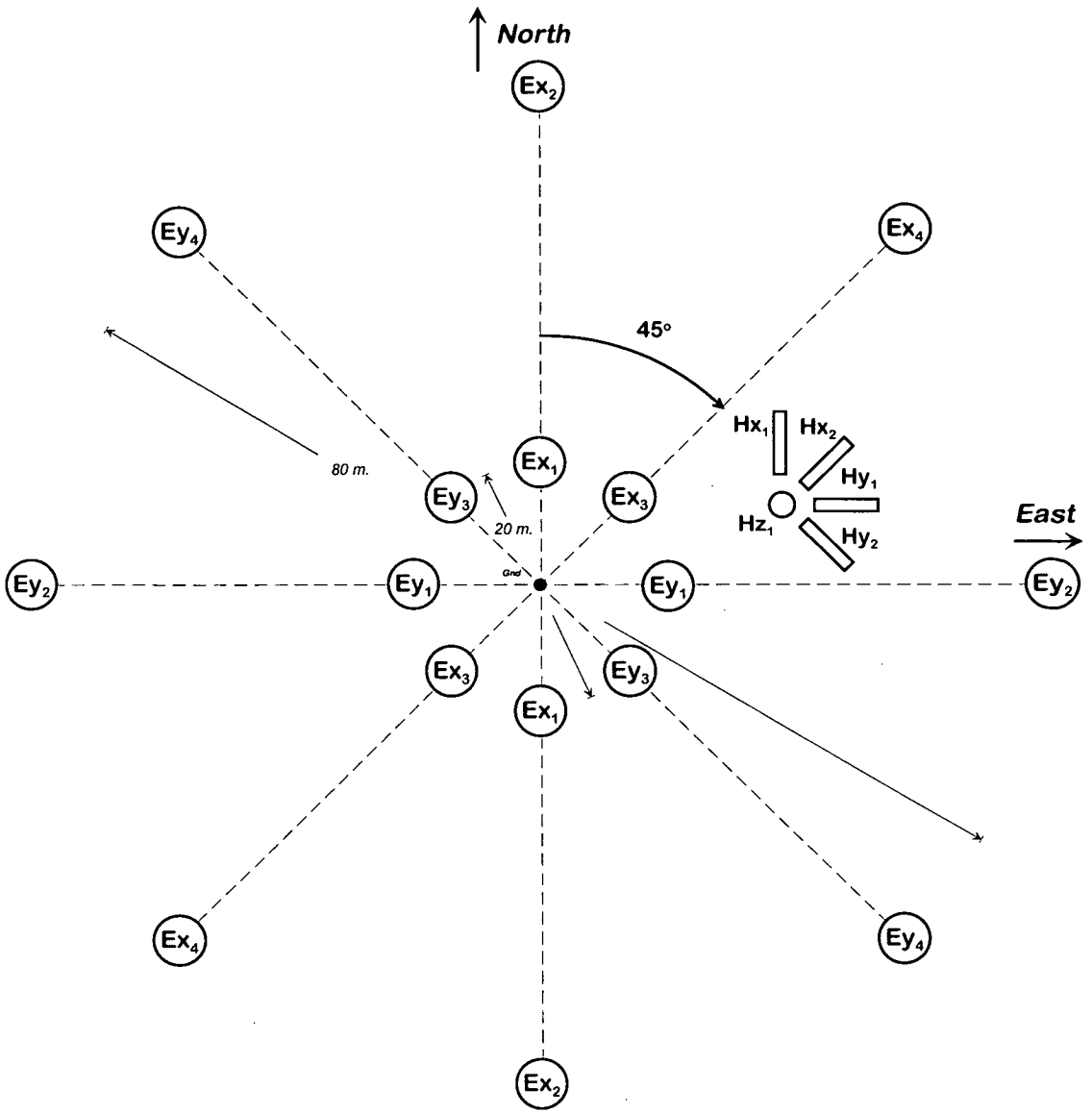

Figure 9.25: Sensor's configuration for measuring the magnetotelluric field simultaneously with normal $\mathcal{S}_0$ and rotated $\mathcal{S}_{45}$ field configuration

Figures 9.27 and 9.28 show typical time series for Band 0 (128–16 Hz). Figure 9.27 shows how strong the 50 Hz noise contamination can be, despite the 40 dB attenuation of the notch filters. The time-segment in figure 9.28, recorded four hours earlier, shows that in the presence of stronger magnetic activity, the expected correlation between orthogonal components of the electric and magnetic fields can be observed (around 19:00:24.00 +1.0s). In the same figure, the E_y component of the electric field (0043) presents a higher 50 Hz contamination than the

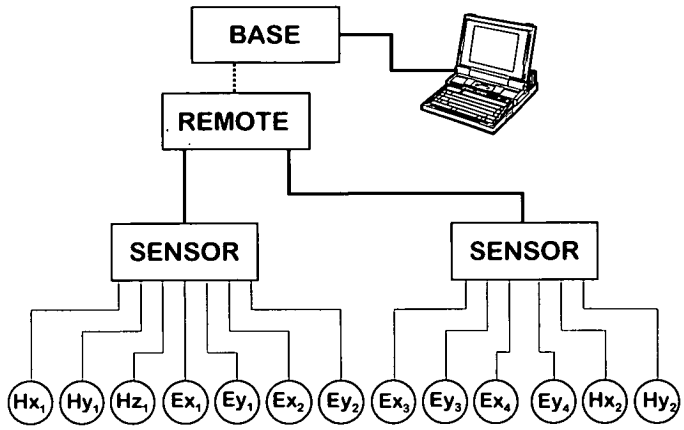

Figure 9.26: Equipment set-up for the sensor layout of figure 9.25

Site	Magnetic	Electric	Direction	Sensor Set
0041	B_x, B_y, B_z	E_x, E_y - 20m	North/East	$\mathcal{S}_0$
0042	-	E_x, E_y - 80m	North/East	$\mathcal{S}_0$
0043	-	E_x, E_y - 20m	North+45 ° /East+45 °	$\mathcal{S}_{45}$
0044	B_x, B_y	E_x, E_y - 80m	North+45 ° /East+45 °	$\mathcal{S}_{45}$

Table 9.5: Sensor configuration per Site for Rotation Experiment

others, this was observed in the first experiment for the same electrode/channel combination, which reinforces the assumption that this is due to a notch filter not accurately tuned for this particular channel.

Figures 9.29 and 9.30 are time series respectively for Bands 3 and 4. In both plots the noise in the electric signals can be observed. Shorter electric line lengths (20m at channels 0041 and 0043) are noisier than longer electric lines (80m at channels 0042 and 0044). This relationship between noise and electric dipoles line separation in not observed for longer periods as shown in figures 9.31 and 9.32 respectively for Bands 6 and 7. However, the expected correlation between orthogonal components of the magnetic and electric fields B_x, E_y and B_y, E_x can be observed and the amplitude of the induced electric fields corrected for the respective line lengths are, as expected, very similar (as they were in the first experiment). Figure 9.29 also shows a noise (switching) in the range 1-10s.

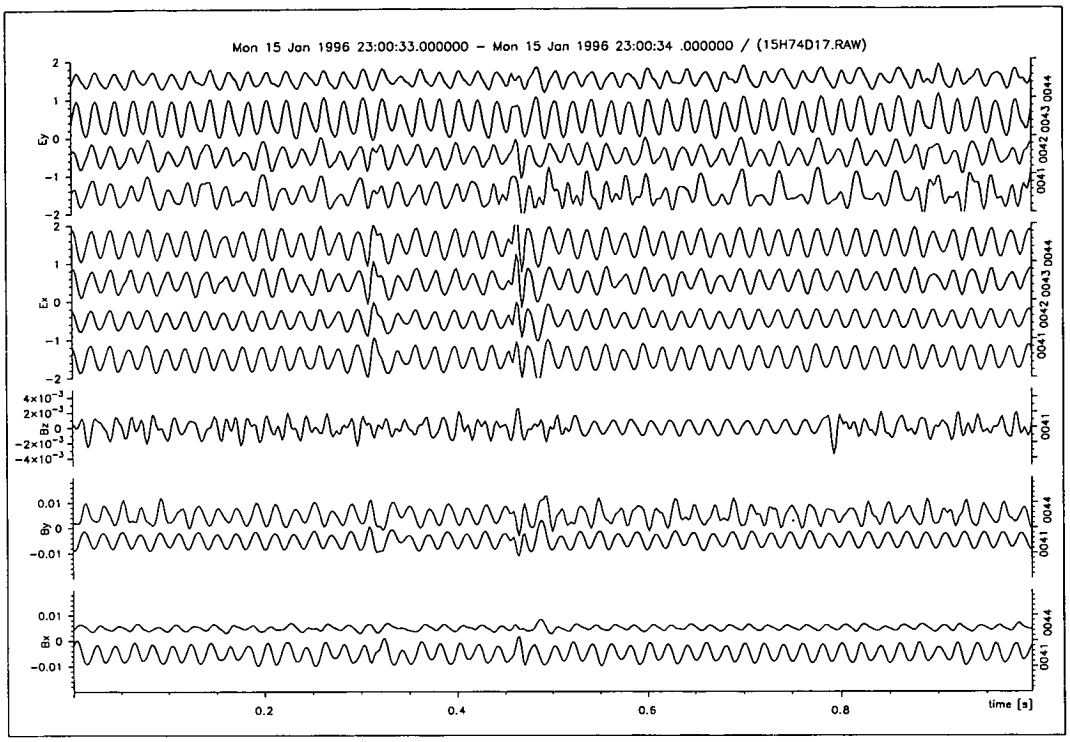

Figure 9.27: Time series of Band 0: 128Hz–16Hz (B(nT), E(mV/km))

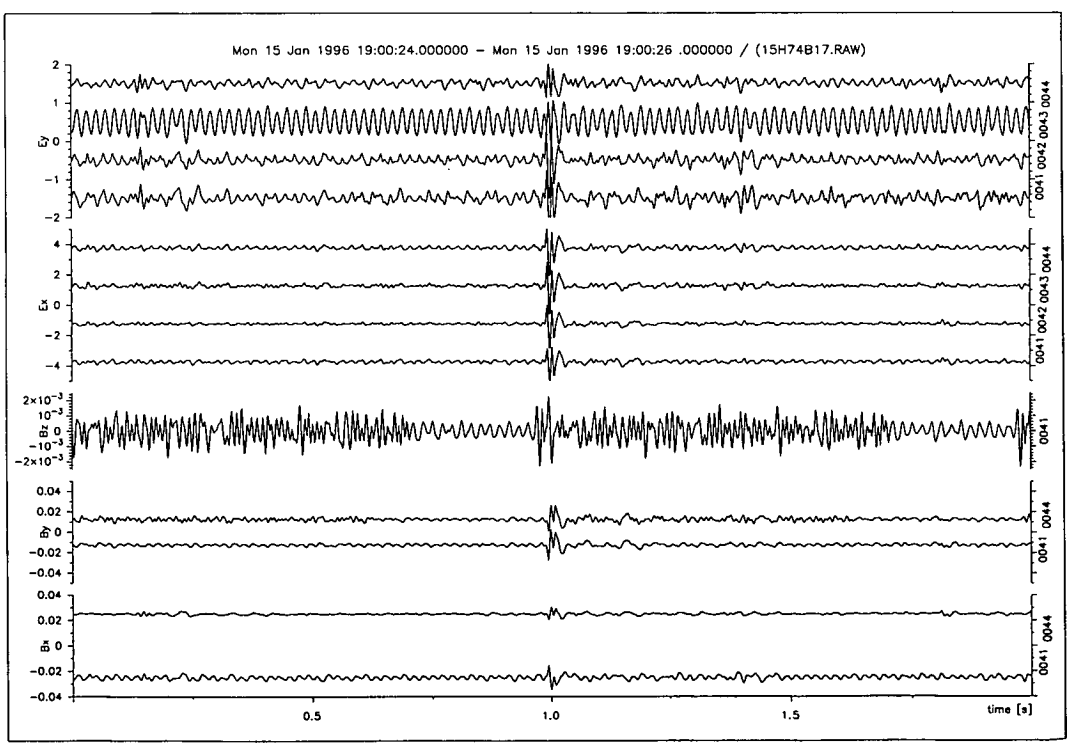

Figure 9.28: Time series of Band 0: 128Hz–16Hz (B(nT), E(mV/km))

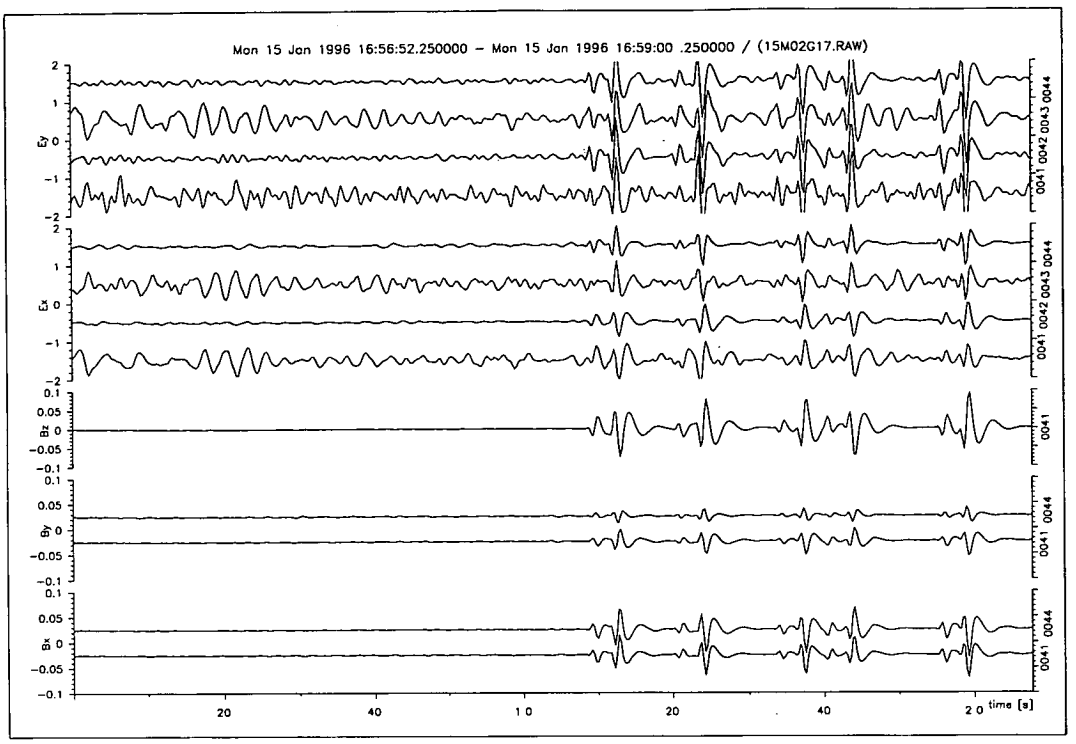

Figure 9.29: Time series Band 3: 1Hz–0.25Hz (1s–4s) (B(nT), E(mV/km))

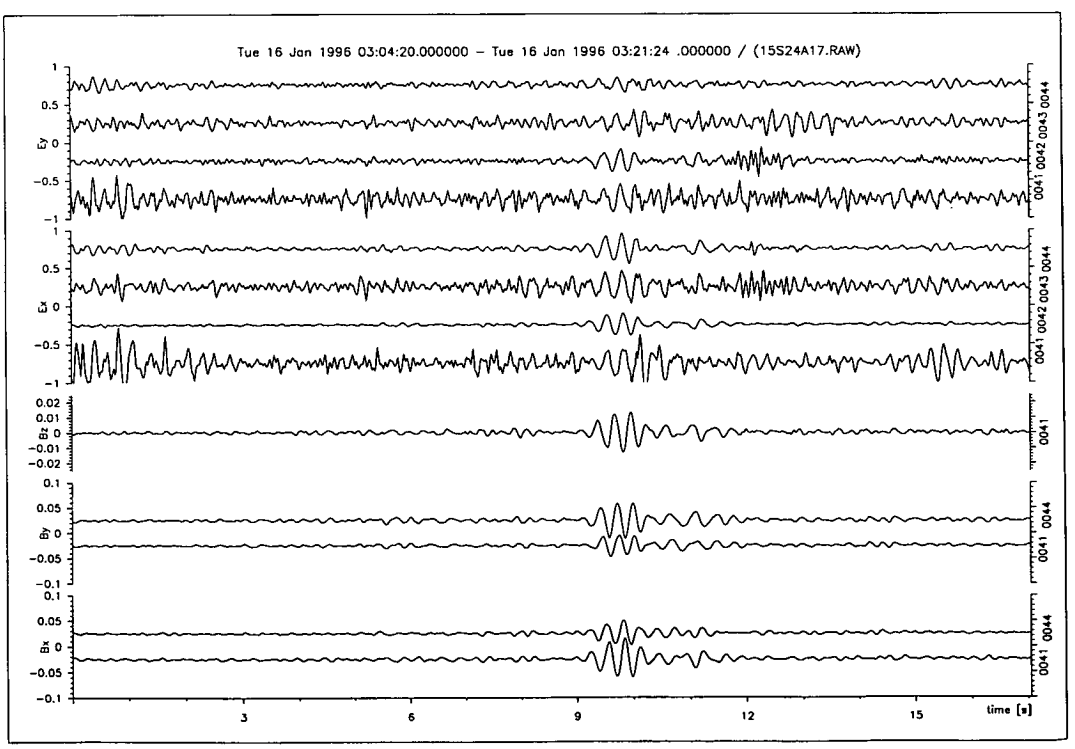

Figure 9.30: Time series Band 4: 0.25Hz–0.0625Hz (4s–16s) (B(nT), E(mV/km))

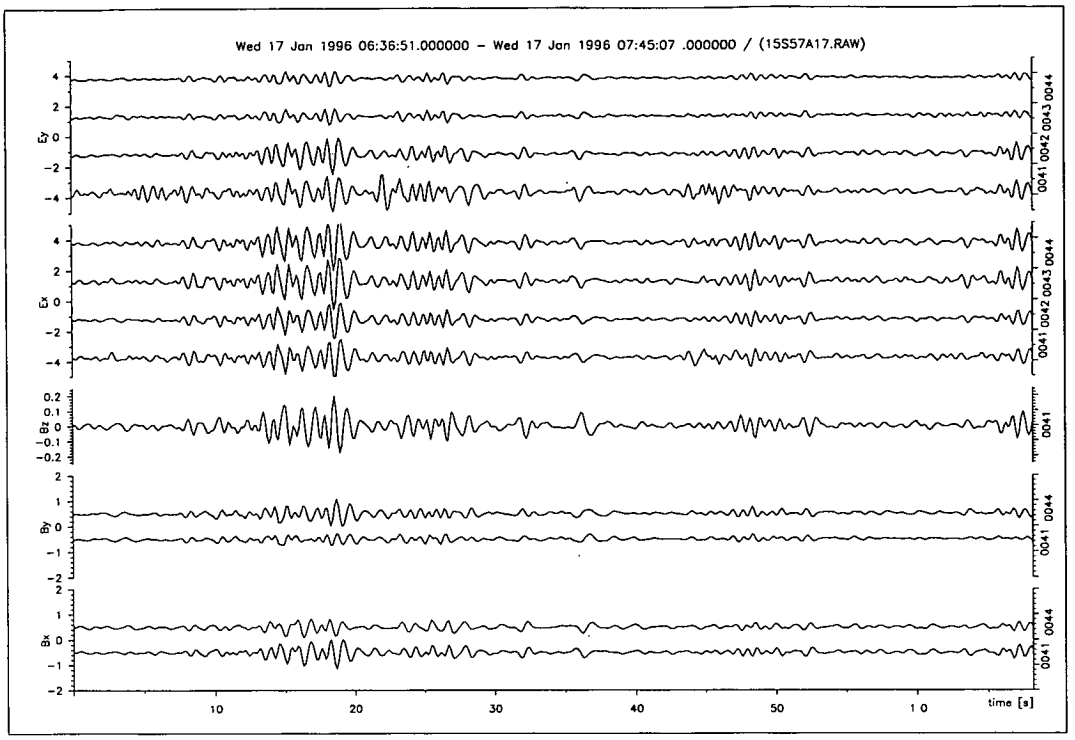

Figure 9.31: Time series of Band 6: 0.0312Hz–0.0078Hz (32s–128s) (B(nT), E(mV/km))

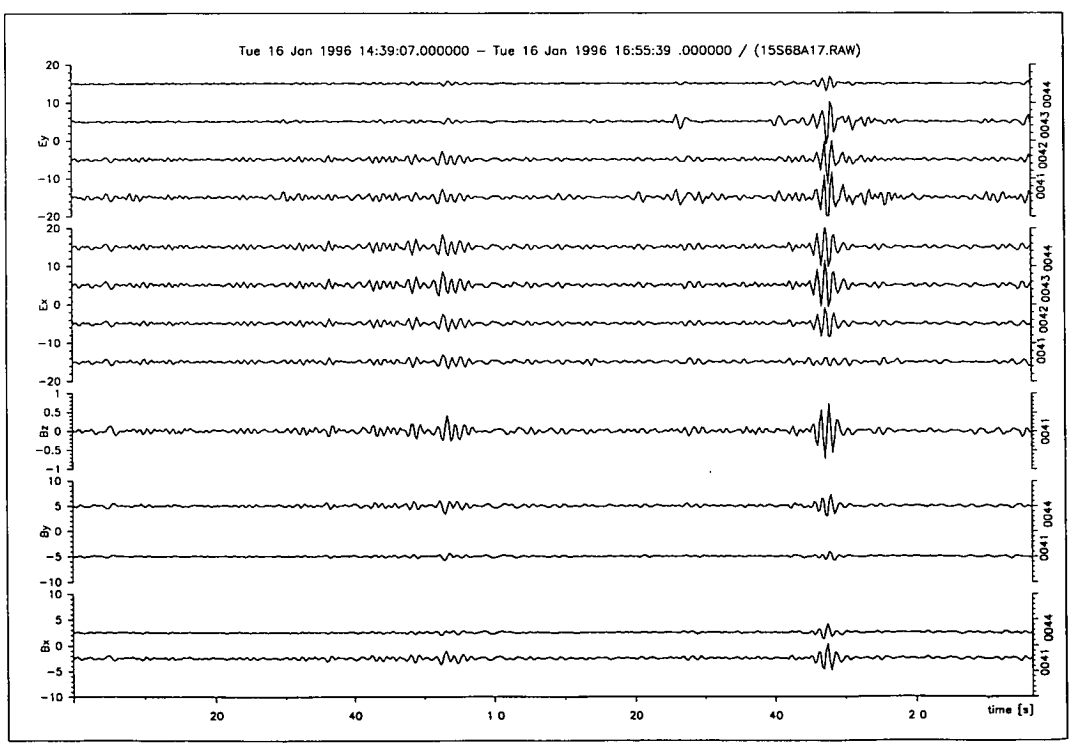

Figure 9.32: Time series of Band 7: 0.0156Hz–0.0039Hz (64s–256s) (B(nT), E(mV/km))

9.6.2 Apparent Resistivity and Phase

The rotational properties of the magnetotelluric (MT) impedance tensor are well known (Sims 1969, Fischer 1975, Vozoff 1972).

A rotation of a right-handed coordinate system about the z-axis by an angle θ will change the electric and magnetic field vectors $\mathcal{E}$ and $\mathcal{H}$ to $\mathcal{E}'$ and $\mathcal{H}'$ by the expression

$$\begin{aligned} \mathcal{E}' &= \mathbf{R}\,\mathcal{E} \\ \mathcal{H}' &= \mathbf{R}\,\mathcal{H} \end{aligned} \qquad \text{where} \qquad \mathbf{R} = \begin{pmatrix} \cos\theta & \sin\theta \\ -\sin\theta & \cos\theta \end{pmatrix}$$

The rotated impedance tensor $Z' = \mathcal{E}'/\mathcal{H}'$ can be expressed as a function of the unrotated impedance tensor Z by the expression

$$Z' = R \cdot Z \cdot R^{-1}$$

In the case of this experiment $\theta = -45^\circ$. To convert the impedance tensor Z_{45} from sensors $\mathcal{S}_{45}$ into Z_0' in same coordinate as $\mathcal{S}_0$ one has to use the relation

$$Z_0' = \mathbf{R}\,(-45) \cdot Z_{45} \cdot \mathbf{R}^{-1}(-45) \tag{9.1}$$

Therefore, Z_0' and Z_0 can be compared.

The observation of the unrotated apparent resistivity and phase plots for $\mathcal{S}_0$ and $\mathcal{S}_{45}$ in figures 9.33 to 9.36 indicates a slight improvement for longer electric lines. Curves for 80m electric lines (Fig.9.34) are smother, present less discontinuity and smaller error bars compared to the 20m electric lines. For instance, the discontinuity observed in the range 1–10s in the apparent resistivity [XY] in figure 9.34 is smaller compared to the apparent resistivity [XY] in figure 9.33. This may be an indication of improvement in the signal-to-noise relationship since this frequency range coincides with the *dead-band*, where the magnetic field strength is weaker. In general, the order of magnitude of the apparent resistivity and phase are similar regardless the electric line lengths and rotation.

The low values of the apparent resistivity [XY] at higher frequencies (10Hz–100Hz) for the $\mathcal{S}_{45}$ configuration (20m and 80m) in figures 9.35 and 9.36 does not correspond to the phase variation in the same period range. A possible explanation for this shape can be related to the frequency response calibration for this particular induction coil magnetometer (Hy_2) , because it is common for both 20m and 80m electric lines.

Figures 9.37 and 9.38 are apparent resistivity and phase calculated from electric and magnetic fields measured by the rotated configuration Z_{45} for $\mathcal{S}_{45}$ (20m and 80m) and the rotated as in 9.1. The same improvements on the signal to noise relationship for the longer electric lines, as observed for the $\mathcal{S}_0$ configuration, can also be noticed. Apparent resistivity [XY] and [YX] show the same pattern at higher frequencies as observed in figures 9.35 and 9.36 (for [XY] only). This is due to the contribution of the original [XY] component to the new rotated [XY] and [YX] elements.

Figures 9.39 to 9.42 are combined plots of unrotated and rotated apparent resistivity and phase derived from figures 9.33, 9.34, 9.37 and 9.38. The annotation is explained in table 9.6. The apparent resistivity scale is limited between 10 and 100Ωm to improve the resolution and the error bars can be observed more accurately.

Legend	**Electric Lines**	**Sensor Configuration**	**App.Resistivity and Phase Plots**
N20	20m	$\mathcal{S}_0$ (North / East)	Unrotated
N80	80m	$\mathcal{S}_0$ (North / East)	Unrotated
N20-45R	20m	$\mathcal{S}_{45}$ (North+45° / East+45°)	Rotated (−45°)
N80-45R	80m	$\mathcal{S}_{45}$ (North+45° / East+45°)	Rotated (−45°)

Table 9.6: Graph legend for combined plots

In general, apparent resistivity and phase present similar responses (curve shape and order of magnitude) for rotated and non-rotated configurations and different electric line lengths separations.

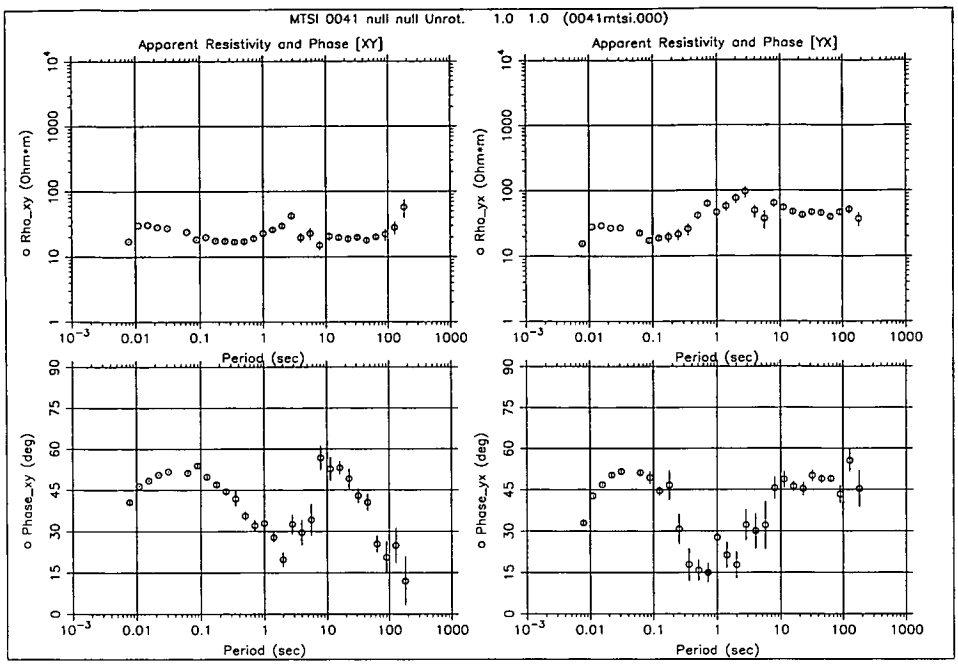

Figure 9.33: Apparent Resistivity and Phase - 20m electric lines for $\mathcal{S}_0$

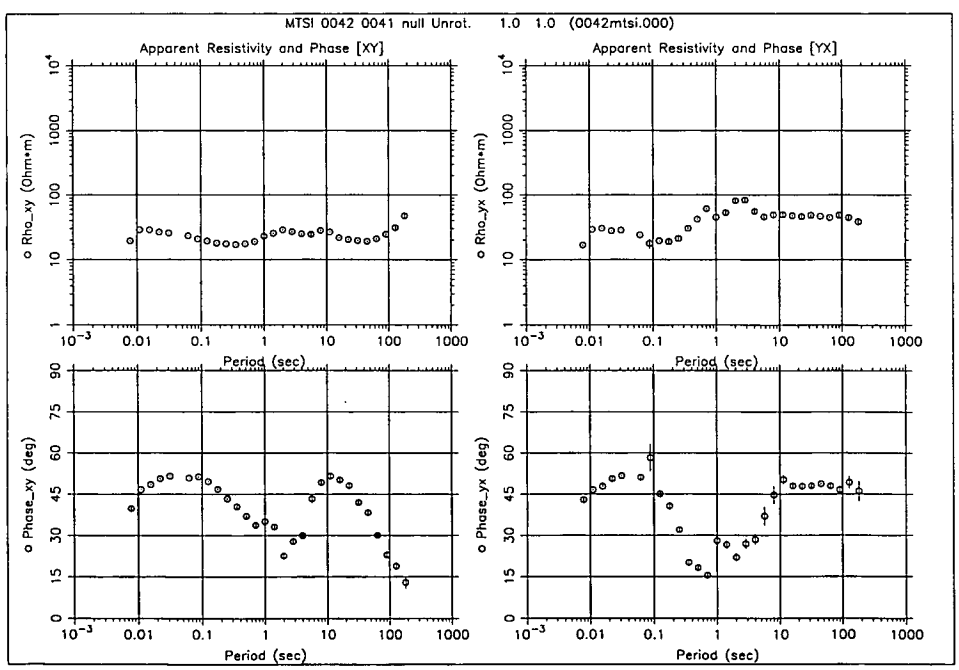

Figure 9.34: Apparent Resistivity and Phase - 80m electric lines for $\mathcal{S}_0$

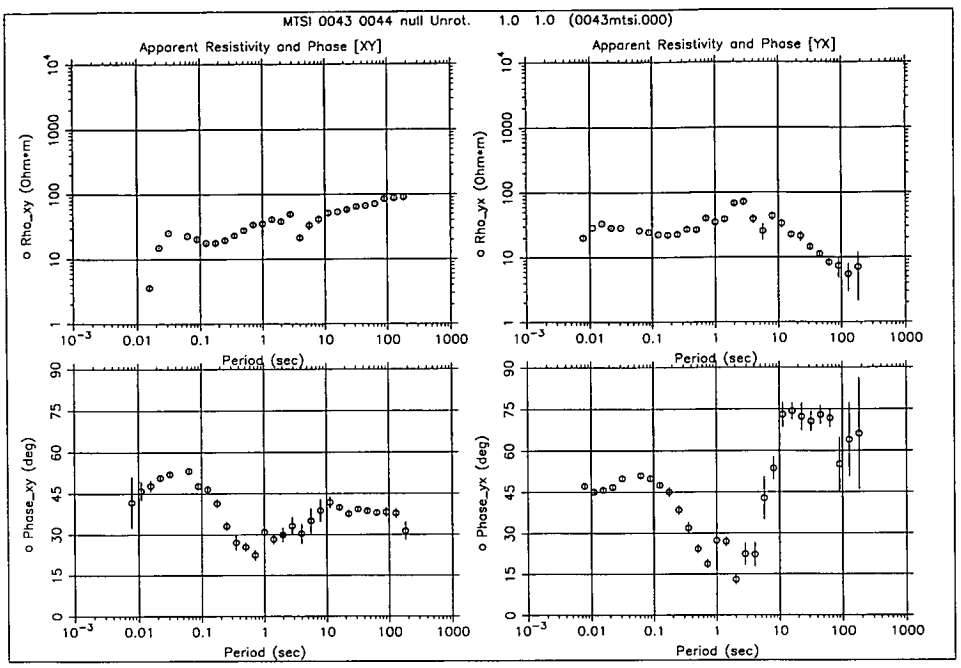

Figure 9.35: Apparent Resistivity and Phase - 20m electric lines for $\mathcal{S}_{45}$

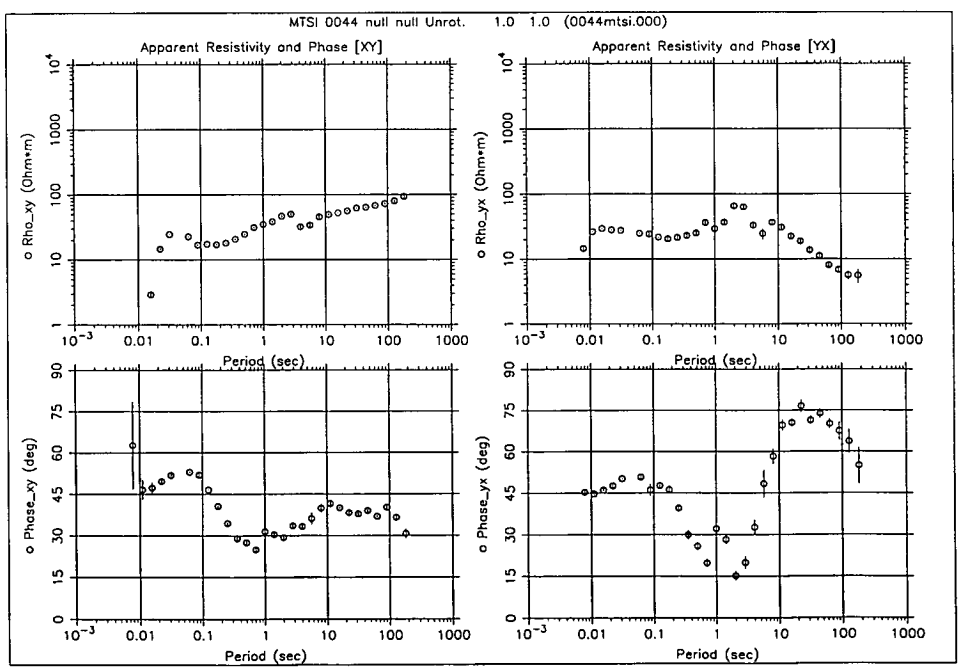

Figure 9.36: Apparent Resistivity and Phase - 80m electric lines for $\mathcal{S}_{45}$

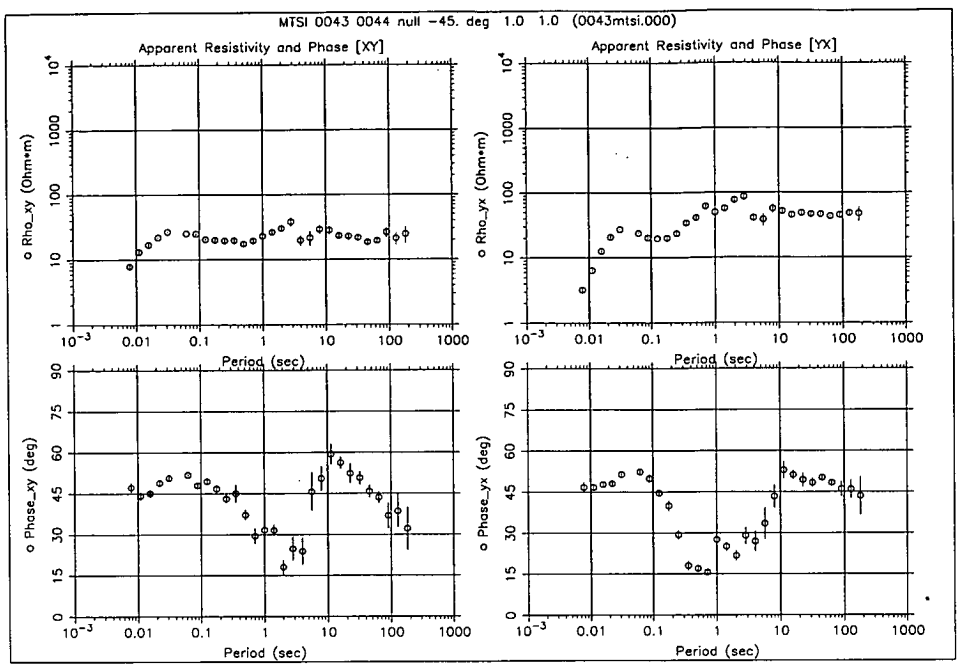

Figure 9.37: Rotated Apparent Resistivity and Phase - 20m electric lines for $\mathcal{S}_{45}$ rotated to $\mathcal{S}_0$ coordinates

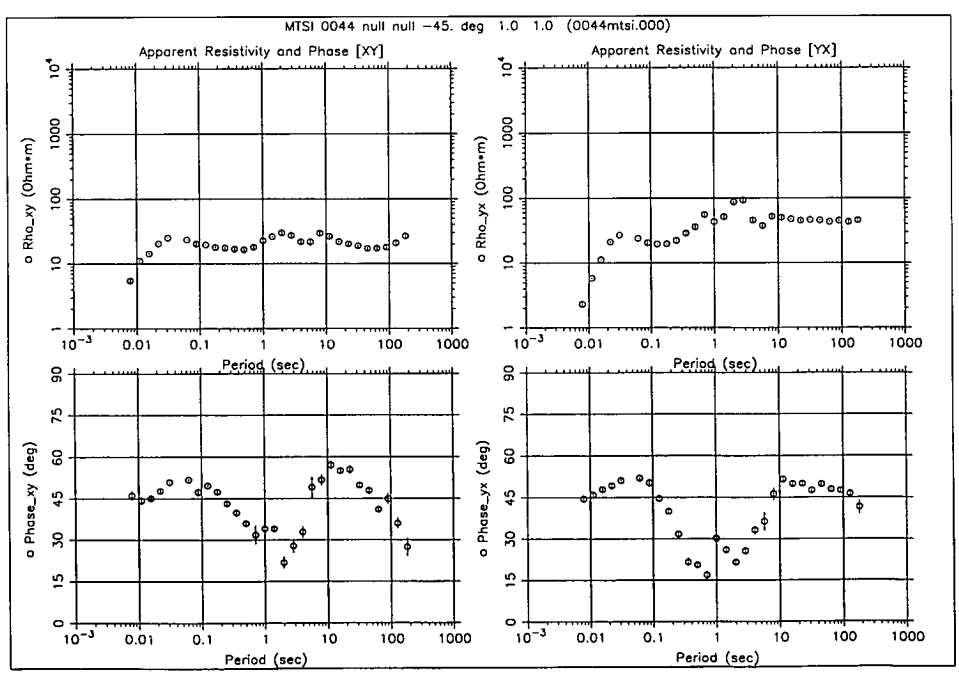

Figure 9.38: Rotated Apparent Resistivity and Phase - 80m electric lines for $\mathcal{S}_{45}$ rotated to $\mathcal{S}_0$ coordinates

Figures 9.39 and 9.41 show a good correlation between all lines within the range 0.03s–2s approximately, then deteriorates beyond 2s. There is a discontinuity in the combined plot of the apparent resistivities between 3s–4s [XY] and [YX], usually associated with noise. In addition to the lower natural activity expected in this period range, the near field noise generated by some machinery used in nearby farms (period $\approx$ 4s) decreases the natural signal to noise relationship which may lead to this discontinuity. This periodic noise has been observed at the time series for Bands 3 (fig 9.29) and Band 4. At higher frequencies, the apparent resistivity [XY] and [YX] related to N20-45R/N80-45R are not expected. However these are similar between then, which reinforces the assumption that a common source to both lines may be the reason. The only common source between the rotated lines is the induction coil magnetometer and, as mentioned, an improper frequency response calibration for Hy_2 is the most probable cause.

The combined phase plots present better results than the combined apparent resistivity plots. Phase for both configurations and electric line lengths separation are quite similar (see Fig.9.40 and 9.42). In particular, the latter figure shows that curves of Phases [YX] match reasonably well within the whole period range, i.e. 0.01s–128s.

The final step is to find the relative errors between curves in fig.9.39 to 9.42, these are shown in fig.9.43 to 9.46.

Apparent resistivity [XY] and [YX] errors (Fig.9.43 and 9.45) are typically less than 10% for period the range between approximately 0.03s–100s. Higher errors at the edges of the bandwidth are probably due to an incorrect frequency response calibration.

Phase [XY] errors (Fig.9.44) are within 5 ° for the period range 0.01s–100s. Figures are even better for the Phase [YX] (see figure 9.46). Phase errors are practically within 2 ° for the whole period range e.g. 0.01s–128s except for the shorter electric dipole lengths (20M and 20M-45) in the period range between 1s–20s.

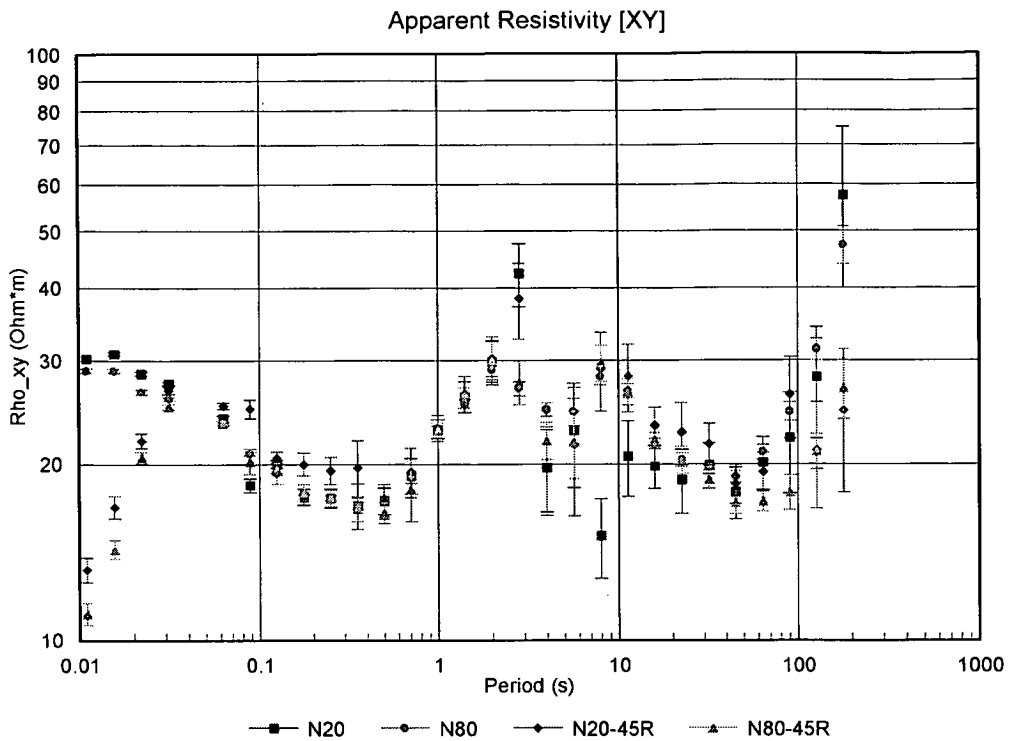

Figure 9.39: Apparent Resistivity [XY] - All lines

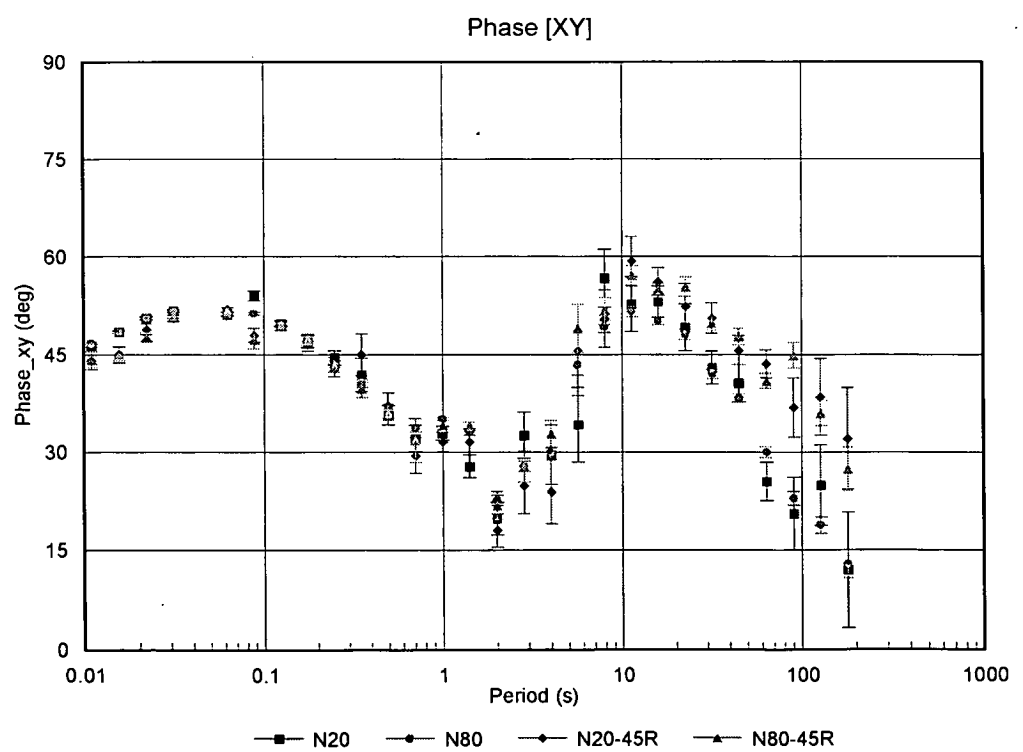

Figure 9.40: Phase [XY] - All lines

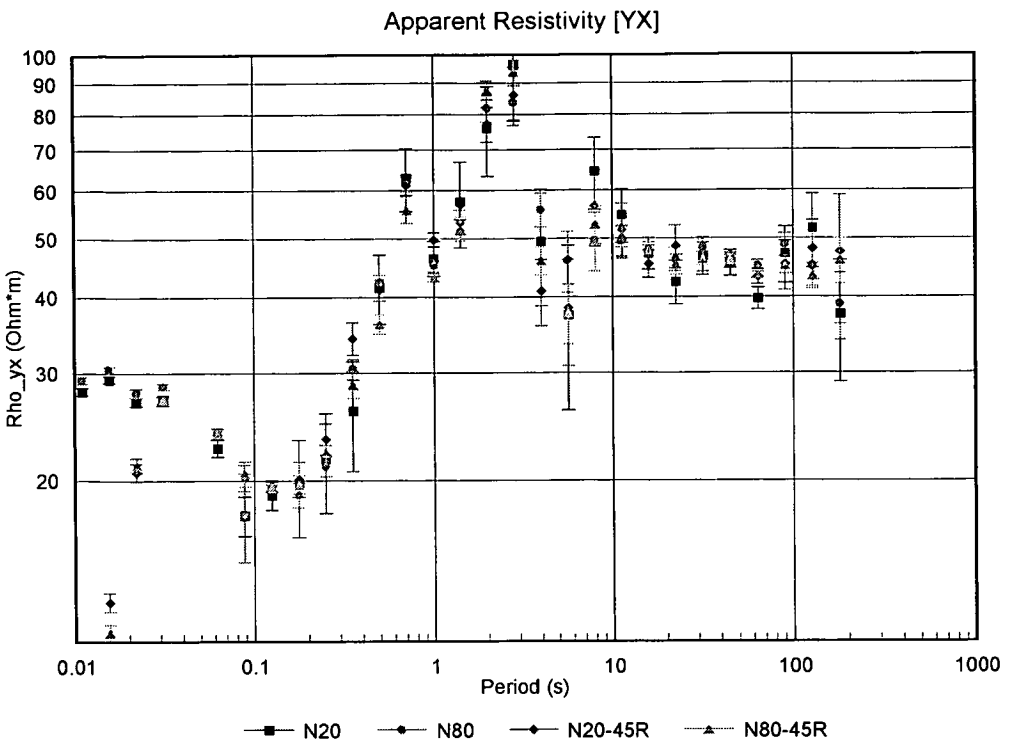

Figure 9.41: Apparent Resistivity [YX] - All lines

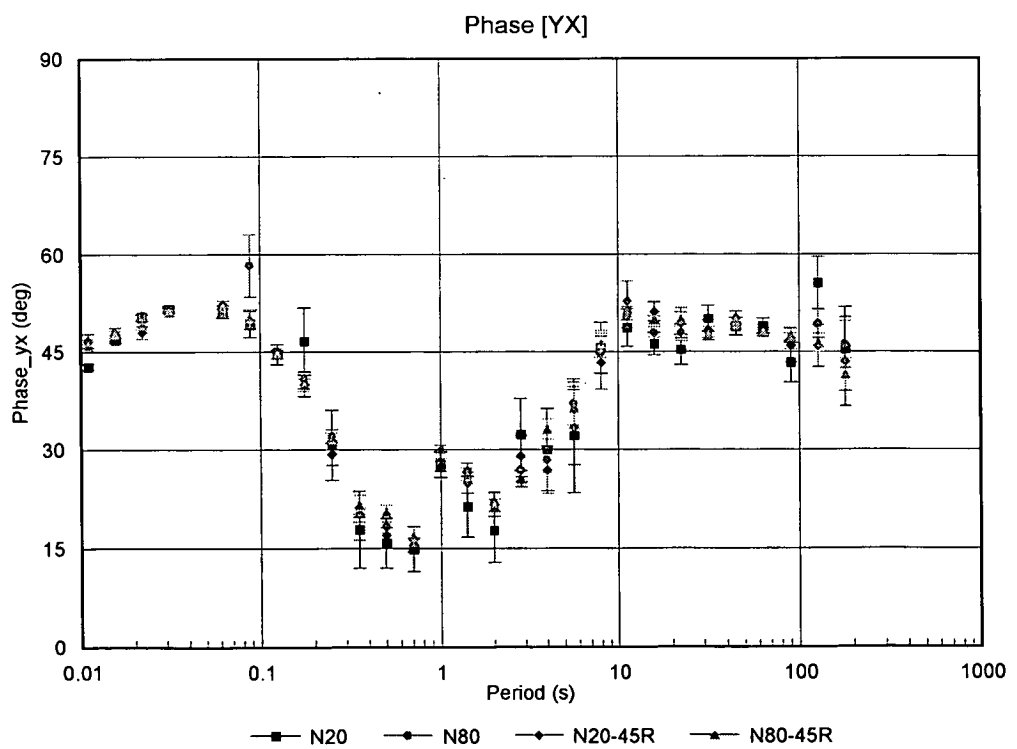

Figure 9.42: Phase [YX] All lines

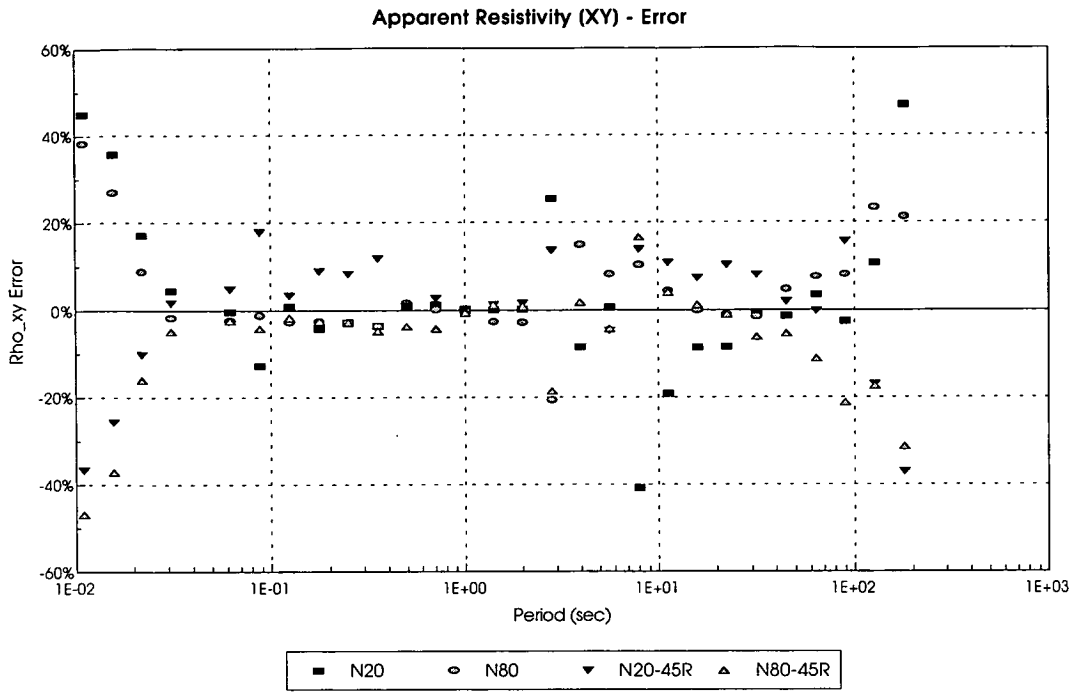

Figure 9.43: Apparent Resistivity Error [XY] - All lines

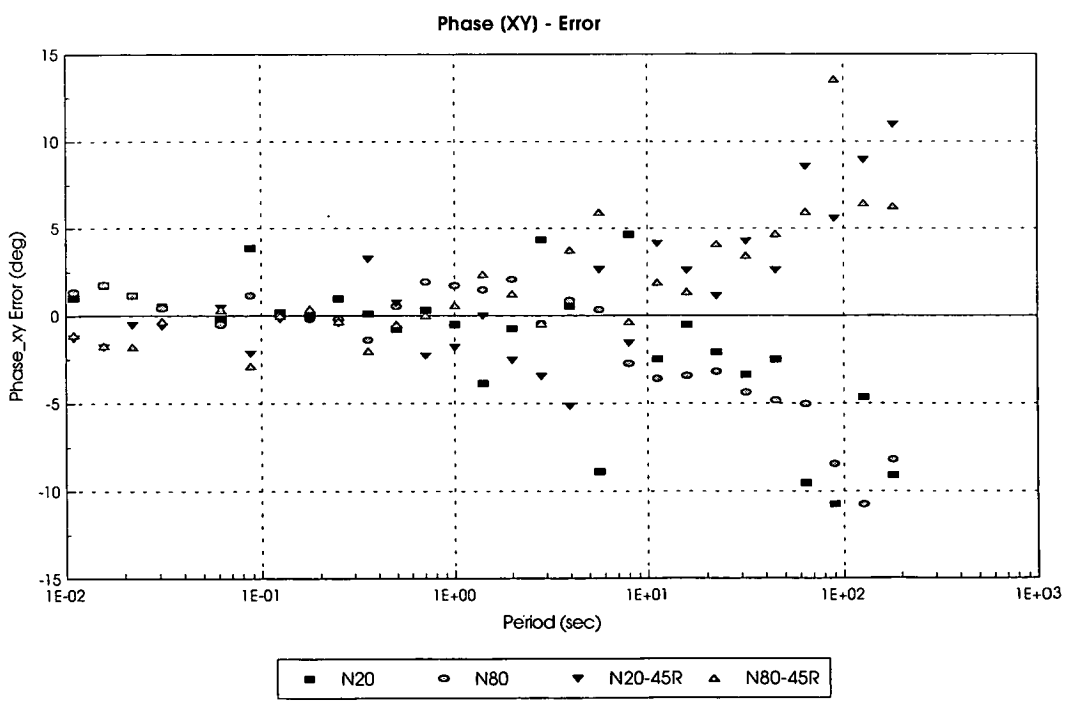

Figure 9.44: Phase Error [XY] - All lines

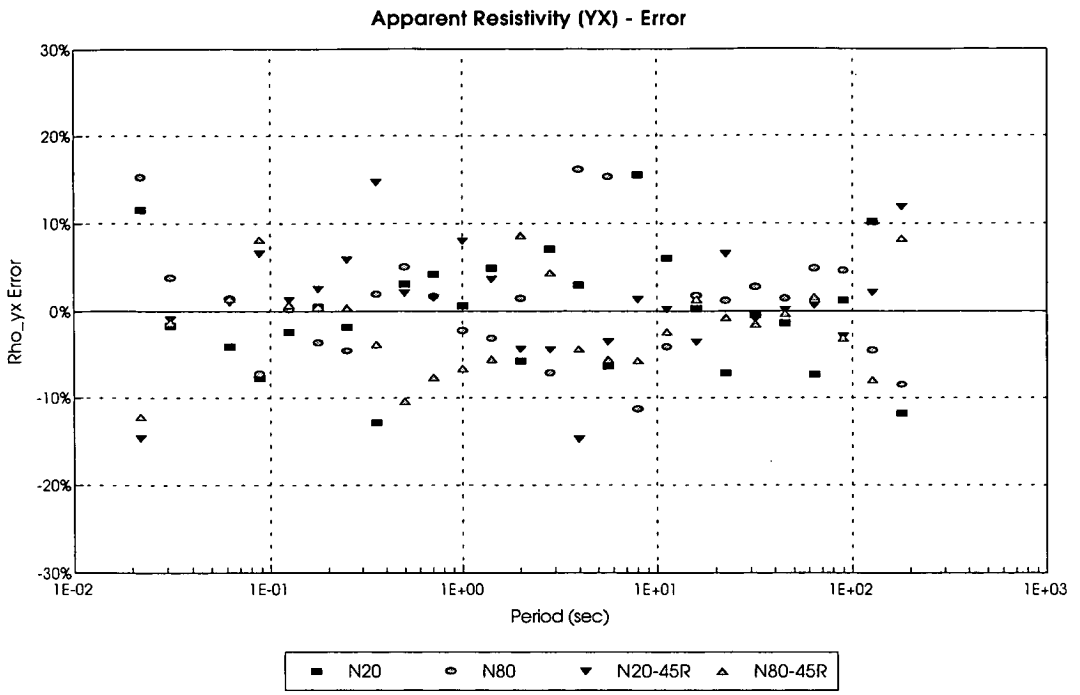

Figure 9.45: Apparent Resistivity Error [YX] - All lines

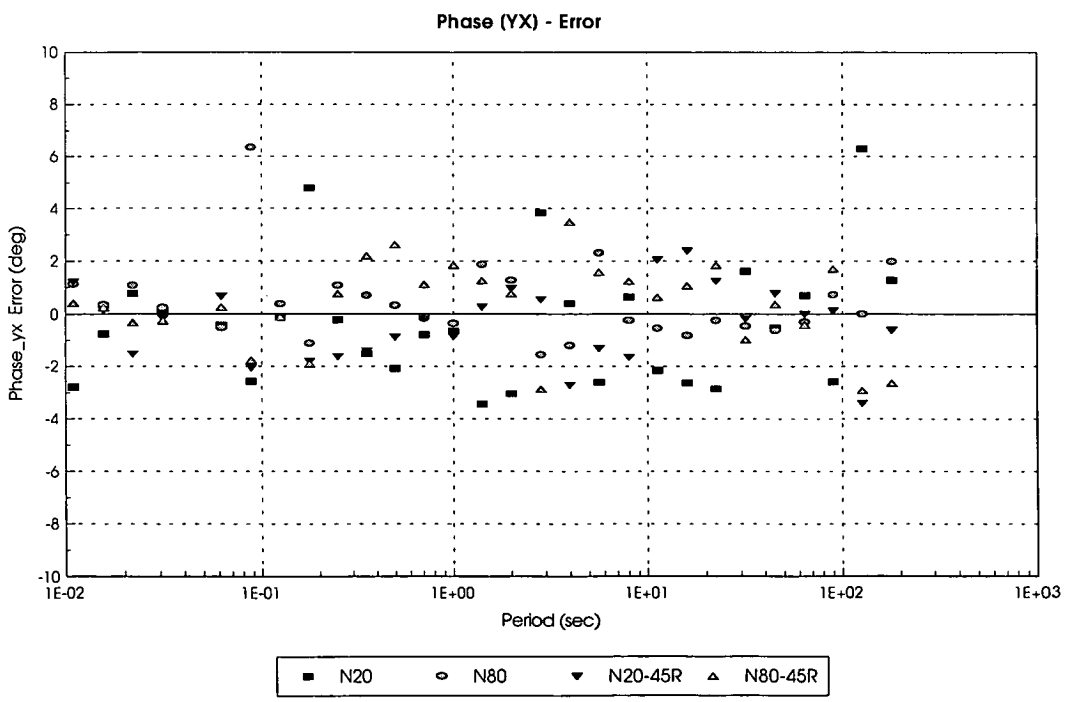

Figure 9.46: Phase Error [YX] - All lines

CHAPTER 10

Conclusions

The development of SPAM Mk-III (Short-Period Automatic Magnetotelluric Data Acquisition and Processing System) and its application to the magnetotelluric method are the objectives of this thesis.

I joined the project in February 1993 as a part of my PhD studies. My contribution to the development consists of the design, construction and testing of the Sensor Box (Chapter 7) and the Repeater Box (Chapter 8) as well as in-depth studies of the operational parameters which led to a number of final system modifications.

SPAM Mk-III is a highly modular equipment where each module can be reconfigured and upgraded easily to incorporate new technologies. Some improvements can be made to in the analogue section and to the digital communication stages. New components should be tried to improve the intrinsic noise and to increase the communication speed without compromising the low-power consumption that has been achieved so far. The new GPS (Global Positioning System) time synchronization facility needs to be fully tested. A major development planned in the near future is to extend the frequency band of operation to much higher frequencies, a requirement for shallower magnetotelluric applications. However, this implies a redesigning of the analogue circuitry and the data acquisition scheme.

In the context of instrumentation I also designed, constructed and tested a set of copper-copper sulphate electrodes (Chapter 3) to be used in conjunction with SPAM Mk-III. These are cheap, practically maintenance free and stable for the frequency range covered by the equipment. However, copper-copper sulphate electrodes are not stable enough for longer period applications. I intend to develop a modified electrode for longer term monitoring with the same mechanical design but with a modified core to accommodate a lead-lead chloride metal salt couple.

The distinctive SPAM Mk-III capabilities of multi-channel data acquisition were essential for the two field experiments (Chapter 9), their aim was to study some concepts assumed by the Magnetotelluric method. The results of the first experiment revealed that it is possible to carry out MT measurements with shorter electrode separations while obtaining apparent resistivity and phase with a reasonable degree of accuracy. The results for the second experiment reinforced the prediction that, for a homogeneous site, the impedance tensor is independent of measuring coordinates.

The site chosen for the field experiments was quite favorable. Neither geological structure nor local noise interfered on the results. However, I carried out similar experiment at a much noisier site, where approximately 1 Gbytes of data was recorded. I intend to analyse this data and to investigate whether it is possible to reduce the influence of the near field noise by using different combinations of sensor configurations and electric line lengths.

Finally, I intend to investigate the effect of the sensor frequency response correction on the apparent resistivity and phase. Even though this is essential to correct the frequency response, the application of an improper calibration can lead to an incorrect apparent resistivity and phase mainly at the extremes of the frequency band as happened in my experiments.

Bibliography

Allsopp, D. et al. (1973). A Wide-Band Digital Magnetotelluric Recording System. *Geophysical Prospecting 22*, 272–278.

Analog Devices (1985, April). Minimization of Noise in Operational Amplifier Applications. In *Application Note 13*. Analog Devices,Inc.,.

Analog Devices (1992). *Amplifier Reference Manual*, Volume 1. Analog Devices,Inc.,.

Anvar-CNRS (1980). Model CM216E - Magnetometer User Manual. License ANVAR - CNRS Garchy.

Anvar-CNRS (1984). Model CM11E - Magnetometer User Manual. License ANVAR - CNRS Garchy.

Arnold, G. et al. (1993). *Linear Design Seminar*, Chapter 4—Data Transmission, pp. 4.1–4.96. Texas Instruments Limited.

Baher, H. (1990). *Analog & Digital Signal Processing*. John Wiley & Sons.

Bahr, K. (1988). Interpretation of the magnetotelluric impedance tensor: Regional induction and local telluric distortion types. *Journal of Geophysics 62*, 119–127.

BGS (1983). Scotland sheet 33w & part of 41. BGS - Institute of Geological Sciences.

Bitterly, J. et al. (1995, April). Long-Term Stability Estimation of Petiau Pb–$PbCl_2$ Electrodes. In *Proceedings of the Workshop "Electrodes"*, pp. 18–19. Edited by G.Clerc and others. Workshop held at the Centre de Recherches Geophysiques de Garchy – France.

Cagniard, L. (1953). Basic theory of the magneto–telluric method of geophysical prospecting. *Geophysics 50*, 605–635.

Cantwell, T. and T. Madden (1960). Preliminary report on crustal magnetotelluric measurements. *Jornal of Geophysical Research 65*, 4202–4205.

Clarke, J., T. Gamble, W. Goubau, R. Kock, and R. Miracky (1983). Remote-reference magnetotellurics: equipment and procedures. *Geophysical Prospecting 31*, 149–170.

Clayton, G. (1982). *Operational Amplifiers* (Second ed.). Butterworth Scientific.

Clerc, G. et al. (1996a, July). One Year Systematic Study of Electrodes for Long Term Monitoring. In *Proceedings of the 13th Workshop on Electromagnetic Induction in the Earth. Onuma-Japan*, pp. 157. Oral presentation.

Clerc, G. et al. (1996b, July). One Year Systematic Study of Electrodes for Long Term Monitoring: Technical Description and Expanded Results. In *Proceedings of the 13th Workshop on Electromagnetic Induction in the Earth. Onuma-Japan.* Poster section.

Crystal Semiconductor (1995, March). *Data Acquisition Products Data Book*, Chapter 2 - 16-bit, 100KHz/20KHz A/D Converters, pp. 2:113–2:158. Crystal Semiconductor Corporation.

Dawes, G. (1989). SPAM IIb Short-Period Automatic Magnetotelluric System - Design and Documentation Manual. Internal Publication – Edinburgh University. Department of Geology and Geophysics.

Dawes, G. (1990). Feasibility Study for Transputer-based Upgrade of the Short-Period Automatic Magnetotelluric (SPAM) System.

Dobin, M. (1988). *Introduction to Geophysical Prospecting* (4 ed.)., Chapter 18.3 - Natural-Source Electromagnetic Techniques, pp. 773–823. McGraw-Hill International Editions.

Eggers, D. (1981). An eigenstate formulation of the magnetotelluric impedance tensor. *Geophysics 47*, 1204–1214.

Erkul, E. and A. Muller (1995, April). Experiences with different electrodes in continuous magnetotelluric measurements at the North Anatolian Fault Zone. In *Proceedings of the Workshop "Electrodes"*, pp. 12–17. Edited by G.Clerc and others. Workshop held at the Centre de Recherches Geophysiques de Garchy – France.

Filloux, J. (1973). Techniques and instrumentation for study of natural electromagnetic induction at the sea. *Physics of the Earth and Planetary Interiors 7*, 323–328.

Fischer, G. (1975). Symmetry properties of the magnetotelluric impedance tensor for structures with a vertical plane of reflection symmetry. *Geophysics 40*, 1046–1050.

Fisher, G. and W. Massero (1994). Rotational properties of the magnetotelluric impedance tensor: the example of the araguainha inpact crater, brazil. *Geophysics Journal International 119*, 548–550.

Fontes, S. (1988). *Electromagnetic Induction Studies in the Italian Alpes.* Ph. D. thesis, University of Edinburgh.

Franco, S. (1988, May). *Design with Operational Amplifiers and Analog Integrated Circuits* (International ed.). McGraw-Hill Book Company.

Geophysics Group (1995a). University of Edinburgh–Department of Geology and Geophysics. Abstracts published by members of the Geophysics Group. Academic and Reseach. Internal Publication.

Geophysics Group (1995b). University of Edinburgh–Department of Geology and Geophysics. Papers published by members of the Geophysics Group. Academic and Reseach. Internal Publication.

Goubau, W., T. Gamble, and J. Clarke (1978). Magnetotelluric data analysis: removal of bias. *Geophysics 43-6*, 1157–1166.

Greef, R. (1990). *Instrumental Methods in Electrochemistry*, Chapter 11.1 - The design of electrochemical cells, pp. 357–370. Ellis Horwood Limited, Chichester, New York. Southampton Electrochemistry Group.

Groom, R. and R. Bailey (1989). Decomposition of magnetotelluric impedance tensor in the presence of local three-dimentional galvanic distortion. *Journal of Geophysical Research 94*, 1913–1925.

Hermance, J. (1973). Processing of magnetotelluric data. *Physics of the Earth and Planetary Interiors 7*, 349–364.

Hibbert, D. (1993). *Introduction to Electrochemistry*, Chapter 4 - Electrodes and electrochemical cells, pp. 59. Macmillan, Basingstoke.

Hobbs, B. (1971). The calculation of geophysical induction effects using surface integrals. *Jornal of Geophysics - Royal Astronomical Society 25*, 481–509.

Hobbs, B. (1992). Terminology and symbols for use in studies of electromagnetic induction in the earth. *Surveys in Geophysics 13*, 489–515.

Hoover, D., C. Long, and R. Centerfit (1978). Some results from audio-magnetotelluric investigations in geothermal areas. *Geophysics 43*, 1501–1514.

Inmos (1989a). *Transputer Applications Notebook — Systems and Performance* (Firts ed.)., Chapter 3–Connecting INMOS links, pp. 30–51. Inmos Corporation. INMOS Databook Series.

Inmos (1989b). *Transputer Data Book* (Second ed.)., Chapter 7–IMS T425 Transputer engineering data, pp. 261–332. Inmos Corporation. INMOS Databook Series.

Inmos (1990). *The Transputer Data Book* (Second ed.). Inmos Corporation. INMOS Databook Series.

Junge, A. (1992). Zur Schätzung der effectiven Anzahl der Freiheitsgrade dei der Bestimmung magnetotellurischer übertragungsfunktionen. In V.Haak and H.Rodermann (Eds.), *Protokoll Kolloquium Elektromagnetische Tiefenforschung*. Borkheide.

Junge, A. (1995). Magnetotelluric in the Long-Period range. EEC Human Capital and Mobility - Individual Fellowship. Contract No. ERBCHBICT 93 0610 - Final Report.

Kaufman, A. and G. Keller (1981). *The Magnetotelluric Sounding Method*. Elsevier Scientific Publishing Company. Methods in Geochemistry and Geophysics, 15.

Kearey, P. (1991). *An Introduction to Geophysical Exploration* (Second ed.). Blackwell Scientific Publications.

Labson, V., A. Becker, H. Morrison, and U. Conti (1985). Geophysical exploration with audiofrequency natural magnetic fields. *Geophysics 50–4*, 656–664.

Lathi, B. (1989). *Modern digital and analog communication systems* (Second ed.). The Dryden Press – Saunders College Publishing.

Lockhart, G. and B. Cheetham (1989). *Basic Digital Signal Processing.* Butterworths & Co. Buterworth Basic Series.

Lynn, P. and W. Fuerst (1990, May). *Introductory Digital Signal Processing with Computer Applicatiions* (Second ed.). John Wiley & Sons.

Macnae, J. (1995, April). Design considerations for capacitive electrodes. In *Proceedings of the Workshop "Electrodes"*, pp. 32–35. Edited by G.Clerc and others. Workshop held at the Centre de Recherches Geophysiques de Garchy – France.

Marven, C. and G. Ewers (1994). *A simple approach to Digital Signal Processing.* Alden Press Limited.

Maxim (1992a). *1992 Analog Design Series*, Volume 1, Chapter MAX638 +5V/Adjustable CMOS Step-Down Switching Regulator, pp. 4–85,4–92. Maxim Corporation.

Maxim (1992b). *1992 Analog Design Series*, Volume 1, Chapter MAX660 CMOS Monolithic Voltage Converter, pp. 4–117,4–124. Maxim Corporation.

Mbipom, E. (1980). *Geoelectric Studies of the Crust and Upper Mantle in Northern Scotland.* Ph. D. thesis, University of Edinburgh.

McCracken, K., M. Oristaglio, and G. Hohmann (1986). A comparison of electromagnetic exploration systems. *Geophysics 51–3*, 810–818.

Metronix (1991). Broadband Inductioncoil Magnetometer Description and Operationg Manual. Technical Documentation.

Meunier, J. (1965). *Contribution à l'ètude expérimentale des problémes d'enregistrement électro–telluriques et á l'amélioration des techniques de prospection..* Ph. D. thesis, Faculté des Sciences de Paris. Laboratoire Géophysique Appliquée.

Meunier, J. (1995, April). Diurnal earthcurrents with short lines and unpolarized copper-sulphate-kaolin electrodes. In *Proceedings of the Workshop "Electrodes"*, pp. 22–25. Edited by G.Clerc and others. Workshop held at the Centre de Recherches Geophysiques de Garchy – France.

Milson, J. (1993). *Field Geophysics* (Second ed.). John Wiley & Sons.

MOTOROLA (1995). Oncore User's Manual. Reproduced by MAPLIN Electronics by permission of Motorola, Inc.

Munaut, M. (1973). Etude d'un nouveau typr d'electrode impolarisable. Diplôme d'ingénieur géophysicien. IPG Strasbourg.

Nail, R. et al. (1993). *Linear Design Seminar*, Chapter 3—Data Conversion, pp. 3.1–3.A27. Texas Instruments Limited. Edited by Dave Cox.

Nascimento, D. (1995, April). Telluric Pre–Amplifiers — Considerations on Noise. In *Proceedings of the Workshop "Electrodes"*, pp. 52–56. Edited by G.Clerc and others. Workshop held at the Centre de Recherches Geophysiques de Garchy – France.

Nascimento, D., G. Dawes, and O. Ritter (1994, May). SPAM Mk–3: a Low–power, Networked, Geophysical Data Acquisition and Processing System. In M.Menvielle and H.Grandis (Eds.), *Proceedings of the 12^{th} Workshop on Electromagnetic Induction in the Earth. Brest–France*, pp. 118. Poster presented at the Workshop.

Newport (1995). *DC-DC Converters*, Chapter NMH05/12/24 Series Dual Output 2W isolated DC-DC Converters, pp. 34–37. Newport Components.

OS (1988). Pathfinder 421 - ormiston & gifford. Ordinance Survey.

Parkinson, W. (1959). Directions of rapid geomagnetic fluctuations. *Jornal of Geophysics - Royal Astronomical Society 2–1*, 1–14.

Pearson, J. (1992). *Basic Communication Theory.* Prentice Hall.

Petiau, G. (1976). Etude spèctrale du bruit et diverses causes de perturbation affectant l'enregistrement du champ électrique tellurique de 0.01Hz. CRG/MTT Garchy–Nièvre.

Petiau, G. (1995, April). Pb–$PbCl_2$ Electrodes: Second Generation. In *Proceedings of the Workshop "Electrodes"*, pp. 49–51. Edited by G.Clerc and others. Workshop held at the Centre de Recherches Geophysiques de Garchy – France.

Petiau, G. and A. Dupis (1980). Noise, Temperature Coefficient, and Long Term Stability of Electrodes for Telluric Observations. In *Geophysical Prospecting*, Volume 28, pp. 792–804. European Association of Exploration Geophysicists. Geophysics reprint series.

Porstendorfer, G. (1975). *Principles of Magneto-Telluric Prospecting.* Geopublication Associates. Geoexploration Monographs - Series 1 - N ° .5.

Ritter, O. (1995). *An audiomagnetotelluric investigation of the Southern Upland Fault: novel instrumentation, field procedures and 3D modelling.* Ph. D. thesis, University of Edinburgh.

Ritter, O. (1996a). Emerald Data Processing V1.0. Private communication.

Ritter, O. and G. Dawes (1992). A Transputer based Multi-stationtudy Multitechnique Geophysical Data Acquisition System–SPAM 3. In V.Haak and H.Rodermann (Eds.), *Protokoll Kolloquium Elektromagnetische Tiefenforschung.*

Ritter, O., G. Dawes, and D. Nascimento (1994, May). New Development on the Way to High Resolution AMT. In *Proceedings of the 12th Workshop on Electromagnetic Induction in the Earth. Brest–France*, pp. 118. M.Menvielle and H.Grandis. Poster presented at the Workshop.Brest–France.

Ritter, P. (1996b). *Separation of Local and Regional Information in Geomagnetic Response Functions using Hypothetical Event Analysis.* Ph. D. thesis, University of Edinburgh.

Ritter, P., O. Ritter, G. D. SPAM Mk–III - User Manual. Internal Publication – Edinburgh University. Department of Geology and Geophysics.

Ruzié, G. (1995, April). Comparison between different electrodes for long term telluric measurements. In *Proceedings of the Workshop "Electrodes"*, pp. 40–48. Edited by G.Clerc and others. Workshop held at the Centre de Recherches Geophysiques de Garchy – France.

Schnegg, P. and G. Fischer (1980). On Line Determination of Apparent Resistivity in Magnetotelluric Soundings. In V.Haak and H.Rodermann (Eds.), *Protokoll Elektromagnetische Tiefenforschung–Berlin.*

Serson, P. (1973). Instrumentation for induction studies on land. *Physics of the Earth and Planetary Interiors 7*, 313–322.

Sims, W. (1969). *Methods of Magnetotelluric A.* Ph. D. thesis, University of Texas.

Sims, W., F. Bostick, and H. Smith (1971). The estimation of magnetotelluric impedance tensor elements from measured data. *Geophysics 36*, 938–942.

Spagnolini, U. (1994). Time-domain estimation of mt impedance tensor. *Geophysics 59–5*, 712–721.

Spies, B. (1989). Depth of investigation in electromagnetic sounding methods. *Geophysics 54–7*, 872–888.

Spitz, S. (1985). The magnetotelluric impedance tensor properties with respect to rotations. *Geophysics 50*, 1610–1617.

Suppan, L. (1995). Achieving reliable data with long-line RS-485. Electronic Product Design - December/1995.

Swift, C. (1967). *A Magnetotelluric Investigation of an Electrical Conductivity Anomaly in the Southwestern United States.* Ph. D. thesis, The Massachusetts Institute of Technology.

Telford, W. (1977). Characteristics of audio and sub-audio telluric signals. *Geophysical Prospecting 25*, 321–333.

Telford, W. (1990). *Applied Gephysics* (Second ed.). Cambridge University Press.

Terrel, T. (1985). *Introduction to Digital Filters.* MacMillan Publishers Ltd.

Tikhonov, A. (1950). On determining electrical characteristics of the deep layers of the earth's crust. *Doklady 73,2*, 295–297.

Tuinega, P. (1992). *SPICE: A guide to circuit simulation and analysis using PSPICE* (Second ed.). Prentice Hall.

Vanyan, L. et al. (1967). *Electromagnetics Depth Soundings.* Consultants Bureau.

Vozoff, K. (1972). The magnetotelluric method in the exploration of sedimentary basins. *Geophysics 37*, 98–141.

Vozoff, K. (1995, April). Campaign for intercomparison between electrodes - The Scientific Issues. In *Proceedings of the Workshop "Electrodes"*, pp. 11. Edited by G.Clerc and others. Workshop held at the Centre de Recherches Geophysiques de Garchy – France.

Vozoff, K. et al. (1963). Results and limitations of magnetotelluric surveys in simple geological situations. *Geophysics 28*, 778–792.

Weidelt, P. (1972). The inverse problem of geomagnetic induction. *Zeitschrift für Geophysik 38*, 257–289.

Wiese, H. (1962). Die streichrichtung der untergrundstrukturen des elektrischen widerstandes, erschlossen aus geomagnetischen variationen. *Pagegeophysiks 52*, 83–103.

Wight, D. (1988). *MT/EMAP Data Interchange Standard.* Society of Exploration Geophysicists.

Wight, D. and F. Bostick (1980). Cascade decimation - A technique for real time estimation of power spectra. In *Proceedings IEEE International Conference on Acoustic Speech and Signal Processing.*

Williams, A. (1981). *Electronic Filter Design Handbook.* McGraw-Hill Book Company.

Word, D., H. Smith, and F. Bostick (1971). Crustal investigations by the magnetotelluric impedance tensor. *The Structure of Physical Properties of the Earth's Crust 1*, 397–416.

APPENDIX A

System Identification

Box	Board	Name	Switch Type	Bits	Comments
Remote	DSP	Box ID	Rotary (HEX)	8	Remote Box Identification Number
Remote	Channel	Board ID	Single-in-Line	8	Board serial number
Remote	Channel	Channel Number	Rotary (HEX)	8	Sequential analogue channel number in the box
Sensor	Panel	Gain	Toggle	1	Electric signal amplification (x20/x100)
Sensor	Panel	High-Pass	Toggle	1	High-pass filter corner frequency (100/1000s)
Sensor	Panel	Low-Pass	Toggle	1	Low-pass filter corner frequency (256/4000Hz)
Sensor	Control	Box ID	Rotary (HEX)	4	Sensor Box Identification Number
Sensor	Control	Channels	Rotary (HEX)	4	Number of Sensors installed in the box
Sensor	Control	Board ID	Single-in-Line	7	Control board serial number
Sensor	Electric/Magnetic	Customer ID	Single-in-Line	3	Customer identification number
Sensor	Electric/Magnetic	Board ID	Single-in-Line	5	Sensor board serial number
Sensor	Electric/Magnetic	Sensor Type	Single-in-Line	3	Electric, Magnetic or Seismic
Sensor	Electric/Magnetic	Sensor Direction	Single-in-Line	3	North(X), East(Y) or Vertical

Table A.1: SPAM Mk-III Box/Board Module Identification and Operational Parameters

APPENDIX B

Schematic Diagrams

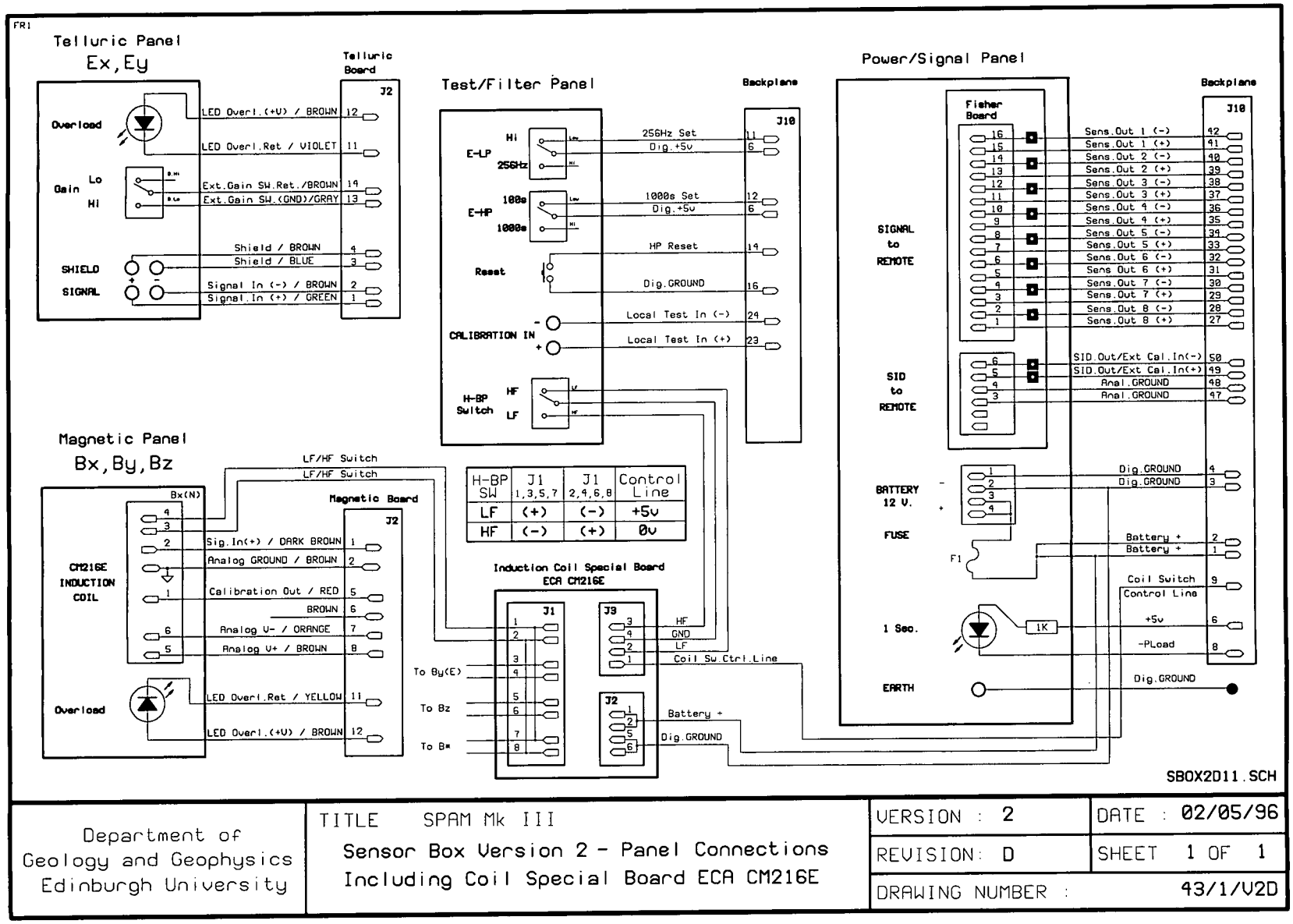

Figure B.1: Sensor box panel connections

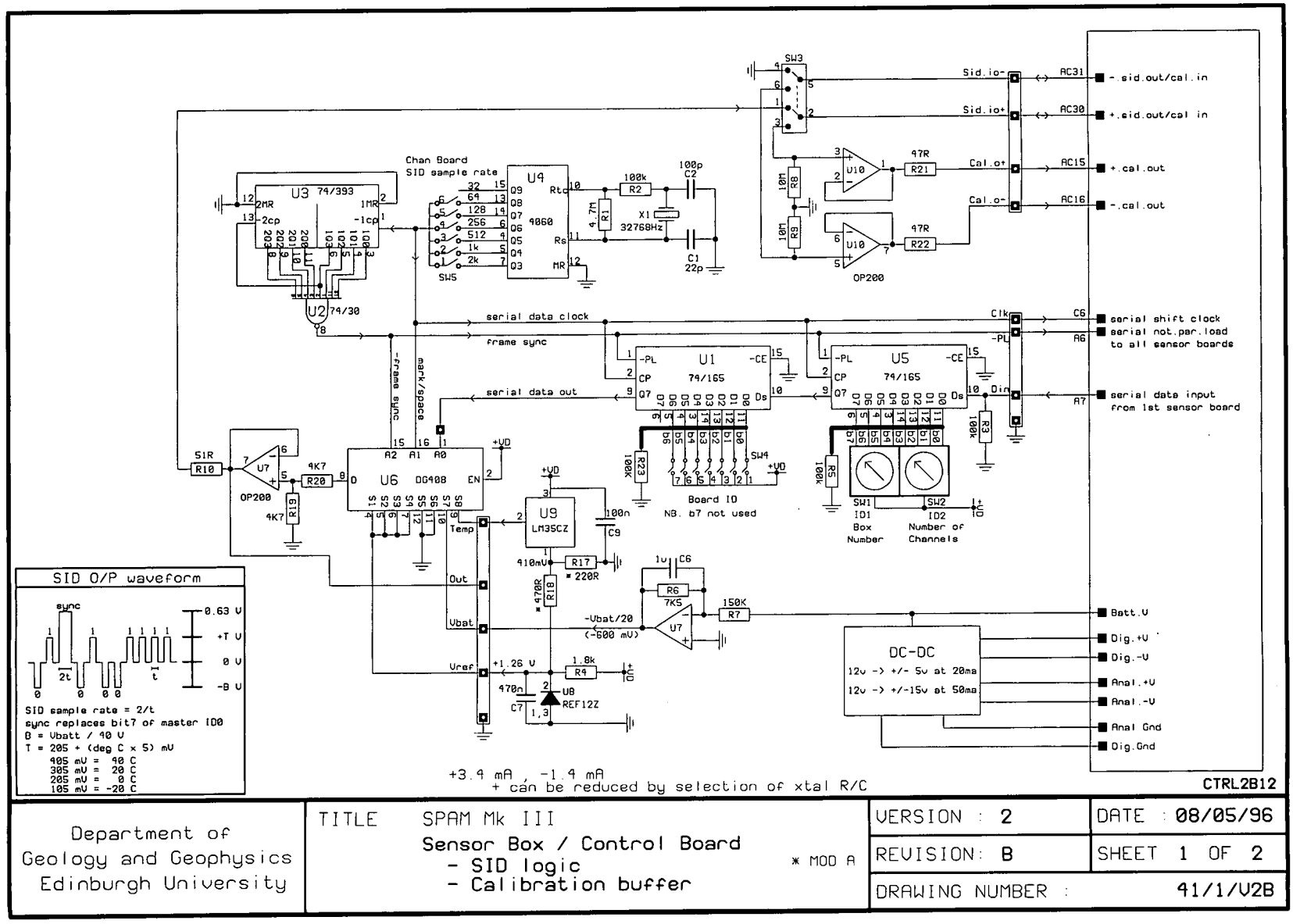

Figure B.2: Control Board - DC-DC Converters

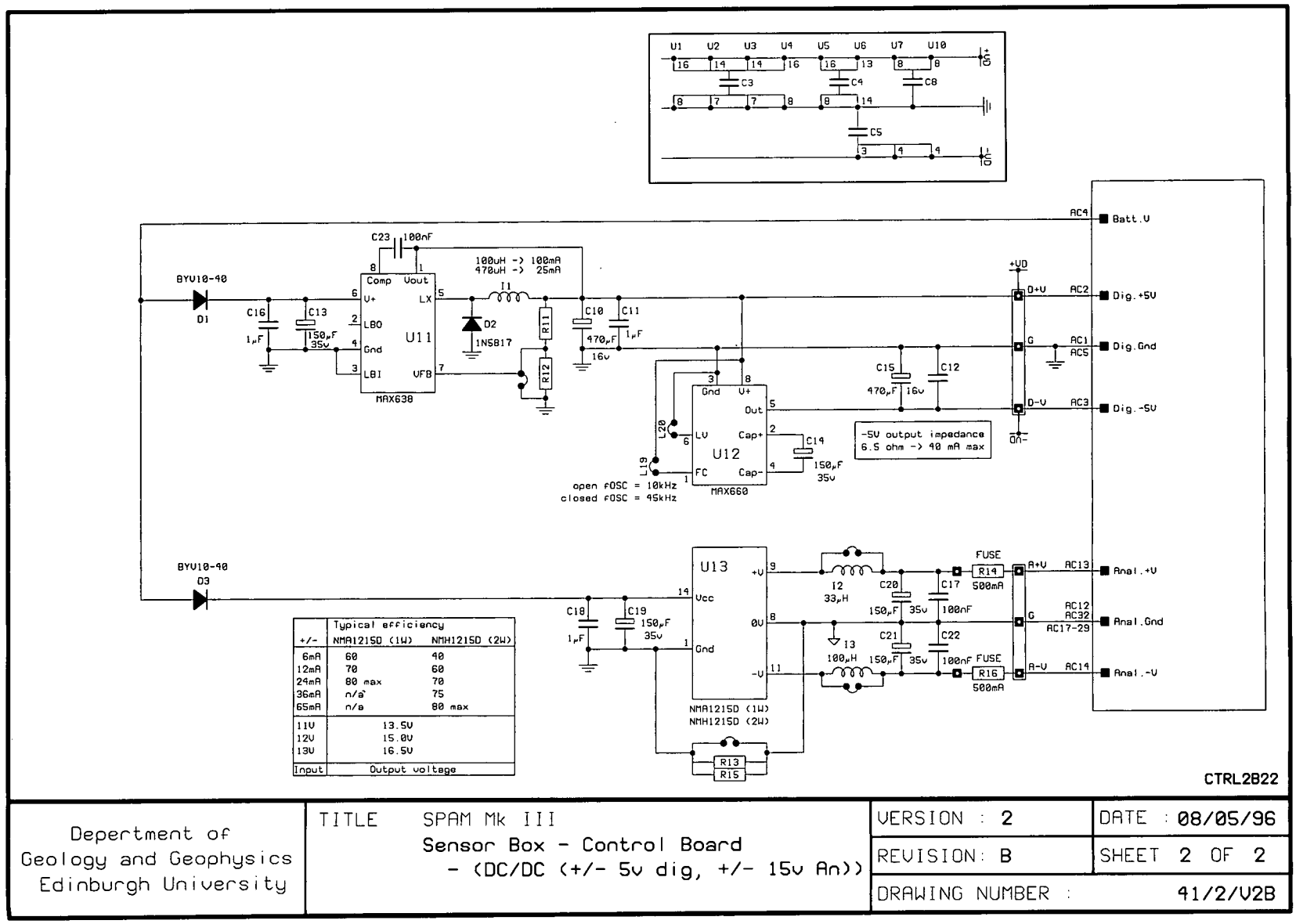

Figure B.3: Control Board - SID Logic and Calibration Buffer

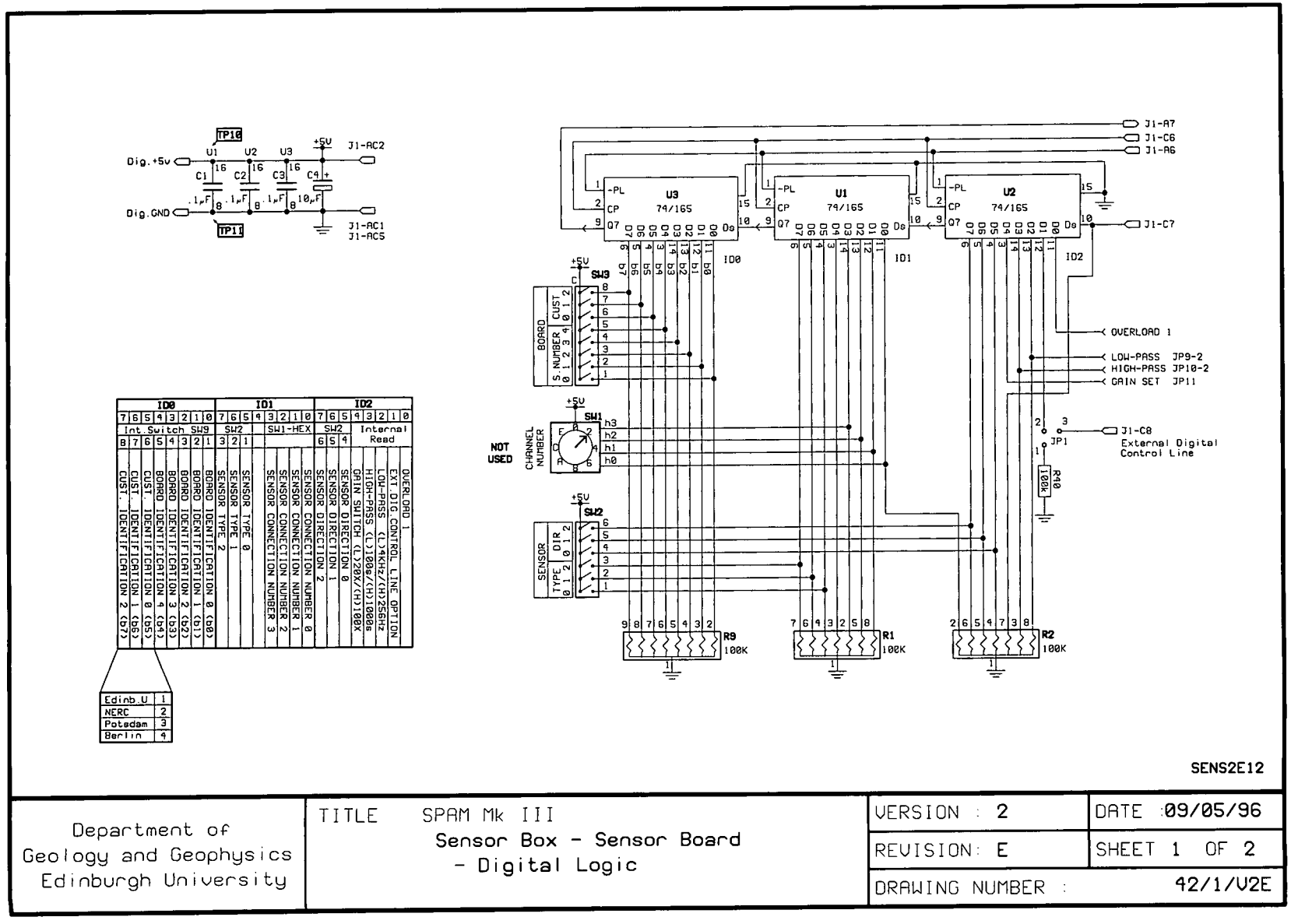

ID0								ID1								ID2							
7	6	5	4	3	2	1	0	7	6	5	4	3	2	1	0	7	6	5	4	3	2	1	0
Int. Switch SW9								SW2				SW1-HEX				SW2			Internal Read				
8	7	6	5	4	3	2	1	3	2	1						6	5	4					
CUST. IDENTIFICATION 2 (97)	CUST. IDENTIFICATION 1 (96)	CUST. IDENTIFICATION 0 (95)	BOARD IDENTIFICATION 4 (94)	BOARD IDENTIFICATION 3 (93)	BOARD IDENTIFICATION 2 (92)	BOARD IDENTIFICATION 1 (91)	BOARD IDENTIFICATION 0 (90)	SENSOR TYPE 2	SENSOR TYPE 1	SENSOR TYPE 0	SENSOR CONNECTION NUMBER 3	SENSOR CONNECTION NUMBER 2	SENSOR CONNECTION NUMBER 1	SENSOR CONNECTION NUMBER 0		SENSOR DIRECTION 2	SENSOR DIRECTION 1	SENSOR DIRECTION 0	GAIN SWITCH (L)20X/(H)100X	HIGH-PASS (L)100s/(H)1000s	LOW-PASS (L)4KHz/(H)256Hz	EXT.DIG.CONTROL LINE OPTION	OVERLOAD 1

Edinb.U	1
NERC	2
Potsdam	3
Berlin	4

Department of Geology and Geophysics Edinburgh University	TITLE SPAM Mk III Sensor Box - Sensor Board - Digital Logic	VERSION : 2	DATE :09/05/96
		REVISION: E	SHEET 1 OF 2
		DRAWING NUMBER :	42/1/V2E

Figure B.4: Electric Board - Digital Logic

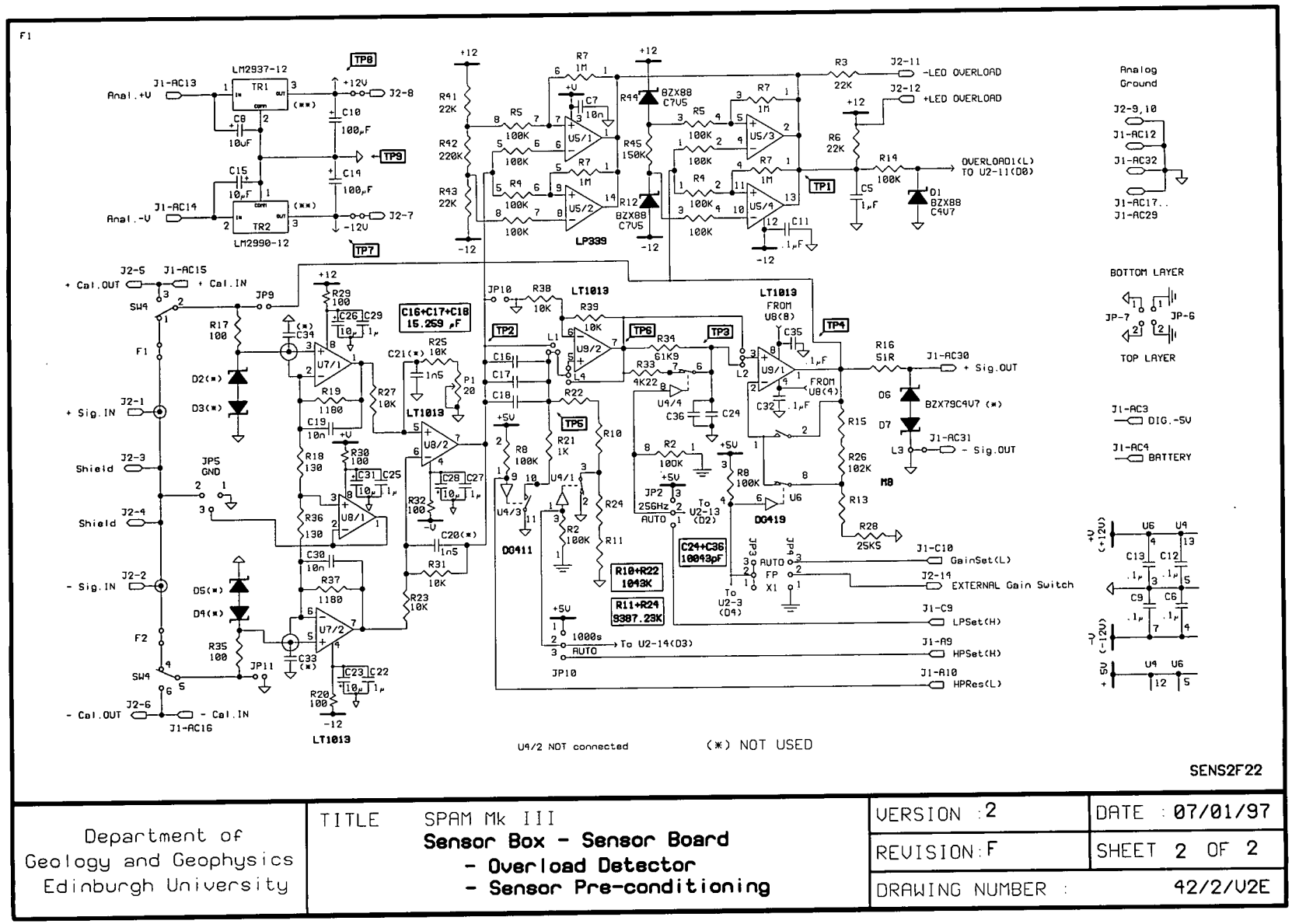

Figure B.5: Electric Board - Signal pre-conditioning and Overload detector

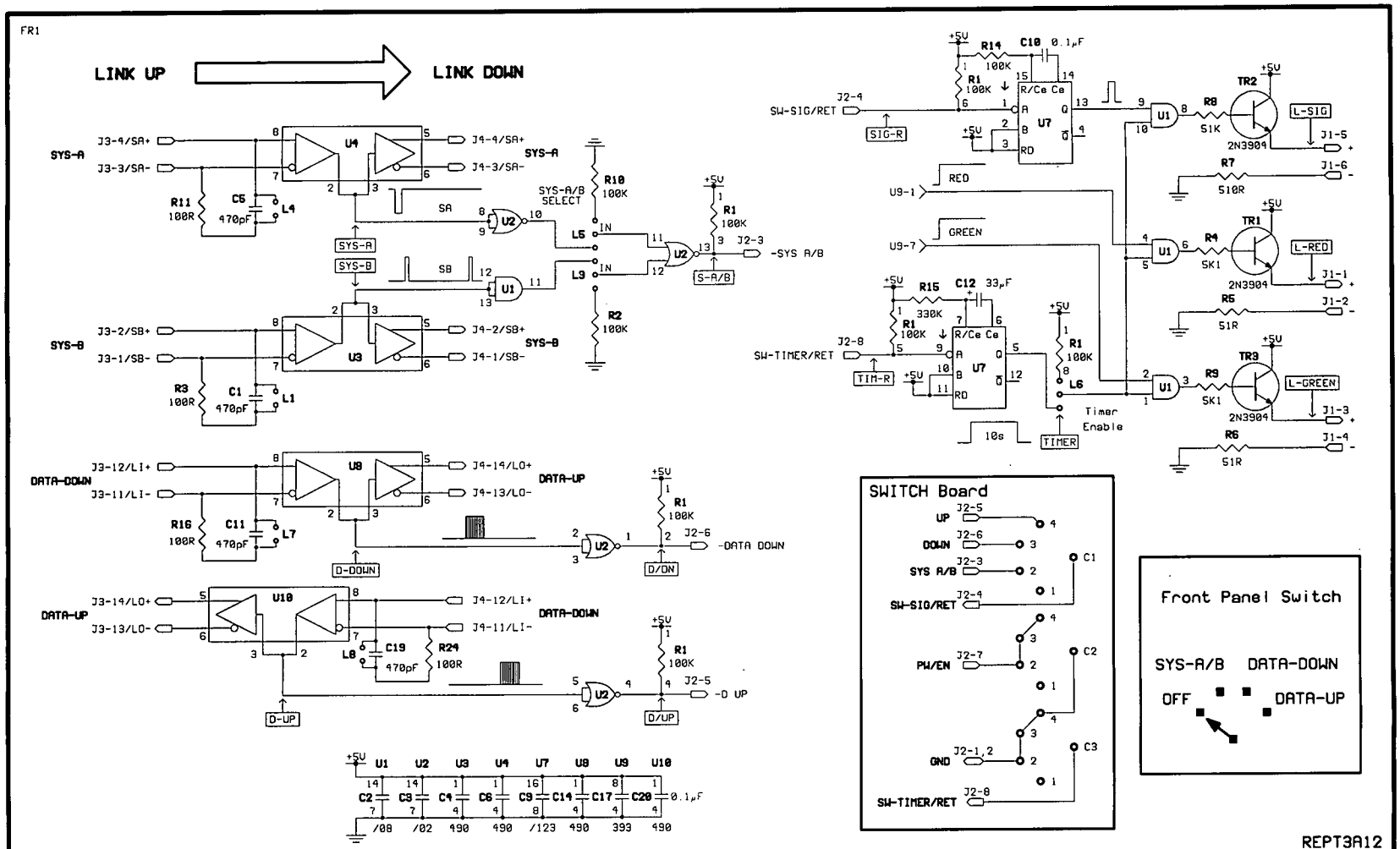

Department of Geology and Geophysics Edinburgh University	TITLE SPAM Mk III **REPEATER BOX** Drivers/Receivers Buffers LED Logic/Timer/Driver	VERSION : 3	DATE 24/07/96
		REVISION: A	SHEET 1 OF 2
		DRAWING NUMBER :	26/1/U3A

Figure B.6: Repeater Box - Driver/Receiver Buffers, LED Logic and Timer

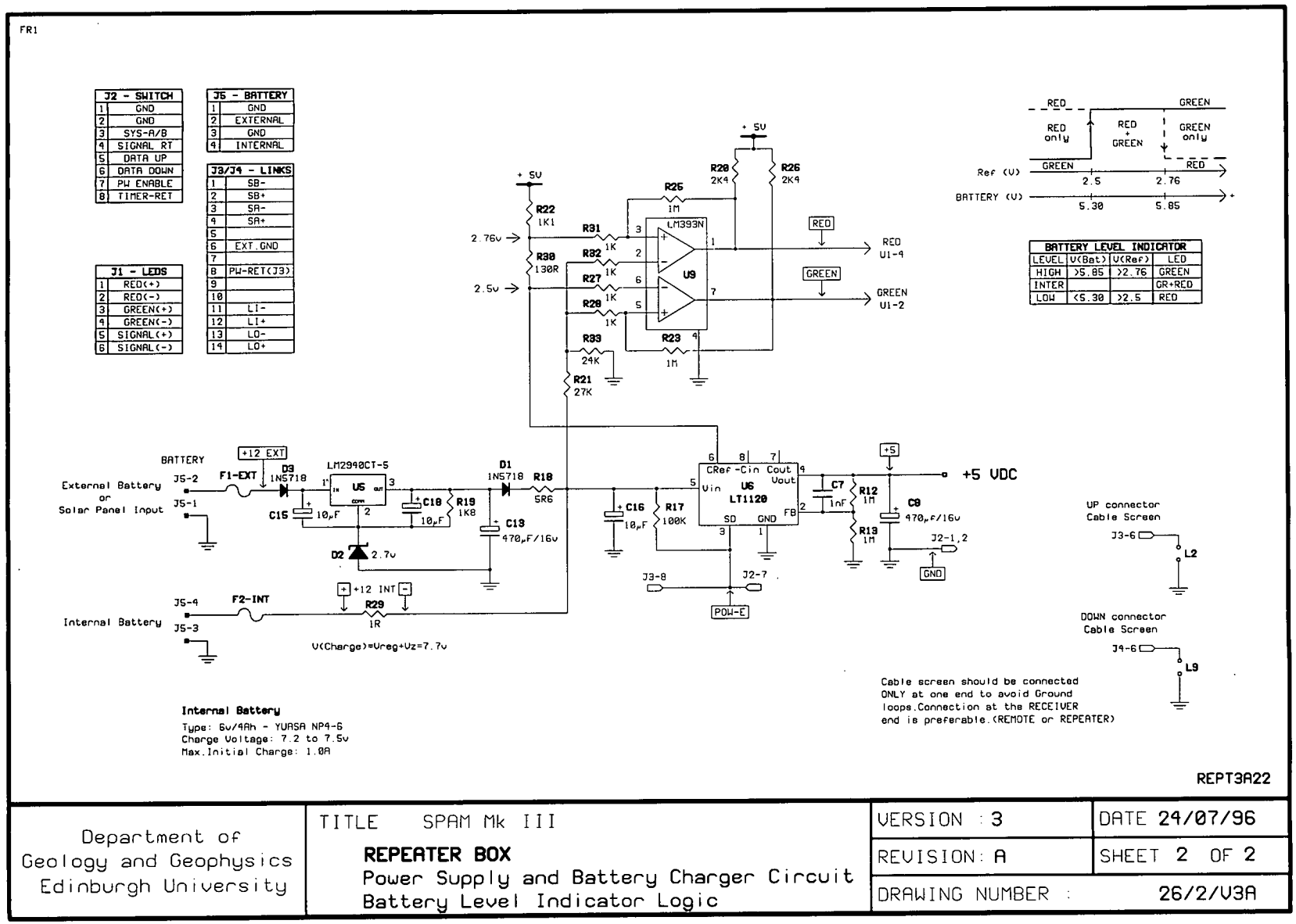

Figure B.7: Repeater Box - Power supply and Battery charger

APPENDIX C

Publications

The following papers have been published during the course of this study:

- D.Nascimento, G.Dawes and O.Ritter [1993]. *SPAM Mk-III A Low-Powered, Networked Geophysical Data Acquisition and Processing System.* 12^{th} Workshop on Electromagnetic Induction in the Earth. Poster Section P.12-05 and Proceedings:118.(Edited by M.Menvielle and H.Grandis)

- O.Ritter, G.Dawes and D.Nascimento [1993]. *New Developments on the Way to Higher Resolution AMT.* 12^{th} Workshop on Electromagnetic Induction in the Earth. Poster Section P.12-04 and Proceedings:118. (Edited by M.Menvielle and H.Grandis)

- D.Nascimento [1995]. *Telluric Pre-Amplifiers - Considerations on Noise.* Proceedings of the Workshop Electrodes Garchy-France: 52-56. (Edited by G.Clerc, F.Perrier, G.Petiau and M.Menvielle).

- D.Nascimento and G.Dawes [1995]. *SPAM Mk-III Sistema de Aquisição, Processamento e Análise de Dados para Aplicação em Geofísica.* 4° Congresso Internacional da Sociedade Brasileira de Geofísica. Resumos Expandidos: 681-683.

- D.Nascimento [submitted 1996]. *An Electrode Design for Magnetotelluric Soundings* Workshop Electrodes Garchy-France. - Technical Report to be published.